



Computational Fluid Dynamics Modelling and Experimental Analysis of Material Extrusion Additive Manufacturing

Mollah, Md. Tusher

Publication date:
2023

Document Version
Publisher's PDF, also known as Version of record

[Link back to DTU Orbit](#)

Citation (APA):
Mollah, M. T. (2023). *Computational Fluid Dynamics Modelling and Experimental Analysis of Material Extrusion Additive Manufacturing*. Technical University of Denmark.

General rights

Copyright and moral rights for the publications made accessible in the public portal are retained by the authors and/or other copyright owners and it is a condition of accessing publications that users recognise and abide by the legal requirements associated with these rights.

- Users may download and print one copy of any publication from the public portal for the purpose of private study or research.
- You may not further distribute the material or use it for any profit-making activity or commercial gain
- You may freely distribute the URL identifying the publication in the public portal

If you believe that this document breaches copyright please contact us providing details, and we will remove access to the work immediately and investigate your claim.

Computational Fluid Dynamics Modelling and Experimental Analysis of Material Extrusion Additive Manufacturing

Md. Tusher Mollah

PhD Thesis

PhD Dissertation

**Computational Fluid Dynamics Modelling and
Experimental Analysis of Material Extrusion Additive
Manufacturing**

by

Md. Tusher Mollah



Technical University of Denmark
Department of Civil and Mechanical Engineering
Section of Manufacturing Engineering

February 2023

Computational Fluid Dynamics Modelling and Experimental Analysis of Material Extrusion Additive Manufacturing

February 2023

PhD Student:

Md. Tusher Mollah, MSc

Department of Civil and Mechanical Engineering

Section of Manufacturing Engineering

Address: Produktionstorvet, Building 425, room 209, 2800 Kgs. Lyngby

E-mail: mtumo@dtu.dk

Main Supervisor:

Jon Spangenberg, Associate Professor, PhD, MSc

Department of Civil and Mechanical Engineering

Section of Manufacturing Engineering

Address: Produktionstorvet, Building 425, room 224, 2800 Kgs. Lyngby

E-mail: josp@dtu.dk

Co-Supervisors:

Raphaël Benjamin Comminal, Researcher, PhD, MSc

Department of Civil and Mechanical Engineering

Section of Manufacturing Engineering

Address: Produktionstorvet, Building 425, room 217, 2800 Kgs. Lyngby

E-mail: rcom@mek.dtu.dk

and

David Bue Pedersen, Senior Researcher, PhD, MSc

Department of Civil and Mechanical Engineering

Section of Manufacturing Engineering

Address: Produktionstorvet, Building 427, room 322, 2800 Kgs. Lyngby

E-mail: dbpe@dtu.dk

Preface and Acknowledgements

This dissertation was prepared in partial fulfilment of the requirements for obtaining the PhD degree in manufacturing engineering at Technical University of Denmark (DTU). The work contained in this dissertation was carried out at the Department of Civil and Mechanical Engineering from 15 July 2019 to 5 February 2023, which included a six-and-a-half-month parental leave. The work also included an external research stay of four months at Loughborough University, UK. The project was funded by the Danish Council for Independent Research (DFF) | Technology and Production Sciences (FTP) (Contract No. 8022-00042B). The study was supervised by Associate Professor Dr. Jon Spangenberg, and co-supervised by Researcher Dr. Raphaël Comminal and Senior Researcher Dr. David Bue Pedersen.

Individual efforts can only result in a prolific and successful outcome with the help of others. Therefore, I express my gratitude and appreciation to the following people who contributed invaluable to the completion of the works appended in this PhD dissertation, as well as the generous funding from the DFF.

Foremost, I would like to express my sincere gratitude, respect, and appreciation to my supervisors for their immense academic guidance, trust, and support during the whole period. Special thanks to Dr. Jon Spangenberg for always having his door open for discussions about both academic and social life. He has been a wonderful mentor and motivator to me throughout the writing of my PhD. I sincerely thank Dr. Raphaël Comminal for his scientific expertise and for being an excellent instructor, especially when I was learning new stuff. I also thank Dr. David Bue Pedersen for his inspirational ideas and invaluable help in decision-making.

I would like to thank all of my collaborators for their support in the manuscripts appended to this dissertation. In particular, my sincere gratitude goes to Dr. Marcin Piotr Serdeczny and Dr. Berin Šeta for their collaboration and for their friendship. Furthermore, I extend my appreciation to all my fellow office colleagues (room 209) and colleagues from other offices in buildings 425 and 427 for creating a great work environment and sharing daily-life activities. I appreciate our Head of Section, Professor Dr. Jesper Henri Hattel, for his positive attitude and support during MUS.

As part of this work, I conducted an external research at Loughborough University, UK. Therefore, I am grateful to Loughborough University for this opportunity. Furthermore, I extend my gratitude to Dr. Andy Gleadall for hosting my visit and for his support of the research carried out over there. Moreover, I would like to thank Otto Mønstedts Fond and Thomas B. Thriges Fond for their partial funding for the external research stay.

Finally, I thank my friends and family members for their support which helped me to get adjusted to Denmark as the very first country I flew to. Finally, yet importantly, I want to thank my wonderful wife Kaniz Fatema and our daughter Tanaz Sehrish Mollah for their endless love and support. Having Tanaz during the PhD years was no less than another PhD study, yet it is infinite happiness when Tanaz says Abbu, Baba, Papa and Daddy!

Copenhagen, 3 January 2023

Md. Tusher Mollah

To my Parents...

Abstract

This PhD dissertation concerns the Computational Fluid Dynamics (CFD) modelling and experimental analysis of Material Extrusion Additive Manufacturing (MEX-AM). MEX-AM is an umbrella term that includes Fused Deposition Modelling (FDM), Robocasting (RC), and 3D Concrete Printing (3DCP). The technology offers fabrication of parts/structures on various scales using a wide range of materials. Despite it being a popular fabrication method, the technology faces several challenges that are yet to be solved. Some of the challenges are addressed in this dissertation. Specifically, numerical and experimental work is presented on FDM printing of dimensionally accurate corners. Furthermore, simulations are carried out to study the geometrical stability (i.e., uniform size) of layers produced by RC and 3DCP. Finally, simulations and experiments are exploited to investigate the possibility of integrating reinforcement bars with 3DCP.

The dissertation outlines the governing equations for the deposition of materials in MEX-AM. It discusses constitutive models such as Newtonian, generalized Newtonian, and elasto-viscoplastic fluid, and how they can be used to simulate MEX-AM of different materials. Subsequently, experimental details and the post-processing of results are presented. Finally, the results are presented in seven appended publications.

The study on the deposition of corners is carried out and compared for different corner angles and for two different extruders, Bowden and direct drive. The Bowden extruder cannot control the amount of material extruded during the nozzle movement at the corner, whereas the direct drive can. It is found that the direct drive extruder produces a more rounded edge at the outer side of the corner. Furthermore, the study enabled novel insight into the accuracy of the CFD model and the state of the material at the corners, as well as the discrepancy between experimental, analytical, and simulation results.

Three different printing strategies are considered when analysing the geometrical stability of layers: wet-on-wet, wet-on-semisolid, and wet-on-solid printing. In wet-on-wet printing, a wet layer is printed on top of a wet layer (i.e., the material properties do not change over time). In the other two cases, the printed layer is semi-solidified or solidified. The cross-section of deposited layers, deformation of the bottom layer, and extrusion pressure are studied when printing wet-on-wet for different material properties (i.e., yield stress and plastic viscosity) and processing parameters (i.e., extrusion speed, printing speed, nozzle diameter, and layer height). The results illustrate that the deformation is highly dependent on these parameters. In addition, the simulations show that the deformation can be reduced but not eliminated, i.e., a stable print without deformation cannot be obtained by wet-on-wet printing. The wet-on-solid printing simulations illustrate stable printing and give a conservative estimate of the yield stress required by the already printed layer in order not to deform. The wet-on-semisolid printing is simulated using a yield stress buildup of the already printed layer. The yield stress buildup is modelled by applying a scalar approach that changes the materials' property between the layers. Based on the results, it is demonstrated that altering the process parameters can reduce the requirement for the yield stress buildup, while still print stable layers.

The bonding between rebars and deposited concrete is analysed in terms of the formation of air voids inside the structure. The simulated cross-sectional shapes of the printed structure are compared with experiments and are found to capture the formation of air

voids accurately. The CFD models are applied to analyse three scenarios: no rebar, a horizontal rebar, and cross-shaped rebars. The models illustrate that by changing the process parameters one can eliminate the air voids around the horizontal rebar, while alterations in the toolpath and rebar geometry are necessary to fully mitigate air voids when printing around cross-shaped rebars.

Danske Resumé

Denne Ph.d.-afhandling omhandler Computational Fluid Dynamics (CFD) modellering samt eksperimentel analyse af ekstruderings-baseret additiv fremstilling (MEX-AM). MEX-AM er et paraplybegreb, som omfatter Fused Deposition Modelling (FDM), robocasting (RC) og 3D beton printning (3DBP). Teknologien muliggør produktion af komponenter/strukturer i forskellig skala ved brug af en lang række materialer. Selvom det er en populær produktionsmetode, så står teknologien overfor adskillige udfordringer, som stadig skal løses. Nogle af udfordringerne adresseres i denne afhandling, så som, hvordan man FDM printer med høj geometrisk præcision in hjørner. Derudover undersøges det numerisk, hvordan de printede lag gøres geometrisk stabile (dvs. gør lagene ensartede i størrelse), når der fremstilles med RC. Endelig anvendes simuleringer og eksperimenter til at undersøge muligheden for integrere armering med 3DBP.

Afhandlingen beskriver hovedligningerne for hvordan materialet flyder under MEX-AM. Afhandlingen præsenterer konstitutive modeller for Newtonske, generaliseret Newtonske og elasto-visoplastiske fluider, og hvordan disse kan bruges til at simulere MEX-AM af forskellige materialer. Afslutningsvis, vises resultaterne i syv vedlagte publikationer.

Undersøgelsen af hvordan man bedst muligt FDM printer et hjørne foretages med forskellige vinkler samt forskellige printhoveder, Bowden og direct drive. Bowden-printhovedet kan ikke styre mængden, der bliver ekstruderet, lige så præcist som direct drive kan. Derudover vises det, at direct drive ekstruderen producerer mere runde kanter på ydersiden af hjørnet. Desuden har undersøgelsen givet ny indsigt i CFD-modellens præcision og materialets geometri i hjørnerne samt forskellen mellem eksperimenter, analytiske løsninger og den numeriske model.

Tre forskellige printstrategier anvendes til at undersøge lagenes geometriske stabilitet: vådt-i-vådt, vådt-i-halvtørt og vådt-i-tørt. Med vådt-i-vådt menes, at et vådt lag placeres ovenpå et vådt lag (dvs. materialeegenskaberne ændrer sig ikke over tid). I de to andre tilfælde printes der på et halvtørt eller tørt lag. Ift. vådt-i-vådt printning undersøges det, hvordan lagene deformerer og ekstruderingsstrykket ændres med forskellige materialeegenskaber (dvs. flydespændingen og plastisk viskositet) samt procesparametre (f.eks. ekstruderingshastighed, printhastighed, dysediameter og laghøjde). Resultaterne viser, at deformationen af lagene i høj grad afhænger af disse parametre. Desuden viser simuleringerne, at deformationen kan reduceres, men ikke elimineres - dvs. et fuldstændigt geometrisk stabilt print kan ikke opnås, når der printes vådt-i-vådt. Simuleringerne af vådt-i-tørt printningen er geometriske stabile og giver et konservativt estimat for den flydespænding, der kræves af det allerede printede lag for ikke at deformere. Modellen simulerer vådt-i-halvtørt printning ved at forøge flydespændingen af det allerede printede lag. Dette opnås med en skalar metodik. Baseret på CFD modellens resultater påvises det, at man ved at ændre procesparametrene kan reducere kravet til forøgelsen af flydespændingen uden at kompromittere stabiliteten af lagene.

Integrationen af armering med 3DBP undersøges mht. hulrumsdannelse mellem betonen og armeringsstængerne. De simulerede tværsnit af den printede struktur sammenlignes med eksperimenter og viser at modellen med høj præcision kan prædiktere hulrumsdannelsen. CFD-modeller anvendes til at analysere tre scenarier: ingen

armeringsstang, en vandret armeringsstang og krydsformede (vandret og horisontal) armeringsstænger. Modellerne viser, at man ved at ændre procesparametrene kan eliminere hulrummene om den vandrette armeringsstang, mens det samme kan opnås for krydsformede armeringsstænger, hvis printstrategien samt geometrien af armeringsstangssammenføjningen ændres.

List of Publications

The dissertation is based on the following publications that are attached at the end:

- [A.1] **M.T. Mollah**, A. Moetazedian, A. Gleadall, J. Yan, W.E. Alphonso, R. Comminal, B. Šeta, T. Lock, J. Spangenberg, Investigation on corner precision at different corner angles in material extrusion additive manufacturing: An experimental and computational fluid dynamics analysis, in: *Solid Freeform Fabrication Symposium 2022: 33rd Annual Meeting*, University of Texas at Austin, 2022: pp. 872–881.
- [A.2] **M.T. Mollah**, R. Comminal, M.P. Serdeczny, D.B. Pedersen, J. Spangenberg, Stability and deformations of deposited layers in material extrusion additive manufacturing, *Additive Manufacturing*. 46 (2021) 102193.
- [A.3] **M.T. Mollah**, R. Comminal, M.P. Serdeczny, D.B. Pedersen, J. Spangenberg, Numerical Predictions of Bottom Layer Stability in Material Extrusion Additive Manufacturing, *JOM*. 74 (2022) 1096–1101.
- [A.4] **M.T. Mollah**, M.P. Serdeczny, R. Comminal, B. Šeta, M. Brander, D.B. Pedersen, J. Spangenberg, A Numerical Investigation of the Inter-Layer Bond and Surface Roughness during the Yield Stress Buildup in Wet-On-Wet Material Extrusion Additive Manufacturing, in: *2022 Summer Topical Meeting: Advancing Precision in Additive Manufacturing*, American Society for Precision Engineering, TN, USA, 2022: pp. 131–134.
- [A.5] **M.T. Mollah**, R. Comminal, M.P. Serdeczny, B. Šeta, J. Spangenberg, Computational analysis of yield stress buildup and stability of deposited layers in material extrusion additive manufacturing. *Submitted to Additive Manufacturing*.
- [A.6] J. Spangenberg, W.R. Leal da Silva, **M.T. Mollah**, R. Comminal, T. Juul Andersen, H. Stang, Integrating Reinforcement with 3D Concrete Printing: Experiments and Numerical Modelling, in: R. Buswell, A. Blanco, S. Cavalaro, P. Kinnell (Eds.), *Third RILEM International Conference on Concrete and Digital Fabrication*, Springer International Publishing, Cham, 2022: pp. 379–384.
- [A.7] **M.T. Mollah**, R. Comminal, W.R. Leal da Silva, B. Šeta, J. Spangenberg, Integration of reinforcement bar and state of air void in 3D concrete printing. *Submitted to Cement and Concrete Research*.

The following publications were contributed during the course of the PhD study. However, these are not a part of this dissertation:

➤ **Journal Publications**

- [B.1] M.P. Serdeczny, R. Comminal, **M.T. Mollah**, D.B. Pedersen, J. Spangenberg, Numerical modeling of the polymer flow through the hot-end in filament-based material extrusion additive manufacturing, *Additive Manufacturing*. 36 (2020) 101454.
- [B.2] J. Spangenberg, W.R. Leal da Silva, R. Comminal, **M.T. Mollah**, T.J. Andersen, H. Stang, Numerical simulation of multi-layer 3D concrete printing, *RILEM Technical Letters*. 6 (2021) 119–123.
- [B.3] **M.T. Mollah**, H.K. Rasmussen, S. Poddar, M.M. Islam, M. Parvine, Md.M. Alam, G. Lorenzini, Ion-Slip Effects on Bingham Fluid Flowing Through an Oscillatory Porous Plate with Suction, *Mathematical Modelling in Engineering Problems*. 8 (2021) 673–681.
- [B.4] **M.T. Mollah**, S. Poddar, M.M. Islam, M.M. Alam, Non-isothermal Bingham fluid flow between two horizontal parallel plates with Ion-slip and Hall currents, *SN Applied Sciences*. 3 (2021) 115.
- [B.5] S. Khatun, M.M. Islam, **M.T. Mollah**, S. Poddar, M.M. Alam, EMHD radiating fluid flow along a vertical Riga plate with suction in a rotating system, *SN Applied Sciences*. 3 (2021) 452.
- [B.6] M.P. Serdeczny, R. Comminal, **M.T. Mollah**, D.B. Pedersen, J. Spangenberg, Viscoelastic simulation and optimisation of the polymer flow through the hot-end during filament-based material extrusion additive manufacturing, *Virtual and Physical Prototyping*. 17 (2022) 205–219.
- [B.7] H. Moghadasia, **M.T. Mollah**, D. Marla, H. Saffari, J. Spangenberg. Computational fluid dynamics modeling of top-down digital light processing additive manufacturing. *In preparation*.
- [B.8] B. Šeta, M. Sandberg, M. Brander, **M.T. Mollah**, D.K. Pokkalla, V. Kumar, J. Spangenberg. Modeling fiber orientation and strand shape morphology in three-dimensional material extrusion additive manufacturing. *Submitted to Composites Part B: Engineering*.
- [B.9] **M.T. Mollah**, A. Moetazedian, A. Gleadall, J. Yan, W.E. Alphonso, R. Comminal, B. Šeta, T. Lock, J. Spangenberg, Influence of printing parameters on the precision of corners of different angles in material extrusion additive manufacturing. *In Preparation*.

➤ **Conference Publications**

- [B.10] B. Šeta, M. Brander, **M.T. Mollah**, V. Kumar, D.K. Pokkalla, S. Kim, J. Spangenberg, Modelling of Additive Manufacturing–Compression Molding Process using Computational Fluid Dynamics, in: *2022 Summer Topical Meeting: Advancing Precision in Additive Manufacturing*, American Society for Precision Engineering, American Society for Precision Engineering, TN, USA, 2022: pp. 119–123.
- [B.11] B. Šeta, **M.T. Mollah**, V. Kumar, D.K. Pokkalla, S. Kim, A.A. Hassen, J. Spangenberg, Modelling Fiber Orientation during Additive Manufacturing–Compression Molding Processes, in: *Solid Freeform Fabrication Symposium 2022: 33rd Annual Meeting*, University of Texas at Austin, 2022: pp. 906–919.
- [B.12] R. Tonello, **M.T. Mollah**, A. Strandlie, J. Spangenberg, D. B. Pedersen, J. R. Frisvad. Influence of the Printing Direction on the Surface Appearance in Multi-Material Fused Filament Fabrication. *In Preparation*.
- [B.13] E.A. Khalid, A.K. Issam, **M.T. Mollah**, J. Spangenberg. Computational Fluid Dynamics Modelling of Mortar Extrusion and Path Planning Strategy at the Corner for 3D Concrete Printing. *Casablanca International Conference on Additive Manufacturing*, November 23-24, 2022, Casablanca, Morocco. *Accepted*.

Contents

Preface and Acknowledgements	iii
Abstract	vii
Danske Resumé	ix
List of Publications	xi
Contents	xiv
Nomenclature	xvi
1 Introduction	1
1.1 Motivation	1
1.2 Material Extrusion Additive Manufacturing	1
1.3 Literature review	3
1.2.1 Corner printing	4
1.2.2 Morphology and stability of multilayer prints	5
1.2.3 Integrating reinforcement bars in 3DCP	5
1.4 Research objectives and outline of this dissertation	6
2 Methodologies	8
2.1 Governing equations	8
2.2 Constitutive models	8
2.2.1 Newtonian Fluid	8
2.2.2 Generalized Newtonian Fluid	9
2.2.3 Elasto-viscoplastic Fluid	10
2.3 CFD models and data post-processing	11
2.3.1 CFD modelling of corner printing	11
2.3.2 Post-processing of corner printing simulations	12
2.3.3 CFD modelling of morphology and stability of multilayer prints	13
2.3.4 Post-processing of morphology and stability of multilayer prints	17
2.3.5 CFD modelling of integrating reinforcement bars in 3DCP	19
2.3.6 Post-processing of integrating reinforcement bars in 3DCP simulations	20
2.4 Experimental methods	21
2.4.1 Corner printing experiments	21
2.4.2 Post-processing of corner printing experiments	23
2.4.3 Integrating reinforcement bars in 3DCP experiments	23
2.4.4 Post-processing of integrating reinforcement bars in 3DCP experiments	24
3 Summary of Appended Papers	26
Overview	26
Publication [A.1]	26
Publication [A.2]	27

Publication [A.3]	27
Publication [A.4]	28
Publication [A.5]	28
Publication [A.6]	29
Publication [A.7]	29
4 Conclusions and future work	30
4.1 Conclusions	30
1.2.4 Corner printing	30
1.2.5 Morphology and stability for multilayer prints	30
1.2.6 Integrating reinforcement bars in 3DCP	32
1.2.7 General comments on findings	32
4.2 Ideas for future works	33
Bibliography	34
Appended Publications	43
Publication [A.1]: Investigation on corner precision at different corner angles in material extrusion additive manufacturing: An experimental and computational fluid dynamics analysis	43
Publication [A.2]: Stability and deformations of deposited layers in material extrusion additive manufacturing	57
Publication [A.3]: Numerical predictions of bottom layer stability in material extrusion additive manufacturing	79
Publication [A.4]: A Numerical Investigation of the Inter-Layer Bond and Surface Roughness during the Yield Stress Buildup in Wet-On-Wet Material Extrusion Additive Manufacturing	89
Publication [A.5]: Computational analysis of yield stress buildup and stability of deposited layers in material extrusion additive manufacturing	96
Publication [A.6]: Integrating reinforcement with 3D Concrete Printing: Experiments and numerical modelling	117
Publication [A.7]: Integration of reinforcement bars in 3D concrete printing	125

Nomenclature

Abbreviations

MEX-AM	Material Extrusion Additive Manufacturing
3D	Three Dimensions
2D	Two Dimensions
CFD	Computational Fluid Dynamics
FDM	Fused Deposition Modelling
FFF	Fused Filament Fabrication
CC	Contour Crafting
RC	Robocasting
3DCP	3D Concrete Printing
NF	Newtonian Fluid
GNF	Generalized Newtonian Fluid
EVP	Elasto-viscoplastic
PLA	Polylactic acid
FVM	Finite Volume Method
FAVOR	Fractional Area/Volume Obstacle Representation
VOF	Volume of Fluid
STL	Standard Tessellation Language

Symbols

ρ	Density of the fluid	kg/m ³
\mathbf{u}	Velocity vector of the fluid	m/s
t	Time	s
p	Pressure	Pa
\mathbf{g}	Gravitational acceleration vector	m/s ²
$\boldsymbol{\sigma}$	Deviatoric stress tensor	Pa
\mathbf{D}_T	Deformation rate tensor	1/s
μ	Fluid viscosity	Pa.s
μ_{app}	Apparent viscosity of fluid	Pa.s
$\dot{\gamma}$	Shear rate	1/s
τ	Magnitude of deviatoric stress tensor	Pa
τ_0	Yield stress	Pa
η_P	Plastic viscosity	Pa.s
$\mu_{max.app}$	Maximum apparent viscosity of fluid	Pa.s
$\dot{\gamma}_c$	Critical shear rate	1/s
$\boldsymbol{\sigma}_V$	Viscous stress tensor	Pa
$\boldsymbol{\sigma}_E$	Elastic stress tensor	Pa
\mathbf{E}	Small deformation rate tensor	1/s
$\boldsymbol{\sigma}_E^*$	Elastic stress tensor of unyielded materials	Pa
G	Shear modulus	kPa
G'	Storage modulus	kPa
\mathbf{W}_T	Vorticity tensor	1/s
σ_{vM}	Von Mises stress	Pa
$II_{\sigma_E^*}$	Second invariant of $\boldsymbol{\sigma}_E^*$	Pa ²
t_0	Initial time	s

Nomenclature

$\tau_{printing}$	Yield stress of printing material	Pa
$\tau_{printed}$	Yield stress of printed material	Pa
S_c	Scalar concentration	kg/m ³
$\mu_{SC.app}$	Apparent viscosity of scalar/printed material	Pa.s
$\mu_{max.SC.app}$	Maximum apparent viscosity of scalar/printed material	Pa.s
μ_{mix}	Mixture of the viscosities of printing and printed materials	Pa.s
$\mu_{cv.app}$	Apparent viscosity in a given control volume	Pa.s
Dn	Diameter of the nozzle	mm
h	Layer height	mm
U	Extrusion speed	mm/s
V	Printing speed	mm/s
S_r	Speed ratio V/U	-
G_r	Geometric ratio h/Dn	-
W	Nominal width of deposited layer	mm
l	Length of deposited layer	mm
De_i	Relative deformation (along the width) of the bottom layer	-
w_i	Width of the bottom layer just after the deposition of the i -th layer	mm
w_1	Initial width of the bottom layer when it is printed	mm
w_2	Bottom layer width when 2 nd layer is printed	mm
w_3	Bottom layer width when 3 rd layer is printed	mm
Ra	Arithmetic mean roughness	mm
P_E	Extrusion pressure	Pa
Dnr	Nozzle-rebar distance	mm
V_V	Percentage of volume of air void	%
Dr	Diameter of rebar	mm
Hr	Distance of horizontal rebar from the substrate	mm

1 | Introduction

This chapter outlines the key topics of the dissertation and their importance. The chapter begins with a description of the motivation for the study. It then discusses the three-dimensional (3D) printing technique, Material Extrusion Additive Manufacturing (MEX-AM) and the technologies it covers. Furthermore, a brief overview of previously published research and accompanying research gaps are presented. Finally, the chapter outlines the research objectives and structure of the dissertation.

1.1 Motivation

In MEX-AM an extrusion nozzle is used to selectively deposition material in two-dimensional layers that are positioned on top of each other until a 3D object is produced [1–6]. MEX-AM has gained significant popularity in recent years due to its versatility, scalability and ease of use. It covers a range of technologies, such as “Fused Deposition Modelling (FDM)” [7], “Robocasting” [8], and “3D Concrete Printing (3DCP)” [9], and can be used for a large number of applications. FDM is widely used for low-cost prototyping, while Robocasting is used to produce parts of complex geometries with high mechanical strength [10,11], as well as to manufacture parts for biomedical applications such as tissue engineering and drug delivery systems [12,13]. 3DCP has the potential to revolutionize the construction industry by enabling efficient and cost-effective production of complex concrete structures [14,15]. In addition to the variety of applications, MEX-AM can be carried out with a broad range of materials, making it one of the most applied additive manufacturing technologies in the world [16].

Despite its popularity, MEX-AM requires attention in order to better understand the printing process and thereby reduce printing time, increase mechanical strength [17], and improve the geometrical precision of the printed part (i.e., improve surface roughness [18], lower internal porosity [19], less deformation of layers [20], etc.). The MEX-AM improvements can be obtained by deep diving into several aspects of the printing process such as the printer setup, the material behaviour inside the nozzle, the material flow during deposition, the post-processing of the part, etc. The goal of this dissertation is to investigate the material flow during deposition.

1.2 Material Extrusion Additive Manufacturing

In MEX-AM, the material in the form of a hot-melt, a paste, a soft-material, or a hydrogel is extruded through a nozzle to build an object layer by layer [21–23]. Consequently, it is possible to print objects of various sizes (from micro components to buildings) with different mechanical and thermal properties. Among the technologies under MEX-AM, FDM is the oldest, first developed in the 1980s by S. Scott Crump [24]. The term FDM and is trademarked by the company Stratasys Inc., which was co-founded by S. Scott Crump [25]. FDM is also known as “Fused Filament Fabrication (FFF)”. In FDM, a solid filament is guided into a liquefier using a drive gear. During the liquefier phase, the filament is heated above the glass transition temperature and is transformed into a hot-melt, which is subsequently deposited by the nozzle [26–32]. There are two types of driver gears, one of which is located outside the print-head, known as the Bowden extruder, and the other inside, called the Direct-drive [33–36]. Materials such as

thermoplastics [37] and reinforced polymers [38–41] have been used in FDM. The thermoplastic filaments include ABS (Acrylonitrile Butadiene Styrene), PLA (Polylactic Acid), Nylon, and TPU (Thermoplastic Polyurethane), which allows for the printing of objects with different mechanical properties [42–44]. Figure 1.1 shows an example of an FDM printer and a printed part.

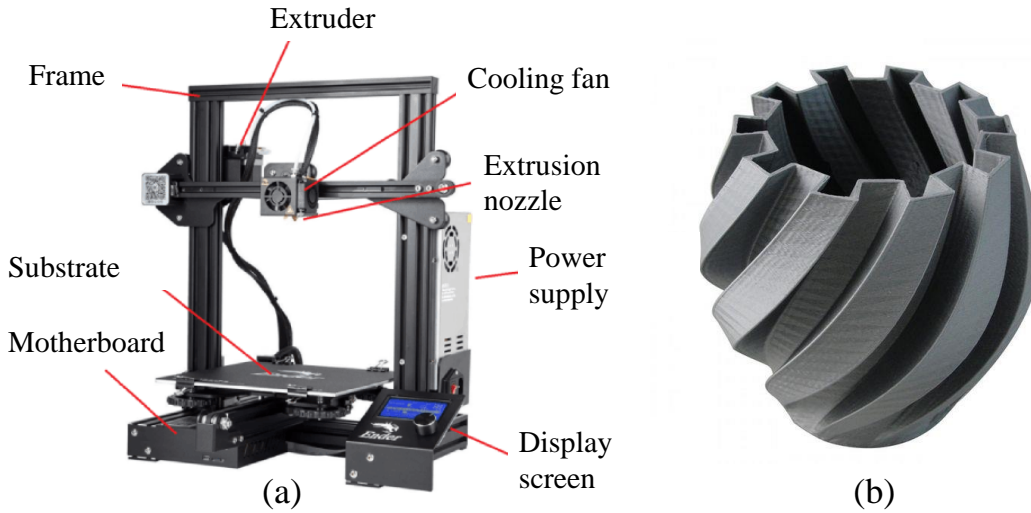


Figure 1.1: Examples of (a) FDM setup [45] and (b) printed part by FDM [46].

RC and 3DCP differs in part from FDM as they omit the liquefier from the extrusion nozzle [47,48]. Figures 1.2 and 1.3 illustrate a printing setup as well as a printed component/structure for RC and 3DCP respectively. When it comes to the printing process, RC and 3DCP are fairly similar. In RC, materials such as ceramics [49], hydrogels [50], colloidal gels [51] and thermosets [52] are printed, whereas cementitious materials (i.e., cement paste, mortar, and concrete) typically are used in 3DCP [53] although one can also use other materials such as geopolymers [54]. RC printing of a ceramic slurry requires a subsequent high-temperature sintering process in order to solidify, whereas deposited concrete in 3DCP typically cures under ambient conditions [55,56]. 3DCP is a relatively new technology and it is being explored as a way to automate the construction process and reduce labour costs. The use of fresh concrete allows for the printing of large-scale construction structures (from pedestrian bridges to buildings) [57–59].

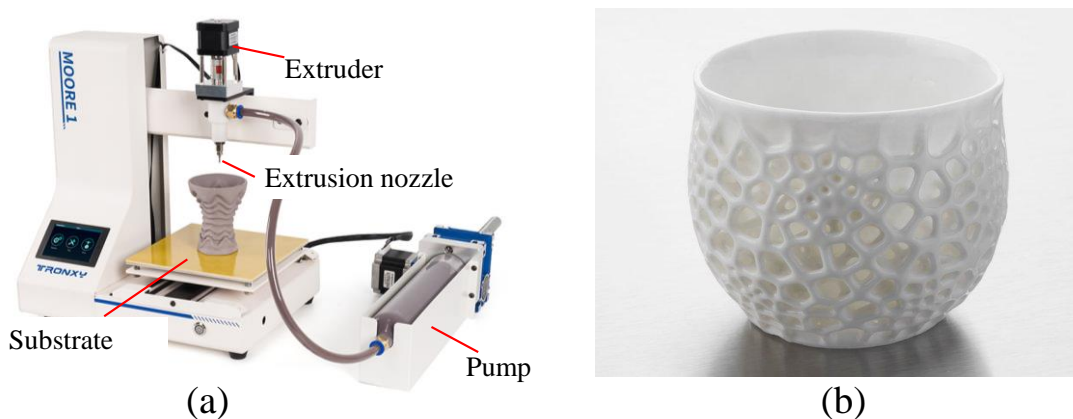


Figure 1.2: Examples of (a) RC setup [60] and (b) part printed by RC [61].

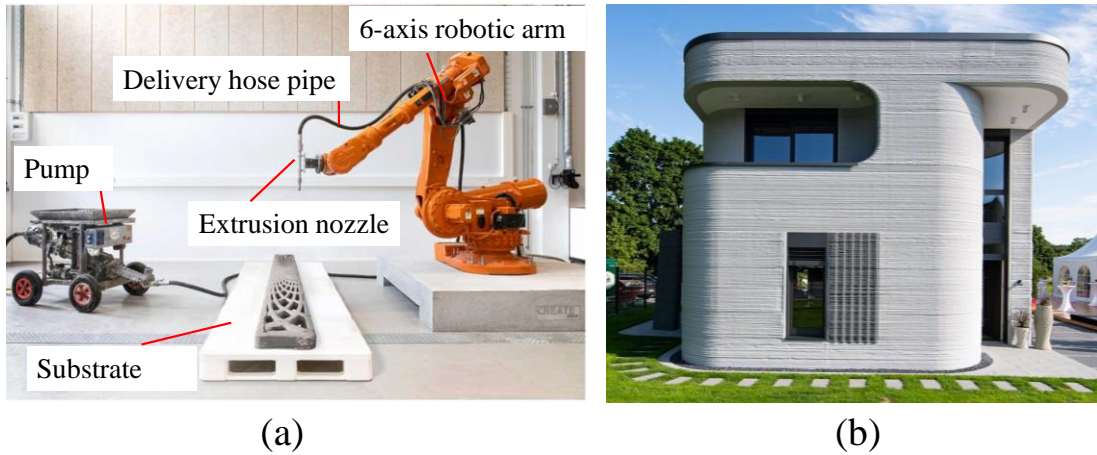


Figure 1.3: Examples of (a) 3DCP setup [62] and (b) building printed by 3DCP [63].

1.3 Literature review

This section provides an overview of MEX-AM research related to the material flow during deposition, which is the focus of this dissertation. In the deposition process, the material is first dispensed onto a built platform/substrate where it is formed into a strand. When a layer is printed, subsequent layers can be printed onto the previously printed layers. The morphology/shape of the deposited strands greatly affects the dimensional accuracy and properties of the printed part/structure.

The software that produces the printing strategy (i.e., the slicer) usually assumes an idealized shape of the deposited strand. This shape could be an ellipse, a rectangle, or a rounded rectangle [64–66] (different slicers may assume different idealized shapes). However, when the strand is deposited, the measured cross-sectional shape deviates from the idealized shape [67,68]. Several investigations have been performed to predict the cross-sectional shape of a deposited strand. For example, Agassant et al. [69] developed analytical equations to predict the height and width of the deposited strand. In addition, Hebda et al. [70] suggested an empirical equation to calculate the width of an elliptic strand using a series of physical measurements.

Unfortunately, in many cases, the predictions above are not consistent with the cross-sectional shapes measured in MEX-AM. In recent years, Computational Fluid Dynamics (CFD) modelling has been applied to better understand and predict the shape of the deposited strands. Serdeczny et al. [71] compared and validated the results of a CFD model developed by Comminal et al. [64] who investigated the morphology of single strands in FDM. The polymeric material was modelled using an isothermal high-viscous Newtonian fluid model. The results showed that the size (width and height) of the deposited strands is a function of two ratios: a geometrical ratio (i.e., the gap distance between nozzle and substrate divided by the nozzle diameter) and a speed ratio (the printing speed divided by the extrusion speeds). Behdani et al. [72] considered a non-isothermal model and found that the inclusion of a temperature-dependent viscosity slightly improved the predictions of the strand size when compared to experiments. In regards to 3DCP, Comminal et al. [73,74] developed a CFD model to investigate the strand shape of cementitious material and validated the results by comparison with experiments.

The complexity of predicting the strand shape increases when the deposited strand interacts with the previously printed material as well as any object other than the material. Typically, corners are printed where the pre- and post-corner strands come into contact, which makes it difficult to achieve a high dimensional accuracy [75]. When depositing multilayer stands it is also difficult to predict the shape of the printed part, which is a necessity in order to achieve geometrical stable (uniform shape) layers as well as to print a mesostructure with no porosities [76–78]. Furthermore, deposition of strands that interacts with objects (such as continuous fiber, micro-cables, bars, etc.) is a non-trivial task [79,80]. One of the limitations in this case is the formation of voids inside the deposited part. As a result, the strength of the part is reduced. During large-scale printing in 3DCP, void content is also observed when introducing reinforcement bars [81–83]. Three of the printing situations mentioned above are studied in detail in this dissertation: corner printing, morphology and stability of multilayer prints, and integrating reinforcement bars in 3DCP. Previously published literature related to the three topics are described in the following subsections along with research gaps.

1.2.1 Corner printing

Sharp corners of acute, right, and obtuse angles are printed in different MEX-AM techniques [84–88]. When printing a sharp corner, the extrusion nozzle decelerates to meet a state where it has no speed, then changes its direction and accelerates to meet the prescribed printing speed. During this deceleration-acceleration phase, the Bowden extruder typically deposits material at a constant rate, which can lead to the formation of a bulge known as corner swelling [75]. For some systems and materials, this swelling may be slightly reduced by synchronizing the extrusion rate with the movement of the nozzle using a direct-drive extruder [89,90]. Still, swelling may occur as two strands (before and after the turn) interact, and it is more pronounced at acute angles [91]. Corners can be more rounded (called corner rounding) due to the smoothening of the sharp corners where the nozzle executes turns at high speed [92]. Furthermore, the sudden change in printing direction may cause vibrations in the printer resulting in corner ringing. To mitigate these defects, a variety of techniques may be employed, such as lowering the maximum acceleration, slowing down printing speeds, or increasing the rigidity of the 3D printer. In the end, some defects may be minimized, but in other cases the mitigation techniques may have a negative effect or result in a longer printing process. Therefore, these issues are difficult to solve without a better understanding of how different corner angles and processing parameters influence the deposited material in the corners.

CFD models have been found successful in predicting the shape and size of the strands, as described in the previous section. In addition, Comminal et al. [93,94] developed a CFD model that investigates the shape of the corners of angles 90° and 30° deposited in FDM for sharp and smoothed trajectories of the toolpath. It was found that the corner swelling can be reduced by using the smoothed trajectories; however, this results in rounded corners that deviate from the sharp-angular shape of the toolpath. These studies must be considered as early efforts since they lack an investigation of a wide range of angles and a comparison to experimental measurements that would better understand the state of the material in the corners printed during FDM.

1.2.2 Morphology and stability of multilayer prints

The deposition process of successive layers can be divided into three categories based on the state of the previously printed ones. These are wet-on-wet, wet-on-semisolid (i.e., partially-hardened or -cured), and wet-on-solid printing [95–99]. In wet-on-solid printing, a layer is printed on top of the previously printed layer that is solidified and not deformable. This is often seen in FDM, where the printed layer is solidified instantaneously after deposition and bonds with the melted printing material by a thermal-driven diffusion process [100–103]. However, in RC and 3DCP, this could affect the printed part/structure. For instance, it results in weak interlayer bonds [95,104] and an increased risk of crack formation [105] of the print with cementitious material. While thermosets can experience residual stresses and thermal warping [106]. Therefore, the other two printing criteria are preferable, where the previously printed layer is wet or semisolid and is still deformable [107–110].

During the deposition of multiple layers, the height of a printed layer can be smaller than the nominal layer height [66,71,111]. If the nominal layer height and the extrusion rate are constant, the shape of a newly printed layer will be more rounded as the effective layer height (i.e., the gap between the nozzle and the previously printed layer) increases. This roundness of newly printed layer is more pronounced when the previously printed layer is deformed [84,112,113]. Since the layers printed in RC and 3DCP deform during printing, it compromises their geometrical stability (i.e., uniformity of the layers). Therefore, controlling the deformation is required to achieve geometrical stability, which is not a simple task [114,115], as depicted in several experimental studies [5,37,48,116].

A few numerical approaches have been developed to address the deposition of successive layers. Finite Element approaches have been utilized to simulate multiple layers of different structures, such as cylindrical- and straight-walls [117–119]. This was to capture the failure of the structure due to deformation and to identify the height of the wall at failure (i.e., the number of layers where failure occurs). The cause of the failure-deformation was attributed to the buckling of the structure under its own weight. Furthermore, it was found that while deformations occurred in all deposited layers, the most significant deformations occurred at the bottom layer.

Following the success of the CFD models for single strands reviewed earlier, a few studies have been carried out for successive deposition of materials. Serdeczny et al. [120,121] developed an isothermal CFD model to address how to reduce porosities during successive deposition of layers in FDM, whereas Zhou et al. [122] considered a non-isothermal model to address the transfer between parallel strands. However, for RC multilayer printing of viscoplastic materials (such as ceramic pastes and thermosets) the origin of the deformation and how to reduce it so that structures can be printed with layers of uniform size are yet to be investigated.

1.2.3 Integrating reinforcement bars in 3DCP

Reinforcement is a necessity (to withstand tensile stresses) in most load-bearing concrete structures. Introducing reinforcement in 3DCP is at present a challenge, and the difficulties were evident in the early stages of the technology [123]. Several design solutions have been tested in practice to either eliminate the need for reinforcements or

introduce reinforcements during printing [124–128]. This has led to the development of several reinforcing techniques, including conventional reinforcement bars [129], micro-cable reinforcements [130,131], fiber reinforcements into the mortar [132,133], a steel reinforcement technique using robotic arc welding [134,135], and in-process bar-mesh reinforcements [136]. The reinforcement method involving rebars and freshly deposited layers is of focus in this dissertation. In this technique, a few methods are available in the literature, for example, penetration of rebars vertically through a multi-layered part [137], placement of rebars along a printed layer followed by the next layer on top [138], and depositing around pre-installed rebars (bi-directional) [139]. These approaches are affected by the presence of air voids around the rebar, which significantly affects the bonding between rebar and concrete, and thereby the load bearing capacity [129,140]. A large amount of trial and error is required to overcome this constraint, which is expensive and time-consuming, and limits the progress of the approaches.

Therefore, it is worth utilizing the potential of the CFD model, as reflected in the earlier sections. However, to the best of the author’s knowledge, CFD models have not been developed to investigate the above issue.

1.4 Research objectives and outline of this dissertation

The goal of this dissertation is to advance the state-of-the-art of MEX-AM. The dissertation deep dives both numerically and experimentally into the three topics mentioned above that all relate to material flow during deposition with the overall aim of improving the quality of the printed parts/structures. The objectives and scope of each of the three topics are specified in Table 1.1.

Table 1.1: Summary of objective and scope of the works appended in the dissertation.

Topic	Objectives	Scope	Ref.
Corner printing	Investigate the printing of corners and its precision	<ul style="list-style-type: none"> • Print corners experimentally with different angles using two different extruders, Bowden and direct drive • Perform CFD simulations of single-strand deposition to mimic experiments • Analyze and compare the microscale geometry of both experimental and numerical corners 	[A.1]
Morphology and stability of multilayer prints	Investigate layer morphology and its stability during multilayer printing	<ul style="list-style-type: none"> • Perform CFD simulations accounting for multilayer deposition of viscoplastic materials • Investigate cross-sections of the layers and their deformations during printing, for different material- and processing-conditions • Extend the CFD model by accounting for a semi-solidification of the printed layers and analyze layer deformation 	[A.2], [A.3], [A.4], and [A.5]

1.4 Research objectives and outline of this dissertation

		<ul style="list-style-type: none"> • Investigate the interlayer bond distance and surface roughness of the deposited layers • Establish printing strategies that stabilizes the deposited layers by reducing its deformation 	
Integrating reinforcement bars in 3DCP	Investigate the integration of reinforcement bars and the presence of air voids in the structure	<ul style="list-style-type: none"> • Perform CFD simulations to predict the deposition of successive layers around integrated reinforcement bars • Perform experiments and compare with the simulations • Predict the air void content inside the structure • Establish printing strategies that reduces the air void content 	[A.6] and [A.7]

This dissertation comprise four chapters that provides the background and methodology for the seven appended papers. The structure is as follows:

Introduction	This chapter provides a motivation for the dissertation, state-of-the-art and research gaps for material flow during MEX-AM deposition, and accompanying objectives.
Methodologies	This chapter describes the CFD models and experimental details of the appended papers. First it presents the governing equations of the material flow dynamics and constitutive models. Then, it outlines the developed CFD models and the data processing techniques. Finally, it describes the methods for conducting the experimental printing and measurements.
Summary of Appended Papers	This chapter provides an overview as well as brief summaries of the appended publications
Conclusions and future work	This chapter summarizes the dissertation and provides directions for further research.

As the dissertation structure indicates, results and discussions will only be presented in the individual appended papers.

2 | Methodologies

The CFD models and experimental methods of the appended works will be explained in this chapter. The CFD models were used in all seven appended papers, whereas the experimental analysis was conducted in three. One of these investigated the corner precision in FDM 3D printing. The other two studied the integration of reinforcement bars in 3DCP.

The chapter starts by describing the governing equations of the material flow during deposition, which are identical for all the investigated CFD models (section 2.1). After that, it outlines the constitutive models applied by CFD models, such as Newtonian, generalized Newtonian, and elasto-viscoplastic fluid models (section 2.2). Details of the CFD models and data post-processing are described in section 2.3. Finally, information about the experimental methods and data processing is presented in section 2.4.

2.1 Governing equations

The dynamics of the deposition flow of materials in MEX-AM can be assumed to be transient and isothermal. Therefore, the flow is unsteady and viscous-incompressible with a constant density of the material ρ . The justification for these assumptions is described in the later sections. Thus, the flow dynamics can be governed by the following mass and momentum conservation equations:

$$\nabla \cdot \mathbf{u} = 0 \quad (2.1)$$

$$\rho \left(\frac{\partial \mathbf{u}}{\partial t} + \mathbf{u} \cdot \nabla \mathbf{u} \right) = -\nabla p + \rho \mathbf{g} + \nabla \cdot \boldsymbol{\sigma} \quad (2.2)$$

where \mathbf{u} is the velocity vector of the material, t is the time, p is the pressure, $\mathbf{g} = (0, 0, -g)$ is the gravitational acceleration vector, and $\boldsymbol{\sigma}$ is the deviatoric stress tensor.

2.2 Constitutive models

Three different constitutive models were used to approximate the rheological behavior of the materials in the appended papers during MEX-AM. The first approach was the Newtonian Fluid (NF) model, where the viscosity of the material was constant (used in publication [A.1] to simulate a thermoplastic). The second approach was a Generalized Newtonian Fluid (GNF) model, which was used in the publications [A.2], [A.3], [A.4], and [A.5] to simulate a viscoplastic material such as a thermoset. Lastly, an elasto-viscoplastic (EVP) model was adapted, where in addition to the viscous stress the elastic stress was taken into account (used in the publications [A.6] and [A.7] to simulate concrete).

2.2.1 Newtonian Fluid

This sub-section is related to Publication [A.1].

The NF model has a linear constitutive behavior, where the deviatoric stress tensor is proportional to the deformation rate tensor $\mathbf{D}_T = ((\nabla \mathbf{u}) + (\nabla \mathbf{u})')/2$ and the fluid viscosity μ is constant:

$$\boldsymbol{\sigma} = 2\mu \mathbf{D}_T \quad (2.3)$$

Therefore, the divergence of the deviatoric stress tensor in Equation (2.2) is simplified into the Laplacian term $\mu \nabla^2 \mathbf{u}$, and Equation (2.2) becomes:

$$\rho \left(\frac{\partial \mathbf{u}}{\partial t} + \mathbf{u} \cdot \nabla \mathbf{u} \right) = -\nabla p + \rho \mathbf{g} + \mu \nabla^2 \mathbf{u} \quad (2.4)$$

One should note that this appended study focused on the deposition of thermoplastics, namely PLA, during FDM. The printing requires a significant phase of heat transfer in practice, where the feedstock filament melts, i.e. is subjected to the glass-liquid transition of the material. However, it was considered isothermal in the CFD model, as in [64,120]. Moreover, the NF model was chosen because the shear thinning behavior of thermoplastics showed a secondary effect on the strand shape [141]. Furthermore, Serdeczny et al. [71] showed that applying the isothermal NF model is a sufficient assumption to predict the strand morphology observed in experiments. However, the temperature-dependent viscosity model (i.e., non-isothermal) is able to improve the prediction slightly as investigated in [72].

2.2.2 Generalized Newtonian Fluid

This sub-section is related to Publications [A.2], [A.3], [A.4], and [A.5].

In GNF model, the deviatoric stress tensor and the deformation rate tensor are related by the apparent viscosity μ_{app} of the material, which is a function of shear rate $\dot{\gamma}$:

$$\boldsymbol{\sigma} = 2\mu_{app}(\dot{\gamma}) \mathbf{D}_T \quad (2.5)$$

where $\dot{\gamma}$ is calculated as the magnitude of the deformation rate tensor, i.e., $\sqrt{2\text{tr}(\mathbf{D}_T^2)}$.

The studies in this case focused on the multilayer deposition of viscoplastic materials used in MEX-AM, particularly in RC. Viscoplastic materials such as ceramics [49] and thermosets [52] can be printed. The non-Newtonian flow behavior of these materials can be approximated by yield stress (τ_0) dependent rheological models such as the Bingham [142], Casson [143], or Herschel-Bulkley [144] models. This study adapted the Bingham material rheological model:

$$\mu(\dot{\gamma}) = \begin{cases} \infty, & \text{when } \tau \leq \tau_0 \\ \eta_p + \frac{\tau_0}{\dot{\gamma}}, & \text{when } \tau > \tau_0 \end{cases} \quad (2.6)$$

where μ is the material's viscosity, η_p is the plastic viscosity, and τ is the magnitude of the deviatoric stress-tensor, calculated as $\tau = \sqrt{2\text{tr}(\boldsymbol{\sigma}^2)}$. The material starts flowing once the stress state in the material exceeds the yield stress. Otherwise, the material stays unyielded, so the viscosity becomes infinite. This causes a numerical singularity, and to avoid it, the apparent viscosity was approximated using a bi-viscous regularization [145] of the Bingham model:

$$\mu_{app}(\dot{\gamma}) = \begin{cases} \mu_{max.app}, & \text{when } \dot{\gamma} < \dot{\gamma}_c \\ \eta_P + \frac{\tau_0}{\dot{\gamma}}, & \text{when } \dot{\gamma} \geq \dot{\gamma}_c \end{cases} \quad (2.7)$$

where $\mu_{max.app} = \eta_P + \tau_0/\dot{\gamma}_c$ is the maximum apparent viscosity and $\dot{\gamma}_c$ is the critical shear rate. The selection of $\dot{\gamma}_c$ depends on the characteristic shear rate of the flow and the time scale of the simulations. It should be small enough to limit the flow in the parts of the domain where the stress state is lower than the yield stress, while large enough to avoid extensive computational time and possible divergence issues.

2.2.3 Elasto-viscoplastic Fluid

This sub-section is related to Publications [A.6] and [A.7].

The EVP constitutive model accounts for both the viscous- and elastic-stress. Therefore, the deviatoric stress tensor $\boldsymbol{\sigma}$ is the sum of the deviatoric parts of the viscous stress tensor $\boldsymbol{\sigma}_V$ and elastic stress tensor $\boldsymbol{\sigma}_E$:

$$\boldsymbol{\sigma} = \boldsymbol{\sigma}_V + \boldsymbol{\sigma}_E \quad (2.8)$$

The deviatoric viscous stress tensor is given by:

$$\boldsymbol{\sigma}_V = 2\eta_P \mathbf{D}_T \quad (2.9)$$

The deviatoric elastic stress tensor is modelled using the Hookean assumption of small deformation rate tensor \mathbf{E} between each small time steps $\Delta t = t - t_0$, to approximate the elastic response of the unyielded material $\boldsymbol{\sigma}_E^*$.

$$\boldsymbol{\sigma}_E^* = 2G \mathbf{E} \quad (2.10)$$

where G is the shear modulus and $\mathbf{E}(t) = \mathbf{E}(t_0) + \Delta t \mathbf{D}_T$ is the deviatoric part of the incremental strain rate tensor approximated by integrating the deformation rate tensor over Δt .

The incremental representation of Equation (2.10) can be written as:

$$\frac{\partial \boldsymbol{\sigma}_E^*}{\partial t} + \nabla \cdot (\mathbf{u} \boldsymbol{\sigma}_E^*) - (\boldsymbol{\sigma}_E^* \cdot \mathbf{W}_T + \mathbf{W}_T' \cdot \boldsymbol{\sigma}_E^*) = 2G \mathbf{D}_T \quad (2.11)$$

where $\mathbf{W}_T = ((\nabla \mathbf{u}) - (\nabla \mathbf{u})')/2$ is the vorticity tensor. The first term of the left-hand side of Equation (2.11) represents the change in elastic stress at a fixed location in space. The change in elastic stress due to its movement and rotation with the material is approximated by the second and third terms, respectively. The right-hand side considers the change in elastic stress due to shearing.

The elastic stress tensor of the yielded material can be approximated by imposing the yield stress τ_0 limit as follows:

$$\boldsymbol{\sigma}_E = \min \left(1, \frac{\tau_0}{\sigma_{vM}} \right) \boldsymbol{\sigma}_E^* \quad (2.12)$$

where σ_{vM} is the von Mises stress defined as:

$$\sigma_{vM} = \left(\frac{2}{3} II_{\sigma_E^*} \right)^{1/2} \quad (2.13)$$

where $II_{\sigma_E^*} = tr(\sigma_E^{*2})$ is the second invariant of σ_E^* . The material is yielded when σ_{vM} exceeds the yield stress.

2.3 CFD models and data post-processing

This section summarizes the CFD models developed in the appended works. The CFD models were developed in **FLOW-3D®** (Version 12.0; 2019; Flow Science, Inc.) [146] in order to mimic the deposition flow during printing in different MEX-AM technologies. The models differ based on the problem statement and the constitutive model used. All the simulation cases of the CFD models were run with 20 cores on a high-performance computing cluster at the Technical University of Denmark. Furthermore, the post-processing of the simulated results is also summarized.

Common for the CFD models is the model geometry that comprises a cylindrical nozzle extruder of diameter Dn , a fixed substrate typically placed $h = Dn/2$ away from the nozzle head, and an artificial solid object placed at the top of the nozzle. Note that the dimensions of the geometry differed for different models. The solid object was used to prevent the material from flowing outside the nozzle orifice since the top plane worked as an inlet boundary. The bottom plane was assigned a wall boundary condition. At time $t = 0$, the nozzle extruder was set at rest and placed above the solid substrate at a distance h . At time $t > 0$, the material started to flow with a fully developed profile. The material flowed with a speed called the extrusion speed U , and the nozzle moved with a printing speed V . The material extruded through the nozzle and deposited onto the substrate results in a strand with a nominal height of h .

2.3.1 CFD modelling of corner printing

This sub-section is related to Publication [A.1].

In this case, the CFD model predicted the extrusion-deposition flow through the cylindrical tip of a E3D V6-nozzle having an inner diameter of 0.4 mm (i.e., Dn) and outer diameter of 1.0 mm. The computational domain of the model geometry and a deposited strand is presented in Figure 2.1. Note that the solid object at the top plane is not illustrated in order to give a better view of the model. Other parametric details follow the experimental details explained in sub-section 2.4.1. Since the specimens were printed to have a width of 0.8 mm and a height of 0.2 mm, calibration was needed to find the true extrusion speed and the height of the nozzle tip from the substrate to match the printed specimens. Therefore, the extrusion speed was calibrated to follow a speed ratio of $S_r = V/U = 0.81$, where $V = 2000$ mm/min, and the height was set to 0.24 mm. The simulated length of the strand is 8 mm at either side of the corner. Moreover, the CFD model mimicked both the physical prints using Bowden and direct drive extruders. Further discussion on extruders can be found in sub-section 2.4.1.

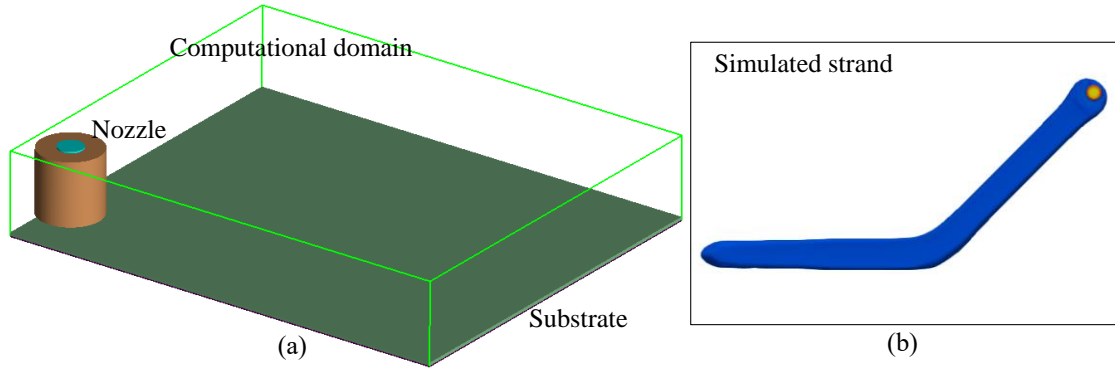


Figure 2.1: CFD model to investigate FDM corner printing. (a) Computational model incl. extruder nozzle and solid substrate; and (b) example of a simulated strand at a corner angle of 135° .

The CFD model solved the governing equations (2.1) and (2.2) with the NF model. The computational domain of the model was meshed with a uniform Cartesian grid of size $2e^{-5}$ m (i.e., 20 cells along the nozzle diameter) and discretized by the Finite Volume Method (FVM). The boundaries (other than the top and bottom) were continuative boundaries, where the material could potentially flow outside; however, the boundaries were placed far from the deposition track. The software used the FAVOR technique (Fractional Area/Volume Obstacle Representation) to represent solid geometries within the computational domain, which assists in simulating the motion of the nozzle. Furthermore, the governing equations are solved by the implicit pressure-velocity solver GMRES (Generalized Minimum Residual) [147–149]. The predictions of the pressure and forces near solid objects are facilitated by the immersed boundary method [150]. The time step size was initially set to a value of $1.0e^{-5}$ s and was automatically controlled by the solver based on the stability criteria [146]. The momentum advection was calculated explicitly with a scheme called second-order monotonically preserving, which ensures second-order accuracy in space and first-order accuracy in time. Moreover, the free surface was modelled with the Volume of Fluid method (VOF) [151,152].

2.3.2 Post-processing of corner printing simulations

This sub-section is related to Publication [A.1].

The simulated corners were post-processed to compare them with the experimental and analytical corners. At first, the simulated corners were visualized in **FLOW-3D[®] POST** [146] to compare with the post-processed experimental corners (explained in sub-section 2.4.1), as shown in Figure 2.2.

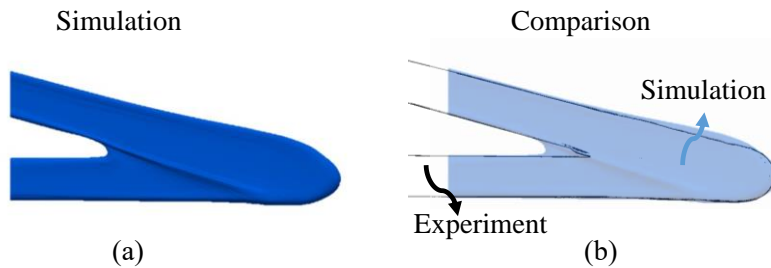


Figure 2.2: Post-processing of simulated corners and comparison with experiments. (a) Simulated corners; and (b) comparison. Note that a 15° turn is used in this example.

The next steps of post-processing were done using ImageJ®, where the primary and secondary mitre cross-sectional widths were measured, see Figure 2.3. Thereafter, a quantitative comparison was made with the analytical corners to measure the area of over- and under-extrusion (cf. Figure 2.3-b). Typically, an analytical corner is the horizontal cut in the middle of the height of the strand that comprises the pre- and post-corner strands, as seen in Figure 2.3-a. During the comparison, the underfill of the analytical corner was not considered, as the polymer did not occupy it in any specimen. The over-extrusion at the inner side of the corner is defined as inner over-extrusion. Furthermore, the over-extrusion at the outer-edge of the pre- and post-corner strands is defined as outer over-extrusion. In contrast, the under-extrusion at the outer edge is defined as outer under-extrusion (cf. Figure 2.3-b).

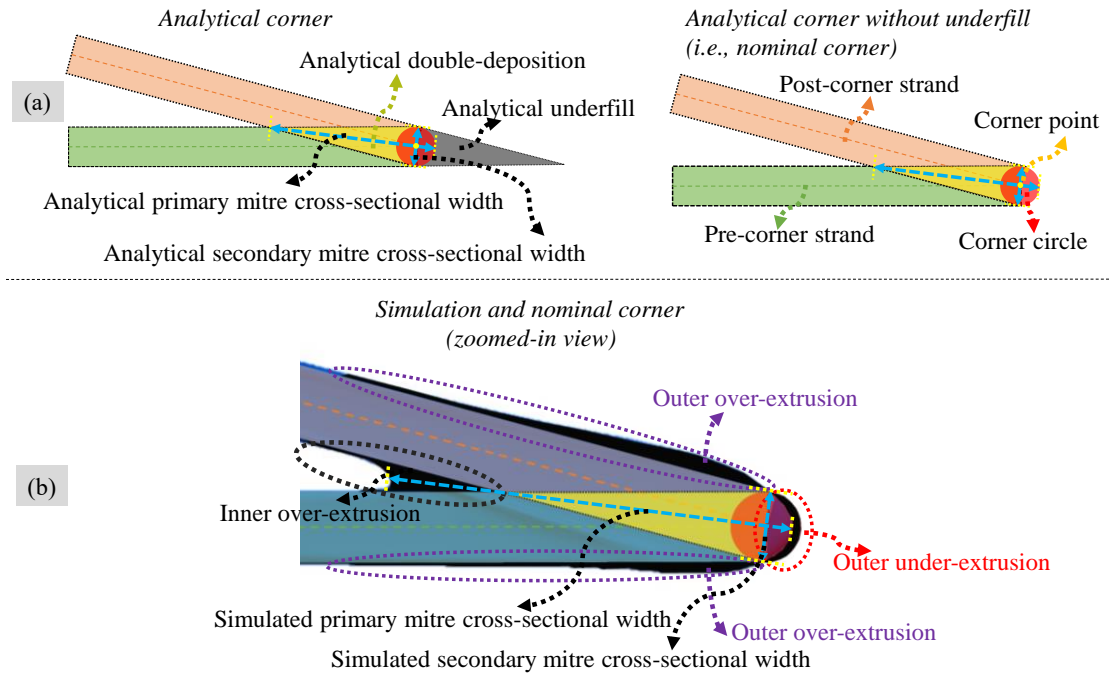


Figure 2.3: Measurements of simulated and analytical corners. (a) Cross-section of analytical corner and analytical corner without underfill; and (b) measurement of simulated mitre cross-sectional widths, and over- and under-extrusion of simulated corners compared to the analytical corner. A corner angle of 15° was used in this example.

2.3.3 CFD modelling of morphology and stability of multilayer prints

This sub-section is related to Publications [A.2], [A.3], [A.4], and [A.5].

Two different CFD models were prepared to mimic the extrusion-deposition flow of viscoplastic materials using the GNF framework with the Bingham constitutive model. In the first model (named CFD model-I), the multilayer deposition of up to five layers was investigated with the wet-on-wet and wet-on-solid printing (related to [A.2]). The other model (named CFD model-II) considered wet-on-semisolid printing of two layers by applying a yield stress buildup to the printed layer when printing the second layer on top (related to [A.3], [A.4], and [A.5]).

Figure 2.4 presents the details of CFD model-I. First, the material is extruded over a length l along the x -direction to deposit the first (i.e., bottom) layer. In the wet-on-wet printing, when the first layer was printed, the nozzle lifted up in the z -direction by the distance h and continued printing along the negative x -direction. The process continued until simulating multiple layers, in some cases three and in others five. When simulating the wet-on-solid printing, the printed first layer was assumed to be a part of the solid substrate using its STL (Standard Tessellation Language) form, and then the next layer was printed on top. The process continued until a 5-layer structure was simulated.

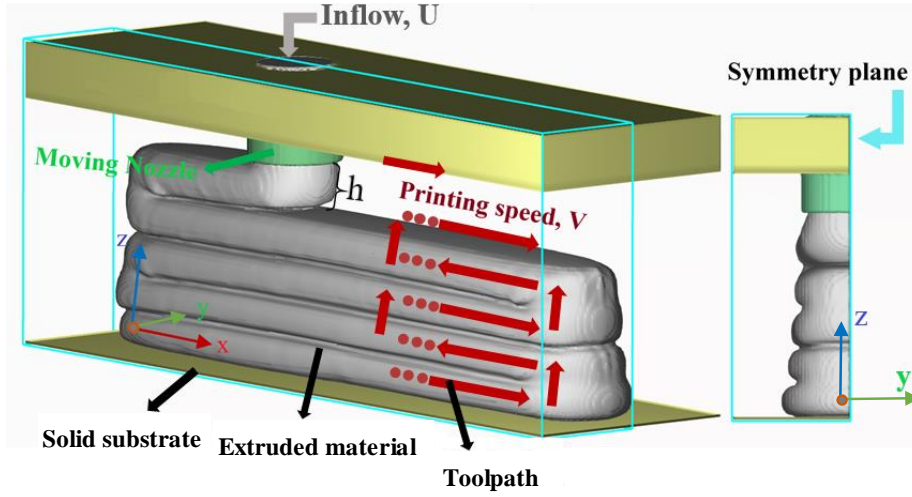


Figure 2.4: CFD model-I to investigate layer morphology and stability. Schematic includes the details of model geometry, toolpath, computational domain, and boundary condition [A.2].

The details of the CFD model-II are illustrated in Figure 2.5. The model simulated a 2-layered structure and investigated to stabilize the first layer when printing the second layer on top. The model adapted a user-defined scalar approach to mimic the yield stress buildup of the printed layer. The yield stress buildup was a consequence of taking into consideration the time-dependent rheological behavior of the viscoplastic materials in a layer-by-layer manner. This means once the first layer was deposited, its yield stress was changed before the second layer was printed on top (i.e., the first layer was now assumed to be semisolid). Note that during the printing of the second layer, the rheological property of the material was the same as the first layer while it was printed. Thus, printing and printed layers had different yield stress and therefore different viscosity functions. The viscosity function of the printing layer is given by:

$$\mu_{app}(\dot{\gamma}) = \begin{cases} \mu_{max.app}, & \text{when } \dot{\gamma} < \dot{\gamma}_c \\ \eta_P + \frac{\tau_{printing}}{\dot{\gamma}}, & \text{when } \dot{\gamma} \geq \dot{\gamma}_c \end{cases} \quad (2.14)$$

which is the same bi-viscous regularization of the Bingham model presented in the equation (2.7). The only difference is the notation of the yield stress of the printing layer $\tau_{printing}$, which is previously denoted by τ_0 .

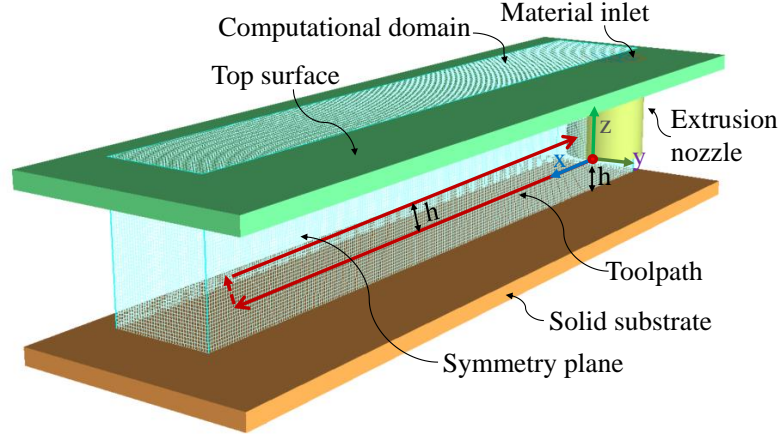


Figure 2.5: CFD model-II to investigate layer morphology and stability. The schematic includes the details of the model geometry, toolpath, computational domain, and boundary condition [A.5].

In order to alter the yield stress of the printed first layer during the printing of the second, the computational cells containing the material of the first layer were assigned a non-zero scalar concentration S_c in terms of mass per fluid volume. For the rest of the computational cells $S_c = 0$. The non-zero scalar carried the following apparent viscosity function:

$$\mu_{SC.app}(\dot{\gamma}) = \begin{cases} \mu_{max.SC.app}, & \text{when } \dot{\gamma} < \dot{\gamma}_c \\ \eta_P + \frac{\tau_{printed}}{\dot{\gamma}}, & \text{when } \dot{\gamma} \geq \dot{\gamma}_c \end{cases} \quad (2.15)$$

where $\mu_{SC.app}$ represents the apparent viscosity of the scalar, and $\mu_{max.SC.app} = \eta_P + \tau_{printed}/\dot{\gamma}_c$ is the maximum apparent viscosity of the scalar. The only difference from equation (2.14) was $\tau_{printed}$ that represents the yield stress of the scalar.

Therefore, the printed material (first layer) was assigned two apparent viscosity contributions, one from the material itself (equation (2.14)) and the other carried by the scalar (equation (2.15)). In contrast, the printing material (second layer) was assigned a single viscosity contribution from the material (equation (2.14)). A viscosity mixture rule governed the viscosity of the layers by a mass average between the apparent viscosities of both the material and scalar [146]:

$$\mu_{mix} = \frac{\rho\mu_{app} + S_c\mu_{SC.app}}{\rho + S_c} \quad (2.16)$$

This implies that μ_{mix} is equal to μ_{app} in the part of the computational domain containing the printing layer where $S_c = 0$. Whereas in the part of the domain containing the printed layer, μ_{mix} is larger than μ_{app} when $S_c > 0$. However, the increased viscosity (when $S_c > 0$) does not comply with the rheological behavior of the semisolid first layer as Equation (2.16) results in a slight increase in magnitude. Therefore, μ_{mix} was used as a classification parameter in the following equation that specifies whether μ_{app} or $\mu_{SC.app}$ is used as the apparent viscosity in a given control volume:

$$\mu_{cv.app}(\dot{\gamma}) = \begin{cases} \mu_{SC.app}, & \text{when } \mu_{mix} > \mu_{app} \\ \mu_{app}, & \text{when } \mu_{mix} \leq \mu_{app} \end{cases} \quad (2.17)$$

Thus, the GNF model used $\mu_{cv.app}$ instead of μ_{app} in Equation (2.5). This approach simulated the wet-on-wet printing (i.e., $\tau_{printed} = \tau_{printing}$) by defining $S_c = 0$, which means the model used Equation (2.14). While wet-on-semisolid printing (i.e., $\tau_{printed} > \tau_{printing}$) was achieved by giving S_c an arbitrary value larger than zero, that means the model used the Equations (2.15) and (2.14). Thus, $\tau_{printed}$ represents the yield stress of the printed material, and $\tau_{printing}$ represents that of the printing material. Figure 2.6 visualizes the dynamic viscosity of CFD model-II based on the above calculation. The model applied $\tau_{printed} = \tau_{printing} = 100$ Pa (wet-on-wet printing); and $\tau_{printing} = 100$ Pa and $\tau_{printed} = 200$ Pa (wet-on-semisolid printing). It can be seen that the model well predicted the viscosity distributions. In the case of wet-on-wet printing, no change took place in predicting the maximum apparent viscosity of the unyielded part of the layers (green color; top in Figure 2.6). Whereas in the case of wet-on-semisolid printing, the model was able to predict a different viscosity in different layers, where red and green colors represent the maximum apparent viscosity of the bottom and top layer, respectively (see bottom picture in Figure 2.6). Consequently, this user-defined scalar approach enabled the simulation of two fluids together with void in the case of wet-on-semisolid printing, where the printed layer is one fluid, the printing layer is another fluid as the viscosity is different, and the rest of the domain except the solid object is the void. The software was by default able to solve the model with either one-fluid and void, or two fluids.

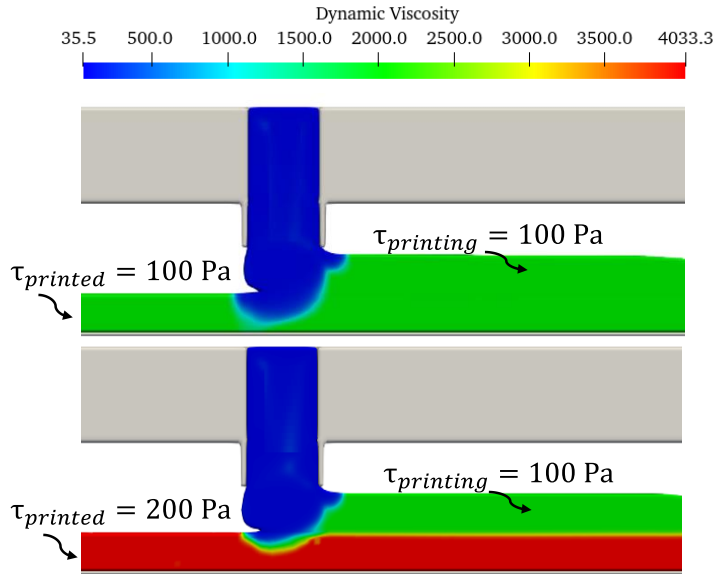


Figure 2.6: Dynamic viscosity of the CFD model-II. The longitudinal-sections were taken during printing the second layer for wet-on-wet (top) and wet-on-semisolid (bottom) printing situations [A.4].

The CFD models (I and II) solved the governing equations (2.1) and (2.2) with the GNF constitutive model (see section 2.2.2). The GNF framework was built in the software. However, for model-II, the viscosity of the material was calculated in a separate subroutine that was developed as described above. The discretization, boundary conditions, and numerical methods were mostly the same as defined for the CFD model described in the previous sub-section 2.3.1. The primary differences are mentioned below.

In these two models, a symmetrical boundary condition in the xz -plane was applied to reduce the computational cost. In addition, an explicit solver calculated the momentum advection, where model-I accounted for second-order accuracy in both time and space. In contrast, model-II used the technique called monotonically preserving upwind-difference that ensures second-order accuracy in space and first-order accuracy in time. This change in models created no significant difference in the prediction of strand shape; however, the latter took less time.

2.3.4 Post-processing of morphology and stability of multilayer prints

This sub-section is related to Publications [A.2], [A.3], [A.4], and [A.5].

The simulated results were post-processed to analyze the geometrical stability of the prints, inter-layer bond, surface roughness, and extrusion pressure. The cross-sectional shapes of the layers were collected to monitor geometrical stability, i.e., showing how the printed layers deformed when the next layers were printed on top, with the extrusion pressure being used to investigate the origin of the deformation. At first, the fluid fractions corresponding to the cross-sectional shapes of layers in a plane parallel to the yz -plane were extracted at the middle of each deposited layers (see Figure 2.7, top). Next, the fluid fractions were processed in MATLAB to visualize the edge of each layer (cf. Figure 2.7, bottom). Then the shapes of the different layers were compared (see Figure 2.8). The relative deformation (along the width) of the bottom layer De_i after the deposition of the i -th layer was calculated as:

$$De_i = (w_i - w_1)/w_1 \quad (2.18)$$

where w_i represents the width of the bottom layer just after the deposition of the i -th layer, and w_1 is the initial width of the bottom layer, as shown in Figure 2.8.

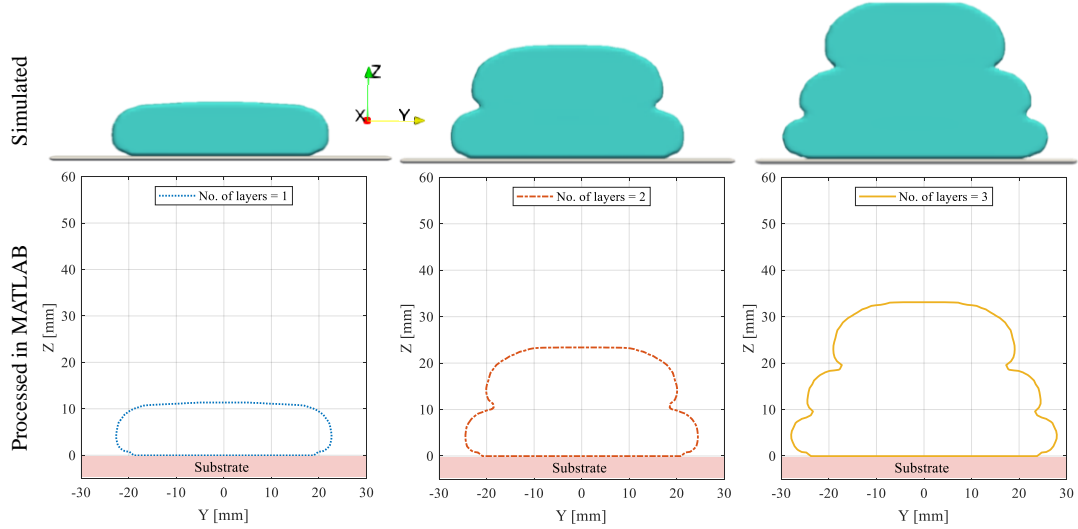


Figure 2.7: Post-processing of cross-sectional shapes: cross-sections from simulation (top) and processed in MATLAB (bottom).

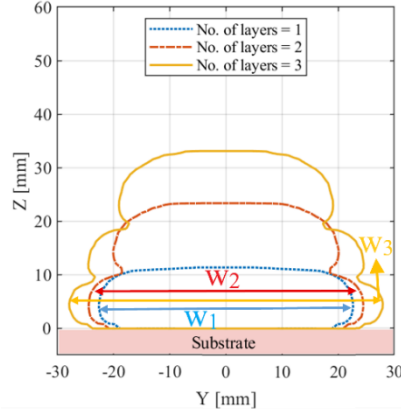


Figure 2.8: Comparison between the post-processed cross-sectional shapes of different number of layers, and width measurements (w_1 , w_2 and w_3) of bottom layer. The parameters w_1 , w_2 and w_3 are the widths of the bottom layer after successive deposition of layers [A.2].

The inter-layer bond and surface roughness was calculated and presented in Publication [A.4]. Increasing the bond distance results in better strength of the part [101], and a good surface roughness is important for many applications [18,153]. The inter-layer bond was calculated as the length of the bond-line between two deposited layers, see Figure 2.9 (left). The vertical surface roughness (i.e., edge smoothness and arithmetic mean roughness R_a) was estimated as an arithmetic mean deviation of the edge profile from a centerline adopted in such a way that the area enclosed by the lines on either side of the edge profile was equal (i.e., green area was equal to blue area), cf. Figure 2.9 (right) [121].

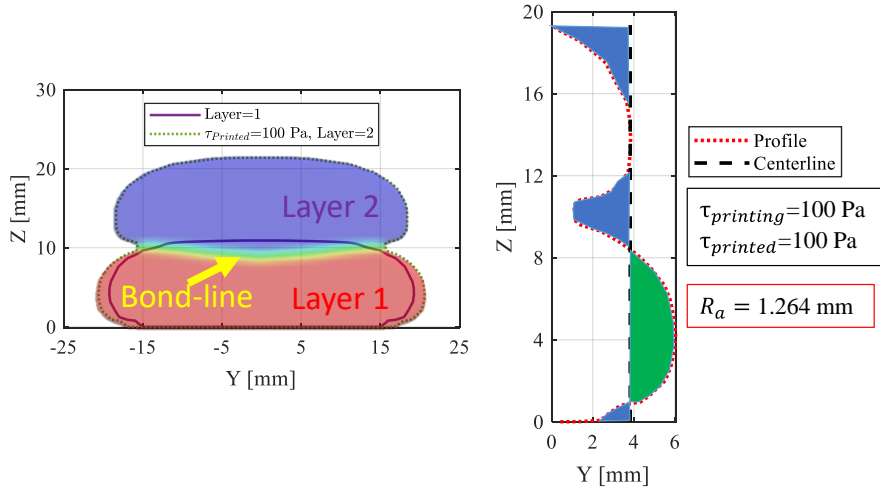


Figure 2.9: Deposited layers and Bond-line (left) and vertical surface roughness (right).

Finally, the extrusion pressure P_E at the nozzle exit, representing both the static and dynamic pressure during extrusion, was calculated. Thus, the extrusion pressure is directly applied to the printing surface [64]. During the deposition of the bottom layer, the solid substrate acts as the printing surface, whereas for the next layers, the layer previously printed does so. Furthermore, the extrusion pressure acts for a short time since the nozzle moves during printing, however, it helps the sideways flow of the depositing material [73]. To calculate the extrusion pressure, the surface-average was taken between the gauge pressure values in a cross-sectional slice taken at the nozzle exit, cf. Figure 2.10. A number of cross-sectional slices were chosen to calculate the surface-average

throughout the toolpath of a layer (see [A.2] and [A.5] for details). Finally, an average of those surface-average values was used to obtain the extrusion pressure.

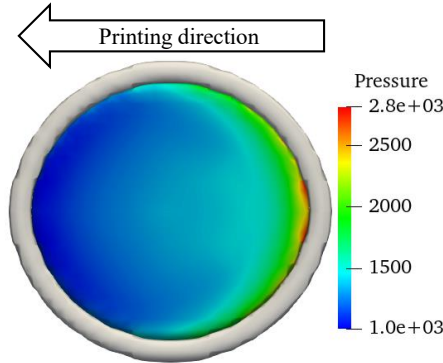


Figure 2.10: Pressure distribution in a cross-sectional slice at the nozzle exit. The slice was taken at a time when the nozzle was in the middle of a layer.

2.3.5 CFD modelling of integrating reinforcement bars in 3DCP

This sub-section is related to Publications [A.6] and [A.7].

The integration of reinforcement bars (rebars) in 3DCP was investigated using three different CFD models (see Figure 2.12). The first model (rebar-model 1) simulated the deposition of four successive layers of parallel strands (125 mm in length) without any rebars. The second model (rebar-model 2) simulated the same, with a horizontal cylindrical solid object introduced in the middle of the strands to represent a horizontal rebar. Finally, the third model (rebar-model 3) included cross-shaped rebars, where solid objects were positioned horizontally and vertically. The lengths of the horizontal and vertical rebars were 50 and 40 mm, respectively. The printing toolpath of the models is illustrated in Figure 2.12. Rebar-models 1 and 2 followed the same toolpath presented in 3D (left). The toolpath for rebar-model 3 is presented in 2D (right), where a stepped toolpath was introduced in order to pass the vertical rebar. In most of the investigated cases, the toolpath of the extrusion nozzle keeps a distance of D_{nr} from the axis of the nearest rebar (i.e., nozzle-rebar distance).

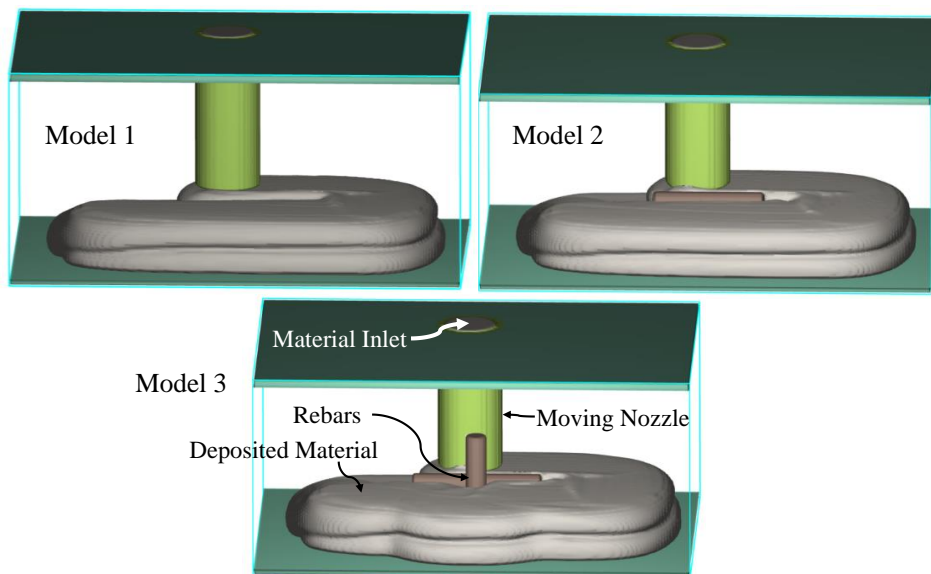


Figure 2.11: CFD models to investigate the integration of reinforcement bars in 3DCP.

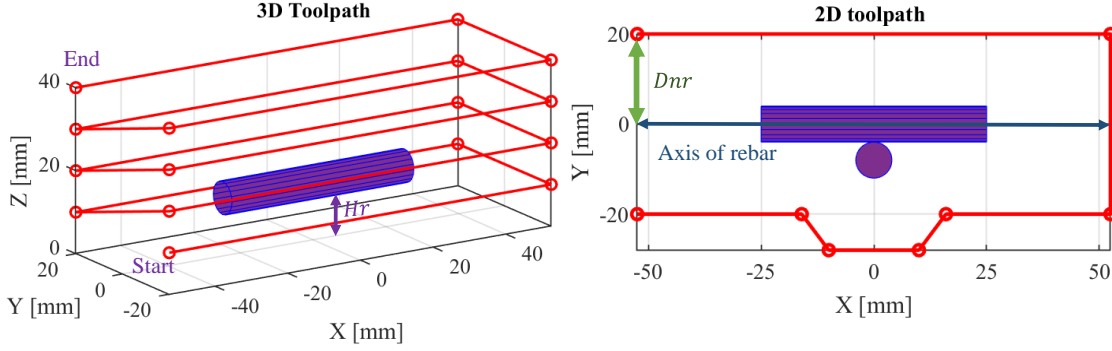


Figure 2.12: Toolpath of the CFD models. Rebar-models 1 and 2 followed the toolpath on the left, and rebar-model 3 followed the toolpath on the right.

All three models were simulated with the EVP constitutive model (cf. sub-section 2.2.3) that mimics the rheological behavior of a cementitious mortar. The discretization, boundary conditions, and numerical methods were mostly the same as those defined for the CFD model described in the earlier sub-section 2.2.2. The exceptions were that no symmetrical boundary condition was applied, and the elastic stress of the EVP model was calculated explicitly. An implicit technique, successive under-relaxation, was used to solve the viscous stress of the EVP model. Furthermore, the study was carried out with a first-order accuracy in both space and time since obtaining a second-order accuracy was found too time-consuming. Yet the computational time was long due to the use of the EVP model. For example, the simulations illustrated in Figure 2.11 took about six days to solve with 20 cores on the cluster, cf. the appended work [A.7].

2.3.6 Post-processing of integrating reinforcement bars in 3DCP simulations

This sub-section is related to Publications [A.6] and [A.7].

The simulated results were processed in two steps. One presented the cross-sectional shapes, and the other calculated the volume of the air voids that takes place inside the printed structure. The cross-sectional shapes were used to investigate the interior of the structure, i.e., the deformation of layers and the concrete-concrete- and rebar-concrete-bonding. The cross-sectional shapes were collected at the middle of a layer by using the post-processing tool **FLOW-3D[®] POST**, as shown in Figure 2.13-a. The figure also presents the positions of the volume sampling object that is used to calculate the volume fraction of air voids in the structure (see details in Ref. [146]). The object was a cuboid of size $20 \times 25 \times 3h$ mm³ that was introduced to the CFD models, as shown in Figure 2.13-b. Note that the size and position of the object were kept constant for all the models and all cases of the parametric study. Finally, the volume fraction of air voids V_V was calculated as follows:

$$V_V = \frac{\text{Volume of air void}}{\text{Volume of cuboid}} \times 100 \% \quad (2.19)$$

2.4 Experimental methods

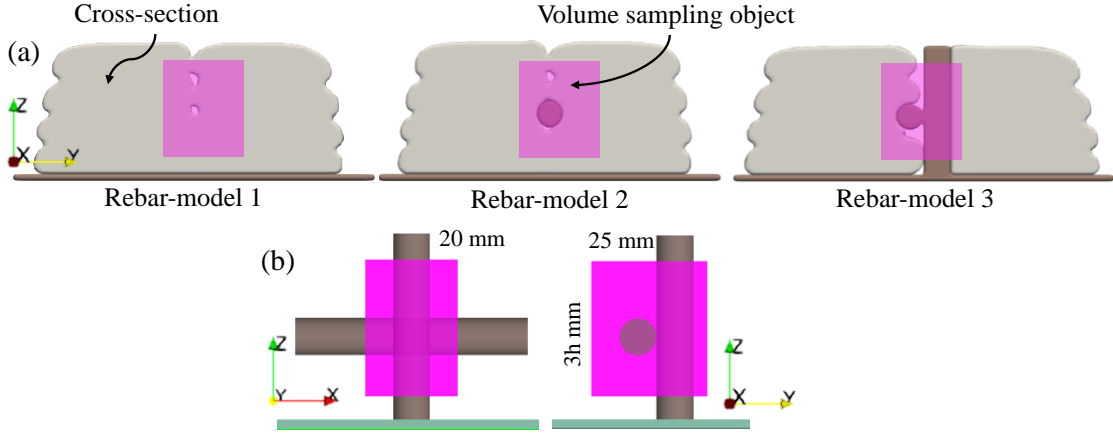


Figure 2.13: Post-processing of results: (a) Cross-sectional shapes and volume sampling object along the cross-section for the different rebar-models, and (b) details about the volume sampling object.

2.4 Experimental methods

MEX-AM experiments were performed for the studies related to corner printing and the integration of reinforcement bars in 3DCP. The corner printing experiments were conducted during an external research stay at Loughborough University, UK. The investigation is described in the appended paper [A.1]. Researchers at the Danish Technological Institute, Denmark, conducted experiments related to the integration of reinforcement bars in 3DCP. See appended publications [A.6] and [A.7].

2.4.1 Corner printing experiments

This sub-section is related to Publication [A.1].

The corner printing experiments were performed to produce single-strand specimens with ten successive layers (with a layer height of 0.2 mm) using a natural PLA feedstock filament of diameter 1.75 mm and density of 1024 kg/m³. The printing setup is shown in Figure 2.14-a, where the solid filament was fed into the nozzle hot-end using a Bowden or direct drive extruder. Moreover, the printed specimens comprise seven right trapezoids having corner angles such as 15°, 30°, 45°, 60°, 75°, 90°, and 135°, cf. Figure 2.14-b. The specimens were produced by direct GCode scripting using the open-source software FullControl GCode Designer [155]. The software uses a parametric setup and follows the printing toolpath to make the GCode; therefore, no slicing software is required.

As mentioned in the earlier sub-section, an E3D V6-nozzle of $D_n = 0.4$ mm was used and the printing speed was set to 2000 mm/min. The nozzle utilized a deceleration phase before reaching the corner point where the printing speed reached to zero. Right after, the nozzle accelerated until reaching the initial printing speed. The magnitude of the acceleration and deceleration phases were 6000 mm/s². The pre- and post-corner strands (i.e., before and after the turn, respectively) were printed along the x -direction and x, y -directions, respectively.

The extrusion speed was set to achieve strand widths of 0.4, 0.6, 0.8, and 1.0 mm. However, the appended study focused on the strand width of 0.8 mm. The other widths are the subject of ongoing research. Printing with the Bowden extruder ensured a constant

extrusion speed throughout the toolpath. In contrast, it was synchronized (not constant) with the acceleration and deceleration of the nozzle during printing with the direct drive extruder. The extrusion temperature was set at 210 °C. Special corner printing parameters such as the jerk speed (i.e., an instantaneous jump of extrusion speed by the amount of jerk when the acceleration and deceleration phases are initiated) and the blending acceleration factor (i.e., the ratio between the acceleration time and the deceleration time) were disabled to simplify the corner printing and thereby obtain fundamental understand of the material flow. Investigating those parameters is left for future research.

Furthermore, the experiments were performed using an E3D tool changer that allowed the implementation of two different extruders (Bowden and direct drive) and a microscopic tool in a single hardware system (i.e., printer) for direct comparability and in-process inspection. When the specimens were printed, a series of images of different angles were captured by the microscopic tool, cf. example in Figure 2.15-a.

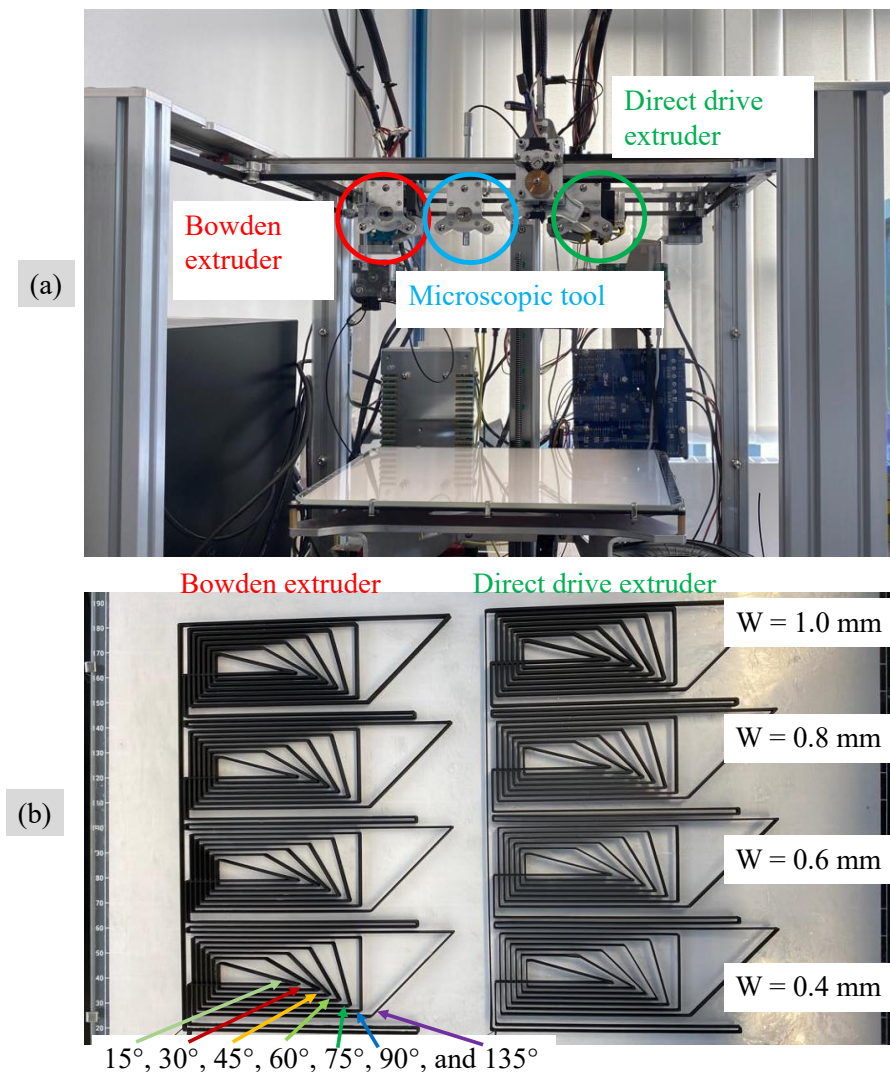


Figure 2.14: (a) Experimental setup with Bowden and direct drive extruders, and microscopic tool. (b) Printed part using both extruders for different strand widths and different angles.

2.4.2 Post-processing of corner printing experiments

This sub-section is related to Publication [A.1].

The microscopic images were post-processed using ImageJ®, as shown in Figure 2.15. At first, the images were transformed into edge-view images, cf. Figure 2.15-a (right). Next, the processed images were compared qualitatively with the simulations, cf. Figure 2.2-b. Furthermore, quantitative comparisons were performed with the analytical corners, and the measurements were taken for the mitre cross-sectional widths and the over- and under-extrusion area (see Figure 2.15-b).

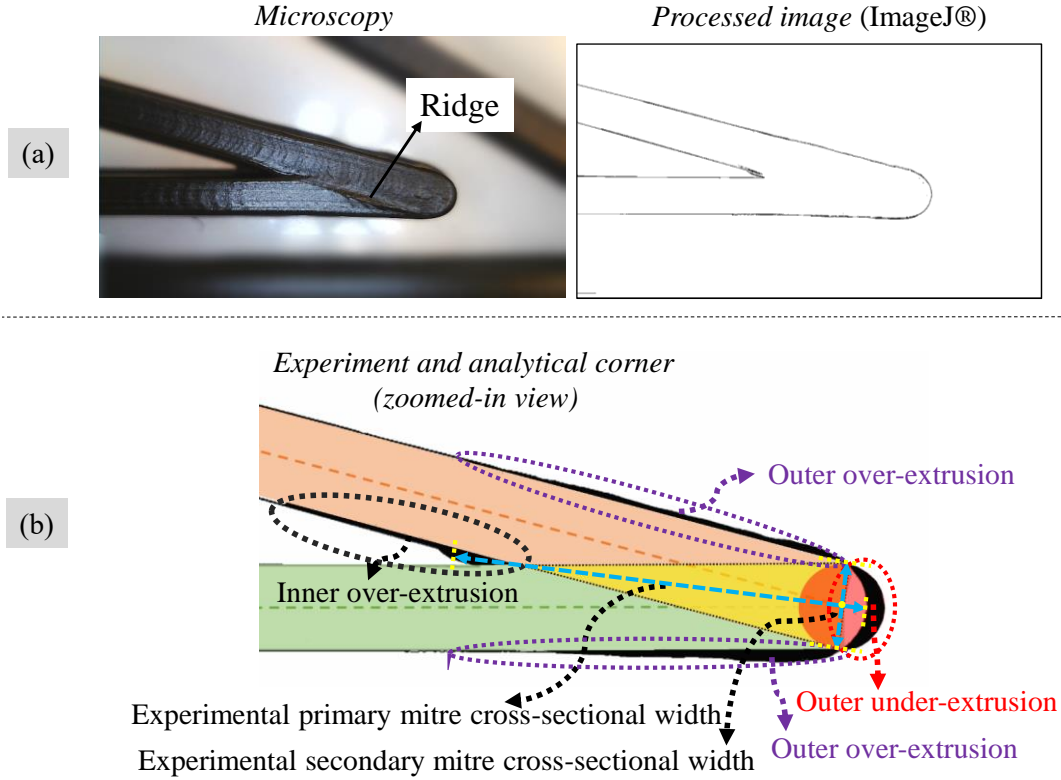


Figure 2.15: Post-processing of microscopy of corners. (a) Full-length microscopy showing the ridge (left) and the processed image showing the edge of the print; and (b) measurement of experimental mitre cross-sectional widths, and over- and under-extrusion of printed corners compared to the analytical corner.

2.4.3 Integrating reinforcement bars in 3DCP experiments

This sub-section is related to Publications [A.6] and [A.7].

The 3DCP experiment around integrated rebars was performed using a 6-axis industrial robot (Fanuc R-2000iC/165F) having a custom-designed nozzle with $\varnothing 20\text{mm}$ (i.e., nozzle diameter, $D_n = 20\text{ mm}$), cf. Figure 2.16-a. For more details on the robot, refer to [73,156]. The built plate/substrate was a 25 mm thick plywood plate as seen in Figure 2.16-b. A one-meter long horizontal rebar of diameter D_r was placed at a distance H_r from the built surface with the support of two vertical rebars that had a height of approximately 37 mm. The setup was used to print a structure of four successive layers of parallel strands around the rebars. The printing toolpath is explained in the earlier sub-section 2.3.5. Prints were carried out with different rebar diameters, i.e., $D_r = 8$ and 12 mm. The extrusion rate of

the material was set at $0.91\text{dm}^3/\text{min}$ and the nozzle speed was 35 mm/s . One of the prints is shown in Figure 2.16-c.

The material used in the experiments was a fresh cement-based mortar that included a white cement CEM I 52.5 R-SR 5 (EA), admixtures, limestone filler with sand (maximum particle size being 0.5 mm), and water. A 75 liter Eirich Intensive Mixer Type Ro8W was used to prepare the binder. The ratio between water and cement was 0.39. The mortar was prepared to have time-independent rheological characteristics for about 2 hours, and the real printing process took about 15 minutes. The density of the mortar was $\rho = 2100\text{ kg/m}^3$. The rheological characterization of the mortar was explained in [73,156]. An Anton Paar Rheometer MCR 502 was used to perform rotational and oscillatory tests in a vane-in-cup measuring device. The tests determined the yield stress $\tau_0 = 630\text{ Pa}$ and plastic viscosity $\eta_p = 7.5\text{ Pa}$, and the storage modulus $G' = 200\text{ kPa}$ for the unyielded mortar within the linear viscoelastic (LVE) region. Therefore, a yield stress limited EVP constitutive model was used to model the rheology of the mortar as explained in sub-section 2.2.3. The storage modulus was used as the linear elastic shear modulus of the unyielded mortar.

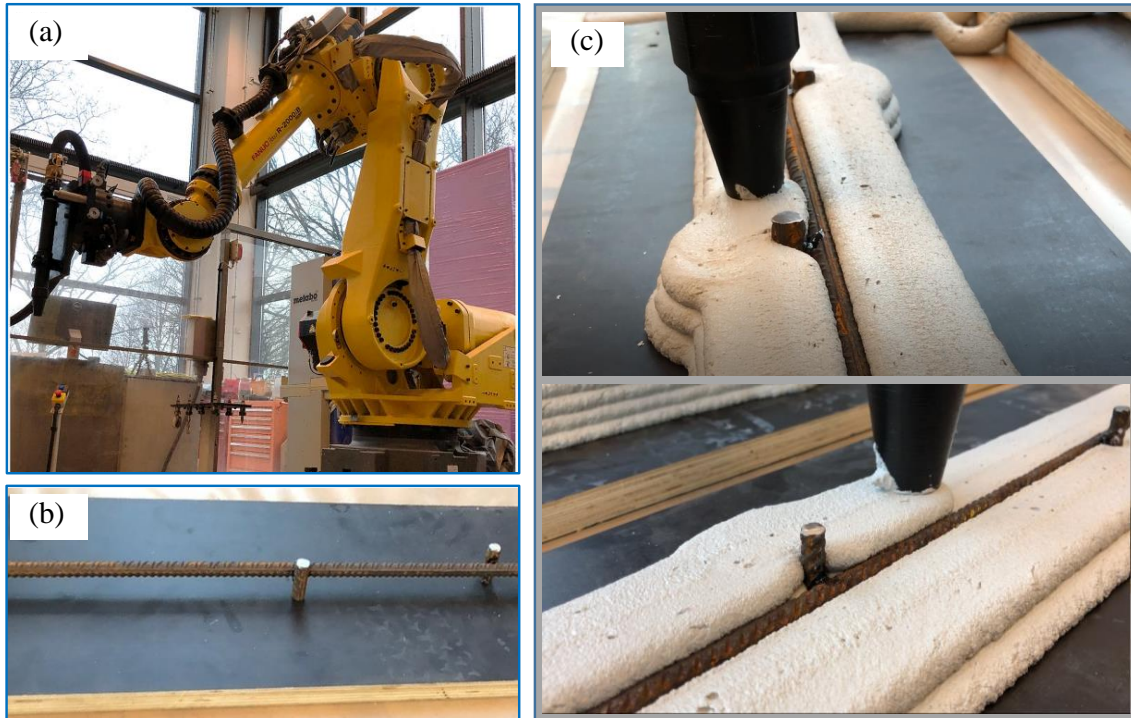


Figure 2.16: Integrating reinforcement bars in 3DCP: (a) 6-axis robotic arm [73]; (b) plywood-built plate with integrated rebars; (c) example of printing (pictures were taken during printing of the third layer).

2.4.4 Post-processing of integrating reinforcement bars in 3DCP experiments

This sub-section is related to Publications [A.6] and [A.7].

The printed parts were post-processed to collect the cross-sections after the prints were hardened to investigate the rebar-concrete bonding. The printed parts were impregnated with epoxy resin in a vacuum chamber to avoid destroying the specimens while slicing them, cf. Figure 2.17.

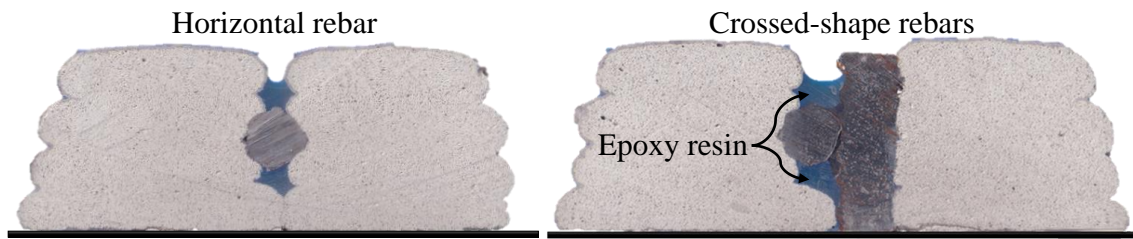


Figure 2.17: Post-processing of integrating reinforcement bar in 3DCP experiments.

3 | Summary of Appended Papers

This chapter starts by presenting an overview of the seven appended publications. Subsequently, summaries of the individual publications are given, which are extended versions of the abstracts.

Overview

Publication [A.1] addressed the single-strand deposition of material along an angular path during filament-based MEX-AM. A CFD model was developed to simulate the deposition flow of PLA in order to investigate the state of the material along the angular path for different corner angles. Experimental, analytical, and simulated corners were compared.

Publications [A.2] to [A.5] concerned multiple layers (unto five layers) deposition of viscoplastic materials in MEX-AM. Publication [A.2] focused on continuous deposition, where the material's property is assumed constant during the deposition, i.e., wet-on-wet printing. In addition, wet-on-solid printing was simulated, where the previously printed layer was assumed to be a part of the solid substrate. The deformation and stability of the deposited layers were studied. Publications [A.3] to [A.5] addressed wet-on-semisolid printing to study the deformation and stability of deposited layers, where the previously printed layer was assumed to develop its yield stress and become semisolid. Publication [A.3] focused on modelling the yield stress buildup and briefly studied the deformation as a function of the yield stress buildup. In Publication [A.4], interlayer bonding of the layers and surface roughness was investigated as a function of the yield stress buildup. Publication [A.5] extended the work in publication [A.3] to provide an in-depth analysis of the yield stress buildup, and both material and processing conditions were varied to find stable prints with no deformation.

Publications [A.6] and [A.7] concerned the experiments and simulations of the integration of reinforcement bars during 3DCP. Publication [A.6] presented a CFD model that simulated the deposition of four layers of parallel strands around the integrated rebars and compared simulations with experiments. Publication [A.7] used the CFD model developed in [A.6] and conducted an in-depth analysis by comparing the simulations with experiments and varying the material and processing conditions to minimize the air void formation inside the deposited structure.

Publication [A.1]

M.T. Mollah, A. Moetazedian, A. Gleadall, J. Yan, W.E. Alphonso, R. Comminal, B. Šeta, T. Lock, J. Spangenberg, Investigation on corner precision at different corner angles in material extrusion additive manufacturing: An experimental and computational fluid dynamics analysis, in: *Solid Freeform Fabrication Symposium 2022: 33rd Annual Meeting*, University of Texas at Austin, 2022: pp. 872–881.

In this paper, the influence of different corner angles on microscale geometry was investigated during filament-based MEX-AM, i.e., FDM. Two different extruders, Bowden and direct drive, were used to print specimens with corner angles of 15°, 30°, 45°, 60°, 75°, 90°, and 135° using PLA feedstock filament. A CFD model was developed to simulate the deposition flow of the material through the extrusion nozzle of both

extruders using the NF model. The simulated corner geometries were compared with experiments to assess simulation accuracy. The comparison included the measurement of the primary and secondary mitre cross-sectional width through the corner point of the 3D-printed and simulated strands. It enabled a new understanding of the predictability of the CFD model and the state of the deposited material at the corners, as well as the deviation of experimental and simulated corners compared to the analytical solution. The comparison is thereafter extended to estimate the over- and under-extrusion around the corner. Furthermore, the results of both extruders are compared. The results provided fundamental knowledge on corner precision for angular print paths.

Publication [A.2]

M.T. Mollah, R. Comminal, M.P. Serdeczny, D.B. Pedersen, J. Spangenberg, Stability and deformations of deposited layers in material extrusion additive manufacturing, *Additive Manufacturing*. 46 (2021) 102193. <https://doi.org/10.1016/j.addma.2021.102193>.

In this paper, a CFD model is developed to simulate the deposition flow during the printing of multiple layers in MEX-AM of viscoplastic materials. The CFD model predicted the morphology of the deposited layers and captured the deformation of layers during the printing. The model used a GNF framework to approximate the rheology of the viscoplastic materials using the Bingham constitutive model. The simulations were used to predict the cross-sectional shapes of the deposited layers, and the deformation of layers was studied for different constitutive parameters of the material (i.e., yield stress and plastic viscosity). It was found that the deformation of layers is due to the combination of the hydrostatic pressure of the printed material and the extrusion pressure during the printing. The simulations showed that higher yield stress could reduce the deformation of the deposited layers, while a higher plastic viscosity leads to substantial deformation. Moreover, the influence of the processing parameters, such as printing speed, extrusion speed, layer height, and nozzle diameter, on the deformation of the printed layers was investigated. Among the processing parameters, the nozzle diameter had the most significant impact on the bottom layer deformation. Finally, the model provided a conservative estimate of the required increase in yield stress that a viscoplastic material demands after deposition to avoid the deformation, i.e., to withstand the applied hydrostatic- and extrusion-pressure of the subsequently printed layers.

Publication [A.3]

M.T. Mollah, R. Comminal, M.P. Serdeczny, D.B. Pedersen, J. Spangenberg, Numerical Predictions of Bottom Layer Stability in Material Extrusion Additive Manufacturing, *JOM*. 74 (2022) 1096–1101. <https://doi.org/10.1007/s11837-021-05035-9>.

This paper extended the study in Publication [A.2] by considering wet-on-semisolid MEX-AM of materials such as ceramic pastes and thermosets. Common for these materials was their viscoplastic behavior during the deposition and structural buildup (i.e., increase in yield stress/semi-solidity) after the deposition. The complex nature of these materials makes it non-trivial to guarantee that printed layers do not deform when depositing additional layers on top (refer to publication [A.2]). Therefore, this paper considered the influence of the yield stress buildup of viscoplastic materials on the

stability of the bottom layer during multilayer printing. Specifically, a novel CFD model was developed that applied a scalar approach to alter the yield stress of the printed layer when printing the next layer on top. The viscosity of the material during printing was investigated to verify the implementation of the yield stress buildup. Moreover, different yield stress buildups were investigated for a particular property of the printing material. The model provided fundamental knowledge on how to design the material's rheology, so the bottom layer can withstand the applied pressure (i.e., both the hydrostatic- and extrusion-pressure).

Publication [A.4]

M.T. Mollah, M.P. Serdeczny, R. Comminal, B. Šeta, M. Brander, D.B. Pedersen, J. Spangenberg, A Numerical Investigation of the Inter-Layer Bond and Surface Roughness during the Yield Stress Buildup in Wet-On-Wet Material Extrusion Additive Manufacturing, in: *2022 Summer Topical Meeting: Advancing Precision in Additive Manufacturing*, American Society for Precision Engineering, TN, USA, 2022: pp. 131–134.

This paper used the CFD model developed in publication [A.3]. The computational model provided the cross-sections of the deposited part of two layers, from which the bottom layer deformation, the inter-layer bond, and the surface roughness were estimated as a function of yield stress buildup of the bottom layer, where the properties of the printing material were kept constant. It was found that the yield stress buildup at the bottom layer reduced the deformation and improved the surface roughness. In contrast, the inter-layer bonding was found to reduce slightly when the yield stress buildup was high. The model can be used to find an optimal yield stress buildup.

Publication [A.5]

M.T. Mollah, R. Comminal, M.P. Serdeczny, B. Šeta, J. Spangenberg, Computational analysis of yield stress buildup and stability of deposited layers in material extrusion additive manufacturing. *Submitted to Additive Manufacturing*.

This paper extended the results in the publication [A.3] to provide an in-depth analysis of the effect of material and processing conditions on the deformation of the bottom layer for different yield stress buildups. The results were compared with wet-on-wet printing (i.e., prints with no yield stress buildup). The simulations showed that a certain yield stress buildup is required to be able to withstand the total applied pressure, although increasing the printing yield stress increased the extrusion pressure. Consequently, stable prints (i.e., a relative deformation of ~1 %) were obtained. Furthermore, the deformation of the bottom layer was dependent on a complex interaction between the extrusion pressure, the shape of the cross-section, and the contact area between the layers. Finally, simulations were performed to identify how process conditions could be changed so that the yield stress buildup could be limited while still providing stable prints. As observed in the wet-on-wet printing (publication [A.2]), the diameter of the nozzle was the parameter that had the most influence on the deformation and thereby on the requirement of the yield stress buildup. It was discovered that the deformation could be reduced to ~1% by decreasing the plastic viscosity for the smaller nozzle diameters and by increasing the yield stress buildup for the larger nozzle diameters.

Publication [A.6]

J. Spangenberg, W.R. Leal da Silva, M.T. Mollah, R. Comminal, T. Juul Andersen, H. Stang, Integrating Reinforcement with 3D Concrete Printing: Experiments and Numerical Modelling, in: R. Buswell, A. Blanco, S. Cavalaro, P. Kinnell (Eds.), *Third RILEM International Conference on Concrete and Digital Fabrication*, Springer International Publishing, Cham, 2022: pp. 379–384. https://doi.org/10.1007/978-3-031-06116-5_56.

This paper focused on the MEX-AM of cementitious material, i.e., 3D Concrete Printing (3DCP). 3DCP is an automated construction technology that offers enormous freedom of structural design and printing scale. One of the limitations of 3DCP is the incorporation of reinforcement bars (rebars) with strong concrete-rebar bonding to produce load-bearing structures. To understand the limitation, while limiting experimental efforts, a novel CFD model was developed to simulate concrete flow around rebars. The CFD model used an EVP constitutive model to simulate the flow behavior of the concrete. Also, 3DCP experiments were conducted around horizontal and cross-shaped rebars to validate the developed CFD model. A good agreement between the experimental and simulated results was found; the presence of air voids was found in both results. The CFD model provided a new venue for specifying printing strategies that ensure better bonding between concrete and reinforcement.

Publication [A.7]

M.T. Mollah, R. Comminal, W.R. Leal da Silva, B. Šeta, J. Spangenberg, Integration of reinforcement bar and state of air void in 3D concrete printing. *Submitted to Cement and Concrete Research*.

In this paper, the preliminary results of [A.6] were extended by comparing the simulated results with a number of experiments. Subsequently, the model was exploited to make an in-depth analysis of the bonding of concrete material with the rebars, i.e., to capture the air void formation using the cross-sections of the deposited part. The comparison was carried out for different configurations and sizes of rebars, and the model was found capable of predicting the air void formation with high accuracy. Afterwards, the simulations were used to investigate three different configurations: i) no-rebar; ii) horizontal rebar; and iii) cross-shaped (horizontal and vertical) rebars. It was found that the integration of any rebar could potentially enhance the presence of air voids around it, which is detrimental to the reinforcement solution in 3DCP. In order to avoid the presence of air voids, the material properties (i.e., yield stress and plastic viscosity) and processing conditions (i.e., rebar diameter, nozzle-rebar distance, geometric ratio, and speed ratio) were varied. The results illustrated that air voids could be eliminated completely in all investigated configurations, but changes in the toolpath, process parameters, and rebar joint geometry were required. This emphasized the great potential of the CFD model, when it comes to rebar integration in 3DCP.

4 | Conclusions and future work

This final chapter summarizes the conclusions of the individual appended papers and provides overall comments on the findings. Moreover, the chapter outlines future work that can benefit the field.

4.1 Conclusions

The work presented in this dissertation concerns the CFD modelling and experimental analysis of the material flow during deposition in MEX-AM. Understanding the material flow and thereby the morphology of strands and layers is essential for the dimensional accuracy and geometrical stability of the printed part as well as its mechanical performance. In the CFD models, the deposition of material was governed by the momentum and continuity equations under the assumptions of a transient and isothermal flow. The conclusions for the three studied topics are described in the following subsections. This is followed by a fourth subsection that lays out general comments on the findings.

1.2.4 Corner printing

The printing of corners by FDM of PLA was studied. Corners of different angles were 3D-printed with two printing strategies: a constant extrusion speed using Bowden drive and a variable extrusion speed using direct drive. The results illustrated that the direct drive extruder produces strands with a rounded shape. A CFD model was developed using the Newtonian fluid constitutive model to simulate the corner printing. The experimental and simulated corners were compared with analytical corners. It was found that the primary and secondary mitre widths in experiments and simulations had the largest deviations from the analytical model at small angles. The simulations predicted a difference between the extruders; the direct drive resulted in under-extrusion at the outer-corner. This was expected to be seen in the experiments as well due to the synchronized extrusion speed, but the experiments did not show such result, which indicated that other corner-printing parameters dominated the print. In addition, it was observed in the simulations that the over-extrusion at the inner- and outer-corner was larger for most angles as compared to the experiments, which was attributed to the interaction between the fluid strands when double deposition occurred. These discrepancies between simulations and experiments could potentially be ascribed to the relatively simple material description (i.e., isothermal Newtonian fluid) that is applied by the model.

1.2.5 Morphology and stability for multilayer prints

CFD models were developed to study the geometrical stability (i.e., uniform size) of layers of viscoplastic materials for three different printing strategies: wet-on-wet, wet-on-semisolid, and wet-on-solid. The viscoplastic materials were modelled using the Bingham rheological equations and implemented with the generalized Newtonian fluid model. The wet-on-wet printing simulations showed printing showed that the bottom layer started to deform under the hydrostatic pressure at low yield stresses. The deformation reduced when the yield stress was larger, although a larger yield stress resulted in larger extrusion pressure. Therefore, the deformation was not fully eliminated. Unlike the yield stress, a

4.1 Conclusions

higher plastic viscosity resulted in larger deformations of the layers due to an increase in the extrusion pressure, as the material had a higher resistance to flow. Furthermore, a higher printing speed led to less deformation due to a decrease in extrusion pressure and a shorter exposure time, whereas a higher extrusion speed led to an opposite pattern of deformation and extrusion pressure. When the layer height increased, the relative deformation of the layers increased, but the absolute deformation was similar. A non-monotonic trend of the layer deformation was observed for different nozzle diameters due to the combined effect of the hydrostatic- and extrusion-pressure. Increasing the nozzle diameter increased the hydrostatic pressure as the layer height increased, while the extrusion pressure decreased due to smaller shear stresses in larger channels. In all the investigated cases of wet-on-wet printing, some relative deformations of the bottom layer were seen.

Wet-on-solid printing illustrated a stable print without deformation and with constant extrusion pressure for all layers (investigated for five layers). The wet-on-solid printing provided a conservative estimate for the yield stress buildup that the material needed to develop before printing the next layer. The yield stress of the printed layers must be higher than the total applied pressure (i.e., the sum of the hydrostatic- and extrusion-pressure) in order not to deform.

Furthermore, a novel CFD model was developed that applied a scalar approach for the yield stress buildup of the previously printed layer and thereby simulated the wet-on-semisolid printing (for two layers). It was found that the CFD model could alter the viscosity between the two fluid layers precisely as formulated. When the yield stress of the printed (bottom) layer was increased, less deformation was observed as compared to wet-on-wet printing. This was due to the higher effective viscosity of the printed layer when printing wet-on-semisolid. Consequently, the surface roughness of the printed layers was improved, and the profile of the vertical edge became smoother. It was also noticed that the largest improvement in reducing deformation was gained from the initial increase in yield stress.

The deformation of the bottom layer was analyzed for different processing conditions while varying the yield stress buildups. The yield stress at which the printed layers gained geometrical stability (i.e., a relative deformation of ~1 %) was the same for all investigated printing- and extrusion-speeds. This indicated a limited gain to be achieved by varying these two parameters when one considers reducing the requirement for yield stress buildup, at least when these parameters are coupled with other processing parameters used in this study. When the layer height was varied, it was observed that a larger layer height required a higher yield stress buildup to reduce the deformation. This was attributed to a complex interaction between the extrusion pressure, the shape of the strands, and the contact area between layers. Consequently, stable prints can be obtained at a lower yield stress buildup when printing with a reduced layer height, which can be advantageous for some materials as a too-quick material development can result in cracks and warping. The nozzle diameter was observed to have a significant influence on deformation, and thereby on the requirement for the yield stress buildup. For all nozzle diameters, it was found though that the deformation could be reduced to ~1% if the extrusion pressure was reduced. For small nozzle diameters, the extrusion pressure could be reduced by reducing the plastic viscosity, which led to a limited requirement of the yield stress buildup. For larger nozzle diameters, the extrusion pressure could be reduced

by decreasing the yield stress of the printing material as long it was higher than the hydrostatic pressure.

1.2.6 Integrating reinforcement bars in 3DCP

The integration of reinforcement bars in 3DCP was studied using experiments and CFD simulations. 3DCP was carried out around horizontal and vertical rebars. The experiments demonstrated that the printing strategy entrapped air voids both below and above the horizontal rebar as well as around the vertical rebar. Thus, it is obvious that the integration of reinforcement is a challenging task when using 3DCP. CFD models were developed to simulate the printing process, and the simulated results were compared with experiments. It was found that the model was able to accurately predict the formation of air voids around the rebars.

Thereafter, the CFD models were exploited to analyze the formation of air voids for different rebar configurations, material properties, and processing conditions. Increasing the yield stress resulted in less air voids as the effective gap in the printing layer was reduced. However, it was not possible to eliminate air voids as the increased yield stress also restricted the material flow in confined spaces. The opposite effect was observed for the plastic viscosity, where the formation of air voids decreased somewhat when decreasing the plastic viscosity. However, the same conclusion was achieved that the air voids could not be fully eliminated. The processing conditions on the other hand appeared to have a substantial influence on the formation of air voids. When the rebar diameter increased, the formation of air voids increased as a result of the resistance to flow around the reinforcement. The air voids could be reduced and for the horizontal rebar fully eliminated by reducing the nozzle-rebar distance. However, in the latter case, it was important to be aware of ridges that may affect the geometry of the final structure. Similarly, the formation of air voids decreased when decreasing the geometric- and speed-ratio. Smaller geometric ratios resulted in wider strands whereas smaller speed ratios increased the cross-sectional area of the strands, both help to occupy more of the space around the rebars.

Therefore, by decreasing the nozzle-rebar distance, geometric ratio, and speed ratio, air voids around the horizontal rebar were fully omitted while they remained present for the cross-shaped rebar. It was evident from the results that those air voids could also be eliminated by changing some processing conditions and the toolpath, as well as by modifying the geometry of the joint between horizontal and vertical rebars in order to have a smooth transition. This study showed that it is not easy to avoid air voids when integrating reinforcement in 3DCP, but the CFD model was found to be a very useful digital tool to define printing strategies able to secure a good bonding between reinforcement and concrete.

1.2.7 General comments on findings

The experimental and numerical findings of this thesis highlight that obtaining a high dimensional accuracy in MEX-AM is a non-trivial task especially when the deposited material interacts with previous printed material or objects. However, the developed CFD models are strong digital tools that can give virtual windows into the processes in order

to better understand the manufacturing techniques as well as provide improved printing strategies.

4.2 Ideas for future works

The study of printing corners can be extended by varying different process conditions in order to figure out printing strategies that can produce dimensionally accurate corners. As part of this process, one might consider extending the CFD model to include heat transfer and solidification of the deposited material as well. This inclusion might potentially enhance the prediction ability of the deposited corners, where the interaction between the pre- and post-corner strands is strong (i.e., for smaller angles). In the case of the study on the stability of layers, the developed CFD model demonstrated enormous potential. The study was generic, so it represented many materials that exhibit structural development over time. However, in practice, different materials or reinforced composites could have different rheological behavior during the deposition that could influence the requirement for yield stress buildup. Hence, the study lacks an experimental comparison with a specific material. The CFD model can also be extended to include non-isothermal printing, as some materials generate heat during solidification/curing, which can affect the rheological behavior of the material and thus the print stability. In addition, as the CFD model with the scalar approach is able to differentiate materials, it could be used to study multi-material MEX-AM.

The CFD model that simulated flow around preinstalled reinforcement bars could be used to investigate other forms of rebar integration, such as placement of horizontal rebars on top of the deposited layer or penetration of vertical rebars through multiple layers. Furthermore, the model could be utilized to investigate reinforcement during micro-scale deposition, such as the integration of micro-cables in FDM.

Bibliography

- [1] ISO/ASTM 52900:2021(en) Additive manufacturing — General principles — Fundamentals and vocabulary, (n.d.). <https://www.iso.org/obp/ui/#iso:std:iso-astm:52900:ed-2:v1:en:sec:A> (accessed December 12, 2022).
- [2] Z. Jiang, B. Diggle, M.L. Tan, J. Viktorova, C.W. Bennett, L.A. Connal, Extrusion 3D Printing of Polymeric Materials with Advanced Properties, *Adv. Sci.* 7 (2020) 2001379. <https://doi.org/10.1002/advs.202001379>.
- [3] S. Kyle, Z.M. Jessop, A. Al-Sabah, I.S. Whitaker, ‘Printability’ of Candidate Biomaterials for Extrusion Based 3D Printing: State-of-the-Art, *Adv. Healthcare Mater.* 6 (2017) 1700264. <https://doi.org/10.1002/adhm.201700264>.
- [4] D. Fico, D. Rizzo, R. Casciaro, C. Esposito Corcione, A Review of Polymer-Based Materials for Fused Filament Fabrication (FFF): Focus on Sustainability and Recycled Materials, *Polymers*. 14 (2022) 465. <https://doi.org/10.3390/polym14030465>.
- [5] M.K. Mohan, A.V. Rahul, G. De Schutter, K. Van Tittelboom, Extrusion-based concrete 3D printing from a material perspective: A state-of-the-art review, *Cement and Concrete Composites*. 115 (2021) 103855. <https://doi.org/10.1016/j.cemconcomp.2020.103855>.
- [6] Y. Chen, S. He, Y. Gan, O. Çopuroğlu, F. Veer, E. Schlängen, A review of printing strategies, sustainable cementitious materials and characterization methods in the context of extrusion-based 3D concrete printing, *Journal of Building Engineering*. 45 (2022) 103599. <https://doi.org/10.1016/j.job.2021.103599>.
- [7] S. Singh, G. Singh, C. Prakash, S. Ramakrishna, Current status and future directions of fused filament fabrication, *Journal of Manufacturing Processes*. 55 (2020) 288–306. <https://doi.org/10.1016/j.jmapro.2020.04.049>.
- [8] Z. Chen, Z. Li, J. Li, C. Liu, C. Lao, Y. Fu, C. Liu, Y. Li, P. Wang, Y. He, 3D printing of ceramics: A review, *Journal of the European Ceramic Society*. 39 (2019) 661–687. <https://doi.org/10.1016/j.jeurceramsoc.2018.11.013>.
- [9] Q. Yuan, D. Zhou, K.H. Khayat, D. Feys, C. Shi, On the measurement of evolution of structural build-up of cement paste with time by static yield stress test vs. small amplitude oscillatory shear test, *Cement and Concrete Research*. 99 (2017) 183–189. <https://doi.org/10.1016/j.cemconres.2017.05.014>.
- [10] Y. Fu, A. Downey, L. Yuan, A. Pratt, Y. Balogun, In situ monitoring for fused filament fabrication process: A review, *Additive Manufacturing*. 38 (2021) 101749. <https://doi.org/10.1016/j.addma.2020.101749>.
- [11] J. Sun, D. Ye, J. Zou, X. Chen, Y. Wang, J. Yuan, H. Liang, H. Qu, J. Binner, J. Bai, A review on additive manufacturing of ceramic matrix composites, *Journal of Materials Science & Technology*. 138 (2023) 1–16. <https://doi.org/10.1016/j.jmst.2022.06.039>.
- [12] T.-S. Jang, H.-D. Jung, H.M. Pan, W.T. Han, S. Chen, J. Song, 3D printing of hydrogel composite systems: Recent advances in technology for tissue engineering, *Int J Bioprint*. 4 (2018) 126. <https://doi.org/10.18063/IJB.v4i1.126>.
- [13] S. Soleymani Eil Bakhtiari, H.R. Bakhsheshi-Rad, S. Karbasi, M. Razzaghi, M. Tavakoli, A.F. Ismail, S. Sharif, S. RamaKrishna, X. Chen, F. Berto, 3-Dimensional Printing of Hydrogel-Based Nanocomposites: A Comprehensive Review on the Technology Description, Properties, and Applications, *Advanced Engineering Materials*. 23 (2021) 2100477. <https://doi.org/10.1002/adem.202100477>.
- [14] A. Siddika, Md.A.A. Mamun, W. Ferdous, A.K. Saha, R. Alyousef, 3D-printed concrete: applications, performance, and challenges, *Journal of Sustainable Cement-Based Materials*. 9 (2020) 127–164. <https://doi.org/10.1080/21650373.2019.1705199>.
- [15] J. Zhang, J. Wang, S. Dong, X. Yu, B. Han, A review of the current progress and application of 3D printed concrete, *Composites Part A: Applied Science and Manufacturing*. 125 (2019) 105533. <https://doi.org/10.1016/j.compositesa.2019.105533>.
- [16] M. Golab, S. Massey, J. Moultrie, How generalisable are material extrusion additive manufacturing parameter optimisation studies? A systematic review, *Heliyon*. 8 (2022) e11592. <https://doi.org/10.1016/j.heliyon.2022.e11592>.
- [17] P. Wang, B. Zou, H. Xiao, S. Ding, C. Huang, Effects of printing parameters of fused deposition modeling on mechanical properties, surface quality, and microstructure of PEEK, *Journal of Materials Processing Technology*. 271 (2019) 62–74. <https://doi.org/10.1016/j.jmatprotec.2019.03.016>.

- [18] M.S. Alsoufi, A.E. Elsayed, How Surface Roughness Performance of Printed Parts Manufactured by Desktop FDM 3D Printer with PLA+ is Influenced by Measuring Direction, *American Journal of Mechanical Engineering*. (n.d.) 12.
- [19] J. Allum, A. Moetazedian, A. Gleadall, V.V. Silberschmidt, Interlayer bonding has bulk-material strength in extrusion additive manufacturing: New understanding of anisotropy, *Additive Manufacturing*. 34 (2020) 101297. <https://doi.org/10.1016/j.addma.2020.101297>.
- [20] N. Ashrafi, Experimental prediction of material deformation in large-scale additive manufacturing of concrete, *Additive Manufacturing*. 37 (2021) 101656. <https://doi.org/10.1016/j.addma.2020.101656>.
- [21] N. Mostafa, H.M. Syed, S. Igor, G. Andrew, A Study of Melt Flow Analysis of an ABS-Iron Composite in Fused Deposition Modelling Process, *Tsinghua Science & Technology*. 14 (2009) 29–37. [https://doi.org/10.1016/S1007-0214\(09\)70063-X](https://doi.org/10.1016/S1007-0214(09)70063-X).
- [22] P. Shakor, S. Nejadi, G. Paul, S. Malek, Review of Emerging Additive Manufacturing Technologies in 3D Printing of Cementitious Materials in the Construction Industry, *Frontiers in Built Environment*. 4 (2019). <https://www.frontiersin.org/articles/10.3389/fbuil.2018.00085> (accessed January 29, 2023).
- [23] F.D.C. Siacor, Q. Chen, J.Y. Zhao, L. Han, A.D. Valino, E.B. Taboada, E.B. Caldon, R.C. Advincula, On the additive manufacturing (3D printing) of viscoelastic materials and flow behavior: From composites to food manufacturing, *Additive Manufacturing*. 45 (2021) 102043. <https://doi.org/10.1016/j.addma.2021.102043>.
- [24] J. Gardan, A. Makke, N. Recho, A Method to Improve the Fracture Toughness Using 3D Printing by Extrusion Deposition, *Procedia Structural Integrity*. 2 (2016) 144–151. <https://doi.org/10.1016/j.prostr.2016.06.019>.
- [25] R.C. Ogle, J. Lee, U.K. Vaidya, Improved Specimen Design for Interlayer Adhesion Parameter Optimization of Material Extrusion, *SSRN Journal*. (2022). <https://doi.org/10.2139/ssrn.4239104>.
- [26] G.P. Greeff, M. Schilling, Closed loop control of slippage during filament transport in molten material extrusion, *Additive Manufacturing*. 14 (2017) 31–38. <https://doi.org/10.1016/j.addma.2016.12.005>.
- [27] J. Go, S.N. Schiffres, A.G. Stevens, A.J. Hart, Rate limits of additive manufacturing by fused filament fabrication and guidelines for high-throughput system design, *Additive Manufacturing*. 16 (2017) 1–11. <https://doi.org/10.1016/j.addma.2017.03.007>.
- [28] M.E. Mackay, The importance of rheological behavior in the additive manufacturing technique material extrusion, *Journal of Rheology*. 62 (2018) 1549–1561. <https://doi.org/10.1122/1.5037687>.
- [29] S. Bakrani Balani, F. Chabert, V. Nassiet, A. Cantarel, Influence of printing parameters on the stability of deposited beads in fused filament fabrication of poly(lactic) acid, *Additive Manufacturing*. 25 (2019) 112–121. <https://doi.org/10.1016/j.addma.2018.10.012>.
- [30] C. Luo, X. Wang, K.B. Migler, J.E. Seppala, Effects of feed rates on temperature profiles and feed forces in material extrusion additive manufacturing, *Additive Manufacturing*. 35 (2020) 101361. <https://doi.org/10.1016/j.addma.2020.101361>.
- [31] M.P. Serdeczny, R. Comminal, Md.T. Mollah, D.B. Pedersen, J. Spangenberg, Numerical modeling of the polymer flow through the hot-end in filament-based material extrusion additive manufacturing, *Additive Manufacturing*. 36 (2020) 101454. <https://doi.org/10.1016/j.addma.2020.101454>.
- [32] M.P. Serdeczny, R. Comminal, M.T. Mollah, D.B. Pedersen, J. Spangenberg, Viscoelastic simulation and optimisation of the polymer flow through the hot-end during filament-based material extrusion additive manufacturing, *Virtual and Physical Prototyping*. 17 (2022) 205–219. <https://doi.org/10.1080/17452759.2022.2028522>.
- [33] P.F. Flowers, C. Reyes, S. Ye, M.J. Kim, B.J. Wiley, 3D printing electronic components and circuits with conductive thermoplastic filament, *Additive Manufacturing*. 18 (2017) 156–163. <https://doi.org/10.1016/j.addma.2017.10.002>.
- [34] R. Guerra Silva, M.J. Torres, J. Zahr Viñuela, A.G. Zamora, Manufacturing and Characterization of 3D Miniature Polymer Lattice Structures Using Fused Filament Fabrication, *Polymers*. 13 (2021) 635. <https://doi.org/10.3390/polym13040635>.
- [35] A. Moetazedian, A.S. Budisuharto, V.V. Silberschmidt, A. Gleadall, CONVEX (CONTinuously Varied EXtrusion): A new scale of design for additive manufacturing, *Additive Manufacturing*. 37 (2021) 101576. <https://doi.org/10.1016/j.addma.2020.101576>.
- [36] V.M. Bruère, A. Lion, J. Holtmannspötter, M. Johlitz, Under-extrusion challenges for elastic filaments: the influence of moisture on additive manufacturing, *Prog Addit Manuf*. 7 (2022) 445–452. <https://doi.org/10.1007/s40964-022-00300-y>.
- [37] T.D. Ngo, A. Kashani, G. Imbalzano, K.T.Q. Nguyen, D. Hui, Additive manufacturing (3D printing): A review of materials, methods, applications and challenges, *Composites Part B: Engineering*. 143 (2018) 172–196. <https://doi.org/10.1016/j.compositesb.2018.02.012>.

- [38] B. Brenken, E. Barocio, A. Favaloro, V. Kunc, R.B. Pipes, Fused filament fabrication of fiber-reinforced polymers: A review, *Additive Manufacturing*. 21 (2018) 1–16. <https://doi.org/10.1016/j.addma.2018.01.002>.
- [39] J. Gonzalez-Gutierrez, S. Cano, S. Schuschnigg, C. Kukla, J. Sapkota, C. Holzer, Additive Manufacturing of Metallic and Ceramic Components by the Material Extrusion of Highly-Filled Polymers: A Review and Future Perspectives, *Materials*. 11 (2018) 840. <https://doi.org/10.3390/ma11050840>.
- [40] Z. Wang, Z. Fang, Z. Xie, D.E. Smith, A Review on Microstructural Formations of Discontinuous Fiber-Reinforced Polymer Composites Prepared via Material Extrusion Additive Manufacturing: Fiber Orientation, Fiber Attrition, and Micro-Voids Distribution, *Polymers*. 14 (2022) 4941. <https://doi.org/10.3390/polym14224941>.
- [41] B.P. Heller, D.E. Smith, D.A. Jack, Effects of extrudate swell and nozzle geometry on fiber orientation in Fused Filament Fabrication nozzle flow, *Additive Manufacturing*. 12 (2016) 252–264. <https://doi.org/10.1016/j.addma.2016.06.005>.
- [42] K. Bates-Green, T. Howie, Materials for 3D printing by fused deposition, Edmonds Community College. (2017) 1–21.
- [43] S.L. Messimer, A.E. Patterson, N. Muna, A.P. Deshpande, T. Rocha Pereira, Characterization and Processing Behavior of Heated Aluminum-Polycarbonate Composite Build Plates for the FDM Additive Manufacturing Process, *Journal of Manufacturing and Materials Processing*. 2 (2018) 12. <https://doi.org/10.3390/jmmp2010012>.
- [44] M. Manoj Prabhakar, A.K. Saravanan, A. Haiter Lenin, I. Jerin Ieno, K. Mayandi, P. Sethu Ramalingam, A short review on 3D printing methods, process parameters and materials, *Materials Today: Proceedings*. 45 (2021) 6108–6114. <https://doi.org/10.1016/j.matpr.2020.10.225>.
- [45] G. Murugesan, Guide on FDM 3D Printing Technology | FDM 3D Printer Working, (n.d.). <https://electroloom.com/fdm-3d-printing-and-printer-guide/> (accessed January 29, 2023).
- [46] PLA 3D Printing Service - Clear Plastic Printing, D3D Printing - Online 3d Print Service. (n.d.). <https://d3dprinting.com/product/pla-3dprinting/> (accessed January 29, 2023).
- [47] C. Okyay, B. Sağbaş, DETERMINING OPTIMAL ROBOCASTING PROCESS PARAMETERS FOR ADDITIVE MANUFACTURING OF CERAMIC PARTS, *International Journal of 3D Printing Technologies and Digital Industry*. (2021). <https://doi.org/10.46519/ij3dptdi.904697>.
- [48] F. Bos, R. Wolfs, Z. Ahmed, T. Salet, Additive manufacturing of concrete in construction: potentials and challenges of 3D concrete printing, *Virtual and Physical Prototyping*. 11 (2016) 209–225. <https://doi.org/10.1080/17452759.2016.1209867>.
- [49] A. Bellini, L. Shor, S.I. Gucer, New developments in fused deposition modeling of ceramics, *Rapid Prototyping Journal*. 11 (2005) 214–220. <https://doi.org/10.1108/13552540510612901>.
- [50] J. Malda, J. Visser, F.P. Melchels, T. Jüngst, W.E. Hennink, W.J.A. Dhert, J. Groll, D.W. Hutmacher, 25th Anniversary Article: Engineering Hydrogels for Biofabrication, *Adv. Mater.* 25 (2013) 5011–5028. <https://doi.org/10.1002/adma.201302042>.
- [51] B. Xie, R.L. Parkhill, W.L. Warren, J.E. Smay, Direct Writing of Three-Dimensional Polymer Scaffolds Using Colloidal Gels, *Adv. Funct. Mater.* 16 (2006) 1685–1693. <https://doi.org/10.1002/adfm.200500666>.
- [52] J. Lindahl, A.A. Hassen, S. Romberg, B. Hedger, P.H. Jr, T. Deluca, W. Morrison, S. Kim, A. Roschli, D. Nuttal, B. Post, L. Love, V. Kunc, Large-scale additive manufacturing with reactive polymers, in: Oak Ridge National Lab. (ORNL), Oak Ridge, TN (United States), 2017: p. 8. <https://www.osti.gov/servlets/purl/1511953>.
- [53] A. du Plessis, A.J. Babafemi, S.C. Paul, B. Panda, J.P. Tran, C. Broeckhoven, Biomimicry for 3D concrete printing: A review and perspective, *Additive Manufacturing*. 38 (2021) 101823. <https://doi.org/10.1016/j.addma.2020.101823>.
- [54] N. Ranjbar, M. Mehrli, C. Kuenzel, C. Gundlach, D.B. Pedersen, A. Dolatshahi-Pirouz, J. Spangenberg, Rheological characterization of 3D printable geopolymers, *Cement and Concrete Research*. 147 (2021) 106498. <https://doi.org/10.1016/j.cemconres.2021.106498>.
- [55] E. Peng, D. Zhang, J. Ding, Ceramic Robocasting: Recent Achievements, Potential, and Future Developments, *Adv. Mater.* 30 (2018) 1802404. <https://doi.org/10.1002/adma.201802404>.
- [56] S.C. Paul, Y.W.D. Tay, B. Panda, M.J. Tan, Fresh and hardened properties of 3D printable cementitious materials for building and construction, *Archives of Civil and Mechanical Engineering*. 18 (2018) 311–319. <https://doi.org/10.1016/j.acme.2017.02.008>.
- [57] R.A. Buswell, W.R.L. da Silva, F.P. Bos, H.R. Schipper, D. Lowke, N. Hack, H. Kloft, V. Mechtcherine, T. Wangler, N. Roussel, A process classification framework for defining and describing

- Digital Fabrication with Concrete, Cement and Concrete Research. 134 (2020) 106068. <https://doi.org/10.1016/j.cemconres.2020.106068>.
- [58] D. Asprone, C. Menna, F.P. Bos, T.A.M. Salet, J. Mata-Falcón, W. Kaufmann, Rethinking reinforcement for digital fabrication with concrete, *Cement and Concrete Research*. 112 (2018) 111–121. <https://doi.org/10.1016/j.cemconres.2018.05.020>.
- [59] B. Zhu, J. Pan, B. Nematollahi, Z. Zhou, Y. Zhang, J. Sanjayan, Development of 3D printable engineered cementitious composites with ultra-high tensile ductility for digital construction, *Materials & Design*. 181 (2019) 108088. <https://doi.org/10.1016/j.matdes.2019.108088>.
- [60] Tronxy Moore 1 Clay 3D Printer DIY Kit Liquid Deposition Molding Ceramic 3D Printer, Tronxy3dprinter.Com. (n.d.). <https://www.tronxy3dprinter.com/en-dk/products/tronxy-moore-1-clay-3d-printer-diy-kit-liquid-deposition-molding-ceramic-3d-printer> (accessed January 26, 2023).
- [61] 3D Printing Materials: Ceramic Resin, Formlabs. (n.d.). <https://formlabs.com/asia/materials/ceramics/> (accessed January 30, 2023).
- [62] L. Breseghello, R. Naboni, Toolpath-based design for 3D concrete printing of carbon-efficient architectural structures, *Additive Manufacturing*. 56 (2022) 102872. <https://doi.org/10.1016/j.addma.2022.102872>.
- [63] Is 3D printing the future for building homes? – DW – 07/30/2021, Dw.Com. (n.d.). <https://www.dw.com/en/is-3d-printing-the-future-for-building-homes/a-58679995> (accessed February 2, 2023).
- [64] R. Comminal, M.P. Serdeczny, D.B. Pedersen, J. Spangenberg, Numerical modeling of the strand deposition flow in extrusion-based additive manufacturing, *Additive Manufacturing*. 20 (2018) 68–76. <https://doi.org/10.1016/j.addma.2017.12.013>.
- [65] D. Ma, X. Tian, S. Wang, H. Liu, S. Chen, J. Han, L. Xia, Strand-Morphology-Based Process Optimization for Extrusion-Based Silicone Additive Manufacturing, *Polymers*. 13 (2021) 3576. <https://doi.org/10.3390/polym13203576>.
- [66] M. Golab, S. Massey, J. Moultrie, Experimental Investigation of Filament Behaviour in Material Extrusion Additive Manufacturing, in: M. Meboldt, C. Klahn (Eds.), *Industrializing Additive Manufacturing*, Springer International Publishing, Cham, 2021: pp. 279–292. https://doi.org/10.1007/978-3-030-54334-1_20.
- [67] B.K. Behera, M.K. Singh, Role of filament cross-section in properties of PET multifilament yarn and fabric. Part II: effect of fibre cross-sectional shapes on fabric hand, *The Journal of The Textile Institute*. 105 (2014) 365–376. <https://doi.org/10.1080/00405000.2013.774132>.
- [68] E.C. Balta, A. Altinkaynak, Numerical and experimental analysis of bead cross-sectional geometry in fused filament fabrication, *Rapid Prototyping Journal*. 28 (2022) 1882–1894. <https://doi.org/10.1108/RPJ-09-2021-0255>.
- [69] J.-F. Agassant, F. Pigeonneau, L. Sardo, M. Vincent, Flow analysis of the polymer spreading during extrusion additive manufacturing, *Additive Manufacturing*. 29 (2019) 100794. <https://doi.org/10.1016/j.addma.2019.100794>.
- [70] M. Hebda, C. McIlroy, B. Whiteside, F. Caton-Rose, P. Coates, A method for predicting geometric characteristics of polymer deposition during fused-filament-fabrication, *Additive Manufacturing*. 27 (2019) 99–108. <https://doi.org/10.1016/j.addma.2019.02.013>.
- [71] M.P. Serdeczny, R. Comminal, D.B. Pedersen, J. Spangenberg, Experimental validation of a numerical model for the strand shape in material extrusion additive manufacturing, *Additive Manufacturing*. 24 (2018) 145–153. <https://doi.org/10.1016/j.addma.2018.09.022>.
- [72] B. Behdani, M. Senter, L. Mason, M. Leu, J. Park, Numerical Study on the Temperature-Dependent Viscosity Effect on the Strand Shape in Extrusion-Based Additive Manufacturing, *JMMP*. 4 (2020) 46. <https://doi.org/10.3390/jmmp4020046>.
- [73] R. Comminal, W.R. Leal da Silva, T.J. Andersen, H. Stang, J. Spangenberg, Modelling of 3D concrete printing based on computational fluid dynamics, *Cement and Concrete Research*. 138 (2020) 106256. <https://doi.org/10.1016/j.cemconres.2020.106256>.
- [74] R. Comminal, W.R.L. da Silva, T.J. Andersen, H. Stang, J. Spangenberg, Influence of Processing Parameters on the Layer Geometry in 3D Concrete Printing: Experiments and Modelling, in: F.P. Bos, S.S. Lucas, R.J.M. Wolfs, T.A.M. Salet (Eds.), *Second RILEM International Conference on Concrete and Digital Fabrication*, Springer International Publishing, Cham, 2020: pp. 852–862. https://doi.org/10.1007/978-3-030-49916-7_83.
- [75] D. Halvorson, A Solid Foundation for: High-Quality Corners, *Printed Solid*, (2016). <https://www.printedsolid.com/blogs/news/a-solid-foundation-for-high-quality-corners>. (accessed November 29, 2021).

- [76] J.F. Rodriguez, J.P. Thomas, J.E. Renaud, Characterization of the mesostructure of fused-deposition acrylonitrile-butadiene-styrene materials, *Rapid Prototyping Journal*. 6 (2000) 175–186. <https://doi.org/10.1108/13552540010337056>.
- [77] Y. Tao, F. Kong, Z. Li, J. Zhang, X. Zhao, Q. Yin, D. Xing, P. Li, A review on voids of 3D printed parts by fused filament fabrication, *Journal of Materials Research and Technology*. 15 (2021) 4860–4879. <https://doi.org/10.1016/j.jmrt.2021.10.108>.
- [78] D.V.A. Ceretti, R. Fiorio, T. Van Waeleghem, A. Desmet, B. Florizoone, L. Cardon, D.R. D’hooge, Exploiting mono- and hybrid nanocomposite materials for fused filament fabrication with ACRYLONITRILE BUTADIENE STYRENE as polymer matrix, *J of Applied Polymer Sci*. 139 (2022). <https://doi.org/10.1002/app.52922>.
- [79] V. Mechtcherine, R. Buswell, H. Kloft, F.P. Bos, N. Hack, R. Wolfs, J. Sanjayan, B. Nematollahi, E. Ivaniuk, T. Neef, Integrating reinforcement in digital fabrication with concrete: A review and classification framework, *Cement and Concrete Composites*. 119 (2021) 103964. <https://doi.org/10.1016/j.cemconcomp.2021.103964>.
- [80] T.H.J. Vaneker, Material Extrusion of Continuous Fiber Reinforced Plastics Using Commingled Yarn, *Procedia CIRP*. 66 (2017) 317–322. <https://doi.org/10.1016/j.procir.2017.03.367>.
- [81] L. Gebhard, J. Mata-Falcón, A. Anton, B. Dillenburger, W. Kaufmann, Structural behaviour of 3D printed concrete beams with various reinforcement strategies, *Engineering Structures*. 240 (2021) 112380. <https://doi.org/10.1016/j.engstruct.2021.112380>.
- [82] T. Marchment, J. Sanjayan, Reinforcement method for 3D concrete printing using paste-coated bar penetrations, *Automation in Construction*. 127 (2021) 103694. <https://doi.org/10.1016/j.autcon.2021.103694>.
- [83] N. Tagscherer, T. Schromm, K. Drechsler, Foundational Investigation on the Characterization of Porosity and Fiber Orientation Using XCT in Large-Scale Extrusion Additive Manufacturing, *Materials*. 15 (2022) 2290. <https://doi.org/10.3390/ma15062290>.
- [84] Y. He, F. Yang, H. Zhao, Q. Gao, B. Xia, J. Fu, Research on the printability of hydrogels in 3D bioprinting, *Sci Rep*. 6 (2016) 29977. <https://doi.org/10.1038/srep29977>.
- [85] L. Friedrich, M. Begley, Corner accuracy in direct ink writing with support material, *Bioprinting*. 19 (2020) e00086. <https://doi.org/10.1016/j.bprint.2020.e00086>.
- [86] L.G. Blok, M.L. Longana, H. Yu, B.K.S. Woods, An investigation into 3D printing of fibre reinforced thermoplastic composites, *Additive Manufacturing*. 22 (2018) 176–186. <https://doi.org/10.1016/j.addma.2018.04.039>.
- [87] J. Xu, R.A. Buswell, P. Kinnell, I. Biro, J. Hodgson, N. Konstantinidis, L. Ding, Inspecting manufacturing precision of 3D printed concrete parts based on geometric dimensioning and tolerancing, *Automation in Construction*. 117 (2020) 103233. <https://doi.org/10.1016/j.autcon.2020.103233>.
- [88] L. Yang, S.M.E. Sepasgozar, S. Shirowzhan, A. Kashani, D. Edwards, Nozzle criteria for enhancing extrudability, buildability and interlayer bonding in 3D printing concrete, *Automation in Construction*. 146 (2023) 104671. <https://doi.org/10.1016/j.autcon.2022.104671>.
- [89] D.S. Ertay, A. Yuen, Y. Altintas, Synchronized material deposition rate control with path velocity on fused filament fabrication machines, *Additive Manufacturing*. 19 (2018) 205–213. <https://doi.org/10.1016/j.addma.2017.05.011>.
- [90] W. Han, M.A. Jafari, Coordination Control of Positioning and Deposition in Layered Manufacturing, *IEEE Trans. Ind. Electron*. 54 (2007) 651–659. <https://doi.org/10.1109/TIE.2006.885468>.
- [91] Y. Jin, Y. He, J. Fu, W. Gan, Z. Lin, Optimization of tool-path generation for material extrusion-based additive manufacturing technology, *Additive Manufacturing*. 1–4 (2014) 32–47. <https://doi.org/10.1016/j.addma.2014.08.004>.
- [92] W. Han, M.A. Jafari, K. Seyed, Process speeding up via deposition planning in fused deposition-based layered manufacturing processes, *Rapid Prototyping Journal*. 9 (2003) 212–218. <https://doi.org/10.1108/13552540310489596>.
- [93] R. Comminal, M.P. Serdeczny, D.B. Pedersen, J. Spangenberg, Numerical Modeling of the Material Deposition and Contouring Precision in Fused Deposition Modeling, in: *Proceedings of the Annual International Solid Freeform Fabrication Symposium*, 2018: pp. 1855–1864.
- [94] R. Comminal, M.P. Serdeczny, D.B. Pedersen, J. Spangenberg, Motion planning and numerical simulation of material deposition at corners in extrusion additive manufacturing, *Additive Manufacturing*. 29 (2019) 100753. <https://doi.org/10.1016/j.addma.2019.06.005>.
- [95] A.J. Babafemi, J.T. Kolawole, M.J. Miah, S.C. Paul, B. Panda, A Concise Review on Interlayer Bond Strength in 3D Concrete Printing, *Sustainability*. 13 (2021) 7137. <https://doi.org/10.3390/su13137137>.

- [96] L.C. Hwa, S. Rajoo, A.M. Noor, N. Ahmad, M.B. Uday, Recent advances in 3D printing of porous ceramics: A review, *Current Opinion in Solid State and Materials Science*. 21 (2017) 323–347. <https://doi.org/10.1016/j.cossms.2017.08.002>.
- [97] G. Liu, X. Zhang, X. Chen, Y. He, L. Cheng, M. Huo, J. Yin, F. Hao, S. Chen, P. Wang, S. Yi, L. Wan, Z. Mao, Z. Chen, X. Wang, Z. Cao, J. Lu, Additive manufacturing of structural materials, *Materials Science and Engineering: R: Reports*. 145 (2021) 100596. <https://doi.org/10.1016/j.mser.2020.100596>.
- [98] G.H. Ahmed, A review of “3D concrete printing”: Materials and process characterization, economic considerations and environmental sustainability, *Journal of Building Engineering*. 66 (2023) 105863. <https://doi.org/10.1016/j.job.2023.105863>.
- [99] M. Chen, L. Yang, Y. Zheng, Y. Huang, L. Li, P. Zhao, S. Wang, L. Lu, X. Cheng, Yield stress and thixotropy control of 3D-printed calcium sulfoaluminate cement composites with metakaolin related to structural build-up, *Construction and Building Materials*. 252 (2020) 119090. <https://doi.org/10.1016/j.conbuildmat.2020.119090>.
- [100] Q. Sun, G.M. Rizvi, C.T. Bellehumeur, P. Gu, Effect of processing conditions on the bonding quality of FDM polymer filaments, *Rapid Prototyping Journal*. 14 (2008) 72–80. <https://doi.org/10.1108/13552540810862028>.
- [101] T.J. Coogan, D.O. Kazmer, Bond and part strength in fused deposition modeling, *RPJ*. 23 (2017) 414–422. <https://doi.org/10.1108/RPJ-03-2016-0050>.
- [102] W. Wu, W. Ye, P. Geng, Y. Wang, G. Li, X. Hu, J. Zhao, 3D printing of thermoplastic PI and interlayer bonding evaluation, *Materials Letters*. 229 (2018) 206–209. <https://doi.org/10.1016/j.matlet.2018.07.020>.
- [103] X. Gao, S. Qi, X. Kuang, Y. Su, J. Li, D. Wang, Fused filament fabrication of polymer materials: A review of interlayer bond, *Additive Manufacturing*. 37 (2021) 101658. <https://doi.org/10.1016/j.addma.2020.101658>.
- [104] T.T. Le, S.A. Austin, S. Lim, R.A. Buswell, R. Law, A.G.F. Gibb, T. Thorpe, Hardened properties of high-performance printing concrete, *Cement and Concrete Research*. 42 (2012) 558–566. <https://doi.org/10.1016/j.cemconres.2011.12.003>.
- [105] S. Markin, V. Mechtcherine, Measuring Plastic Shrinkage and Related Cracking of 3D Printed Concretes, in: R. Buswell, A. Blanco, S. Cavalaro, P. Kinnell (Eds.), *Third RILEM International Conference on Concrete and Digital Fabrication*, Springer International Publishing, Cham, 2022: pp. 446–452. https://doi.org/10.1007/978-3-031-06116-5_66.
- [106] P. Sreejith, K. Kannan, K. Rajagopal, A thermodynamic framework for additive manufacturing, using amorphous polymers, capable of predicting residual stress, warpage and shrinkage, *International Journal of Engineering Science*. 159 (2021) 103412. <https://doi.org/10.1016/j.ijengsci.2020.103412>.
- [107] J. Hergel, K. Hinz, S. Lefebvre, B. Thomaszewski, Extrusion-based ceramics printing with strictly-continuous deposition, *ACM Trans. Graph.* 38 (2019) 1–11. <https://doi.org/10.1145/3355089.3356509>.
- [108] S.A.O. Nair, H. Alghamdi, A. Arora, I. Mehdipour, G. Sant, N. Neithalath, Linking fresh paste microstructure, rheology and extrusion characteristics of cementitious binders for 3D printing, *Journal of the American Ceramic Society*. 102 (2019) 3951–3964. <https://doi.org/10.1111/jace.16305>.
- [109] B. Panda, C. Unluer, M.J. Tan, Extrusion and rheology characterization of geopolymer nanocomposites used in 3D printing, *Composites Part B: Engineering*. 176 (2019) 107290. <https://doi.org/10.1016/j.compositesb.2019.107290>.
- [110] C. Sun, J. Xiang, M. Xu, Y. He, Z. Tong, X. Cui, 3D extrusion free forming of geopolymer composites: Materials modification and processing optimization, *Journal of Cleaner Production*. 258 (2020) 120986. <https://doi.org/10.1016/j.jclepro.2020.120986>.
- [111] J. Reinold, V.N. Nerella, V. Mechtcherine, G. Meschke, Extrusion process simulation and layer shape prediction during 3D-concrete-printing using the Particle Finite Element Method, *Automation in Construction*. 136 (2022) 104173. <https://doi.org/10.1016/j.autcon.2022.104173>.
- [112] C.Y. Huang, Extrusion-based 3D Printing and Characterization of Edible Materials, Master Thesis, University of Waterloo, 2018. <https://uwaterloo.ca/handle/10012/12899> (accessed January 20, 2023).
- [113] W. Lao, M. Li, T.N. Wong, M.J. Tan, T. Tjahjowidodo, Improving surface finish quality in extrusion-based 3D concrete printing using machine learning-based extrudate geometry control, *Virtual and Physical Prototyping*. 15 (2020) 178–193. <https://doi.org/10.1080/17452759.2020.1713580>.

- [114] R.J.M. Wolfs, T.A.M. Salet, N. Roussel, Filament geometry control in extrusion-based additive manufacturing of concrete: The good, the bad and the ugly, *Cement and Concrete Research*. 150 (2021) 106615. <https://doi.org/10.1016/j.cemconres.2021.106615>.
- [115] N. Ashrafi, S. Nazarian, N.A. Meisel, J.P. Duarte, Experimental calibration and compensation for the continuous effect of time, number of layers and volume of material on shape deformation in small-scale additive manufacturing of concrete, *Additive Manufacturing*. 47 (2021) 102228. <https://doi.org/10.1016/j.addma.2021.102228>.
- [116] P. Wu, J. Wang, X. Wang, A critical review of the use of 3-D printing in the construction industry, *Automation in Construction*. 68 (2016) 21–31. <https://doi.org/10.1016/j.autcon.2016.04.005>.
- [117] T. Ooms, G. Vantighem, R. Van Coile, W. De Corte, A parametric modelling strategy for the numerical simulation of 3D concrete printing with complex geometries, *Additive Manufacturing*. 38 (2021) 101743. <https://doi.org/10.1016/j.addma.2020.101743>.
- [118] R.J.M. Wolfs, F.P. Bos, T.A.M. Salet, Triaxial compression testing on early age concrete for numerical analysis of 3D concrete printing, *Cement and Concrete Composites*. 104 (2019) 103344. <https://doi.org/10.1016/j.cemconcomp.2019.103344>.
- [119] R.J.M. Wolfs, F.P. Bos, T.A.M. Salet, Early age mechanical behaviour of 3D printed concrete: Numerical modelling and experimental testing, *Cement and Concrete Research*. 106 (2018) 103–116. <https://doi.org/10.1016/j.cemconres.2018.02.001>.
- [120] M.P. Serdeczny, R. Comminal, D.B. Pedersen, J. Spangenberg, Numerical prediction of the porosity of parts fabricated with fused deposition modeling, in: *Proceedings of the Annual International Solid Freeform Fabrication Symposium, Laboratory for Freeform Fabrication*, n.d.: pp. 1849–1854.
- [121] M.P. Serdeczny, R. Comminal, D.B. Pedersen, J. Spangenberg, Numerical simulations of the mesostructure formation in material extrusion additive manufacturing, *Additive Manufacturing*. 28 (2019) 419–429. <https://doi.org/10.1016/j.addma.2019.05.024>.
- [122] M. Zhou, L. Si, P. Chen, M. Li, Y. Zhang, H. Zhou, D. Li, Experimental investigation and numerical simulations of temperature and morphology in material extrusion additive manufacturing, *Int J Adv Manuf Technol*. 119 (2022) 4863–4876. <https://doi.org/10.1007/s00170-022-08663-w>.
- [123] B. Khoshnevis, Automated construction by contour crafting—related robotics and information technologies, *Automation in Construction*. 13 (2004) 5–19. <https://doi.org/10.1016/j.autcon.2003.08.012>.
- [124] F.P. Bos, C. Menna, M. Pradena, E. Kreiger, W.R.L. da Silva, A.U. Rehman, D. Weger, R.J.M. Wolfs, Y. Zhang, L. Ferrara, V. Mechtcherine, The realities of additively manufactured concrete structures in practice, *Cement and Concrete Research*. 156 (2022) 106746. <https://doi.org/10.1016/j.cemconres.2022.106746>.
- [125] H. Kloft, M. Empelmann, N. Hack, E. Herrmann, D. Lowke, Reinforcement strategies for 3D-concrete-printing, *Civil Engineering Design*. 2 (2020) 131–139. <https://doi.org/10.1002/cend.202000022>.
- [126] F.P. Bos, Z.Y. Ahmed, R.J.M. Wolfs, T.A.M. Salet, 3D Printing Concrete with Reinforcement, in: D.A. Hordijk, M. Luković (Eds.), *High Tech Concrete: Where Technology and Engineering Meet*, Springer International Publishing, Cham, 2018: pp. 2484–2493. https://doi.org/10.1007/978-3-319-59471-2_283.
- [127] J. Xiao, G. Ji, Y. Zhang, G. Ma, V. Mechtcherine, J. Pan, L. Wang, T. Ding, Z. Duan, S. Du, Large-scale 3D printing concrete technology: Current status and future opportunities, *Cement and Concrete Composites*. 122 (2021) 104115. <https://doi.org/10.1016/j.cemconcomp.2021.104115>.
- [128] Z. Wu, A.M. Memari, J.P. Duarte, State of the Art Review of Reinforcement Strategies and Technologies for 3D Printing of Concrete, *Energies*. 15 (2022) 360. <https://doi.org/10.3390/en15010360>.
- [129] B. Baz, G. Aouad, P. Leblond, O. Al-Mansouri, M. D’hondt, S. Remond, Mechanical assessment of concrete – Steel bonding in 3D printed elements, *Construction and Building Materials*. 256 (2020) 119457. <https://doi.org/10.1016/j.conbuildmat.2020.119457>.
- [130] G. Ma, Z. Li, L. Wang, G. Bai, Micro-cable reinforced geopolymer composite for extrusion-based 3D printing, *Materials Letters*. 235 (2019) 144–147. <https://doi.org/10.1016/j.matlet.2018.09.159>.
- [131] Z. Li, L. Wang, G. Ma, Mechanical improvement of continuous steel microcable reinforced geopolymer composites for 3D printing subjected to different loading conditions, *Composites Part B: Engineering*. 187 (2020) 107796. <https://doi.org/10.1016/j.compositesb.2020.107796>.
- [132] A.R. Arunothayan, B. Nematollahi, R. Ranade, S.H. Bong, J. Sanjayan, Development of 3D-printable ultra-high performance fiber-reinforced concrete for digital construction, *Construction and Building Materials*. 257 (2020) 119546. <https://doi.org/10.1016/j.conbuildmat.2020.119546>.

- [133] B. Nematollahi, P. Vijay, J. Sanjayan, A. Nazari, M. Xia, V. Naidu Nerella, V. Mechtcherine, Effect of Polypropylene Fibre Addition on Properties of Geopolymers Made by 3D Printing for Digital Construction, *Materials*. 11 (2018) 2352. <https://doi.org/10.3390/ma11122352>.
- [134] V. Mechtcherine, J. Grafe, V.N. Nerella, E. Spaniol, M. Hertel, U. Füssel, 3D-printed steel reinforcement for digital concrete construction – Manufacture, mechanical properties and bond behaviour, *Construction and Building Materials*. 179 (2018) 125–137. <https://doi.org/10.1016/j.conbuildmat.2018.05.202>.
- [135] J. Müller, M. Grabowski, C. Müller, J. Hensel, J. Unglaub, K. Thiele, H. Kloft, K. Dilger, Design and Parameter Identification of Wire and Arc Additively Manufactured (WAAM) Steel Bars for Use in Construction, *Metals*. 9 (2019) 725. <https://doi.org/10.3390/met9070725>.
- [136] T. Marchment, J. Sanjayan, Mesh reinforcing method for 3D Concrete Printing, *Automation in Construction*. 109 (2020) 102992. <https://doi.org/10.1016/j.autcon.2019.102992>.
- [137] T. Marchment, J. Sanjayan, Bond properties of reinforcing bar penetrations in 3D concrete printing, *Automation in Construction*. 120 (2020) 103394. <https://doi.org/10.1016/j.autcon.2020.103394>.
- [138] V2 Vesta Beton-3D-Drucker baut kleines Haus, (n.d.). <https://3druck.com/drucker-und-produkte/v2-vesta-beton-3d-drucker-baut-kleines-haus-2846225/> (accessed October 27, 2022).
- [139] M. Classen, J. Ungermann, R. Sharma, Additive Manufacturing of Reinforced Concrete—Development of a 3D Printing Technology for Cementitious Composites with Metallic Reinforcement, *Applied Sciences*. 10 (2020) 3791. <https://doi.org/10.3390/app10113791>.
- [140] L. Gebhard, L. Esposito, C. Menna, J. Mata-Falcón, Inter-laboratory study on the influence of 3D concrete printing set-ups on the bond behaviour of various reinforcements, *Cement and Concrete Composites*. 133 (2022) 104660. <https://doi.org/10.1016/j.cemconcomp.2022.104660>.
- [141] M.P. Serdeczny, R. Comminal, D.B. Pedersen, J. Spangenberg, Numerical Study of the Impact of Shear Thinning Behaviour on the Strand Deposition Flow in the Extrusion-Based Additive Manufacturing, in: 18th International Conference of the European Society for Precision Engineering and Nanotechnology (Euspen 18), The European Society for Precision Engineering and Nanotechnology, 2018.
- [142] E.C. Bingham, An investigation of the laws of plastic flow, US Government Printing Office, 1917.
- [143] N. Casson, A flow equation for pigment-oil suspensions of the printing ink type, *Rheology of Disperse Systems*. (1959) 84–104.
- [144] W.H. Herschel, R. Bulkley, Konsistenzmessungen von Gummi-Benzollösungen, *Kolloid Zeitschrift*. 39 (1926) 291–300.
- [145] E.J. O'Donovan, R.I. Tanner, Numerical study of the Bingham squeeze film problem, *Journal of Non-Newtonian Fluid Mechanics*. 15 (1984) 75–83. [https://doi.org/10.1016/0377-0257\(84\)80029-4](https://doi.org/10.1016/0377-0257(84)80029-4).
- [146] FLOW-3D® Version 12.0 [Computer software], (2019). <https://www.flow3d.com> (accessed May 10, 2022).
- [147] S.F. Ashby, T.A. Manteuffel, P.E. Saylor, A Taxonomy for Conjugate Gradient Methods, *SIAM J. Numer. Anal.* 27 (1990) 1542–1568. <https://doi.org/10.1137/0727091>.
- [148] R. Barrett, M. Berry, T.F. Chan, J. Demmel, J.M. Donato, J. Dongarra, V. Eijkhout, R. Pozo, C. Romine, H.V.D. Vorst, *Templates for the Solution of Linear Systems: Building Blocks for Iterative Methods*, 1994.
- [149] Y. Saad, *Iterative Methods for Sparse Linear Systems*, The PWS Series in Computer Science, 1996. <http://books.google.com/books?id=jLtiQgAACAAJ>.
- [150] Modeling Capabilities- Immersed Boundary Method | FLOW-3D | Solving The World's Toughest CFD Problems, FLOW SCIENCE. (n.d.). <https://www.flow3d.com/modeling-capabilities/immersed-boundary-method/> (accessed August 21, 2021).
- [151] C.W. Hirt, B.D. Nichols, Volume of fluid (VOF) method for the dynamics of free boundaries, *Journal of Computational Physics*. 39 (1981) 201–225. [https://doi.org/10.1016/0021-9991\(81\)90145-5](https://doi.org/10.1016/0021-9991(81)90145-5).
- [152] R. Comminal, J. Spangenberg, J.H. Hattel, Cellwise conservative unsplit advection for the volume of fluid method, *Journal of Computational Physics*. 283 (2015) 582–608. <https://doi.org/10.1016/j.jcp.2014.12.003>.
- [153] R.J. Urbanic, L. DiCecco, Investigating Surface Finish for Material Extrusion Process using Graphical Programming Tools, *IFAC-PapersOnLine*. 49 (2016) 36–41. <https://doi.org/10.1016/j.ifacol.2016.12.158>.
- [154] FLOW-3D | Solving The World's Toughest CFD Problems, FLOW SCIENCE. (n.d.). <https://www.flow3d.com/products/flow-3d-post/> (accessed April 1, 2022).

- [155] A. Gleadall, FullControl GCode Designer: Open-source software for unconstrained design in additive manufacturing, *Additive Manufacturing*. 46 (2021) 102109. <https://doi.org/10.1016/j.addma.2021.102109>.
- [156] J. Spangenberg, W.R. Leal da Silva, R. Comminal, M.T. Mollah, T.J. Andersen, H. Stang, Numerical simulation of multi-layer 3D concrete printing, *RILEM Tech Lett.* 6 (2021) 119–123. <https://doi.org/10.21809/rilemtechlett.2021.142>.

Appended Publications

Publication [A.1]: Investigation on corner precision at different corner angles in material extrusion additive manufacturing: An experimental and computational fluid dynamics analysis

Md. Tusher Mollah^{*†}, Amirpasha Moetazedian[†], Andy Gleadall[†], Jiongyi Yan[†],
Wayne Edgar Alphonso^{*}, Raphaël Comminal^{*§}, Berin Šeta^{*}, Tony Lock[‡], and Jon
Spangenberg^{*}

^{*}Department of Civil and Mechanical Engineering, Technical University of Denmark,
Denmark.

[†]Wolfson School of Mechanical and Manufacturing Engineering, Loughborough
University, United Kingdom.

[§]Flow Science, Inc., USA.

[‡]Duet3D Ltd, United Kingdom.

Published in:

*Solid Freeform Fabrication 2022: Proceedings of the 33rd Annual International Solid
Freeform Fabrication Symposium – An Additive Manufacturing Conference*, Austin,
Texas, USA, 25-27 July 2022.

Publication [A.1]: Investigation on corner precision at different corner angles in material extrusion additive manufacturing: An experimental and computational fluid dynamics analysis

The layout has been revised.

Abstract

This paper investigates the influence of different corner angles on microscale geometry in material extrusion additive manufacturing. Polylactic acid (PLA) was 3D-printed with corner angles of 15°, 30°, 45°, 60°, 75°, 90°, and 135° using Bowden and Direct-drive extruders. A computational fluid dynamics (CFD) model was developed to simulate the polymer flow through the extrusion nozzle of both extruders. The simulated corner geometries were compared with experiments to assess simulation accuracy. This included the primary and secondary mitre cross-sectional width through the corner point of the 3D-printed strands. This enabled a new understanding about the prediction accuracy of the CFD model as well as the state of material at the corners, and the deviation of experimental and simulated corners from the analytical one. Moreover, the amount of over- and under-extrusion around the corner was estimated for experimental and simulated studies compared with the analytical corner, which provided fundamental knowledge on corner precision for angular print paths.

Keywords: Microscale Corner Precision, Bowden and Direct-drive Extruders, Experiments, Computational Fluid Dynamics, Material Extrusion Additive Manufacturing

1. Introduction

Filament-based Material Extrusion Additive Manufacturing (MEX-AM), also known as Fused Deposition Modelling (FDM) and Fused Filament Fabrication (FFF), is a 3D printing technology where feedstock filament is melted in a liquefier and extruded through a nozzle onto a print platform in layer-wise manner [1–3]. In the last decade, filament-based MEX-AM has evolved from a rapid prototyping tool and is currently used in electronics, medical and automotive sectors [4]. Therefore, a demand for high-quality printed parts with an improved surface roughness [5], high mechanical properties [6], lower internal porosity [3], and high geometrical precision [5] is a growing requirement, in addition to increasing the productivity i.e., reduction in printing time. These properties of the printed part are controlled by the shape of the strands, which typically is a function of two dimensionless parameters- geometrical and speed ratios (i.e., the ratio of layer height by the nozzle diameter and the ratio between printing speed (i.e., speed of nozzle) and extrusion speed (i.e., speed of material extrusion), respectively) [7]. However, it becomes complex when it comes to achieve a precise shape of the strands along the corners, where the print head maneuvers a change in printing direction.

Corner precision in filament-based MEX-AM is affected by common defects such as corner rounding, swelling, and ringing, as reflected in [8]. Corner rounding occurs due to smoothing of the sharp corners where the nozzle executes turns at high speed and can be avoided by implementing lower printing speeds at the cost of increase in printing time [9]. Corner swelling occurs due to over-extrusion of the material at the corner forms wider and thicker strands. Before turning into the corner, the print head must decelerate while the extruder deposits material at a constant rate, leading to a bulge formation. For some systems and materials, this swelling may be reduced by synchronizing the extruder and the printing speed by a closed loop control system with a dynamic calibrated model of the extruder to manage the time lag. Corner ringing occurs due to vibrations of the printer caused by a sudden change in the printing direction. These defects can be mitigated with lower printing speeds, lower maximum acceleration or by increasing the rigidity of the

3D printer, but such changes may result in improvements for some defects whilst negatively affecting others. Corner defects like the above mentioned were also observed in micro-scale MEX-AM of materials other than thermoplastics, for instance, composite filament printing with acoustophoresis [10]. Solving these issues is non-trivial without a better understanding of the influence of different corner angles and corresponding processing parameters.

Computational Fluid Dynamics (CFD) models predicted the shape and size of the strands printed in MEX-AM under different processing conditions [7,11–14]. The predictions were validated with the experiments in different studies [15–17]. In the case of the filament-based MEX-AM, the material flow through the tiny nozzle is a creeping flow having a very low Reynolds number that can be predicted with a high viscous Newtonian fluid model [18]. Within the same assumption, Comminal et al. [19,20] investigated the sharp and smoothed trajectories of the toolpath of the corner of angles 90° and 30° to analyze the shape of the strand. It was found that the smoothed trajectories result in rounded corners and less over-extrusion; however, the toolpath deviates from its angular shape.

This study focused on the corners between two straight lines with angles of 15°, 30°, 45°, 60°, 75°, 90°, and 135°. The specimens were 3D-printed with PLA using a Bowden extruder and Direct-drive extruder. A CFD model was developed to simulate the corner of different angles for both printing strategies. The shape of the corners in simulations and experiments were compared to analytical geometry expected for the toolpath. The primary and secondary mitre widths were measured in simulations and experiments and compared with the analytical measurements. Moreover, the amount of over- and under-extrusion at the inner- and outer-corners were measured to compare their behavior with the change in angles as well as for both the printing strategies.

2. Methodology

The MEX-AM experiment was performed using the natural Polylactic acid (PLA) feedstock filament with a diameter of 1.75 mm and density of 1024 kg.m⁻³. The printing parameters and setup can be seen in Figure 1a, where the filament was fed into the nozzle hot-end using a Bowden or Direct-drive extruder. Single-wide-specimens with 10 layers (layer height = 0.2 mm) were printed that comprises seven right trapezoids of investigating corner angles such as 15°, 30°, 45°, 60°, 75°, 90°, and 135°, cf. Figure 1b.

An E3D V6-nozzle of diameter 0.4 mm was used, where the printing speed was set at 2000 mm.min⁻¹. The nozzle utilized acceleration and deceleration phases near the corner by the magnitude of 6000 mm.s⁻². The primary and secondary strands (i.e., before and after turn, respectively) were printed along the x-direction and x, y-directions. Special corner printing parameters such as blending acceleration factor (i.e., the ratio of the acceleration time to the deceleration time) and the jerk speed (i.e., an instantaneous jump of velocity by the amount of jerk when acceleration and deceleration are initiated) were disabled to ensure fundamental understanding to be achieved and for repeatability. The extrusion speed was set to achieve strands width of 0.8 mm. Other widths are the subject of ongoing research. In the case of printing with the Bowden extruder, the extrusion speed was constant throughout the toolpath, whereas the Direct-drive extruder used extrusion speed that was synchronized with the acceleration and deceleration of the nozzle near the

corner. The extrusion temperature was set at 210 °C. The experiments were performed in an E3D tool changer because it allowed two different extruders (Bowden or Direct-drive) and a microscope to be implemented in a single hardware system for direct comparability and in-process inspection. Specimens were produced by direct Gcode scripting using open-source software FullControl GCode Designer [21]. After printing the specimens, the microscopic tool was used to capture a series of images of different angles (showed later in this section).

A CFD model was developed in FLOW-3D® (Version 12.0; 2019; Flow Science, Inc.) [22] in order to mimic the extrusion-deposition flow during printing corners in MEX-AM. The model comprises a cylindrical nozzle mimicking the tip of the E3D V6-nozzle (i.e., a cylinder of 0.4 mm orifice and 1.0 mm outer diameter), and a static substrate/build plate, as seen in Figure 1c. The cruising speed and acceleration values were imported to model as the experiment was done. However, the extrusion speed was calibrated based on the uniform cross-sectional width of the strands (i.e., 0.8 mm) of the 3D-printed specimens. The simulated length of the strand is 8 mm at either side of the corner. The height of the nozzle end from the substrate was also calibrated to achieve a strand of the height of 0.2 mm, to match printed specimens.

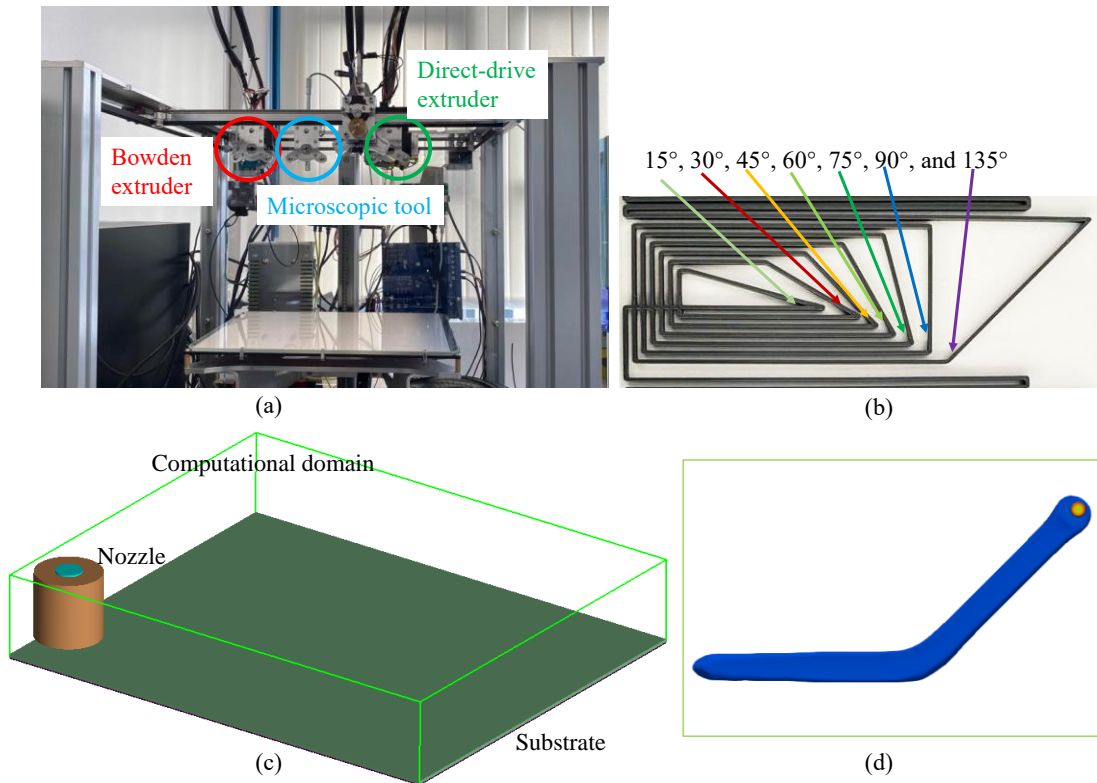


Figure 1: (a) Experimental setup with printing (Bowden and Direct-drive extruders) and microscopic tools; (b) printed sample of different corner angles (for example, Bowden extruder); (c) geometry of the CFD model with nozzle, substrate, and computational domain; and (d) simulated strand of corner angle 135° as an example.

The deposition flow of the material was modeled as a transient and isothermal Newtonian fluid, as in [7,11]. Serdeczny et al. [15] showed that those are sufficient assumption to

predict the strands size observed in experiments. Thus, the flow dynamics is governed by the continuity and momentum equations:

$$\nabla \cdot \mathbf{q} = 0 \quad (1)$$

$$\rho \left(\frac{\partial \mathbf{q}}{\partial t} + \mathbf{q} \cdot \nabla \mathbf{q} \right) = -\nabla p + \rho \mathbf{g}_0 + \mu \nabla^2 \mathbf{q} \quad (2)$$

where \mathbf{q} denotes the velocity vector, p is the pressure, \mathbf{g}_0 is the acceleration vector due to the gravity $\mathbf{g}_0 = (0, 0, -g_0)$, t is the time, $\rho = 1024 \text{ kg.m}^{-3}$ is the density, and $\mu = 1000 \text{ Pa.s}$ is the constant viscosity of the Newtonian fluid.

The computational domain was meshed with a uniform Cartesian grid and discretized by the Finite Volume Method (FVM). The top plane of the domain was assigned an inlet boundary where an artificial solid object was inserted in order to prevent flow apart from the nozzle orifice. The bottom plane containing the substrate was assigned to a wall boundary condition. Other boundaries were assigned to a continuative boundary condition. The pressure and velocity components are solved implicitly in time. The momentum advection was calculated explicitly with second-order accuracy in space and first-order accuracy in time. Moreover, the free surface was modelled with the Volume of Fluid method (VOF) [23,24].

The microscale geometries of both the printed and simulated strands of all the angles were post-processed using ImageJ® in order to compare the strands shape, measure the primary and secondary mitre cross-sectional widths, and calculate the amount of over- and under-extrusion. The method for post-processing results is presented in Figure 2 for a corner with angle 15° as an example. At first, the experimental microscopy was processed to show the edges of the print, as seen in Figure 2a. This is to compare the experimental prints of Bowden and Direct-drive extruders, as well as to compare those individual ones with the simulated and analytical corners. The analytical corner (i.e., the horizontal cut in the middle of the oblong shape of the strand) is presented in Figure 2b (left) indicating the double-deposition and analytical underfill phases on the strand. Moreover, the measurements of primary and secondary mitre cross-sectional widths are shown, where the primary one was measured as the distance between the inner-groove and the outer edge through the corner-point at an angle equal to half of the corner, and the secondary one was measured as the distance between the outer edges before and after the turn which is perpendicular to the primary mitre and passes through the corner-point.

Furthermore, all the 3D-printed and simulated strands were compared with the analytical corner in order to calculate the area of over- and under-extrusion observed at the inner- and outer-corners as depicted in Figure 2c. Over-extrusion observed at the inner-corner is defined as inner over-extrusion, whereas under-extrusion was not available. Furthermore, at the outer-edge, over-extrusion observed before and after the turn is defined as outer over-extrusion, whereas under-extrusion observed at the circular track of the corner having a diameter of 0.8 mm (same as the width) is defined as outer under-extrusion. The analytical underfill (Figure 2b) was not occupied by polymer in any specimen, so is not characterized quantitatively.

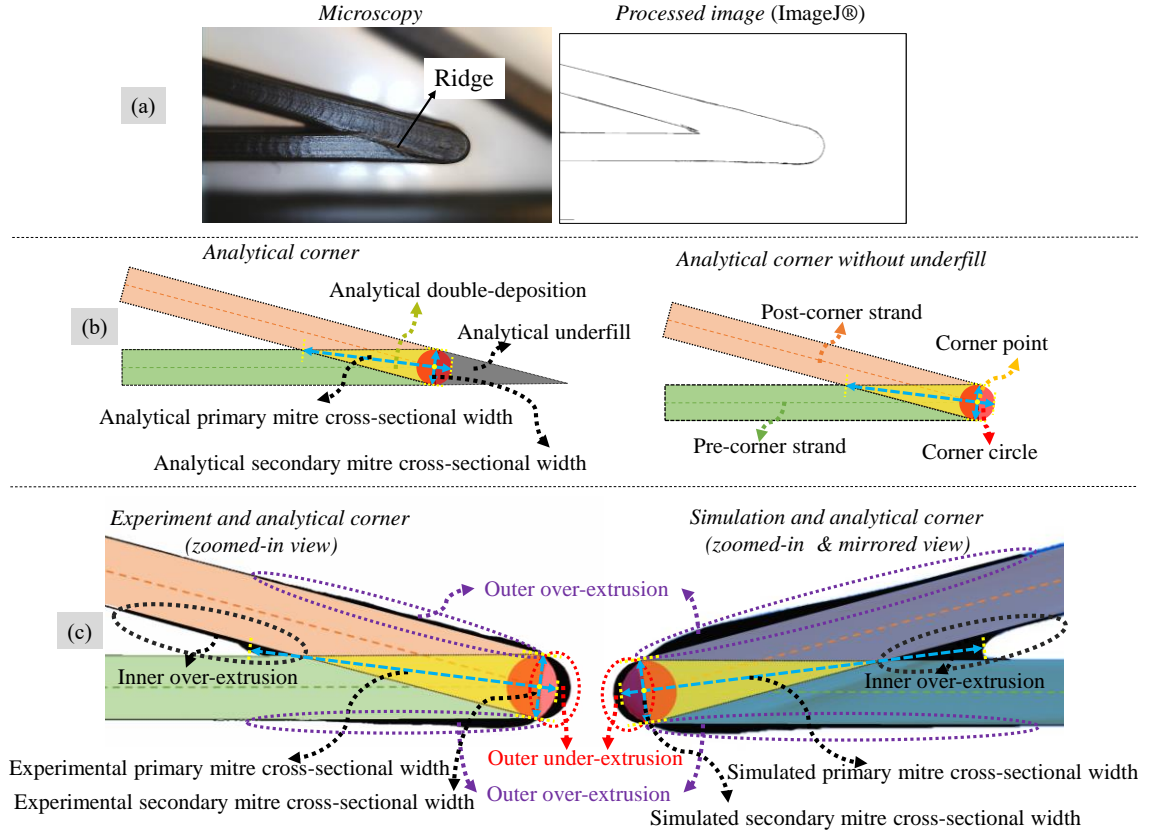


Figure 2: Post-processing of results: (a) processing of microscopy using ImageJ®, (b) Analytical cross-section of corner and measurement of primary and secondary cross-sectional width (left), and Analytical corner without the underfill to compare with experiments and simulations (right), and (c) measurement of over- and under-extrusion of experimental (left) and simulated (right) corners compared to the analytical corner. Moreover, post-processing showed for a corner with angle 15° as an example.

3. Results and discussion

The MEX-AM experiment and simulated results for different angular turns with angles of 15° , 30° , 45° , 60° , 75° , 90° , and 135° are presented in Figures 3 to 5. Figure 3 shows the microscopic images of the strands obtained using the Bowden extruder as well as simulated strands and a qualitative comparison between the two approaches. The corner with the largest angle (135°) seemed to have a uniform shape, whereas smaller angles resulted in larger swelling at the corner due to double-deposition. Furthermore, the corner with larger angles appeared to have ringing effect on the surface of the post-corner strand, i.e., the presence of repeated curves on the printed surface. This is typically due to the vibration after the sudden direction change. The ringing seemed to disappear gradually with decreasing the angle. This could be attributed to the amount the double-deposition at the corner, where already deposited material on the pre-corner strands helped in limiting the vibration. Simulations predicted the shape of the corners quite well and were able to predict the existence of a ridge between the pre- and post-corner strands caused by the nozzle ploughing through previously deposited material, as seen in the experiment.

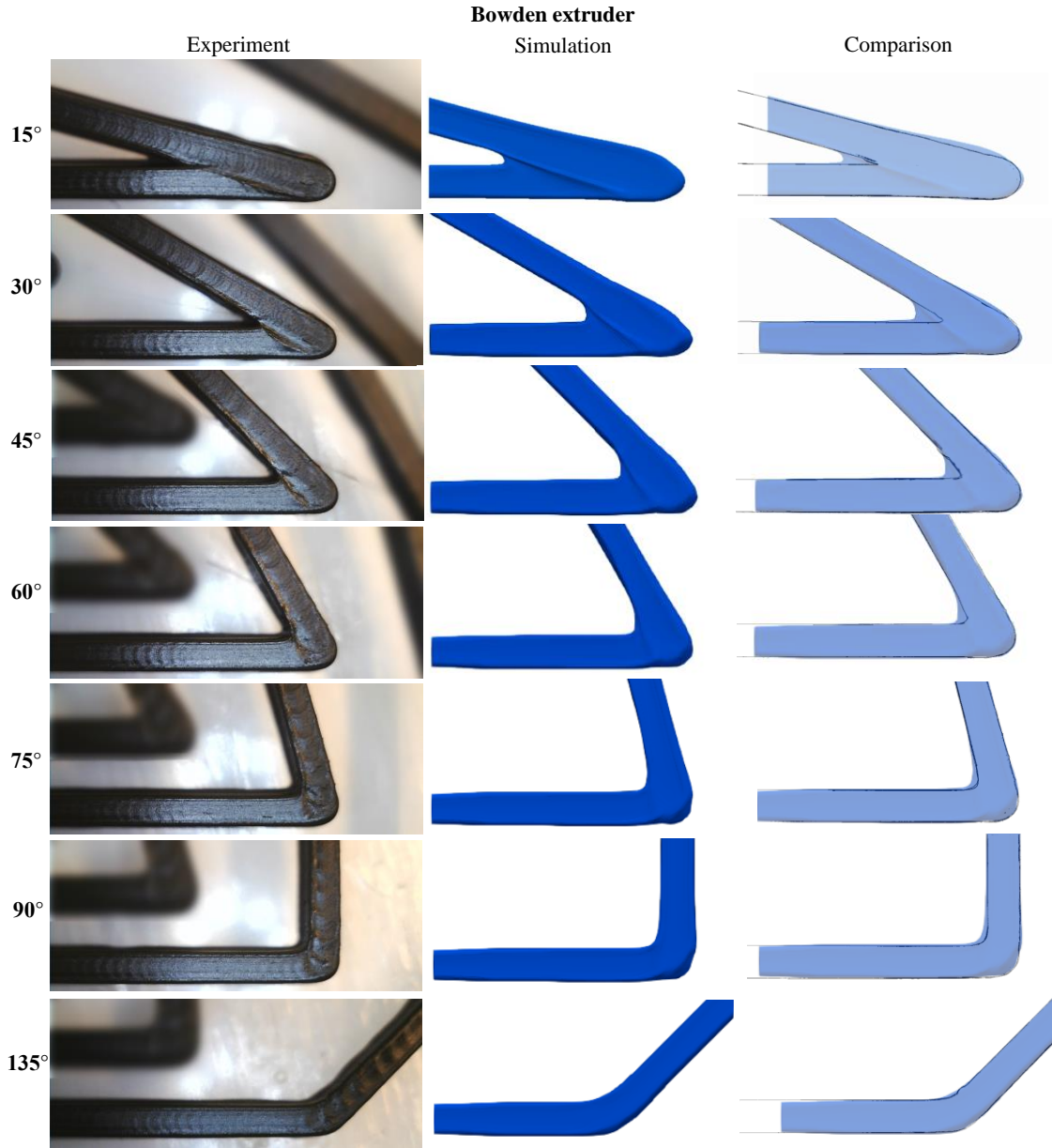


Figure 3: Microscopic images of corners of different angles using Bowden extruder (left column), simulated results (middle column), and comparison between simulations and experiments (right column).

Comparison between experiments and simulations showed that the simulations predict the corners to an acceptable accuracy, cf. Figure 3-right column. However, compared to the experiments, simulations predicted more over-extrusion observed at the inner-corner for most of the angles. This could partly be attributed to the fact that when the nozzle is ploughing through previously deposited material, fluid adjacent to the nozzle moves in the printing direction as well as spreading sideways, therefore, creating wider width. Discrepancies could also come from the Newtonian fluid assumption of the CFD model. Different constitutive fluid models could be tested in future investigations.

Figure 4 presents the microscale images of the corners obtained using the Direct-drive extruder along with the simulated corners and a qualitative comparison between

experiment and simulated results. Like the corners from Bowden extruder, the ringing effect observed at the corners with larger angles disappeared gradually when decreasing the angle. Simulations predicted corners quite similar to the ones with Bowden extruder, including the ridge prediction. However, like the Bowden extruder, the observed ridge in the experiments seemed to be larger than the simulations. Furthermore, the ridge in the simulations showed a smooth transition on the presence of material in both phases from pre-corner strand to ridge and from ridge to post-corner strand. On the contrary, a straight transition was observed between the pre-corner strand and ridge in experiment, indicating that the already deposited material in the pre-corner strand may be solidified during printing of the post-corner strand. This effect could be investigated more by including the solidification of strands in the simulations. By qualitative comparison, it appears that the simulations predicted more over-extrusion at the inner-corner than was found experimentally. Moreover, a discrepancy was found in the outer-corner, where the simulations predicted less rounded shape than experiments. This is because the Direct-drive extruder is more responsive than the Bowden one, it may be more able to synchronize extrusion rate with the acceleration and deceleration of the printing speed, and therefore it is expected to have less material extrusion at the corners, which was predicted accurately in the simulations. Although it is dependent on the values of acceleration which determines for how long extrusion is reduced before and after the corner (note that the acceleration is 6000 ms^{-2}). The discrepancy pointed out that the experimental shapes got dominated by additional corner parameters that could be investigated in future studies.

Furthermore, Figure 5(a and b) qualitatively compares the corners at different turns for both Bowden and Direct-drive extruders. The full range of angles can be seen to clearly identify trends in changes to shape and position of the outer edge of the strands. The Direct-drive extruder resulted in more rounded corners than the Bowden extruder, where the outer edge before the turn shifted gradually upwards and left in the figure with the increase in angles. Furthermore, the outer edge after the turn showed a straight release in Bowden extruder, whereas, for Direct-drive extruder, a rounded shape can be seen.

Furthermore, the primary and secondary mitre widths in experiments and simulations, as well as their deviation with the analytical mitre widths, and the amount of over- and under-extrusion were quantified and presented in Figure 5(c to h) for both the Bowden and Direct-drive extruders. It can be seen in Figure 5(c and f) that the primary mitre width for experiments and simulations showed a slight difference for smaller angles, and the difference reduced when the angle was increased for both the extruders. However, an opposite trend was observed in the secondary mitre widths for Bowden and Direct-drive extruders, where Bowden extruder resulted in smaller differences between the experiments and simulations for smaller angles, and the difference increased when increasing the angle. This trend was seen as the Direct-drive simulations extruded less material near the corner point due to the prescribed extrusion speed that was synchronized with the printing speed. In contrast, the experiment was anticipated to be affected by additional corner printing parameters, as discussed in the earlier section. As a result, the secondary mitre width got smaller in simulations and larger in the experiments than the analytical mitre width (i.e., deviation with the negative and positive values, respectively) for Direct-drive extruder, cf. Figure 5g. In contrast, secondary mitre width for Bowden extruder showed minor deviation from the analytical one except for the case of 135° , cf. Figure 5d. Moreover, both the experimental and simulated primary mitre widths observed

conspicuous deviation from the analytical one, which reduced as a function of angles as seen in Figure 5(d and g).



Figure 4: Microscopic images of corners of different angles using Direct extruder (left column), simulated results (middle column), and comparison between simulations and experiments (right column).

The area of over- and under-extrusion were measured at both the inner- and outer-sides of the corner for both the experiments (bars with solid border) and simulations (colored bars with dotted border) comparing with the analytical corner. Figure 5(e and h) show the measurement for Bowden and Direct-drive extruders, respectively. It can be seen that the largest area of over-extrusion was observed at the outer corner for the smallest angle in both extruders. Simulations were found to predict more over- and under-extrusion than experiments except for the under-extrusion observed at the outer corner of Bowden extruder, where experiments showed larger under-extrusion. This is simply a consequence of the fact that the corner shape was predicted to be larger in simulations than in experiments, which occupies a greater part of the analytical circle at the corner

point. In contrast, over prediction of the under-extrusion for Direct-drive was observed due to the underfilling of the analytical rectangular pre- and post-corner strands and a part of the circle, which was caused due to the decrease in extrusion speed near the corner point. Furthermore, the over-extrusion at the outer corner in Direct-drive extruder showed a gradual decrease with the angles and met zero over-extrusion for higher angles. Simulated over-extrusion at the inner-corner had a decreasing trend with increasing angles, whereas the experimental one deviates from the trend.

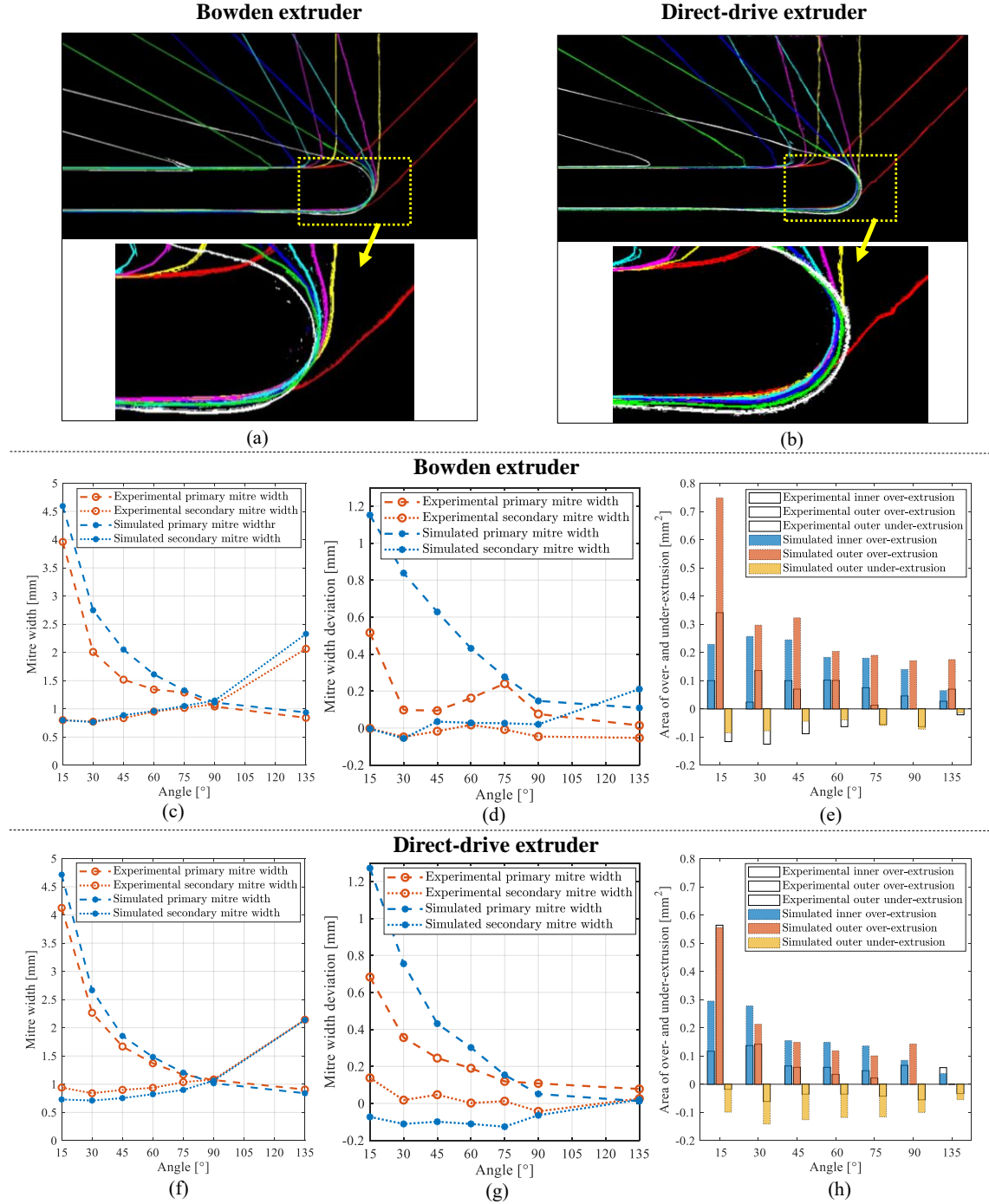


Figure 5: Qualitative and quantitative comparison of corners with different angles: (a) prints with Bowden extruder; (b) prints with Direct extruder; (c) mitre width as a function of angles- Bowden extruder; (d) mitre width deviation as a function of angles- Bowden

extruder; (e) over- and under-extrusion as a function of angles- Bowden extruder; (f) mitre width as a function of angles- Direct-drive extruder; (g) mitre width deviation as a function of angles- Direct-drive extruder; (h) over- and under-extrusion as a function of angles- Direct-drive extruder. Moreover, the deviations in Figure 5 (d and g) were calculated relative to the analytical measures.

4. Conclusion

This study investigated the precision of 3D-printed corners of different angles in filament-based MEX-AM. Two different printing strategies were considered, which include printing with a constant extrusion speed using Bowden extruder and printing with a variable extrusion speed synchronized with the speed of nozzle using Direct-drive extruder. It was found that strands with Direct-drive extruder results in a more rounded shape at the corner of different angles. 3D-printed corners and the simulated corners under the Computational Fluid Dynamics paradigm were compared with the analytical corners. It was seen that the predicted primary and secondary mitre widths in simulations and experiments showed larger deviation with the analytical widths for smaller angles that decreased with increasing angles.

Furthermore, the simulations predict the actual difference between the extruders, where larger under-extrusion was observed at the outer-corner for the Direct-drive due to the syncretized extrusion speed. However, this was not clearly understandable in the experiments indicating the domination of other corner printing parameters. Moreover, the predicted over-extrusion at the inner- and outer-corner in simulations is larger than the one measured in experiment for most of the angles, which is due to the nozzle ploughing within the double-deposition zone. This over prediction could be a drawback of the Newtonian fluid model as there exist an interaction between the fluid strands. The study is currently being extended to investigate several constitutive models as well as the influence of different processing conditions such as nozzle diameter, layer height, acceleration, etc.

Acknowledgements

MTM and JS would like to acknowledge the support from the Danish Council for Independent Research (DFF) | Technology and Production Sciences (FTP) (Contract No. 8022-00042B). Moreover, MTM, WEA, RC, and JS thank **FLOW-3D**[®] for their support in regard to licenses. MTM would like to thank Loughborough University for the opportunity to continue an external research stay of four months. Furthermore, he would like to thank Otto Mønstedts Fond and Thomas B. Thriges Fond for their partial funding for the external research stay. AG thanks Sanjay Mortimer from E3D-Online, for supporting the research with an E3D tool changer and for his invaluable advice.

References

- [1] B. Brenken, E. Barocio, A. Favaloro, V. Kunc, R.B. Pipes, Fused filament fabrication of fiber-reinforced polymers: A review, *Addit. Manuf.* 21 (2018) 1–16. <https://doi.org/10.1016/j.addma.2018.01.002>.
- [2] T.D. Ngo, A. Kashani, G. Imbalzano, K.T.Q. Nguyen, D. Hui, Additive manufacturing (3D printing): A review of materials, methods, applications and challenges, *Compos. Part B Eng.* 143 (2018) 172–196. <https://doi.org/10.1016/j.compositesb.2018.02.012>.

- [3] J. Allum, A. Moetazedian, A. Gleadall, V.V. Silberschmidt, Interlayer bonding has bulk-material strength in extrusion additive manufacturing: New understanding of anisotropy, *Addit. Manuf.* 34 (2020) 101297. <https://doi.org/10.1016/j.addma.2020.101297>.
- [4] H.K. Dave, J.P. Davim, *Materials Forming, Machining and Tribology*, in: 2022. <http://www.springer.com/series/11181>.
- [5] M.S. Alsoufi, A.E. Elsayed, How Surface Roughness Performance of Printed Parts Manufactured by Desktop FDM 3D Printer with PLA+ is Influenced by Measuring Direction, *Am. J. Mech. Eng.* (n.d.) 12.
- [6] P. Wang, B. Zou, H. Xiao, S. Ding, C. Huang, Effects of printing parameters of fused deposition modeling on mechanical properties, surface quality, and microstructure of PEEK, *J. Mater. Process. Technol.* 271 (2019) 62–74. <https://doi.org/10.1016/j.jmatprotec.2019.03.016>.
- [7] R. Comminal, M.P. Serdeczny, D.B. Pedersen, J. Spangenberg, Numerical modeling of the strand deposition flow in extrusion-based additive manufacturing, *Addit. Manuf.* 20 (2018) 68–76. <https://doi.org/10.1016/j.addma.2017.12.013>.
- [8] D. Halvorson, *A Solid Foundation for: High-Quality Corners, Printed Solid*, (2016). <https://www.printedsolid.com/blogs/news/a-solid-foundation-for-high-quality-corners>. (accessed November 29, 2021).
- [9] W. Han, M.A. Jafari, K. Seyed, Process speeding up via deposition planning in fused deposition-based layered manufacturing processes, *Rapid Prototyp. J.* 9 (2003) 212–218. <https://doi.org/10.1108/13552540310489596>.
- [10] L. Friedrich, M. Begley, Corner accuracy in direct ink writing with support material, *Bioprinting.* 19 (2020) e00086. <https://doi.org/10.1016/j.bprint.2020.e00086>.
- [11] M.P. Serdeczny, R. Comminal, D.B. Pedersen, J. Spangenberg, Numerical prediction of the porosity of parts fabricated with fused deposition modeling, in: *Proc. Annu. Int. Solid Free. Fabr. Symp., Laboratory for Freeform Fabrication*, n.d.: pp. 1849–1854.
- [12] M.T. Mollah, R. Comminal, M.P. Serdeczny, D.B. Pedersen, J. Spangenberg, Stability and deformations of deposited layers in material extrusion additive manufacturing, *Addit. Manuf.* (2021) 102193. <https://doi.org/10.1016/j.addma.2021.102193>.
- [13] R. Comminal, M.P. Serdeczny, D.B. Pedersen, J. Spangenberg, Numerical simulation of extrusion-based additive manufacturing – effect of the nozzle geometry on the strand cross-section, in: *18th Int. Conf. Eur. Soc. Precis. Eng. Nanotechnol. Euspen 18, The European Society for Precision Engineering and Nanotechnology*, 2018.
- [14] M.T. Mollah, R. Comminal, M.P. Serdeczny, D.B. Pedersen, J. Spangenberg, Numerical Predictions of Bottom Layer Stability in Material Extrusion Additive Manufacturing, *JOM.* (2022). <https://doi.org/10.1007/s11837-021-05035-9>.
- [15] M.P. Serdeczny, R. Comminal, D.B. Pedersen, J. Spangenberg, Experimental validation of a numerical model for the strand shape in material extrusion additive manufacturing, *Addit. Manuf.* 24 (2018) 145–153. <https://doi.org/10.1016/j.addma.2018.09.022>.
- [16] R. Comminal, W.R. Leal da Silva, T.J. Andersen, H. Stang, J. Spangenberg, Modelling of 3D concrete printing based on computational fluid dynamics, *Cem. Concr. Res.* 138 (2020) 106256. <https://doi.org/10.1016/j.cemconres.2020.106256>.

- [17] J. Spangenberg, W.R. Leal da Silva, R. Comminal, M.T. Mollah, T.J. Andersen, H. Stang, Numerical simulation of multi-layer 3D concrete printing, *RILEM Tech. Lett.* 6 (2021) 119–123. <https://doi.org/10.21809/rilemtechlett.2021.142>.
- [18] M.P. Serdeczny, R. Comminal, D.B. Pedersen, J. Spangenberg, Numerical simulations of the mesostructure formation in material extrusion additive manufacturing, *Addit. Manuf.* 28 (2019) 419–429. <https://doi.org/10.1016/j.addma.2019.05.024>.
- [19] R. Comminal, M.P. Serdeczny, D.B. Pedersen, J. Spangenberg, Numerical Modeling of the Material Deposition and Contouring Precision in Fused Deposition Modeling, in: *Proc. Annu. Int. Solid Free. Fabr. Symp.*, 2018: pp. 1855–1864.
- [20] R. Comminal, M.P. Serdeczny, D.B. Pedersen, J. Spangenberg, Motion planning and numerical simulation of material deposition at corners in extrusion additive manufacturing, *Addit. Manuf.* 29 (2019) 100753. <https://doi.org/10.1016/j.addma.2019.06.005>.
- [21] A. Gleadall, FullControl GCode Designer: Open-source software for unconstrained design in additive manufacturing, *Addit. Manuf.* 46 (2021) 102109. <https://doi.org/10.1016/j.addma.2021.102109>.
- [22] FLOW-3D® Version 12.0 [Computer software], Santa Fe, NM: Flow Science, Inc., 2019. <https://www.flow3d.com> (accessed May 10, 2022).
- [23] C.W. Hirt, B.D. Nichols, Volume of fluid (VOF) method for the dynamics of free boundaries, *J. Comput. Phys.* 39 (1981) 201–225. [https://doi.org/10.1016/0021-9991\(81\)90145-5](https://doi.org/10.1016/0021-9991(81)90145-5).
- [24] R. Comminal, J. Spangenberg, J.H. Hattel, Cellwise conservative unsplit advection for the volume of fluid method, *J. Comput. Phys.* 283 (2015) 582–608. <https://doi.org/10.1016/j.jcp.2014.12.003>.

Publication [A.2]: Stability and deformations of deposited layers in material extrusion additive manufacturing

Md. Tusher Mollah, Raphaël Comminal, Marcin P. Serdeczny, David B. Pedersen, Jon Spangenberg

Department of Mechanical Engineering, Technical University of Denmark, Denmark.

Published in:
Additive Manufacturing, Vol. 46, pp. 102193, 2021,
<https://doi.org/10.1016/j.addma.2021.102193>.

Reproduced with permission from ELSEVIER.

The layout has been revised.

Table 1 has been transposed to fit with the layout of the thesis.

Abstracts

This paper presents computational fluid dynamics simulations of the deposition flow during printing of multiple layers in material extrusion additive manufacturing. The developed model predicts the morphology of the deposited layers and captures the layer deformations during the printing of viscoplastic materials. The physics is governed by the continuity and momentum equations with the Bingham constitutive model, formulated as a generalized Newtonian fluid. The cross-sectional shapes of the deposited layers are predicted, and the deformation of layers is studied for different constitutive parameters of the material. It is shown that the deformation of layers is due to the hydrostatic pressure of the printed material, as well as the extrusion pressure during the extrusion. The simulations show that a higher yield stress results in prints with less deformations, while a higher plastic viscosity leads to larger deformations in the deposited layers. Moreover, the influence of the printing speed, extrusion speed, layer height, and nozzle diameter on the deformation of the printed layers is investigated. Finally, the model provides a conservative estimate of the required increase in yield stress that a viscoplastic material demands after deposition in order to support the hydrostatic and extrusion pressure of the subsequently printed layers.

Keywords: Viscoplastic Materials, Material Extrusion Additive Manufacturing (MEX-AM), Multiple-Layers Deposition, Computational Fluid Dynamics (CFD), Deformation Control.

1. Introduction

Three-dimensional printing of viscoplastic materials has grown in popularity over the recent years, due to the success of Material Extrusion Additive Manufacturing (MEX-AM) [1]. Viscoplastic materials, such as ceramic pastes [2, 3], hydrogels [4], thermosets [5], and concrete [6], behave like solids when the applied load is below their yield stress, and like a fluid when the applied load exceeds their yield stress [7]. Viscoplastic materials are typically used in MEX-AM techniques such as Robocasting [8], and 3D concrete printing [9, 10]. The differences between these technologies lie in the processing of the material before the extrusion and in the printing scale (from microscale to big area additive manufacturing). In these extrusion-based technologies, the structure is fabricated in a layer-by-layer approach onto a solid surface/support [11, 12]. During the process, the material is typically deposited on top of the previously printed layers that may be already solidified (wet-on-dry printing) or still deformable (wet-on-wet printing) [1].

In wet-on-wet printing, control over the deformation of layers is important for the stability and geometrical accuracy of the prints. If the material is too liquid after the deposition, it cannot support the pressure of the subsequently deposited layers. On the other hand, the material flowability is a necessity during extrusion through the nozzle. Several experimental studies have been performed to analyze the physics of the extrusion and deposition of viscoplastic materials, as reviewed in [13, 14, 15, 16]. The experimental measurements can be supplemented with Computational Fluid Dynamics (CFD) simulations to gain a more complete picture of MEX-AM. A review of the CFD studies within the material processing and deposition in 3D concrete printing was presented by Roussel et al. [17]. Wolfs et al. [18] predicted numerically the failure-deformation of a cylindrical structure due to the self-weight by calculating the stiffness and strength of the individual layers. It was found that the deformations can take place in all layers, however

the most critical deformation occurs in the bottom layer. Comminal et al. [19, 20] presented three-dimensional simulations of the material deposition in MEX-AM, where the fluid was approximated as Newtonian. Subsequently, the model was experimentally validated in [21] for polymer-based MEX-AM, and extended to simulate the deposition of multiple layers in [22], where the previously printed material was assumed solid. Xia et al. [23] simulated the influence of the viscoelastic effects on the shape of deposited layers in MEX-AM. A numerical model for simulating the deposition of a viscoplastic material was recently presented and experimentally validated in [24] and [25]. These studies focused on predicting the cross-sectional shape of a single printed layer for different processing conditions (relative printing speed, and layer height). Despite these research efforts, a limited number of studies have focused on investigating the material deformations in wet-on-wet printing when multiple layers are deposited on top of each other.

This paper presents CFD simulations of the extrusion-deposition flow of a viscoplastic material for several subsequent layers (viz. three- and five-layers). The material is continuously printed one layer over another on a fixed solid surface. The rheology of the viscoplastic material is approximated by the Bingham constitutive equation that is formulated using the Generalized Newtonian Fluid (GNF) model. The CFD model is used to predict the cross-sectional shapes of the layers and their deformations while printing the next layers on top. Moreover, the simulations are used to quantify the extrusion pressure applied by the deposited material on the substrate, and the previously printed layers. Numerically, it is investigated how the process parameters (i.e., the extrusion speed, printing speed, nozzle diameter, and layer height) and the material rheology affect the deformations of the deposited layers. Section 2 describes the methodology of the study. Section 3 presents and discusses the results. The study is summarized and concluded in Section 4.

2. Methodology

2.1. Governing equations and numerical model

The CFD simulation captures the extrusion-deposition flow of a viscoplastic material with the Bingham constitutive model. The fluid is extruded through a cylindrical nozzle with an inner diameter D , and it is deposited on a fixed solid surface. At time $t = 0$, the extrusion nozzle is at rest and located above the solid surface at a distance h , which is the theoretical layer height. At time $t > 0$, the material starts to flow through the nozzle with a fully developed profile and a constant average velocity U , called the extrusion speed. The nozzle remains at rest until the extruded fluid touches the substrate. Then, the extrusion nozzle starts to move with a constant velocity V , called the printing speed, along the horizontal x -direction. The material is extruded over a length l . After the layer is printed, the nozzle lifts up in the z -direction by the distance h , and the next layer is printed.

The model geometry along with the boundary conditions, nozzle toolpath, and the computational domain are presented in Figure 1. The bottom plane of the domain is a stationary wall (the substrate). The top plane is an inlet boundary, where an artificial solid component obscures the most of the plane except the region that coincides with the nozzle orifice. A no-slip boundary condition is applied to all solid surfaces. The remaining planes have prescribed a continuative boundary condition that assumes a zero derivative of the velocity field across the boundary plane, and these planes are not in contact with the

extruded material. Finally, the flow is assumed to be symmetrical with respect to the xz -plane.

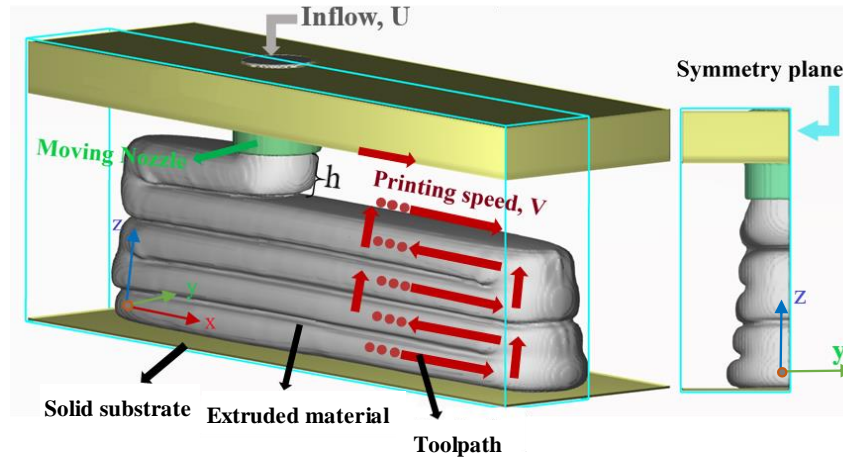


Figure 1: Model geometry with the computational domain, extrusion nozzle, toolpath, and boundary conditions. The model is presented while printing the fifth layer.

The computational domain is meshed with a uniform Cartesian grid. The cell size is adapted in order to have between 25 to 32 cells along the nozzle diameter. The dimensions of the computational domain and the total number of discrete cells depend on the simulation case. The values of different processing parameters as well as meshing information for all the computational model cases are summarized in Table 1.

Table 1: Processing and meshing parameters of the computational models for different simulation cases.

Model cases	Case 1	Case 2	Case 3	Case 4	Case5	Case 6	Case 7
Nozzle diameter D (mm)	25	50	1.5	0.4	25	25	25
Gap ratio h/D	0.5	0.5	0.5	0.5	0.75	1	0.5
l/D	8	8	8	12	8	8	8
Number of layers N	3	3	3	3	3	3	5
Printing speed V (mm/s)	20 - 50	20	20	20	40	40	50
Extrusion speed U (mm/s)	20 - 40	20	20	20	40	40	40
Speed ratio $S_r = V/U$	0.75 - 1.5	1	1	1	1	1	1.25
Dimensions of Computational domain (mm)	250×35×88.5	500×70×128	15×1.5×5.35	5.9×0.6×1.43	250×35×95	250×30×101	250×35×105
Number of cells	8,04,204	7,80,624	9,63,000	14,73,920	8,67,456	7,60,530	9,48,780
Cell size (mm)	0.8	1.78	0.05	0.015	0.98	1	0.8

The flow is assumed to be transient and isothermal. The material is treated as incompressible with a constant density ρ . Therefore, the flow dynamics is governed by the continuity and momentum equations:

$$\nabla \cdot \mathbf{q} = 0 \quad (1)$$

$$\rho \left(\frac{\partial \mathbf{q}}{\partial t} + \mathbf{q} \cdot \nabla \mathbf{q} \right) = -\nabla p + \rho \mathbf{g}_0 + \nabla \cdot \mathbf{S}_T \quad (2)$$

where \mathbf{q} is the velocity vector, t is the time, p is the pressure, \mathbf{g}_0 denotes the acceleration vector due to the gravity $\mathbf{g}_0 = (0, 0, -g_0)$, and \mathbf{S}_T represents the deviatoric stress-tensor. The non-Newtonian flow behavior of viscoplastic materials can be predicted by a constitutive equation that accounts for the yield stress τ_0 , such as the Bingham [26], Casson [27], or Herschel-Bulkley (generalized Bingham) models [28]. In this study, the viscosity μ of the viscoplastic material is modeled with the Bingham rheological model:

$$\mu(\dot{\gamma}) = \begin{cases} \infty, & \text{for } \tau \leq \tau_0 \\ \eta_p + \frac{\tau_0}{\dot{\gamma}}, & \text{for } \tau > \tau_0 \end{cases} \quad (3)$$

where τ is the magnitude of the deviatoric stress-tensor, calculated as $\tau = \sqrt{2\text{tr}(\mathbf{S}_T^2)}$, η_p is the plastic viscosity, and $\dot{\gamma}$ is the strain rate. Equation 3 prevents the flow of material when $\tau \leq \tau_0$.

The Bingham rheological model (see Equation 3) is used to calculate the deviatoric stress-tensor according to the generalized Newtonian fluid model:

$$\mathbf{S}_T = \mu(\dot{\gamma}) \mathbf{D}_T \quad (4)$$

where $\mathbf{D}_T = (1/2)((\nabla \mathbf{q}) + (\nabla \mathbf{q})')$ is the deformation rate tensor, the prime (') stands for the transpose notation, and $\dot{\gamma} = \sqrt{2\text{tr}(\mathbf{D}_T^2)}$. It should be noted that in this study, the rheological properties are assumed to be independent of time during the whole printing process.

The model represented by Equations 1 and 2 is solved numerically with the finite volume method, using the CFD software **FLOW-3D**, version 12.0 [29]. **FLOW-3D** has previously been successfully used for the simulations of the flow of viscoplastic materials [30, 24]. The Bingham constitutive model (Equation 3) is implemented using a bi-viscous regularization [31] (Equation 5), to avoid the computational singularity, due to the infinite viscosity that appears in the theoretical model (Equation 3). This is done by considering that the material have a maximum apparent viscosity $\mu_{max.app}$, for shear rates $\dot{\gamma}$ smaller than a critical shear rate $\dot{\gamma}_c$. Thus, the apparent viscosity μ_{app} in the numerical model is:

$$\mu_{app}(\dot{\gamma}) = \begin{cases} \mu_{max.app} = \eta_p + \frac{\tau_0}{\dot{\gamma}_c}, & \text{for } \dot{\gamma} < \dot{\gamma}_c \\ \eta_p + \frac{\tau_0}{\dot{\gamma}}, & \text{for } \dot{\gamma} \geq \dot{\gamma}_c \end{cases} \quad (5)$$

The viscous stress is solved implicitly by the successive under-relaxation technique, which allows to stabilize the convergence, when a high viscous stress gradient is observed. The pressure and velocity equations are solved implicitly in time to ensure the stability of the solution. The free surface tracking is captured by the Volume-Of-Fluid method (see e.g. [32, 33] for details). An explicit solver calculated the momentum advection, which is second-order accurate in space and first-order accurate in time. The time step size is automatically controlled by the solver based on the stability criteria [29].

The material properties used in the simulations are presented in Table 2. Furthermore, The hydrostatic pressure applied by the printed layer to the bottom of the printed part is calculated as $P_H = N\rho g_0 h$, where N is the number of deposited layers and $g_0 = 9.81 \text{ ms}^{-2}$. Figure 1 presents the simulated results of five successive layers using the parameters, $V = 50 \text{ mms}^{-1}$, $U = 40 \text{ mms}^{-1}$, $D = 25 \text{ mm}$, $h = 12.5 \text{ mm}$, $\tau_0 = 1000 \text{ Pa}$ and $\eta_p = 33 \text{ Pa.s}$. The material is continuously dispensed through a nozzle and creates a vertical 5-layers structure. It can be seen that the CFD model predicts the deformation of the printed layers while printing the next layers on top.

Table 2: Material properties.

Parameter	Denoted by	Unit	Values
Density	ρ	kg.m^{-3}	1000
Dynamic yield stress	τ_0	Pa	100 – 2500
Plastic viscosity	η_p	Pa.s	12 – 900
Critical shear rate	$\dot{\gamma}_c$	s^{-1}	0.1

2.2. Post-processing

The CFD results are post-processed in MATLAB to obtain the cross-sectional shapes of the layers as well as the extrusion pressure. The cross-sectional shapes are used to monitor how the printed layers deform when other layers are printed on top, and the extrusion pressure is used to investigate the origin of the deformation. The cross-sectional shapes of the layers are reconstructed based on the fluid fractions in the computational cells. The fluid fractions are collected in a plane parallel to the yz -plane (see Figure 1) that is located at the half of the length of the deposited layer ($l/2$) at the time step that corresponded to the end of each layer deposition. Next, the total relative width deformation of the bottom layer De_i after the deposition of the i -th layer is calculated as:

$$De_i = \frac{w_i - w_1}{w_1} \quad (6)$$

where w_i represents the width of the bottom layer just after the deposition of the i -th layer, and w_1 is the initial width of the bottom layer, as presented in Figure 2.

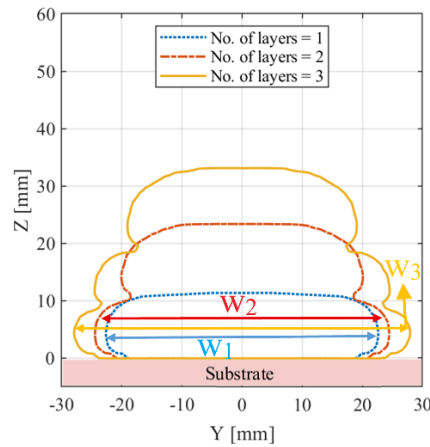


Figure 2: Cross-sections after one, two and three deposited layers. w_1 , w_2 and w_3 are the width of the bottom layer after successive layer deposition.

The extrusion pressure P_E is the total pressure at the nozzle exit, which includes both the static and dynamic pressure. The extrusion pressure is applied by the extruded material to the closest surface (solid or fluid) [19]. In the case of the first layer, the nearest surface to the orifice is the substrate, while for the other layers, it is the already deposited material. To calculate P_E , the absolute pressure is extracted from the computational cells at the horizontal xy -plane passing through the nozzle exit. A surface average of the absolute pressure is calculated at three time steps when the extrusion nozzle is approximately at the middle of the deposited layer. Next, the absolute pressure from those three time-steps are averaged and then subtracted by the atmospheric pressure (1 atm) to obtain the extrusion pressure.

3. Results and discussions

In this section, the influence of the constitutive parameters and process conditions on the cross-sectional shapes of the layers is investigated. Moreover, the deformation of the bottom layer is analyzed and related to the magnitude of the extrusion pressure.

3.1 Effect of the constitutive parameters

In Figures 3 to 6, Case 1 (see Table 1) is simulated for different values of the yield stress and plastic viscosity. For reference, the hydrostatic pressure of a single deposited layer in the following simulations is $P_H = N\rho g_0 h \approx 123$ Pa, where $h = 12.5$ mm and $N = 1$.

Effect of the yield stress:

The cross-sectional shapes of the deposited layers are shown in Figure 3 for varying yield stress. Also, the relative bottom layer deformation and the extrusion pressure are presented in Figure 4 as a function of τ_0 , where $V = U = 40$ mms⁻¹, and $\eta_p = 33$ Pa.s. Figure 3 shows that for the lowest yield stress ($\tau_0 = 100$ Pa), a large deformation of layers is observed when the subsequent layers are deposited. This is due to the combined effect of the hydrostatic and extrusion pressure that exceed the yield stress of the material. When the yield stress is increased, less deformation of layers is observed, and the prints become more stable. This is due to the fact that a higher yield stress allows a higher load on the material before the deformation occurs.

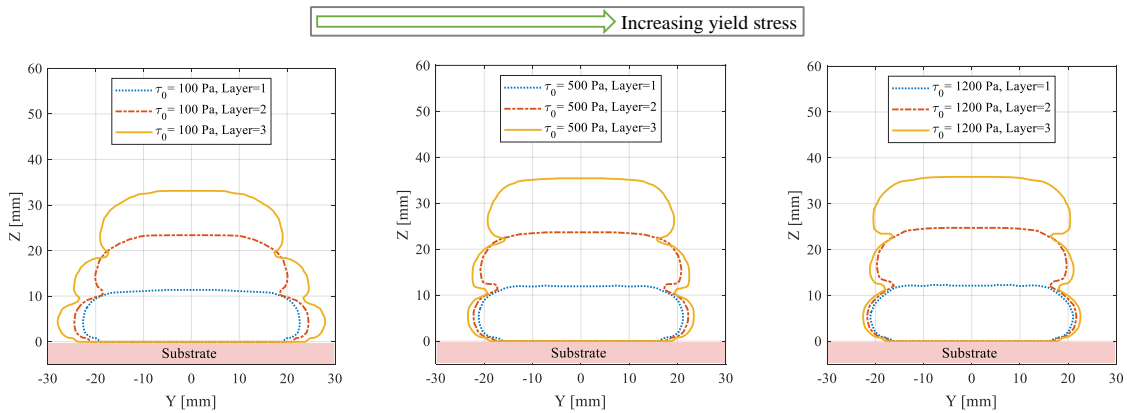


Figure 3: Cross-sectional shapes for different yield stress (τ_0).

Figure 4 shows the relative bottom layer deformation (left) and the extrusion pressure (right) as a function of the yield stress. The relative deformation of the bottom layer is

observed to decrease non-linearly with the increasing yield stress. It is found that for the highest simulated yield stress, some deformations are still present. This is due to the extrusion pressure that increases with the yield stress, and becomes a driving force for the material deformations, next to the hydrostatic pressure. Note that the calculated extrusion pressure (Figure 4 (right)), is much larger than the hydrostatic pressure but it acts locally for a short period of time (as the nozzle moves), which limits its contribution to the total deformation. Figure 4 (right) also shows that P_E is higher when printing the first layer than the second and third layers. This is due to the fact that the first layer is deposited on a rigid substrate that does not deform whereas the second and third layers deform the previously deposited material, which reduces the pressure. In other words, the deformations of the sublayers increase the effective gap (i.e., the effective distance between the nozzle and previously printed material), which reduces the extrusion pressure required to spread the extruded material with shear deformations.

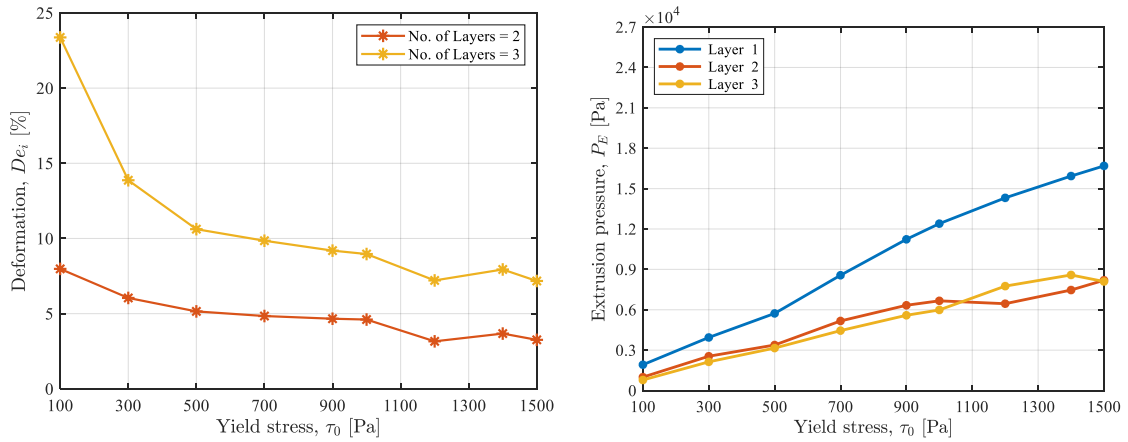


Figure 4: Relative bottom layer deformation (De_i) (left) and extrusion pressure (P_E) (right) as a function of the yield stress (τ_0).

Effect of the plastic viscosity:

The cross-sectional shapes, extrusion pressure and the relative bottom layer deformation for different values of the plastic viscosity are presented in Figure 5 and Figure 6. In these simulations $V = U = 40 \text{ mms}^{-1}$, and $\tau_0 = 500 \text{ Pa}$. In Figure 5, it is seen that increasing the plastic viscosity leads to higher deformations in the printed layers. This can partly be attributed to the increase in extrusion pressure, see Figure 6, which arises due to the higher resistance to flow (i.e., increased plastic viscosity) in the previous printed layers. Another contributing factor comes from the choice of applying a constant critical shear rate in all simulations, which will reduce the ratio between $\mu_{max.app}$ and the average apparent viscosity during deposition, when increasing the plastic viscosity. This will lead to more uniform deformations throughout the layers. Figure 6 also shows that the relative deformation of the bottom layer and extrusion pressure are almost independent of the plastic viscosity below 100 Pa.s , which indicates that the deformation at this point start to be dominated by the other processing parameters.

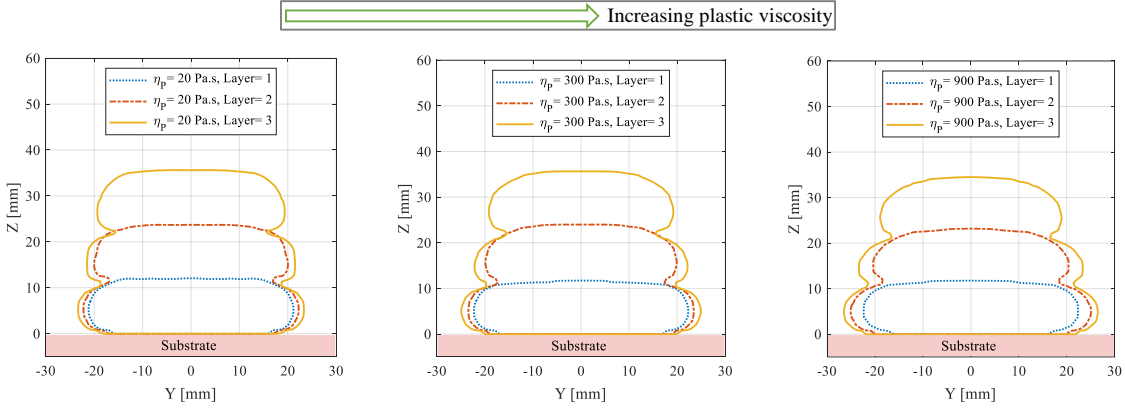


Figure 5: Cross-sectional shapes for different plastic viscosity (η_p).

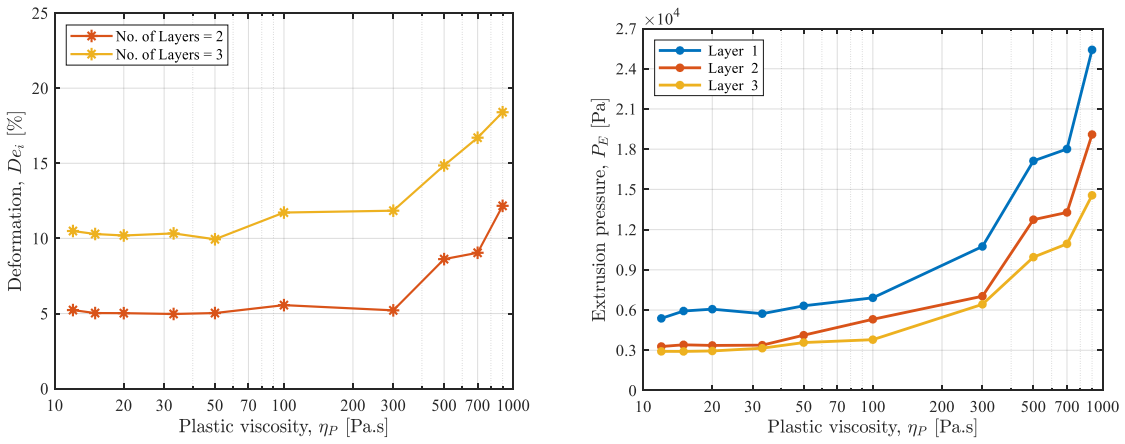


Figure 6: Relative bottom layer deformation (De_i) (left) and extrusion pressure (P_E) (right) as a function of plastic viscosity (η_p).

3.2 Effect of the processing parameters

In this subsection, the effect of the processing parameters (i.e., the printing speed, extrusion speed, layer height, and nozzle diameter) on the cross-sectional shapes of the layers, the extrusion pressure, and the relative deformation of the bottom layer is discussed. Based on the results of the previous section, a large yield stress ($\tau_0 = 1000$ Pa) and a small plastic viscosity ($\eta_p = 33$ Pa.s) are chosen in order to pursue a stable printing scenario. Furthermore, the density was kept constant, as it was found to have a negligible effect on the extrusion pressure and deformation, as long as the hydrostatic pressure was below the yield stress.

Effect of the printing speed:

The effect of the printing speed on the cross-sectional shapes for Case 1 (see Table 1), is presented in Figure 7, where $U = 40$ mm s⁻¹. It can be observed that the layers become narrower, when the printing speed is increased, as there is less material deposited per unit length. Moreover, the layers deform less with the increase of the printing speed, as seen specifically for the bottom layer in Figure 8 (left). The reduced relative deformation is not a consequence of the hydrostatic pressure ($P_H = N\rho g_0 h$), as it does not change with the printing speed, but rather due to the fact that the extrusion pressure decreases with increasing print speed (see Figure 8 (right)) and it acts for a shorter time $t \sim D/V$. The

extrusion pressure decreases because less material experience shear deformation per unit length.

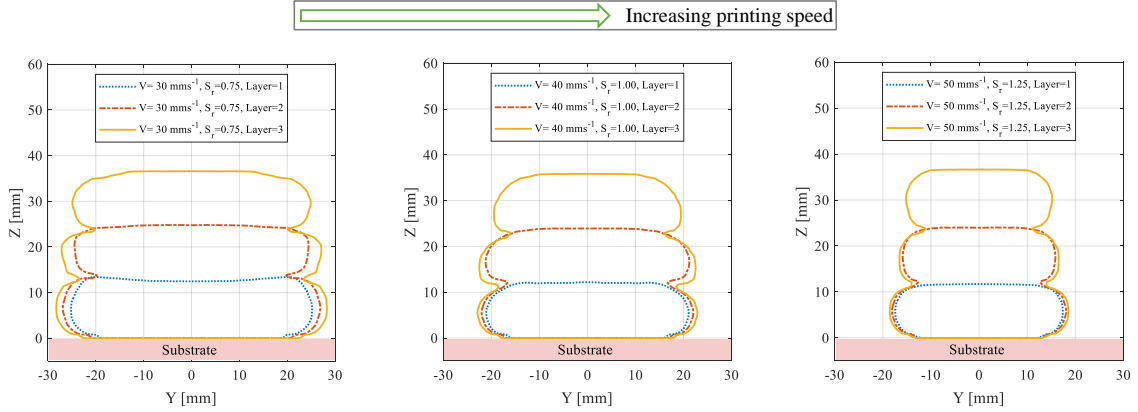


Figure 7: Cross-sectional shapes for different printing speed (V).

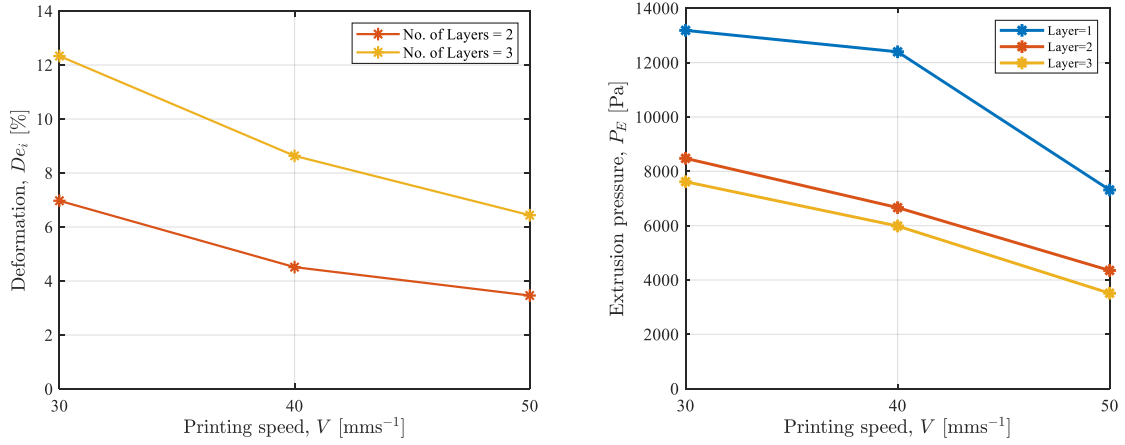


Figure 8: Relative bottom layer deformation (De_i) (left) and extrusion pressure (P_E) (right) as a function of the printing speed (V).

Effect of the extrusion speed:

The effect of the extrusion speed is presented in Figures 9 and 10 for Case 1 (see Table 1), where $V = 30 \text{ mm/s}$. The cross-sectional shapes that are presented in Figure 9 become wider with an increasing extrusion speed, as there is more material deposited per unit length for a constant printing speed. Moreover, a larger deformation of layers is observed when increasing the extrusion speed. Figure 10 shows the relative bottom layer deformation (left) and the extrusion pressure (right) as a function of the extrusion speed. As the hydrostatic pressure ($P_H = N\rho g_0 h$) does not change with the variation of the extrusion speed, the cause of the increasing deformation (Figure 10 (left)) is partly the increase in extrusion pressure, see Figure 10 (right), which is due to more material experiencing shear deformation per unit length. Another effect is that the increased extrusion speed leads to higher shear rates and thus reduce viscosities, which also increase deformations. The reduction in viscosities should also reduce the extrusion pressure, but that effect seems not to be dominant in this case.

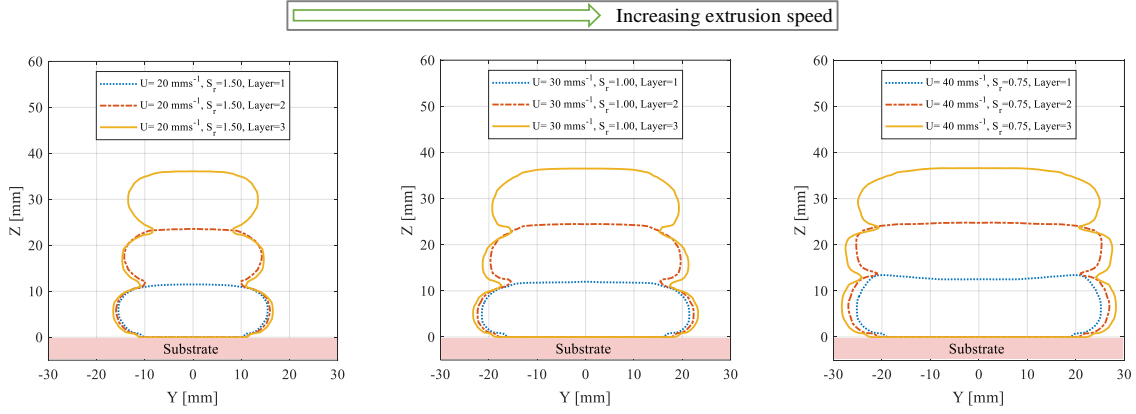


Figure 9: Cross-sectional shapes for different extrusion speed (U).

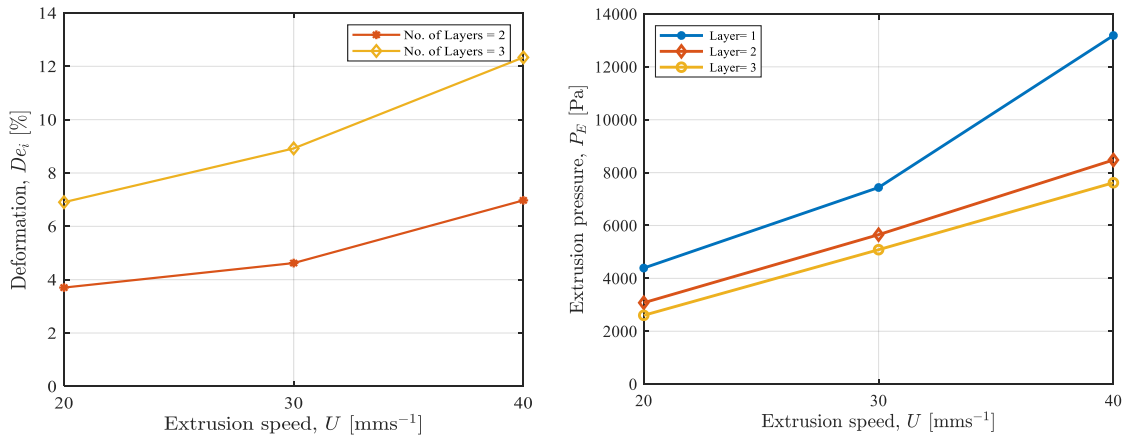


Figure 10: Relative bottom layer deformation (De_i) (left) and extrusion pressure (P_E) (right) as a function of extrusion speed (U).

In the results presented in Figures 7 to 10, it is seen that increasing the printing speed and the extrusion speed have opposite effects on the deformation of the layers, when the other parameters are held constant. Figures 11 and 12 show the effect of increasing both the extrusion speed and printing speed at the same time such that the speed ratio is unchanged, $S_r = 1$. The opposing effects of these two parameters leads to a situation, where the relative bottom layer deformation decreases between $U = V = 20 \text{ mm/s}$ and $U = V = 30 \text{ mm/s}$, while the extrusion pressure is approximately constant; whereas for U and V between 30 mm/s and 40 mm/s , De_i is approximately constant and P_E increases. Thus, within the investigated parameters range, the effect of increasing the printing speed has a dominating effect on the bottom layer deformation, while the increased extrusion speed dominates the extrusion pressure.

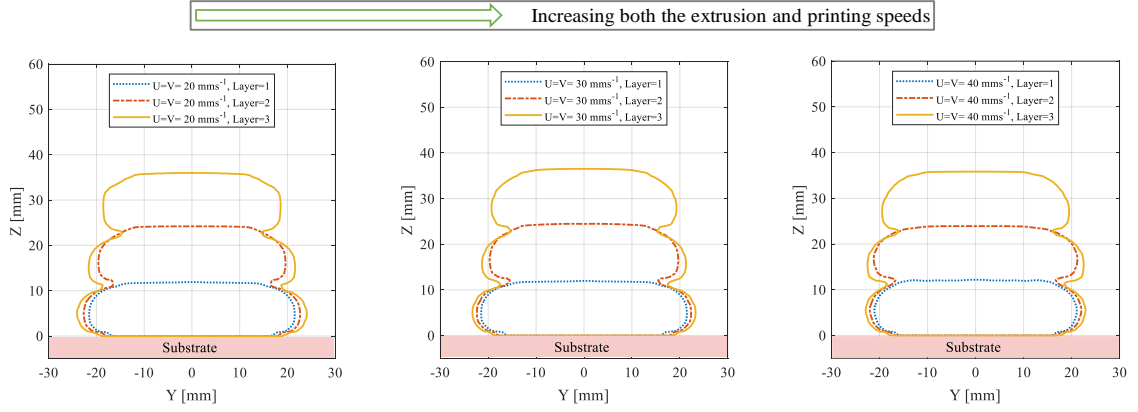


Figure 11: Cross-sectional shapes for different pair of extrusion speed (U) and printing speed (V) with same speed ratio ($S_r = 1$).

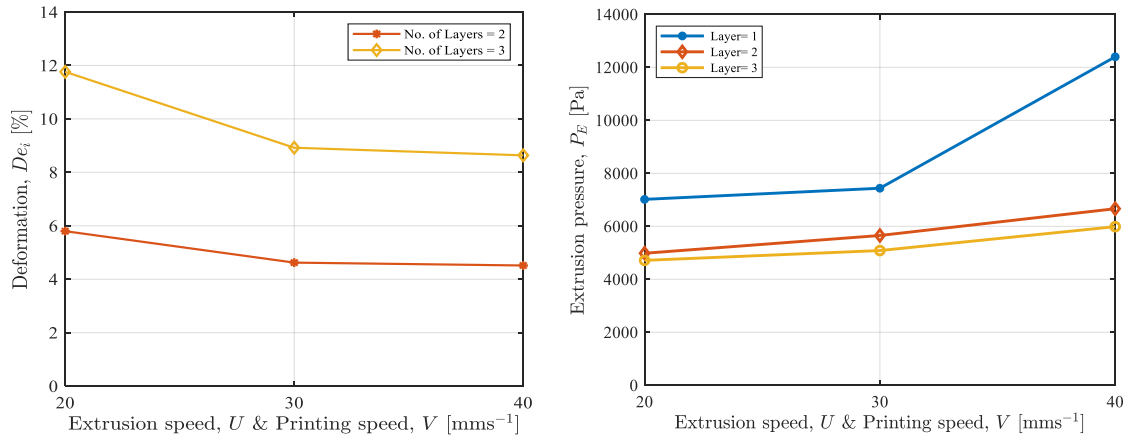


Figure 12: Relative bottom layer deformation (De_i) (left) and extrusion pressure (P_E) (right) for different pair of extrusion speed (U) and printing speed (V) with the same speed ratio ($S_r = 1$).

Effect of the layer height:

In this subsection, the deposition of material is simulated for different layer heights, $h = 12.5$ mm (Case 1), 18.75 mm (Case 5) and 25 mm (Case 6), cf. Table 1, with $V = U = 40 \text{ mm/s}$. Figure 13 shows that the cross-sectional shapes of the layers become more rounded and narrower when the layer height is increased. Figure 14 presents the relative bottom layer deformation (left) and the extrusion pressure (right) as a function of the layer height. The relative deformation De_i is observed to increase with the layer height, whereas the extrusion pressure is observed to decrease. The increase in De_i is however caused by the decreasing width of the bottom layer, when the layer height is increased. In fact, the absolute deformation of the bottom layer were similar for the different layer heights. For reference, the maximum hydrostatic pressure for three printed layers where $h = 25$ mm and $N = 3$ is $P_H \approx 736$ Pa, which is below the yield stress (1000 Pa).

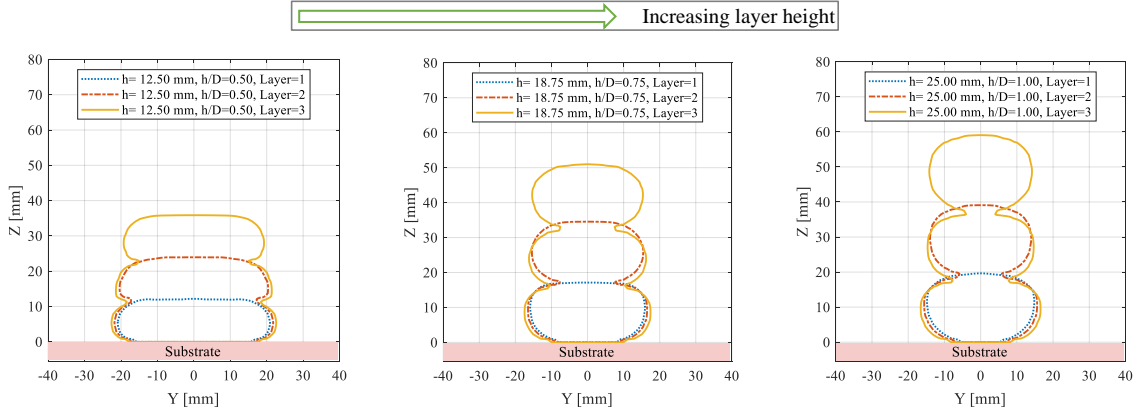


Figure 13: Cross-sectional shapes for different layer height (h).

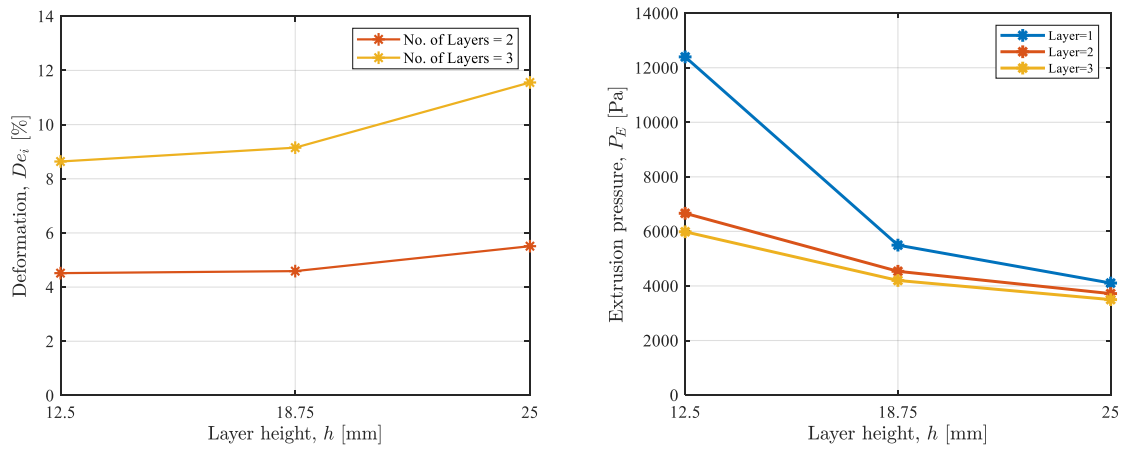


Figure 14: Relative bottom layer deformation (De_i) (left) and extrusion pressure (P_E) (right) as a function of layer height (h).

Effect of the nozzle diameter:

The influence of the nozzle diameter on the cross-sectional shapes of the deposited layers is presented in Figure 15. The following nozzle diameters are investigated: $D = 0.4$ mm (Case 4), $D = 1.5$ mm (Case 3), $D = 25$ mm (Case 1), and $D = 50$ mm (Case 2), with the gap ratio $h/D = 0.5$ in each cases; see Table 1. The speeds $V = U = 20 \text{ mms}^{-1}$ are chosen to fit the range of processes represented by the different nozzle diameters. The axes in Figure 15 are non-dimensionalized with the corresponding nozzle diameter to ease the comparison between the cross-sections. The results illustrate that the prints performed with larger diameters show larger deformation. The relative bottom layer deformation and extrusion pressure are shown in Figure 16. The relative bottom layer deformation presents a minimum when $D = 1.5$ mm. This non-monotonic trend is due to the combined influence of the hydrostatic pressure and the extrusion pressure. The hydrostatic pressure ($P_H = N\rho g_0 h$, where $h = 0.5D$) increases with the nozzle diameter, while the extrusion pressure decreases with the increasing nozzle diameter, due to smaller shear stresses in the channels with larger cross-sectional area (see Figure 16 (right)). Moreover, as the printing speed is the same in the simulated cases, the extrusion pressure acts locally for a longer period of time, when the nozzle diameter is larger, which additionally contributes to the deformation.

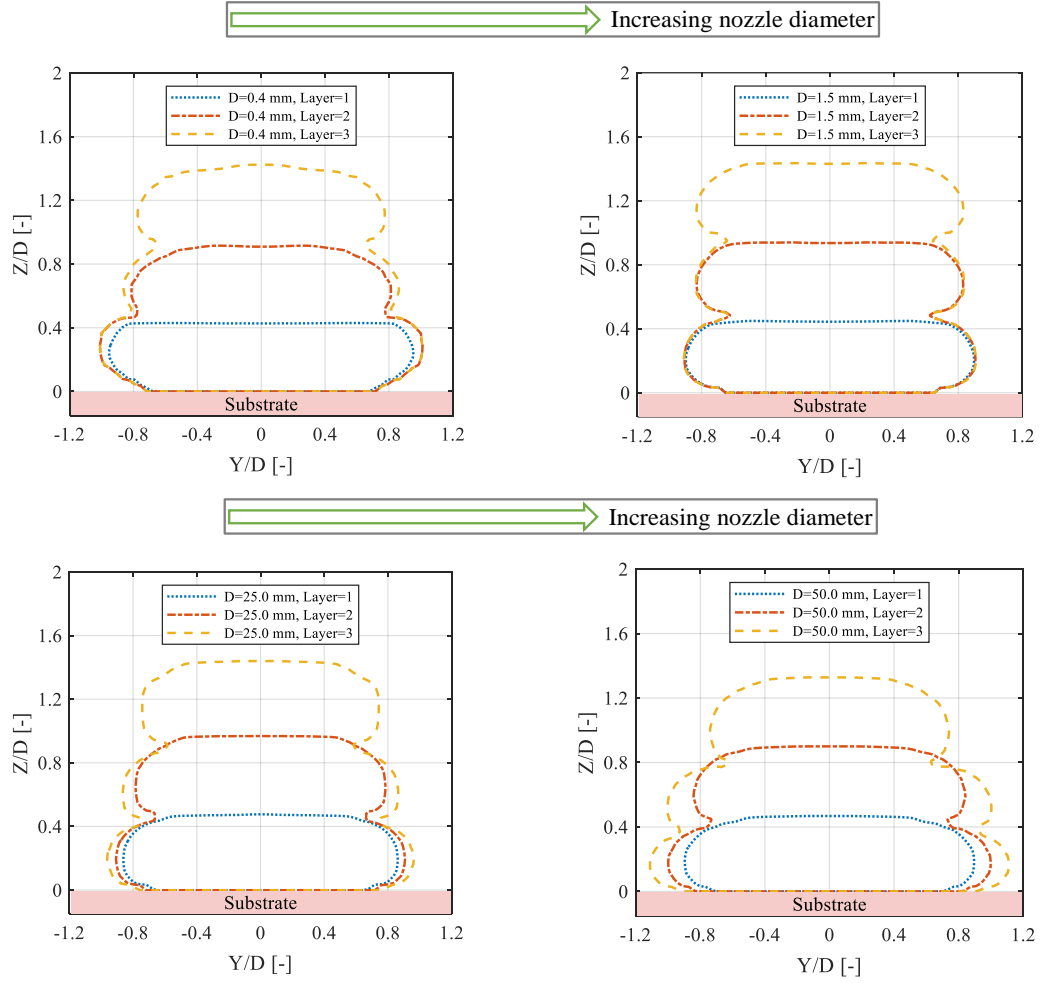


Figure 15: Cross-sectional shapes for different nozzle diameter (D).

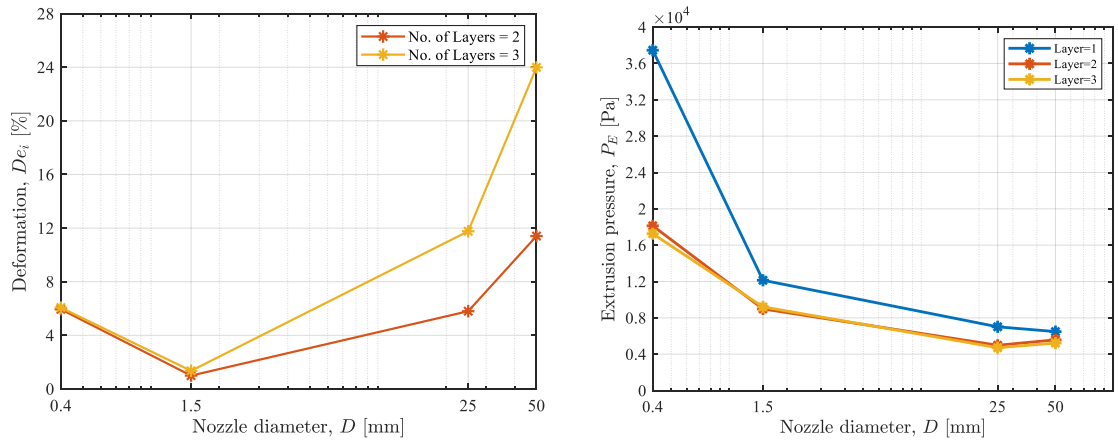


Figure 16: Relative bottom layer deformation (De_i) (left) and extrusion pressure (P_E) (right) as a function of nozzle diameter (D).

Comparison of the effect of the processing parameters:

In order to compare the effect of the parameters discussed above, a bar diagram is presented in Figure 17. The amount of deformation of the bottom layer is shown as a

function of different combinations of processing parameters. The combinations of the parameters are labeled with the symbol and magnitude of the parameters (excluding units), and refers to the simulations presented in Figures 7 to 16. Figure 17 shows that within the investigated parameter intervals, changes in the nozzle diameter have the largest effect on the deformation. Furthermore, the results illustrate that variations in layer height, extrusion speed, and printing speed leads to very similar sized deformations.

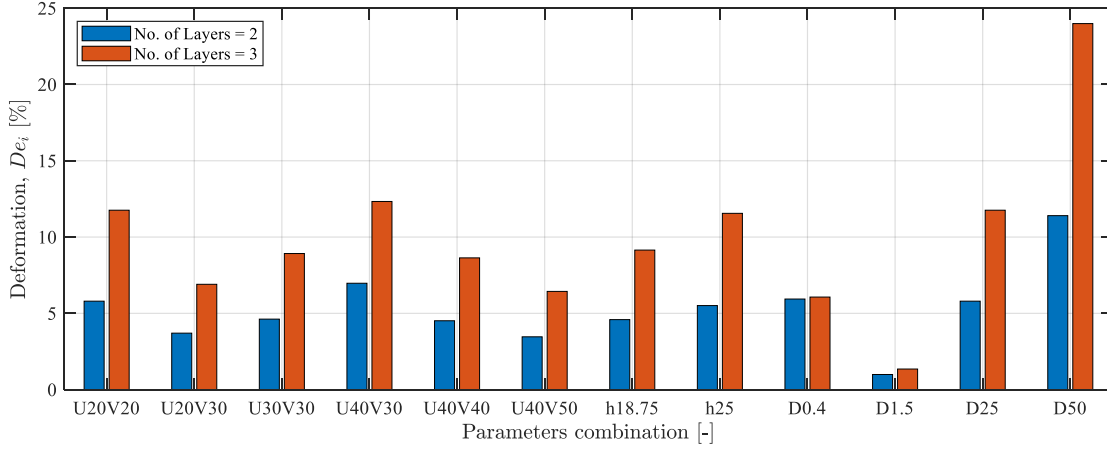


Figure 17: Comparison among the parameters in terms of observed deformation.

3.3 5-Layers deposition

In this subsection, the CFD model is used to simulate the wet-on-wet deposition of 5 subsequent layers (Case 7 in Table 1) to investigate whether the same conclusions hold as for the presented 3-layers simulations. Based on the above results, the processing parameters: $D = 25$ mm, $h = 12.5$ mm, $h/D = 0.5$, $V = 50$ mms⁻¹, $U = 40$ mms⁻¹ and $S_r = 1.25$, are chosen in order to get an optimal print with less deformation. The results are presented for varying yield stress and a constant plastic viscosity, $\eta_p = 33$ Pa.s.

Figure 18 (left) presents the theoretical height ($N \times h$) and the actual height (simulated) of the part, as a function of the number of layers N , for different yield stress, $\tau_0 = 100, 500, 1000, 1800, 2500$ Pa. It is found that, in all cases, the actual height of the deposited material is lower than the theoretical height. Therefore, the effective distance between the nozzle exit and the previously deposited material (in simulations) is larger than the nominal layer height $h = 12.5$ mm. This effect is amplified as the number of layers increases. As a result, the cross-sectional shapes of layers become narrower and more circular with the deposition of each subsequent layer. This effect is also observed in real-world prints [34]. To avoid the round and narrow shape of the new layers, the effective distance at each layer needs to be adjusted by the distance the previous layers have deformed. Figure 18 (right) presents the cross-sectional shapes of a 5-layer structure for uncorrected h (i.e. the effective distance increases after each layer), and for the corrected h (i.e. the nozzle height is adjusted after each layer to have the same effective distance h of 12.5 mm). It can be seen that the round and narrow shape of a new layer due to an increase in effective distance is mitigated by the corrected h . Thus, the following simulations are carried out with the corrected h .

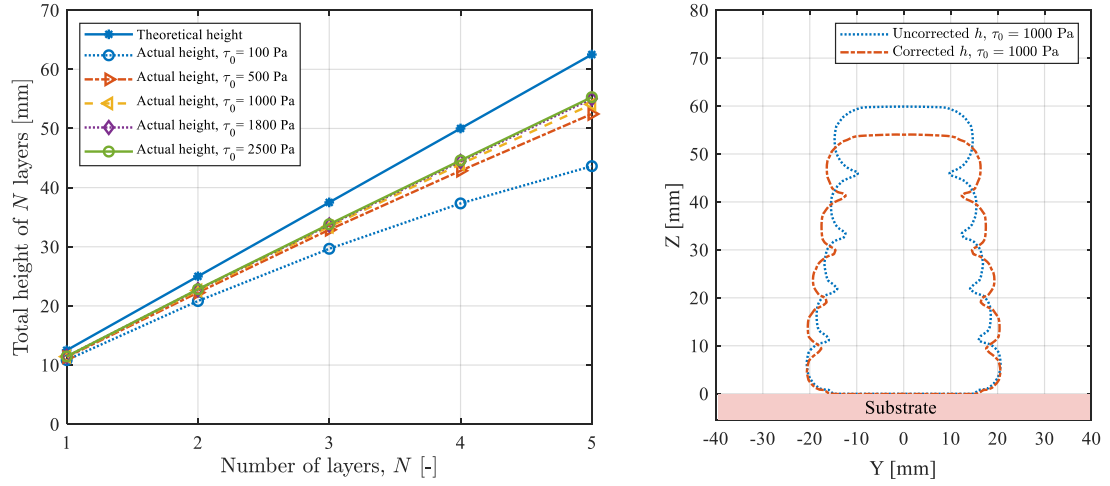


Figure 18: Total height of N deposited layers (left) with corrected layer height, and cross-sectional shapes (right) for uncorrected and corrected layer heights in wet-on-wet deposition.

The cross-sectional shapes for the different τ_0 are presented in Figure 19, and show similar trends as for 3-layer deposition (see Figure 3). The material is observed to continue deforming when two additional layers are added on top of the three-layer print. The relative bottom layer deformation is presented in Figure 20 (left) as a function of the layer number. It can be seen that increasing the yield stress can reduce the amount of deformation, but it never vanishes. This is because the higher yield stress produces a higher extrusion pressure that contributes to the deformation, see Figure 20 (right). Interestingly, for $\tau_0 = 1800$ Pa and $\tau_0 = 2500$ Pa, almost the same amount of layer deformations are predicted by the model, see Figure 20 (left). Thus, it is anticipated that a further increase of the yield stress would not result in significant improvements.

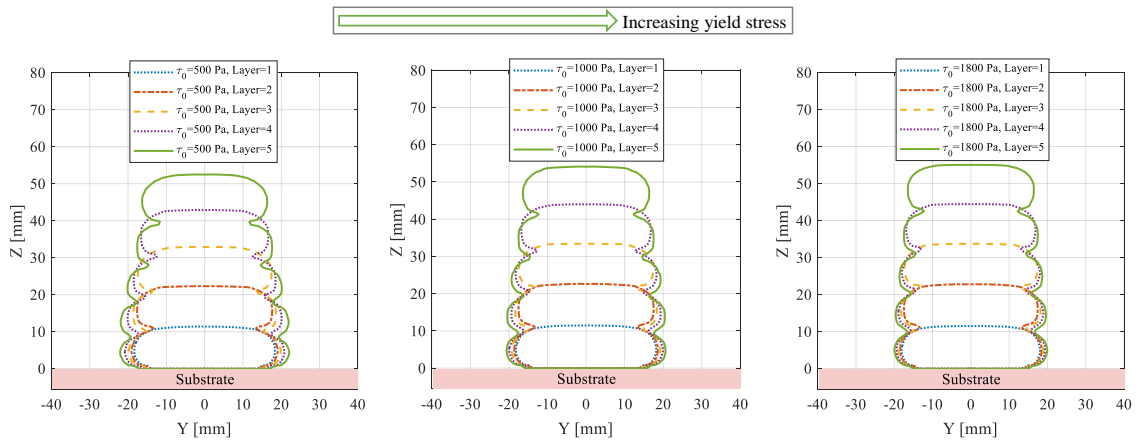


Figure 19: Cross-sectional shapes for different yield stress (τ_0) in wet-on-wet deposition.

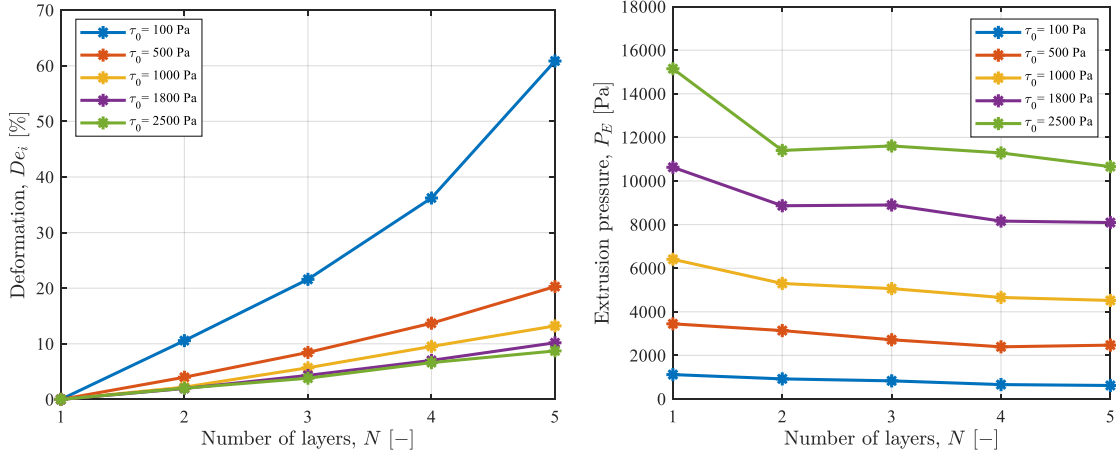


Figure 20: Relative bottom layer deformation (De_i) (left) and extrusion pressure (P_E) (right) as a function of number of layers (N) in wet-on-wet deposition.

3.4 Wet-on-dry deposition of 5-layers

Within the range of the investigated parameters, the previous section showed that the deformation of layers cannot be completely eliminated, if the material has a yield stress that is constant in time. In order to eradicate the deformations, the deposited material should ideally increase its yield stress before the next layers are printed. In this section, the numerical model is used to study a situation where the previously printed material solidifies right after being deposited (i.e. wet-on-dry printing). This means that the already printed layers are regarded as solids in the computational model.

In Figures 21 and 22, the cross-sectional shapes and extrusion pressure are shown, respectively, for simulations with 5 subsequent layers (i.e., Case 7 in Table 1). The simulations are carried out with three different yield stress values and $\eta_p = 33$ Pa.s. The cross-sectional shapes of the layers during the wet-on-dry printing are very stable, see Figure 21. In the previous sections, it was observed that the extrusion pressure is the largest for the first layer (see Figure 20), as it cannot deform the solid substrate. Figure 22 supports this observation and shows that if the previously deposited layers do not deform, the extrusion pressure becomes the same for all the layers. The extrusion pressure results also provide important information about how much the materials' yield stress needs to increase in order to produce stable prints. The sum of the hydrostatic and extrusion pressure is a conservative estimate of the yield stress that is required by the previously deposited layer in order not to deform when subsequent layers are printed on top.

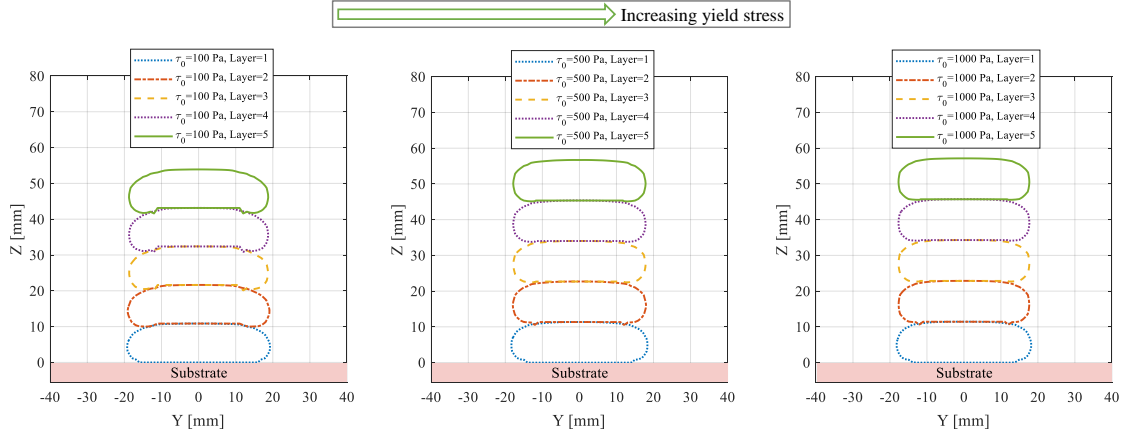


Figure 21: Cross-sectional shapes for different yield stress (τ_0) in wet-on-dry deposition.

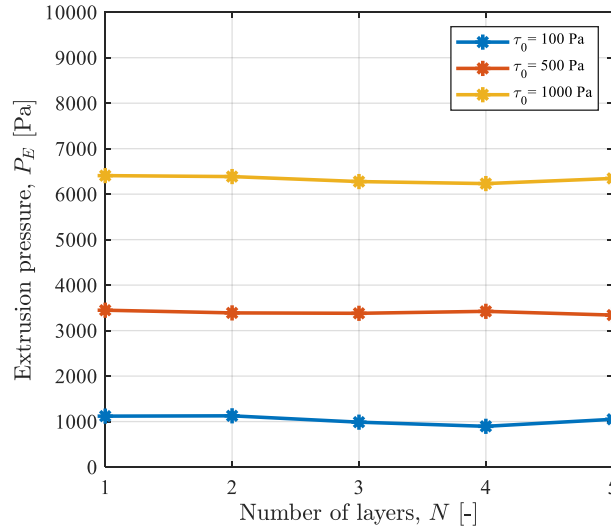


Figure 22: Extrusion pressure (P_E) as a function of number of layers (N) in wet-on-dry deposition.

4. Conclusions

In this work, a CFD model was used to capture the extrusion-deposition flow of viscoplastic fluids during MEX-AM. The material was modelled with the Bingham constitutive equation, and the free surface of the fluid was tracked to quantify the deformation of layers during and after the deposition. The influence of the constitutive parameters and process conditions on the cross-sectional shapes of the layers were analysed. It was found that when the yield stress is small, the layers deform due to the hydrostatic pressure generated by the subsequently deposited material, as well as the extrusion pressure of the extruded material. Increasing the yield stress of the material led to smaller deformations of the deposited layers. On the other hand, a higher plastic viscosity led to larger deformations of the layers, due to an increase in the extrusion pressure, as the material had a higher resistance to flow.

Increasing the printing speed resulted in smaller deformations of the layers, due to the decreasing extrusion pressure that acted for a shorter time, whereas increasing the extrusion speed behaved oppositely with regards to deformations and extrusion pressure. When the printing speed and extrusion speed were increased at the same time, a

combination of the two opposing effects was observed for the investigated range of parameters. Furthermore, the increase of the layer height led to larger relative deformation of the layers, but similar absolute deformations. The dependency of the layer deformation on the nozzle diameter was non-monotonic, due to the combined effect of the hydrostatic and extrusion pressure. When the nozzle diameter was increased, the hydrostatic pressure increased as the layer height increased with the nozzle diameter, while the extrusion pressure decreased due to the smaller shear stresses in larger channels. In all of the investigated cases of the wet-on-wet deposition, some deformations of the bottom layer were observed.

Finally, a wet-on-dry deposition of 5-layers was simulated, where the previously deposited material was assumed to be solidified before the deposition of the next layer. In that case, the extrusion pressure is the same for all layers and it was possible to get a stable print. Furthermore, from the wet-on-dry simulations, one could extract a conservative estimate for the required yield stress increment that the material needs to develop before the deposition of a subsequent layer, in order not to deform. The yield stress of the previous layers must be higher than the sum of the hydrostatic and extrusion pressure. In future work, the presented CFD model could be used to predict the deposition of materials, where the rheological behavior changes continuously as a function of time, which could lead to a less conservative yield stress criterion.

Acknowledgements

The authors would like to acknowledge the support of the Danish Council for Independent Research (DFF) | Technology and Production Sciences (FTP) (Contract No. 8022-00042B). Moreover, the authors thank **FLOW-3D** for their support in regards to licenses.

Appendix A. Supporting information

Supplementary data associated with this article can be found in the online version at doi:10.1016/j.addma.2021.102193.

References

- [1] R. A. Buswell, W. R. Leal De Silva, S. Z. Jones and J. Dirrenberger, "3D printing using concrete extrusion: A roadmap for research," *Cement and Concrete Research*, vol. 112, pp. 37-49, 2018.
- [2] Z. Chen, Z. Li, J. Li, C. Liu, C. Lao, Y. Fu, C. Liu, Y. Li, P. Wang and Y. He, "3D printing of ceramics: A review," *Journal of the European Ceramic Society*, vol. 39, no. 4, pp. 661-687, 2019.
- [3] A. Bellini, L. Shor and S. I. Guceri, "New developments in fused deposition modeling of ceramics," *Rapid Prototyping Journal*, vol. 11, no. 4, pp. 214-220, 2005.
- [4] S. Aktas, D. M. Kalyon, B. M. Marín-Santibáñez and J. Pérez-González, "Shear viscosity and wall slip behavior of a viscoplastic hydrogel," *Journal of Rheology*, vol. 58, no. 2, pp. 513-535, 2014.
- [5] J. Lindahl, A. Hassen, S. Romberg, B. Hedger, P. Hedger Jr, M. Walch, T. Deluca, W. Morrison, P. Kim, A. Roschli and D. Nuttall, "Large-scale additive manufacturing with reactive polymers," Oak Ridge National Lab.(ORNL), Oak Ridge, TN (United States), 2018.

- [6] V. N. Nerella and V. Mechtcherine, "Studying the Printability of Fresh Concrete for Formwork-Free Concrete Onsite 3D Printing Technology (CONPrint3D)," *3D Concrete Printing Technology*, pp. 333–347, 2019.
- [7] C. Tiu, J. Guo and P. H. T. Uhlherr, "Yielding behaviour of viscoplastic materials," *Journal of Industrial and Engineering Chemistry*, vol. 12, no. 5, pp. 653-662, 2006.
- [8] B. Dietemann, F. Bosna, M. Lorenz, N. Travitzky, H. Kruggel-Emden, T. Kraft and C. Bierwisch, "Modeling robocasting with smoothed particle hydrodynamics: Printing gapspanning filaments," *Additive Manufacturing*, vol. 36, p. 101488, 2020.
- [9] B. Khoshnevis, R. Russell, H. Kwon and S. Bukkapatnam, "Contour Crafting – A Layered Fabrication," *Special Issue of IEEE Robotics and Automation Magazine*, vol. 8, no. 3, pp. 33-42, 2001.
- [10] D. Asprone, F. Auricchio, C. Menna and V. Mercuri, "3D printing of reinforced concrete elements: Technology and design approach," *Construction and Building Materials*, vol. 165, pp. 218-231, 2018.
- [11] J. Jiang and Y. Ma, "Path Planning Strategies to Optimize Accuracy, Quality, Build Time and Material Use in Additive Manufacturing: A Review," *Micromachines*, vol. 11, no. 7, p. 633, 2020.
- [12] J. Jiang, "A novel fabrication strategy for additive manufacturing processes," *Journal of Cleaner Production*, vol. 272, p. 122916, Nov. 2020.
- [13] F. Bos, R. Wolfs, Z. Ahmed and T. Salet, "Additive manufacturing of concrete in construction: potentials and challenges," *Virtual and Physical Prototyping*, vol. 11, no. 3, pp. 209-225, 2016.
- [14] P. Wu, J. Wang and X. Wang, "A critical review of the use of 3-D printing in the construction industry," *Automation in Construction*, vol. 68, pp. 21-31, 2016.
- [15] T. D. Ngo, A. Kashani, G. Imbalzano, K. T. Nguyen and D. Hui, "Additive manufacturing (3D printing): A review of materials, methods, applications and challenges," *Composites Part B: Engineering*, vol. 143, pp. 172-196, 2018.
- [16] M. Valente, A. Sibai and M. Sambucci, "Extrusion-Based additive manufacturing of concrete products: Revolutionizing and remodeling the construction industry," *Journal of Composites Science*, vol. 3, no. 3, p. 88, 2019.
- [17] N. Roussel, J. Spangenberg, J. Wallevik and R. Wolfs, "Numerical simulations of concrete processing: from standard formative casting to additive manufacturing," *Cement and Concrete Research*, vol. 135, p. 106075, 2020.
- [18] R. J. M. Wolfs, F. P. Bos and T. A. M. Salet, "Early age mechanical behaviour of 3D printed concrete: Numerical modelling and experimental testing," *Cement and Concrete Research*, vol. 106, pp. 103-116, 2018.
- [19] R. Comminal, M. P. Serdeczny, D. B. Pedersen and J. Spangenberg, "Numerical modeling of the strand deposition flow in extrusion-based additive manufacturing," *Additive Manufacturing*, vol. 20, pp. 68-76, 2018.
- [20] R. Comminal, M. P. Serdeczny, D. B. Pedersen and J. Spangenberg, "Numerical modeling of the material deposition and contouring precision in fused deposition modeling," in *Proceedings of the 29th Annual International Solid Freeform Fabrication Symposium*, Austin, TX, USA, pp. 1855-1864, 2018.
- [21] M. P. Serdeczny, R. Comminal, D. B. Pedersen and J. Spangenberg, "Experimental validation of a numerical model for the strand shape in material extrusion additive manufacturing," *Additive Manufacturing*, vol. 24, pp. 145-153, 2018.

- [22] M. P. Serdeczny, R. Comminal, D. B. Pedersen and J. Spangenberg, "Numerical simulations of the mesostructure formation in material extrusion additive manufacturing," *Additive Manufacturing*, vol. 28, pp. 419-429, 2019.
- [23] H. Xia, J. Lu and G. Tryggvason, "A numerical study of the effect of viscoelastic stresses in fused filament fabrication," *Computer Methods in Applied Mechanics and Engineering*, vol. 346, pp. 242-259, 2019.
- [24] R. Comminal, W. R. L. da Silva, T. J. Andersen, H. Stang and J. Spangenberg, "Influence of Processing Parameters on the Layer Geometry in 3D Concrete Printing: Experiments and Modelling," *Second RILEM International Conference on Concrete and Digital Fabrication*, vol. 28, pp. 852-862, 2020.
- [25] R. Comminal, W. R. L. da Silva, T. J. Andersen, H. Stang and J. Spangenberg, "Modelling of 3D concrete printing based on computational fluid dynamics," *Cement and Concrete Research*, vol. 138, p. 106256, 2020.
- [26] E. C. Bingham, "An investigation of the laws of plastic flow," *US Bureau of Standards Bulletin*, vol. 13, pp. 309-352, 1916.
- [27] N. Casson, "A flow equation for pigment-oil suspensions of the printing ink type," *Rheology of disperse systems*, pp. 84-104, 1959.
- [28] W. H. Herschel and R. Bulkley, "Konsistenzmessungen von Gummi-Benzollösungen," *Kolloid Zeitschrift*, vol. 39, p. 291-300, 1926.
- [29] "FLOW-3D | We solve The World's Toughest CFD Problems," FLOW SCIENCE, [Online]. Available: <https://www.flow3d.com/>. [Accessed 27 06 2020].
- [30] S. Jacobsen, R. Cepuritis, Y. Peng, M. R. Geiker and J. Spangenberg, "Visualizing and simulating flow conditions in concrete form filling using pigments," *Construction and Building Materials*, vol. 49, pp. 328-342, 2013.
- [31] E. J. O'Donovan and R. I. Tanner, "Numerical study of the Bingham squeeze film problem," *Journal of Non-Newtonian Fluid Mechanics*, vol. 15, no. 1, pp. 75-83, 1984.
- [32] C. W. Hirt and B. D. Nichols, "Volume of fluid (VOF) method for the dynamics of free boundaries," *Journal of computational physics*, vol. 39, no. 1, pp. 201-225, 1981.
- [33] R. Comminal, J. Spangenberg and J. H. Hattel, "Cellwise conservative unsplit advection for the volume of fluid method," *Journal of computational physics*, vol. 283, pp. 582-608, 2015.
- [34] A. Negar, S. Nazarian, N. A. Meisel and J. P. Duarte, "Experimental prediction of material deformation in large-scale additive manufacturing of concrete," *Additive Manufacturing*, vol. 37, p. 101656, 2021.

Publication [A.3]: Numerical predictions of bottom layer stability in material extrusion additive manufacturing

Md. Tusher Mollah, Raphaël Comminal, Marcin P. Serdeczny, David B. Pedersen, Jon Spangenberg

Department of Mechanical Engineering, Technical University of Denmark, Denmark.

Published in:

JOM- The Journal of The Minerals, Metals & Materials Society (TMS), Vol. 74, pp. 1096–1101, 2022, <https://doi.org/10.1007/s11837-021-05035-9>.

Reproduced with permission from Springer.

The layout has been revised.

Abstract

Robocasting and 3D concrete printing are technologies that belong under the umbrella term material extrusion additive manufacturing. These two free form fabrication methods are used to produce 3D structures/components in materials such as ceramic pastes, thermosets, and concrete. Common for the materials is their viscoplastic behavior during deposition and structural buildup (i.e., increase in yield stress) after deposition. The material's complex nature makes it a non-trivial task to ensure that printed layers do not deform when depositing additional layers on top. In this paper, we numerically investigate the influence of the yield stress buildup of viscoplastic materials on the stability of the bottom layer during multilayer printing. Specifically, we have developed a computational fluid dynamics model that applies a scalar approach to alter the yield stress. The novel model provides fundamental knowledge on how to design the material's rheology, so the bottom layer can withstand both the hydrostatic- and extrusion-pressure.

1. Introduction

Recently, Material Extrusion Additive Manufacturing (MEX-AM) of viscoplastic materials has received more attention when trying to produce micro components and large-scale structures [1]. Visoplastic materials such as ceramic pastes, thermosets, and concrete are typically used in free form fabrication technologies like 3D concrete printing and Robocasting, which belong under the umbrella term MEX-AM [1–3]. In these technologies, a layer-by-layer approach is used to fabricate the structure. The material is extruded through a nozzle and deposited onto a solid support for the first layer, while the following layers are deposited onto the already printed layer [4]. The already printed layer can be deformable (i.e., wet or partially solidified) or solidified. When printing on a solidified material, it is fairly easy to obtain a stable print (i.e., layers with equal width and height), however, it can have detrimental consequences on the interlayer strength of the fabricated parts [5]. Consequently, it is often preferable to print on a deformable layer although it is non-trivial to obtain a stable print.

The geometrical accuracy and stability of the prints in MEX-AM require significant consideration [6–8]. Numerical models have with success been applied to improve various manufacturing processes [9]. Specifically, Computational Fluid Dynamics (CFD) models have shown to be a very beneficial tool to understand MEX-AM, e.g., improve the quality of printed corners [10,11], reducing porosities [12], and increase the inter- and intra-layer bonding of deposited layers [13]. Other CFD models [14–16] have shown that the extruded material also applies a pressure, called the extrusion pressure, to the closest surface (solid/fluid) during the deposition. Comminal et al. [17], Roussel et al. [18], and Spangenberg et al. [19] all discussed the consequences of extrusion pressure on the stability of a deposited layer in MEX-AM. Recently, Mollah et al. [20] investigated how to reduce the extrusion pressure and its effect on the stability of the structure. However, the stability of the structure during multilayer prints is still to be fully understood.

This work aims to numerically investigate the stability of layers during multilayer printing of viscoplastic materials in MEX-AM. Specifically, a two-layered structure is investigated where the second layer is printed onto a partially solidified bottom layer. Numerically this is obtained by assigning a different yield stress for the bottom layer. The CFD model is used to predict the cross-sectional shapes of deposited layers and analyze the deformation of the bottom layer as well as the extrusion pressure.

2. Computational model

The CFD model simulates the extrusion-deposition flow of the viscoplastic materials that is assumed to be incompressible with a constant density ρ . The deposition flow properties are laminar, time dependent and isothermal. The fluid is introduced with a fully developed profile at an extrusion speed of 40 mm/s. The material is deposited through a cylindrical nozzle with a 25 mm diameter onto a solid substrate located at a distance 12.5 mm from the nozzle exit. The nozzle moves with a printing speed of 50 mm/s. The model geometry along with the computational domain is presented in Figure 1. Only half of the domain is solved by imposing a symmetry plane. An inlet boundary is assigned to the top plane of the domain designed with an artificial solid component that coincides with the nozzle orifice to prevent flow from the rest of the plane. The bottom plane is a stationary wall having the substrate. The rest of the planes have no interaction with the fluid and have assigned a continuative boundary condition that considers a null derivative of the velocity profile across the plane. A no-slip boundary condition is assigned to the solid surfaces that are in contact with the fluid. The computational domain is meshed with the Cartesian grid. The cell size is defined to have 25 cells along the diameter of the nozzle.

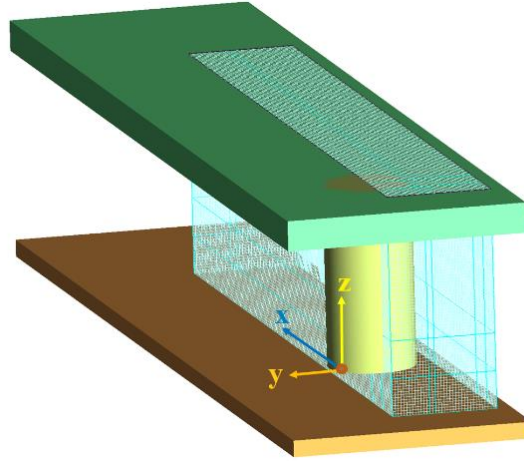


Figure 1: Model geometry with the symmetrical computational domain.

The viscosity of the material is modeled by the bi-viscous regularization [21] of the Bingham constitutive equation [22]. The apparent viscosity of the material μ_{ap} is:

$$\mu_{ap}(\dot{\gamma}) = \begin{cases} \mu_{M.ap} = \eta_P + \frac{\tau_{printing}}{\dot{\gamma}_c}, & \text{for } \dot{\gamma} < \dot{\gamma}_c \\ \eta_P + \frac{\tau_{printing}}{\dot{\gamma}}, & \text{for } \dot{\gamma} \geq \dot{\gamma}_c \end{cases} \quad (1)$$

where, $\mu_{M.ap}$ is the maximum apparent viscosity for the shear rates $\dot{\gamma}$ below a critical value $\dot{\gamma}_c$, $\tau_{printing}$ is the yield stress, and η_P is the plastic viscosity. A time dependent yielding behavior of the material is considered. This means that the yield stress of previously deposited material is assumed to increase before the deposition of the following layer begins. Numerically, the yield stress difference between the layers is introduced by the scalar approach of **FLOW-3D**[®], version 12.0 [23]. This is done by assigning a constant scalar concentration to the already deposited material. The scalar carries a viscosity that is modelled, with a different yield stress $\tau_{printed}$, according to Equation 1. The apparent viscosity of the scalar contribution $\mu_{SC.ap}$ is:

$$\mu_{sc.ap}(\dot{\gamma}) = \begin{cases} \mu_{sc.M.ap} = \eta_P + \frac{\tau_{printed}}{\dot{\gamma}_c}, & \text{for } \dot{\gamma} < \dot{\gamma}_c \\ \eta_P + \frac{\tau_{printed}}{\dot{\gamma}}, & \text{for } \dot{\gamma} \geq \dot{\gamma}_c \end{cases} \quad (2)$$

where, $\mu_{sc.M.ap}$ is the maximum apparent viscosity contribution from the scalar. Thus, the deposited material has two viscosity contributions, one from the scalar (Equation 2) and the other from the material itself (Equation 1). They are governed with a mixture viscosity approach:

$$\mu_{mix} = \frac{\rho\mu_{ap} + S_c\mu_{sc.ap}}{\rho + S_c} \quad (3)$$

Equation 3 represents that the already printed material carries a slightly larger viscosity $\mu_{mix} > \mu_{ap}$ for a constant scalar concentration $S_c > 0$ and the material being deposited have the viscosity $\mu_{mix} = \mu_{ap}$. In order to produce a large viscosity difference between the two layers, the following characterization is used:

$$\mu_{mix.ap}(\dot{\gamma}) = \begin{cases} \mu_{sc.ap}, & \text{for } \mu_{mix} > \mu_{ap} \\ \mu_{ap}, & \text{for } \mu_{mix} \leq \mu_{ap} \end{cases} \quad (4)$$

which means the viscosity of the bottom and top layer is presented by Equation 2 and Equation 1, respectively. Equation 4 is used to calculate the deviatoric stress tensor \mathbf{S}_T by using the generalized Newtonian fluid approach:

$$\mathbf{S}_T = 2\mu_{mix.ap}(\dot{\gamma}) \mathbf{D}_T \quad (5)$$

where $\mathbf{D}_T = (1/2)((\nabla \mathbf{u}) + (\nabla \mathbf{u})')$ represents the deformation rate tensor and $\dot{\gamma} = \sqrt{2\text{tr}(\mathbf{D}_T^2)}$ is the strain rate.

Within the above assumptions, the flow dynamics is governed by the continuity and momentum equations:

$$\nabla \cdot \mathbf{u} = 0 \quad (6)$$

$$\rho \left(\frac{\partial \mathbf{u}}{\partial t} + \mathbf{u} \cdot \nabla \mathbf{u} \right) = -\nabla p + \rho \mathbf{g} + \nabla \cdot \mathbf{S}_T \quad (7)$$

where $\mathbf{g} = (0,0,-g)$ is the gravitational acceleration vector, \mathbf{u} is the velocity vector, t is the time, and p is the pressure. The properties of the material used in the CFD model are presented in Table 1.

Table 1: Material properties.

Parameters	Units	Values
Density, ρ	kg. m ⁻³	1000
Dynamic yield stress of printing layer, $\tau_{printing}$	Pa	100
Dynamic yield stress of printed layer, $\tau_{printed}$	Pa	100 – 1500
Plastic viscosity, η_P	Pa. s	33
Critical shear rate, $\dot{\gamma}_c$	s ⁻¹	0.05

Equations 6 and 7 are solved numerically with the finite volume technique, using the commercial CFD software **FLOW-3D**[®]. The viscous stress, pressure, and velocity components are solved implicitly. The momentum advection is calculated explicitly with second-order accuracy. Furthermore, the free surface tracking is done by the Volume-of-Fluid technique, see details in Ref. [24,25]. Figure 2 visualizes the dynamic viscosity of the CFD model. The longitudinal-section (top) and cross-section (bottom) are taken through the nozzle diameter with side and front views, respectively. The model is simulated with $\tau_{printing} = 100$ Pa and $\tau_{printed} = 400$ Pa. It can be seen that the model is able to predict different viscosity distributions in different layers, where red and greenish-blue colors respectively represent the maximum apparent viscosity of the bottom and top layer.

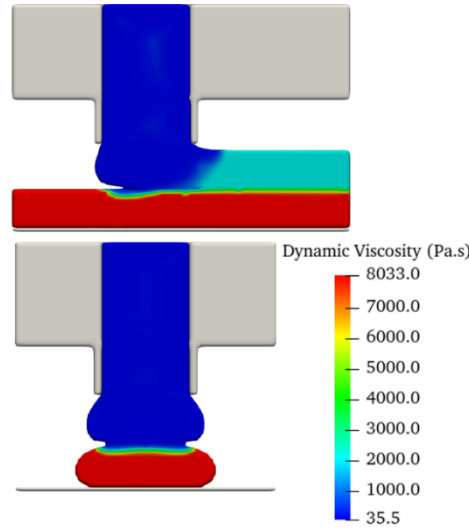


Figure 2: Viscosity evaluation of the CFD model. Moreover, the yield stress of bottom layer is 400 Pa while the top layer is printing with a yield stress of 100 Pa.

3. Results and discussion

In Figures 3 to 5, the developed CFD model is executed with different values of yield stress of the printed layer $\tau_{printed}$, which is presented in terms of the viscosity distributions, cross-sections, deformation of bottom layer, and extrusion pressure. The cross-sectional shapes are plotted at the middle of the length of the printed layer. The bottom layer deformation represents the percentile relative width of the bottom layer after printing the next layer. The extrusion pressure represents the pressure at the nozzle exit that is required to spread the printing material with shear deformation. Note that the hydrostatic pressure for a single layer is approximately 123 Pa.

The viscosity distributions for different values of $\tau_{printed}$ are presented in Figure 3. It shows that the viscosity profiles of the printing layer are similar to each other, whereas that of the printed layer are different for $\tau_{printed} = 100, 200,$ and 400 Pa. In the case of $\tau_{printed} = \tau_{printing}$ (Figure 3a), most of the material of the printed layer underneath the nozzle is found yielded (blue) because an effective decrease in viscosity is observed due to the total pressure that includes both the hydrostatic- and extrusion-pressure. The yielded zone reduces when increasing the $\tau_{printed}$ (Figure 3b and 3c). This is because the increased yield stress permits a higher load before yielding.

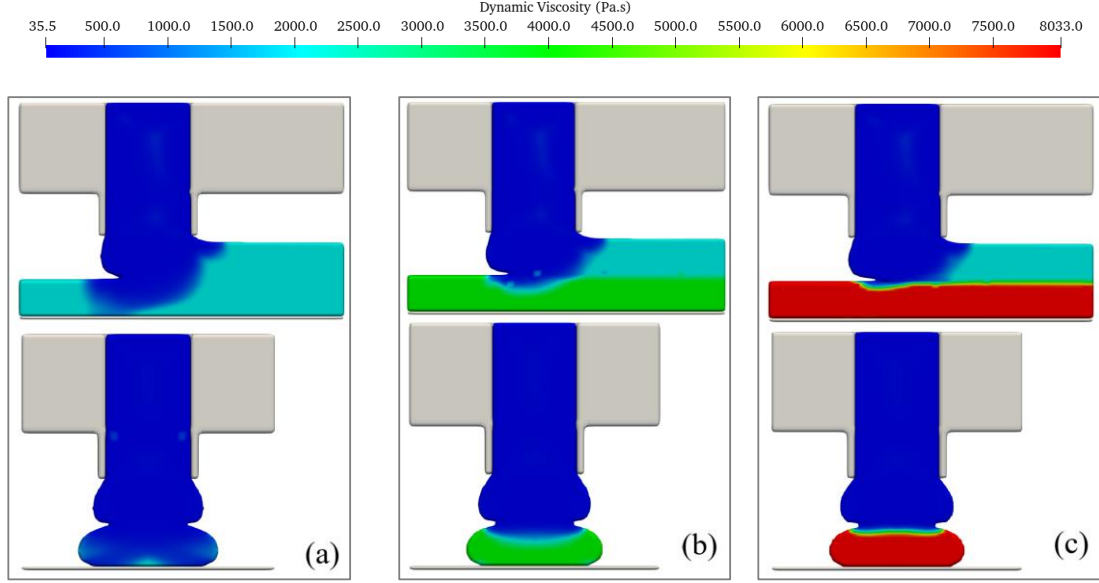


Figure 3: Effect of the yield stress of printed material $\tau_{printed}$ on the viscosity distributions, where $\tau_{printing} = 100$ Pa. (a) $\tau_{printed} = 100$ Pa; (b) $\tau_{printed} = 200$ Pa; and (c) $\tau_{printed} = 400$ Pa.

The impact of $\tau_{printed}$ on the cross-sectional shapes is presented in Figure 4. It shows that the bottom layer deforms less with increasing $\tau_{printed}$. Furthermore, it is found that most of the deformation can be eliminated by increasing $\tau_{printed}$ as to the double of $\tau_{printing}$ (Figure 4b). However, further increase in $\tau_{printed}$ results in a little improvement in deformation, and for $\tau_{printed} \geq 400$ Pa, the cross-sectional shapes of bottom layer seem to coincide (Figure 4d to 4f). The amount of deformation that occurred at the bottom layer is quantified in Figure 5a, and for $\tau_{printed} \geq 400$ Pa, the deformation is less than 1%.

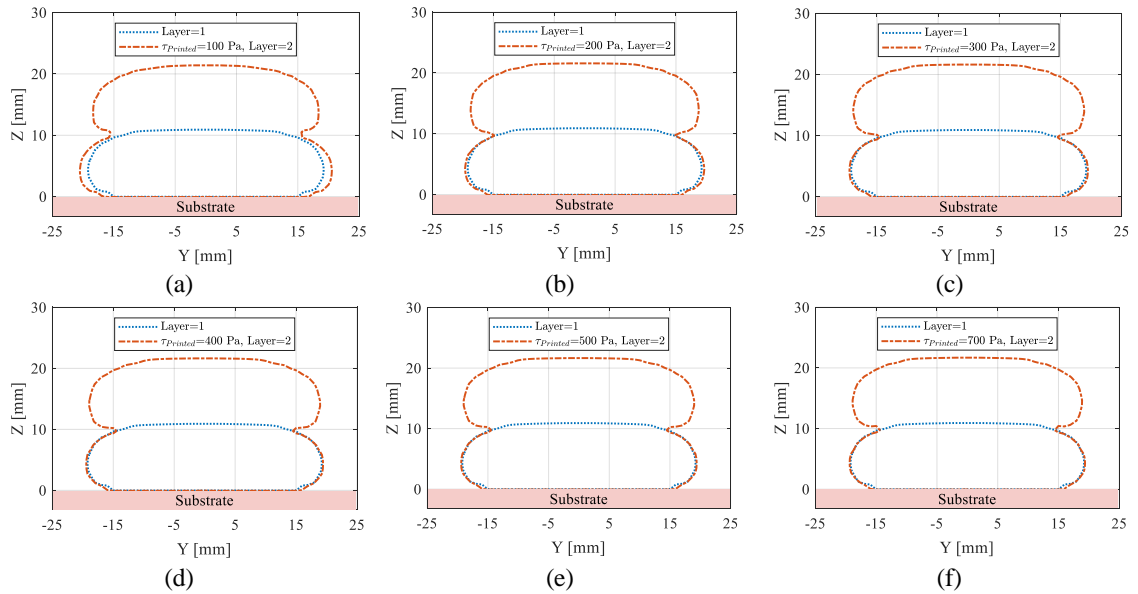


Figure 4: Effect of the yield stress of printed material $\tau_{printed}$ on the cross-sectional shapes, where $\tau_{printing} = 100$ Pa. (a) $\tau_{printed} = 100$ Pa; (b) $\tau_{printed} = 200$ Pa; (c)

$\tau_{printed} = 300$ Pa; (d) $\tau_{printed} = 400$ Pa; (e) $\tau_{printed} = 500$ Pa; and (f) $\tau_{printed} = 700$ Pa.

The extrusion pressure is presented in Figure 5b as a function of the yield stress of the printed layer. The extrusion pressure during printing of the bottom layer is represented by the straight line that has no influence for different $\tau_{printed}$. The maximum extrusion pressure is observed for the bottom layer that is printed into the non-deformable solid substrate, whereas for the other layer, the extrusion pressure varies depending on the deformability of the printed layer. The more the printed layer deforms, the effective distance between the nozzle exit and the printed layer increases; hence, less extrusion pressure is observed. Moreover, for $\tau_{printed} \geq 400$ Pa the extrusion pressure starts to converge, which is due to the effective distance does not change.

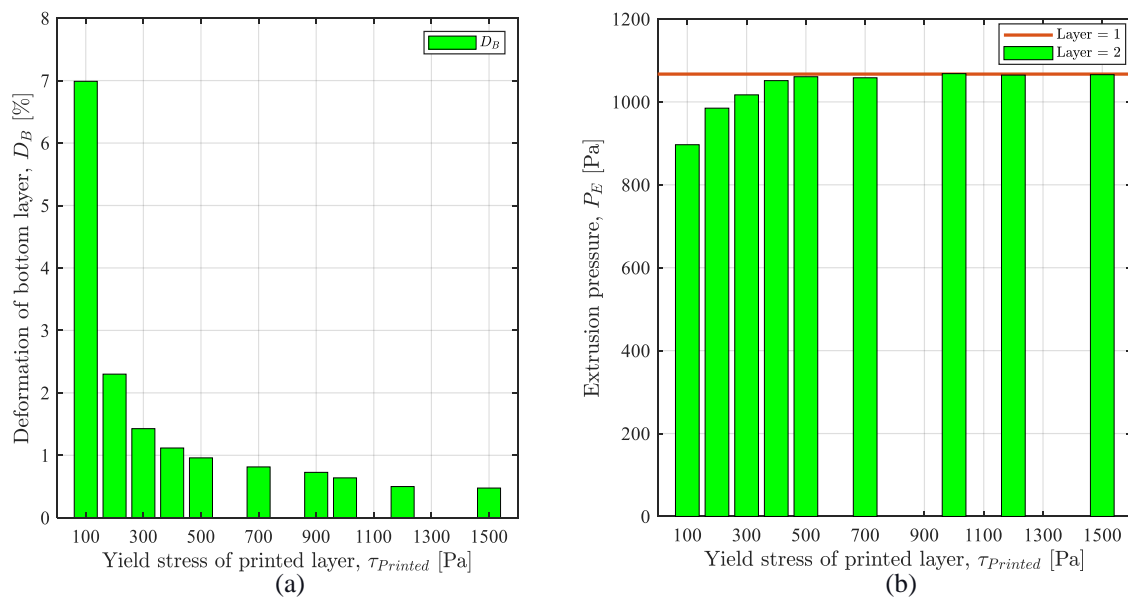


Figure 5: (a) Deformation of bottom layer and (b) extrusion pressure as a function of the yield stress of printed material $\tau_{printed}$, where $\tau_{printing} = 100$ Pa.

4. Conclusion

A CFD model was developed to predict the extrusion-deposition flow of the viscoplastic material that develops its properties over time. The materials property requires two different yield stress approaches (for the printed and printing layers) that were modelled with the Bingham constitutive equations. The CFD model was found capable of differing the viscosity between the fluid layers precisely as formulated. We numerically analyzed the influence of yield stress buildup on the bottom layer deformation. Within the investigated parameters, the preliminary outcomes showed that most of the deformation could be eliminated by having the bottom layer develop the yield stress to twice the value of the printing material. Thus, this study showcase that CFD models have a potential to assist in finding the optimal material development that leads to stable MEX-AM printing.

Acknowledgements

The authors would like to acknowledge the support from the Danish Council for Independent Research (DFF) | Technology and Production Sciences (FTP) (Contract No.

8022-00042B). Moreover, the authors thank **FLOW-3D**[®] for their support in regards to licenses.

Conflict of interest

On behalf of all authors, the corresponding author states that there is no conflict of interest.

References

1. Z. Chen, Z. Li, J. Li, C. Liu, C. Lao, Y. Fu, C. Liu, Y. Li, P. Wang, and Y. He, *J. Eur. Ceram. Soc.* **39**, 661 (2019).
2. J. Lindahl, A. A. Hassen, S. Romberg, B. Hedger, P. Hedger Jr, M. Walch, T. DeLuca, W. Morrison, P. Kim, A. Roschli, D. Nuttal, J. Czachowski, B. Post, L. Love, and V. Kunc, in *United States (Oak Ridge National Lab. (ORNL), Oak Ridge, TN (US))*, (2018).
3. V. Mechtcherine, F. P. Bos, A. Perrot, W. R. L. da Silva, V. N. Nerella, S. Fataei, R. J. M. Wolfs, M. Sonebi, and N. Roussel, *Cem. Concr. Res.* **132**, 106037 (2020).
4. J. Jiang and Y. Ma, *Micromachines* **11**, 633 (2020).
5. T. T. Le, S. A. Austin, S. Lim, R. A. Buswell, R. Law, A. G. F. Gibb, and T. Thorpe, *Cem. Concr. Res.* **42**, 558 (2012).
6. O. A. Mohamed, S. H. Masood, and J. L. Bhowmik, *Addit. Manuf.* **18**, 164 (2017).
7. H. Xia, J. Lu, and G. Tryggvason, *Comput. Methods Appl. Mech. Eng.* **346**, 242 (2019).
8. H. Xia, J. Lu, and G. Tryggvason, *Int. J. Heat Mass Transf.* **138**, 1310 (2019).
9. M. Jabbari, I. Baran, S. Mohanty, R. Comminal, M. R. Sonne, M. W. Nielsen, J. Spangenberg, and J. H. Hattel, *Adv. Mech. Eng.* **10**, 5 (2018).
10. R. Comminal, M. P. Serdeczny, D. B. Pedersen, and J. Spangenberg, *Addit. Manuf.* **29**, 100753 (2019).
11. R. Comminal, M. P. Serdeczny, D. B. Pedersen, and J. Spangenberg, in *Proc. Annu. Int. Solid Free. Fabr. Symp.* 1855 (2018).
12. M. P. Serdeczny, R. Comminal, D. B. Pedersen, and J. Spangenberg, in *Proc. Annu. Int. Solid Free. Fabr. Symp.* 1849 (2018).
13. M. P. Serdeczny, R. Comminal, D. B. Pedersen, and J. Spangenberg, *Addit. Manuf.* **28**, 419 (2019).
14. R. Comminal, M. P. Serdeczny, D. B. Pedersen, and J. Spangenberg, *Addit. Manuf.* **20**, 68 (2018).
15. R. Comminal, M. P. Serdeczny, D. B. Pedersen, and J. Spangenberg, in *18th Int. Conf. Eur. Soc. Precis. Eng. Nanotechnol. Euspen 18*, (2018).
16. M. P. Serdeczny, R. Comminal, D. B. Pedersen, and J. Spangenberg, in *18th Int. Conf. Eur. Soc. Precis. Eng. Nanotechnol. Euspen 18*, (2018).
17. R. Comminal, W. R. Leal da Silva, T. J. Andersen, H. Stang, and J. Spangenberg, *Cem. Concr. Res.* **138**, 106256 (2020).
18. N. Roussel, J. Spangenberg, J. Wallevik, and R. Wolfs, *Cem. Concr. Res.* **135**, 106075 (2020).
19. J. Spangenberg, W. R. Leal da Silva, R. Comminal, M. T. Mollah, T. J. Andersen, and H. Stang, *RILEM Tech. Lett.* **6**, 119 (2021).
20. M. T. Mollah, R. Comminal, M. P. Serdeczny, D. B. Pedersen, and J. Spangenberg, *Addit. Manuf.* **46**, 102193 (2021).
21. E. J. O'Donovan and R. I. Tanner, *J. Non-Newton. Fluid Mech.* **15**, 75 (1984).

22. E. C. Bingham, *An Investigation of the Laws of Plastic Flow* (US Government Printing Office, 1917).
23. FLOW-3D, "Solving The World's Toughest CFD Problems", (FLOW Sci. (n.d.)).
<https://www.flow3d.com/products/flow-3d/> (accessed May 10, 2020).
24. C. W. Hirt and B. D. Nichols, *J. Comput. Phys.* **39**, 201 (1981).
25. R. Comminal, J. Spangenberg, and J. H. Hattel, *J. Comput. Phys.* **283**, 582 (2015).

Publication [A.4]: A Numerical Investigation of the Inter-Layer Bond and Surface Roughness during the Yield Stress Buildup in Wet-On-Wet Material Extrusion Additive Manufacturing

Md. Tusher Mollah*, Marcin P. Serdeczny*§, Raphaël Comminal*§, Berin Šeta*,
Marco Brander*, David B. Pedersen*, Jon Spangenberg*

*Department of Civil and Mechanical Engineering, Technical University of Denmark,
Denmark.

§Flow Science, Inc., USA.

Published in:
2022 Summer Topical Meeting: Advancing Precision in Additive Manufacturing,
American Society for Precision Engineering, TN, USA, 11-15 July 2022.

Publication [A.4]: A Numerical Investigation of the Inter-Layer Bond and Surface Roughness during the Yield Stress Buildup in Wet-On-Wet Material Extrusion Additive Manufacturing

The layout has been revised.

Abstract

Performance of wet-on-wet material extrusion additive manufacturing (MEX-AM) requires attention to the printed layer before printing the next layer on top. This is for instance the case of thermoset resins that require curing, or concrete, which hardening reaction may take minutes to hours. In this work, a computational rheology model is used to simulate wet-on-wet MEX-AM. The model includes the partial curing/hardening of the printed layer by a yield stress buildup. The results highlight how the yield stress buildup of the previously deposited layers affects the inter-layer bond and surface roughness.

1. Introduction

Wet-on-wet printing of materials has recently gained attention when it comes to 3D printing different scales/sizes of components/structures. Materials such as thermoset, ceramic paste, and concrete can be printed wet-on-wet in large-scale using Robocasting and 3D concrete printing technologies [1-4]. These are freeform fabrication techniques under the umbrella term Material Extrusion Additive Manufacturing (MEX-AM). In these technologies, materials are extruded through a nozzle following a layer-by-layer approach similar to Fused Deposition Modelling [5-7].

Wet-on-wet printing can lead to unwanted deformation of previously deposited layers when printing on top of them [8]. Furthermore, larger deformation could negatively affect the surface roughness of layers. Therefore, it can be important to let a printed layer partially solidify before depositing the next layer on top. This is simply equivalent to allowing a yield stress buildup of the printed layer [9]. A higher yield stress buildup could potentially solidify the printed layer that negatively affects the interlayer bond [2]. However, it requires an investigation on how much yield stress buildup is necessary to achieve a homogeneous layer size as well as have a better inter-layer bond and surface roughness.

In this work, we developed a computational rheology model that simulates a two-layer structure by MEX-AM. Both layers are modelled with different yield stress to represent the printing of a wet layer onto a partially solidified bottom layer. The computational model provides the cross-sections of the deposited layers, from which the bottom layer deformation, the inter-layer bond, and the surface roughness were estimated.

2. Computational Model

The computational fluid dynamics (CFD) model developed in *FLOW-3D*® (Version 12.0; 2019; Flow Science, Inc.) [10] solves the transient and isothermal deposition flow of materials using the continuity and momentum balance equations given below:

$$\nabla \cdot \mathbf{u} = 0 \quad (1)$$

$$\rho \left(\frac{\partial \mathbf{u}}{\partial t} + \mathbf{u} \cdot \nabla \mathbf{u} \right) = \rho \mathbf{g} - \nabla p + \nabla \cdot \mathbf{S}_T \quad (2)$$

where \mathbf{u} is the velocity vector, $\rho = 1000 \text{ kg.m}^{-3}$ is the constant density, p is the pressure, \mathbf{g} is the gravitational acceleration vector with components $(0,0,-g)$, t is the time, and

\mathbf{S}_T the deviatoric stress-tensor. The \mathbf{S}_T is modelled within the following generalized Newtonian fluid constitutive framework:

$$\mathbf{S}_T = 2\mu_{APP}(\dot{\gamma}) \mathbf{D}_T \quad (3)$$

where $\dot{\gamma} = \sqrt{2\text{tr}(\mathbf{D}_T^2)}$ is the strain rate magnitude, $\mathbf{D}_T = ((\nabla \mathbf{u}) + (\nabla \mathbf{u})^T)/2$ is the deformation rate tensor, and μ_{APP} is the apparent viscosity of the viscoplastic material. The viscoplastic nature is modelled by the regularized bi-viscous Bingham model [11]. In addition, the model uses a scalar approach to differentiate the material of layers and assign different yield stress. Details of the scalar approach can be found in [9], whereas a simple representation together with the bi-viscous Bingham model is given in Equation 4 that identifies the printed material by the presence of a non-dimensional scalar identifier S . The two layers have different yield stresses, resulting in a different apparent viscosity. The printing layer uses Equation 4 with $S = 0$ and it is the printed bottom layer when $S = 1$.

$$\begin{aligned} \mu_{APP} &= (1 - S)\mu_{ap}(\dot{\gamma}) + S\mu_{printed.ap}(\dot{\gamma}) \\ &= \begin{cases} \eta_P + \frac{(1 - S)\tau_{printing} + S\tau_{printed}}{\dot{\gamma}_c}, & \text{for } \dot{\gamma} < \dot{\gamma}_c \\ \eta_P + \frac{(1 - S)\tau_{printing} + S\tau_{printed}}{\dot{\gamma}}, & \text{for } \dot{\gamma} \geq \dot{\gamma}_c \end{cases} \quad (4) \end{aligned}$$

where μ_{ap} and $\mu_{printed.ap}$ are the apparent viscosity of the printing and printed layers, respectively, $\eta_P = 33 \text{ Pa}\cdot\text{s}$ is the plastic viscosity, $\tau_{printing} = 100 \text{ Pa}$ is the printing yield stress, $\tau_{printed}$ is the printed yield stress, which was varied between 100 Pa to 400 Pa, and $\dot{\gamma}_c = 0.05 \text{ s}^{-1}$ is the critical shear rate.

The computational domain of the CFD model includes a cylindrical nozzle of diameter 25 mm that extrudes the material with an extrusion speed of 40 mm/s, cf. Figure 1. The nozzle moves with a printing speed of 50 mm/s. The nominal layer height is 12.5 mm. A uniform Cartesian grid is used to mesh the computational domain that is discretized by the Finite Volume Method (FVM). The top and bottom plane of the domain is an inlet and wall boundary, respectively. A symmetrical boundary is assigned through the nozzle diameter along the printing direction. Other boundaries are assigned to a continuative boundary condition. Moreover, the open channel flow is modelled with the Volume of Fluid Method (VOF) [12]. The pressure and velocity components are solved implicitly in time. The viscous solver utilizes the scalar identifier based on a self-customization to alter the viscosity between the layers. Figure 2 illustrates the dynamic viscosity distribution. It can be seen that the model predicts the yield stress buildup at the bottom layer accurately (bottom).

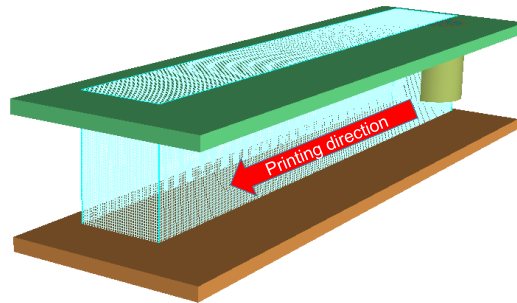


Figure 1. CFD model with the computational domain, extrusion nozzle, and substrate.

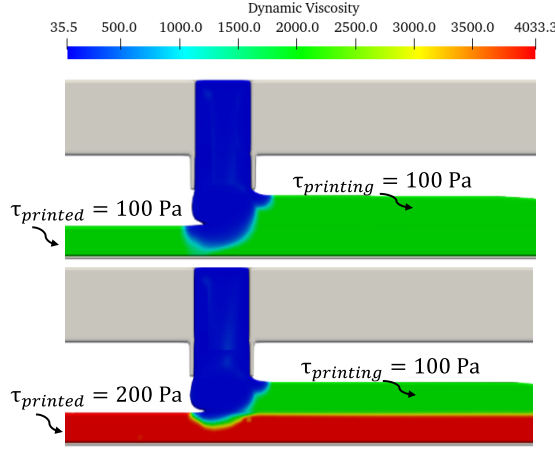


Figure 2. Dynamic viscosity distributions between the layers for pure wet-on-wet printing (top) and yield stress buildup during wet-on-wet (bottom).

The simulated results are post-processed in order to obtain the cross-sectional shapes. The cross-sections are taken in the middle of the computational domain.

3. Results and discussion

The cross-sectional shapes of the deposited layers and inter-layer bond lines are presented in Figure 3. It can be seen that the shape of the bottom layer deviates less when the yield stress increases. Furthermore, the bond lines can be observed to move from concave to convex state with the buildup. It is also seen that the bond lines move their position from below the initial height of the bottom layer to the exact position of the initial height. These behaviors are seen because the yield stress increased before the load of the second layer was applied. As a result, both the deformation of the bottom layer (i.e., ratio of the width difference (between the bottom layer width after printing the second layer and width at the end of the first layer $W1$) by $W1$) and inter-layer bond (i.e., ratio of the length of bond line and $W1$) decreases with yield stress buildup, cf., Figure 4. Although it is a mild decrease for inter-layer bonds, and for higher yield stress buildups (i.e., $\tau_{printed} = 300$ and 400 Pa), it is almost identical.

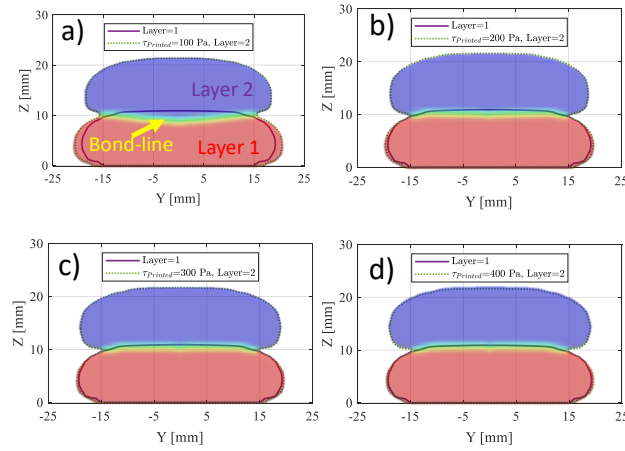


Figure 3. Cross-sectional shapes and inter-layer bond lines for different yield stress buildup. Moreover, a) $\tau_{printed} = 100$ Pa; b) $\tau_{printed} = 200$ Pa; c) $\tau_{printed} = 300$ Pa; d) $\tau_{printed} = 400$ Pa.

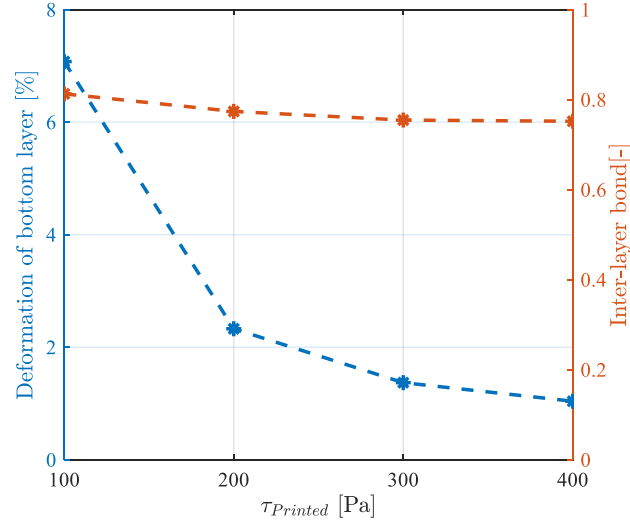


Figure 4. Deformation of the bottom layer and inter-layer bond for different yield stress buildup.

Figure 5 illustrates the surface roughness (i.e., edge smoothness and arithmetic mean roughness Ra) of the vertical edge profile of the simulated part for different $\tau_{printed}$. The profile smoothness is represented by the centerline positioned where the areas above and below the line are equal, and the arithmetic mean roughness is estimated as the mean deviation of the profile from the centerline, cf. [13] for details. It is seen that the yield stress buildup improves the surface quality as well as makes the vertical edges smoother. However, Ra is almost the same for larger $\tau_{printed} = 300$ and 400 Pa.

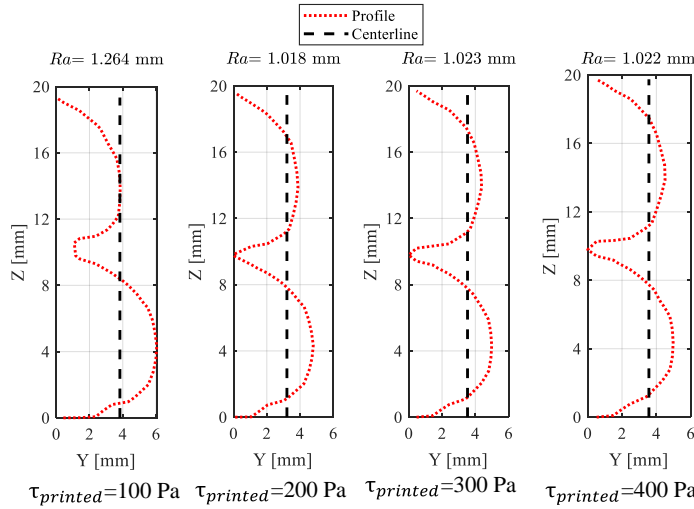


Figure 5. Surface roughness for different yield stress buildup, $\tau_{printed}$.

4. Summary

A computational fluid dynamics model is used to predict the deposition flow of viscoplastic materials during the yield stress buildup in wet-on-wet MEX-AM. The cross-sectional shapes of the layers are predicted to investigate the bottom layer's deformation, interlayer bond, and surface roughness of layers.

The yield stress buildup at the bottom layer reduces its deformation and improves the surface roughness and smoothness. On the other hand, it can be detrimental for the inter-layer bonding when the buildup is too high as it slightly decreases with buildup. Thus, an optimal balance in the yield stress buildup is required as depicted in this study.

ACKNOWLEDGEMENTS

The authors would like to acknowledge the support of the Danish Council for Independent Research (DFF) | Technology and Production Sciences (FTP) (Contract No. 8022-00042B). Moreover, the authors thank *FLOW-3D®* for their support in regards to licenses.

REFERENCES

- [1] J. Lindahl, A.A. Hassen, S. Romberg, B. Hedger, P.H. Jr, T. Deluca, W. Morrison, S. Kim, A. Roschli, D. Nuttal, B. Post, L. Love, V. Kunc, Large-scale additive manufacturing with reactive polymers, in: Oak Ridge National L., Oak Ridge, TN, USA, 2017,p. 8.
- [2] T.T. Le, S.A. Austin, S. Lim, R.A. Buswell, R. Law, A.G.F. Gibb, T. Thorpe, Hardened properties of high-performance printing concrete, *Cem. Concr. Res.* 42 (2012) 558–566.
- [3] R. Comminal, W.R. Leal da Silva, T.J. Andersen, H. Stang, J. Spangenberg, Modelling of 3D concrete printing based on computational fluid dynamics, *Cem. Concr. Res.* 138 (2020) 106256.
- [4] N. Ranjbar, M. Mehrli, C. Kuenzel, C. Gundlach, D. B. Pedersen, A. Dolatshahi-Pirouz, J. Spangenberg, Rheological characterization of 3D printable geopolymers. *Cement and Concrete Research*, 147(2021), 106498.
- [5] B. Brenken, E. Barocio, A. Favaloro, V. Kunc, R.B. Pipes, Fused filament fabrication of fiber-reinforced polymers: A review, *Addit. Manuf.* 21 (2018) 1–16.
- [6] R. Comminal, J. H. Hattel, J. Spangenberg, Numerical simulations of planar extrusion and fused filament fabrication of non-Newtonian fluids. *Annu. Trans. Nord. Rheol. Soc.*, 25(2017), 263-270.
- [7] M.P. Serdeczny, R. Comminal, D.B. Pedersen, J. Spangenberg, Numerical prediction of the porosity of parts fabricated with fused deposition modeling. In *2018 International Solid Freeform Fabrication Symposium*. University of Texas at Austin.
- [8] M.T. Mollah, R. Comminal, M.P. Serdeczny, D.B. Pedersen, J. Spangenberg, Stability and deformations of deposited layers in material extrusion additive manufacturing, *Addit. Manuf.* (2021) 102193.
- [9] M.T. Mollah, R. Comminal, M.P. Serdeczny, D.B. Pedersen, J. Spangenberg, Numerical Predictions of Bottom Layer Stability in Material Extrusion Additive Manufacturing, *JOM*. (2022).
- [10] *FLOW-3D®* Version 12.0 [Computer software]. (2019). Santa Fe, NM: Flow Science, Inc. <https://www.flow3d.com>.
- [11] E.J. O'Donovan, R.I. Tanner, Numerical study of the Bingham squeeze film problem, *J. Non-Newton. Fluid Mech.* 15 (1984) 75–83.
- [12] C.W. Hirt, B.D. Nichols, Volume of fluid (VOF) method for the dynamics of free boundaries, *J. Comput. Phys.* 39 (1981) 201–225.
- [13] M.P. Serdeczny, R. Comminal, D.B. Pedersen, J. Spangenberg, Numerical simulations of the mesostructure formation in material extrusion additive manufacturing, *Addit. Manuf.* 28 (2019) 419–429.

Publication [A.5]: Computational analysis of yield stress buildup and stability of deposited layers in material extrusion additive manufacturing

Md. Tusher Mollah*, Raphaël Comminal*§, Marcin P. Serdeczny*§, Berin Šeta*, Jon Spangenberg*

*Department of Civil and Mechanical Engineering, Technical University of Denmark, Denmark.

§Flow Science, Inc., USA.

Submitted to:
Additive Manufacturing, ELSEVIER.

Appended Publications

The layout has been revised.

Abstracts

This paper investigates the stability of deformable layers produced by material extrusion additive manufacturing. A Computational Fluid Dynamics (CFD) model is developed to predict the deposition flow of viscoplastic materials such as ceramic pastes, thermosets, and concrete. The viscoplastic materials are modelled with the Bingham rheological equations and implemented with a generalized Newtonian fluid model. The developed CFD model applies a scalar approach to differentiate the rheology of two layers in order to capture the deposition of a wet layer onto a semi solidified printed layer (i.e., wet-on-semisolid printing). The semi solidification is modelled by a yield stress buildup. The cross-sectional shapes of the deposited layers are predicted, and the relative deformation of the first layer is studied for different yield stress buildups and processing conditions such as printing- and extrusion-speed, layer height, and nozzle diameter. The results of the CFD model illustrate that the relative deformation of the first layer decreases non-linearly with an increase in yield stress, and that stable prints can be obtained when taking into account the semi solidification. Furthermore, it is found that the deformation is dependent on a non-trivial interplay between the extrusion pressure, the shape of the cross-section, and the contact area between the layers. Finally, the results highlight which process conditions that can be changed with benefit in order to limit the requirement on the yield stress buildup and still provide stable prints.

Keywords: Material Extrusion Additive Manufacturing, Computational Fluid Dynamics (CFD), Viscoplastic Materials, Yield Stress Buildup, and Stable Printing.

1. Introduction

Three-dimensional fabrication of structures produced by Material Extrusion Additive Manufacturing (MEX-AM) is an attractive technology for a wide range of industries [1–3]. MEX-AM is an umbrella term that covers multidisciplinary fabrication techniques such as “Fused Deposition Modelling (FDM) or Fused Filament Fabrication (FFF)”[4], “Robocasting” [5], and “3D concrete printing” [6]. Thermoplastics have been a commonly used material in MEX-AM, but recently viscoplastic materials such as ceramics [7], thermosets [8], and concrete [9] have received attention. These materials are typically extruded through a nozzle and deposited onto a solid substrate following a layer-by-layer approach [10]. Control over the material properties is crucial when attempting to retain the layered shape of deposited viscoplastic materials, as the layered shape can be flattened due to the applied pressure (from subsequent layers) when the material is too liquid, while a too rigid material rarely flows through the nozzle.

During MEX-AM of viscoplastic materials, a printed layer can be considered as wet, semisolid, or solidified, depending on the material state. Depositing a new layer onto a solidified layer typically results in a geometrically stable print (i.e., homogeneous width and height of layers), but it is often not ideal from a printing time perspective (if the solidification time is long) and it can be detrimental for the interlayer bonding [11]. Consequently, printing on a wet or semisolid layer is in many cases preferable. However, in this case, printing geometrically stable layers is not a simple task [12,13], as discussed in several experimental studies on MEX-AM of viscoplastic materials [14–17]. Different studies showed that all layers potentially could deform during the deposition, however the most critical deformation takes place at the first layer [18].

Computational Fluid Dynamics (CFD) modelling of extrusion-deposition flows has been found very advantageous when analyzing experimental MEX-AM results [19,20]. In regards to MEX-AM with thermoplastic, Xia et al. [21] estimated the geometrical shape of the deposited layers using numerical simulations. In addition, Comminal et al. [22,23] and Mollah et al. [24] developed CFD models with the aim to predict and discuss precision of printed corners, while Serdeczny et al. [25,26] addressed through numerical modelling how to reduce porosities and enhance the bonding between subsequent layers. Numerical results have also pointed out that a deposited layer undergoes two pressure contributions: the hydrostatic pressure due to the layers weight and the extrusion pressure applied by the extruded material [27]. Comminal et al. [20,28] explained the effect of extrusion pressure on the geometry of a single layer. When printing on top of a wet layer that behaves viscoplastic, the extrusion pressure facilitates sideways flow of the depositing material and it affects the geometrical shape of the already printed layer [29]. Consequently, material deposition on a wet as well as a semisolid layer (which typically is the case for MEX-AM with ceramics, thermosets and concrete) requires special attention in order to achieve geometrically stable prints.

This paper presents the first CFD model of two-layered viscoplastic prints by MEX-AM that accounts for the time dependent material development during the process (i.e., the second layer is deposited onto a semisolid first layer). The semi solidification is modelled by increasing the yield stress of the first layer while the second layer is deposited; thereby mimicking a yield stress buildup of the material. The model is exploited to investigate geometrical stability of prints performed with materials with various yield stress buildup under a wide range of process conditions. The outline of the work is as follows. In section 2, details about the CFD model are presented. The simulated results predicting the influence of material development and processing parameters on geometrical stability are discussed in section 3. Finally, conclusions are summarized in section 4.

2. Methodology

2.1. Computational model

The CFD model presented in this study is an extension of a model developed to simulate MEX-AM with non-Newtonian materials, which previously was validated by comparison with single and multi-layer experimental results [28,30]. The extension consist of adding a time dependency to the material behavior, which is typically seen when printing thermosets and concrete. Details about this time dependent material modelling is given in section 2.2. The CFD model simulates the deposition flow of the time-dependent viscoplastic material inside a computational domain of $10D \times 1.5D \times (1.5D + h)$ that includes a cylindrical nozzle of diameter D and a planar solid substrate placed at a distance h from the nozzle orifice, which is the nominal height of the first layer (Figure 1). The nozzle extrudes the material onto the substrate in a layer-by-layer manner and the material is extruded with a fully developed profile at a constant extrusion speed U . When the material touches the substrate, the nozzle starts to travel along a straight toolpath with a prescribed printing speed V . The nozzle travels a distance of $8D$ while printing the layers. The second layer is also printed with the distance h between the nozzle orifice and the first layer.

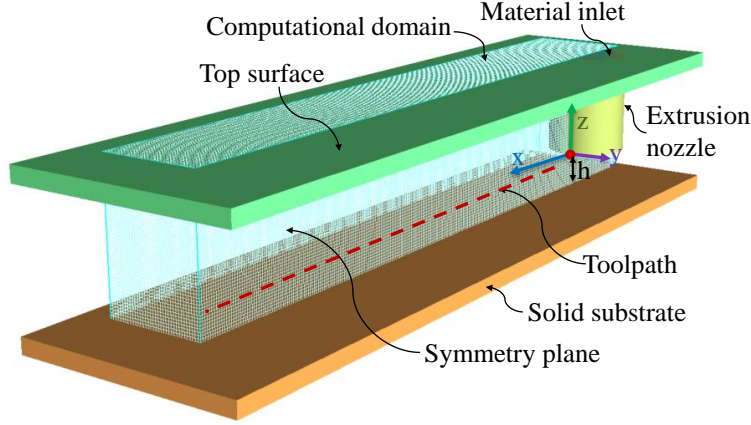


Figure 1: Geometry with toolpath, computational domain, and boundary conditions of the CFD model.

A uniform Cartesian grid is used to mesh the computational domain. The top plane of the computational domain is treated as an inlet boundary, however a solid surface is superimposed to it. This permits the material to enter the domain only through the nozzle orifice that is attached to the top plane. A stationary wall condition is assigned to the bottom plane that carries the solid substrate. In the xz -plane, a symmetry boundary is applied to reduce the computational cost. Other planes are assigned with continuative boundary conditions that allow the fluid to freely exit the computational domain, although the deposited material does not interact with those planes. The solid (i.e., nozzle and substrate) and fluid interaction is prescribed with a no-slip boundary condition.

2.2. Rheology of layers

In this study, the viscoplastic constitutive model adapted by the CFD model is the Bingham material model [31]:

$$\tau = \eta_P \dot{\gamma} + \tau_{printing} \quad (1)$$

where τ is the shear stress, η_P is the plastic viscosity, $\dot{\gamma}$ is the shear rate, and $\tau_{printing}$ is the yield stress of the material while being deposited. The latter is typically represented by τ_0 , but the material changes yield stress over time as described in detail later in the section and for that reason this nomenclature is chosen. When the stress state in the material exceeds the yield stress, the fluid starts flowing. The apparent viscosity function describing the Bingham material model is given by:

$$\mu_{app}(\dot{\gamma}) = \eta_P + \tau_{printing}/\dot{\gamma} \quad (2)$$

This becomes infinite at zero shear rate, so in order to avoid the numerical singularity, a bi-viscous regularization [32] of the Bingham material model is used in the CFD model:

$$\mu_{app}(\dot{\gamma}) = \begin{cases} \mu_{max.app}, & \text{when } \dot{\gamma} < \dot{\gamma}_c \\ \eta_P + \frac{\tau_{printing}}{\dot{\gamma}}, & \text{when } \dot{\gamma} \geq \dot{\gamma}_c \end{cases} \quad (3)$$

where $\mu_{max.app} = \eta_P + \tau_{printing}/\dot{\gamma}_c$ is the maximum apparent viscosity and $\dot{\gamma}_c$ is the critical shear rate. The selection of $\dot{\gamma}_c$ is arbitrary, however it should be small enough to limit the flow in the parts of the domain where the stress state is lower than the yield stress, while large enough to avoid extensive computational time and possible divergence issues.

As previously mentioned, the CFD model takes into account that the viscoplastic material changes its rheological behavior over time. Once the first layer is deposited, its yield stress is changed before the second layer is printed on top (i.e., the first layer is now assumed semisolid). Here it should be noted that the second layer is printed with the initial rheological properties of the first layer. The change in yield stress is modelled with a scalar approach. This is done by assigning a scalar S_c in terms of mass per fluid volume, which is larger than zero, exclusively to the first layer after deposition with an accompanying apparent viscosity function:

$$\mu_{sc.app}(\dot{\gamma}) = \begin{cases} \mu_{max.sc.app}, & \text{when } \dot{\gamma} < \dot{\gamma}_c \\ \eta_P + \frac{\tau_{printed}}{\dot{\gamma}}, & \text{when } \dot{\gamma} \geq \dot{\gamma}_c \end{cases} \quad (4)$$

where $\mu_{max.sc.app} = \eta_P + \tau_{printed}/\dot{\gamma}_c$. The only difference as compared to Equations 1 is $\tau_{printed}$ that represent the yield stress of the already deposited material, whereas $\tau_{printing}$ is the yield stress of the material while being deposited. Thus, two apparent viscosity functions are assigned to the first layer, one from the material itself (Equation 3) and the other from the scalar (Equation 4). They are governed with a viscosity mixture-rule that uses a mass-average between the apparent viscosities of both material and scalar [33]:

$$\mu_{mix} = \frac{\rho\mu_{app} + S_c\mu_{sc.app}}{\rho + S_c} \quad (5)$$

where ρ is the density. This means, in the part of the domain where $S_c = 0$, μ_{mix} is equal to μ_{app} , while in the part of the domain where $S_c > 0$, μ_{mix} is larger than μ_{app} . However, the increased viscosity (when $S_c > 0$) does not comply with the rheological behavior of the first layer after being deposited. Therefore, μ_{mix} is used as a classification parameter in Equation 4 that specifies whether μ_{app} or $\mu_{sc.app}$ is used as the apparent viscosity in a given control volume:

$$\mu_{cv.app}(\dot{\gamma}) = \begin{cases} \mu_{sc.app}, & \text{when } \mu_{mix} > \mu_{app} \\ \mu_{app}, & \text{when } \mu_{mix} \leq \mu_{app} \end{cases} \quad (6)$$

With this procedure, wet-on-wet printing (i.e., $\tau_{printed} = \tau_{printing}$) is simulated by specifying $S_c = 0$, while wet-on-semisolid printing (i.e., $\tau_{printed} > \tau_{printing}$) is achieved by given S_c an arbitrary value larger than zero.

2.3. Governing equations

The transient and isothermal flow dynamics of the incompressible, viscoplastic material are modelled by the continuity and momentum equations:

$$\nabla \cdot \mathbf{u} = 0 \quad (7)$$

$$\rho \left(\frac{\partial \mathbf{u}}{\partial t} + \mathbf{u} \cdot \nabla \mathbf{u} \right) = \rho \mathbf{g} - \nabla p + \nabla \cdot \mathbf{S}_T \quad (8)$$

where \mathbf{u} is the velocity vector, \mathbf{g} is the gravitational acceleration vector with components $(0, 0, -g)$, p is the pressure, t is the time, and \mathbf{S}_T the deviatoric stress-tensor. The apparent viscosity function is seen in the constitutive stress-tensor, which is modelled as:

$$\mathbf{S}_T = 2\mu_{cv.app}(\dot{\gamma}) \mathbf{D}_T \quad (9)$$

where $\dot{\gamma} = \sqrt{2\text{tr}(\mathbf{D}_T^2)}$ represents the strain rate magnitude and \mathbf{D}_T represents the deformation rate tensor, defined as:

$$\mathbf{D}_T = \frac{1}{2}((\nabla \mathbf{u}) + (\nabla \mathbf{u})^T) \quad (10)$$

where the superscript T represents the transpose notation.

2.4. Simulation framework

The CFD model is developed in the commercial software **FLOW-3D**[®], version 12.0 [33]. The governing equations are discretized by the Finite Volume Method (FVM) and the viscoplastic behavior is predicted by the built-in generalized Newtonian fluid framework. The viscosity is calculated in a separate subroutine that has been customized according to section 2.2. An implicit technique, successive under-relaxation, is used to solve the viscous stress of the momentum equation. The momentum advection is calculated explicitly by a monotonically preserving upwind-difference technique that ensures second-order accuracy in space and first-order accuracy in time. The pressure and velocity components are solved implicitly in time. The predictions of pressure and forces near walls are facilitated by the immersed boundary method, which assists in the prediction of the extrusion pressure [34]. The time step size is initially set to a value of $1e^{-5}$, however it is dynamically determined by the solver accordingly to a stability criteria in order to avoid numerical instabilities [33]. The software uses the FAVOR technique (Fractional Area/Volume Obstacle Representation) to represent solid geometries within the computational domain, which assists in simulating the motion of the nozzle. The free surface tracking is done by the Volume-of-Fluid (VOF) method, see details in [35,36].

Several cases are simulated in this study. A description of the cases and the corresponding processing parameters are presented in Table 1. The hydrostatic pressure is calculated as $P_H = N\rho gh$ (cf. Table 1), where $g = 9.81 \text{ ms}^{-2}$ and N is the number of layers. The material properties used in the study are presented in Table 2.

Table 1: Model descriptions with processing parameters and hydrostatic pressure.

Case ID	Nozzle diameter D (mm)	Layer height h (mm)	Gap ratio h/D	Extrusion speed U (mm/s)	Printing speed V (mm/s)	Speed ratio $S_r = V/U$	Hydrostatic pressure P_H (Pa) (for a single layer)
1	25	12.5	0.5	40	50	1.25	123
2	25	12.5	0.5	40	40	1	123

3	25	12.5	0.5	40	30	0.75	123
4	25	12.5	0.5	30	30	1	123
5	25	12.5	0.5	20	30	1.5	123
6	25	18.75	0.75	40	50	1.25	184
7	25	25	1.0	40	50	1.25	246
8	0.4	0.2	0.5	40	50	1.25	2
9	1.5	0.75	0.5	40	50	1.25	7
10	50	25	0.5	40	50	1.25	246

Table 2: Material properties.

Parameter	Symbol (Unit)	Value
Density	ρ (kg. m ⁻³)	1000
Dynamic yield stress of printing layer (printing yield stress)	$\tau_{printing}$ (Pa)	100 – 300
Dynamic yield stress of printed layer (printed yield stress)	$\tau_{printed}$ (Pa)	100 – 1500
Plastic viscosity	η_P (Pa. s)	0.01 – 33
Critical shear rate	$\dot{\gamma}_c$ (s ⁻¹)	0.05

2.5. Data processing

The geometrical stability of the prints and extrusion pressure are analyzed by importing the fluid fraction and pressure field from the CFD software into MATLAB. The cross-sections of layers are extracted at the middle of the deposited layer, see Figure 2. The relative deformation of the first layer after printing both layers is calculated by:

$$D_B = \frac{BW_2 - BW_1}{BW_1} \times 100\% \quad (11)$$

where BW_1 is the width of the first layer at the end of its deposition and BW_2 is the width of first layer at the end of the second layer deposition. Thus, the D_B value is small for stable prints.

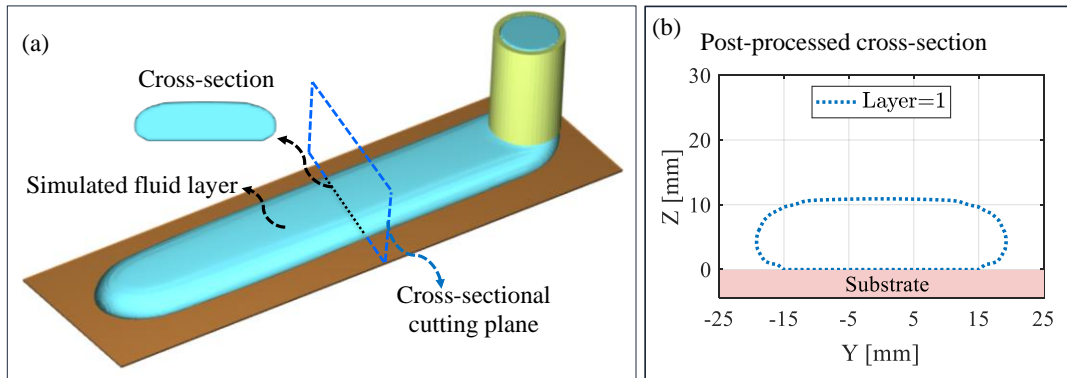


Figure 2: Data processing; (a) Example of cross-sectional cutting plane that is used for evaluation, and (b) Post-processed result.

The extrusion pressure P_E represents both the static and dynamic pressure at the nozzle orifice. It is directly applied to the printing surface by the extruding material [27]. During the deposition of the first layer, the printing surface is the solid substrate, whereas for second layer, it is the already printed first layer. The extrusion pressure acts for a short time since the nozzle moves [29], however, it helps the sideways flow of the depositing material [28]. To calculate the extrusion pressure, the gauge pressure values are directly extracted from the cross-sectional slice taken at the nozzle exit. Then, a surface-average of the gauge pressure values is calculated at six different moments during the travel of the nozzle. Finally, an average of those six gauge pressure is taken to obtain P_E .

3. Results and discussions

This section investigates the influence of various parameters on the stability of the first layer when a new layer is printed above. The parameters include the change in rheological behavior (i.e., the yield stress buildup) and processing conditions (i.e., the extrusion speed, printing speed, layer height, and nozzle diameter). The simulated results are discussed in terms of cross-sections of the deposited layers, the relative deformation of the first layer, and the extrusion pressure during deposition.

3.1 Effect of yield stress buildup

The influence of time-dependent rheological properties, represented by the yield stress buildup, is seen in Figures 3 and 4 for Case ID 1 (see Table 1), where $V = 50$ mm/s, $U = 40$ mm/s, and $\eta_p = 33$ Pa.s. Figure 3 illustrates, as expected, that when printing wet-on-wet larger deformation in the first layer is observed as compared to printing wet-on-semisolid. This is due to the higher effective viscosity in the first layer when printing wet-on-semisolid. Furthermore, it is seen that almost no visible deformation in the first layer is obtained when printing with $\tau_{printed} = 3 \times \tau_{printing}$.

In Figure 4-a, the relative deformation of the first layer is quantified as a function of $\tau_{printed}$, and a non-linear decrease in D_B is observed. By far the largest improvement in geometrical stability is obtained by the initial increase in $\tau_{printed}$, however it is pronounced for $\tau_{printing} = 100$ Pa. This is attributed to the fact that the hydrostatic pressure exceeds $\tau_{printed}$ (≤ 200 Pa), which means in these cases the deformation takes place during the whole print and not only while the extrusion pressure is active on a given point of the print (i.e., when $P_H + P_E > \tau_{printed}$). For all investigated $\tau_{printing}$, the D_B reduces to less than 1% when $\tau_{printed} \geq 600$ Pa, which for many applications would be an acceptable precision. In this regard, one has to remember that having a too high $\tau_{printed}$ (i.e., wet-on-solid printing) can lead to reduced interlayer bonding strength [11]. In addition, it can be adverse for some materials to have a very fast yield stress buildup, e.g., for concrete this can increase the risk of crack formation [37], while thermosets can be more prone to residual stresses and thermal warpage [38].

Figure 4-b presents the extrusion pressure during printing of both layers for different values of $\tau_{printing}$ as a function of $\tau_{printed}$. For any $\tau_{printing}$, the first layer experiences a higher P_E than the second layer because it is printed onto a non-deformable solid substrate. In addition, it is to be noticed that the extrusion pressure experienced by the second layer varies with $\tau_{printed}$. This is due to the effective distance between the printing

surface (first layer) and the nozzle exit increases when the first layer deforms. At higher values of $\tau_{printed}$, the extrusion pressure of the second layer seems to coincide with P_E of first layer, which is a consequence of the first layer increasingly starting to act like a solid substrate.

In Figure 4-b, it is also seen that the extrusion pressure increases with increasing $\tau_{printing}$, which affect the relative deformation to also increase as seen in Figure 4-a when comparing the three values of $\tau_{printing}$ at $\tau_{printed} = 300$ Pa. However, the correlation between increased extrusion pressure and increased relative deformation is not a general trend as seen for the data points when $\tau_{printed} \geq 600$ Pa. This is attributed to the precision of the modelling, and in this regard, it should be noted that the relative deformation is less than 1 %, which in absolute size represents a deformation of ~ 0.4 mm. Considering that the mesh cell size is around 1 mm, it is reasonable to doubt whether the results smaller than 1 % of relative deformation are accurate and reliable enough to draw any significant conclusions from.

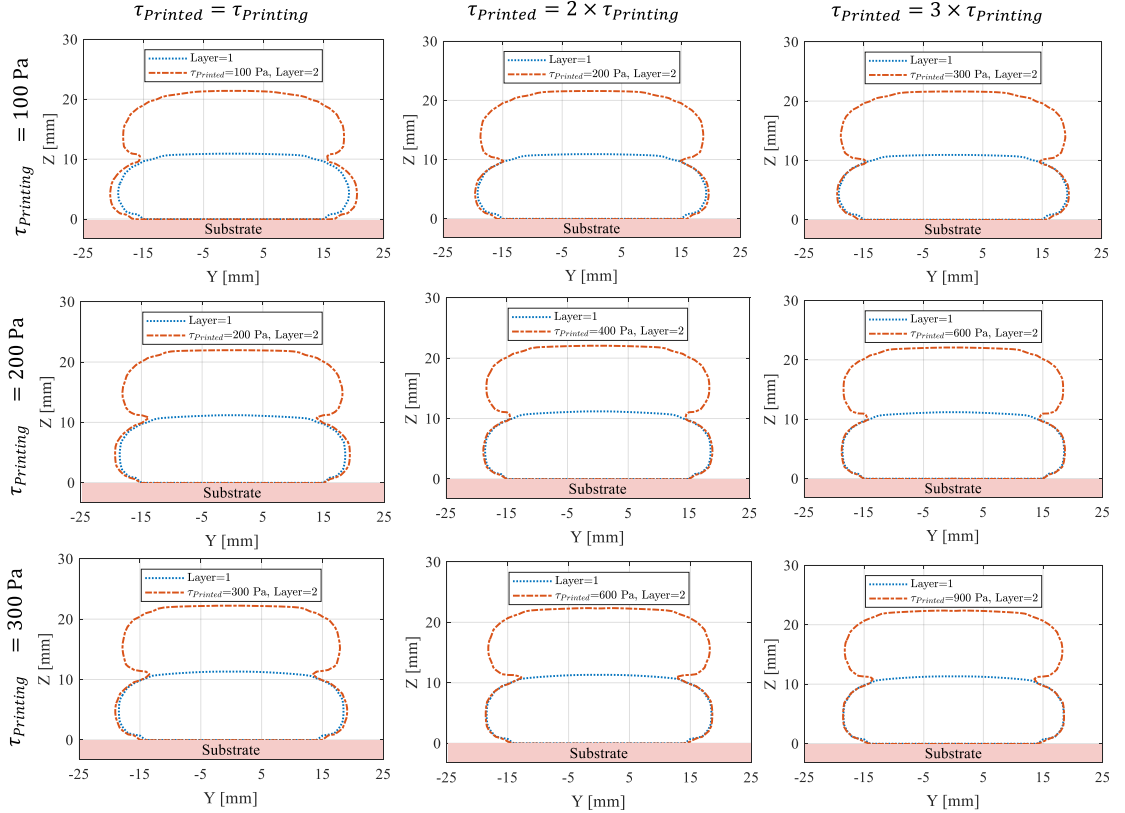


Figure 3: Cross-sections of deposited layers for different printing yield stress $\tau_{printing}$ as well as printed yield stress $\tau_{printed}$.

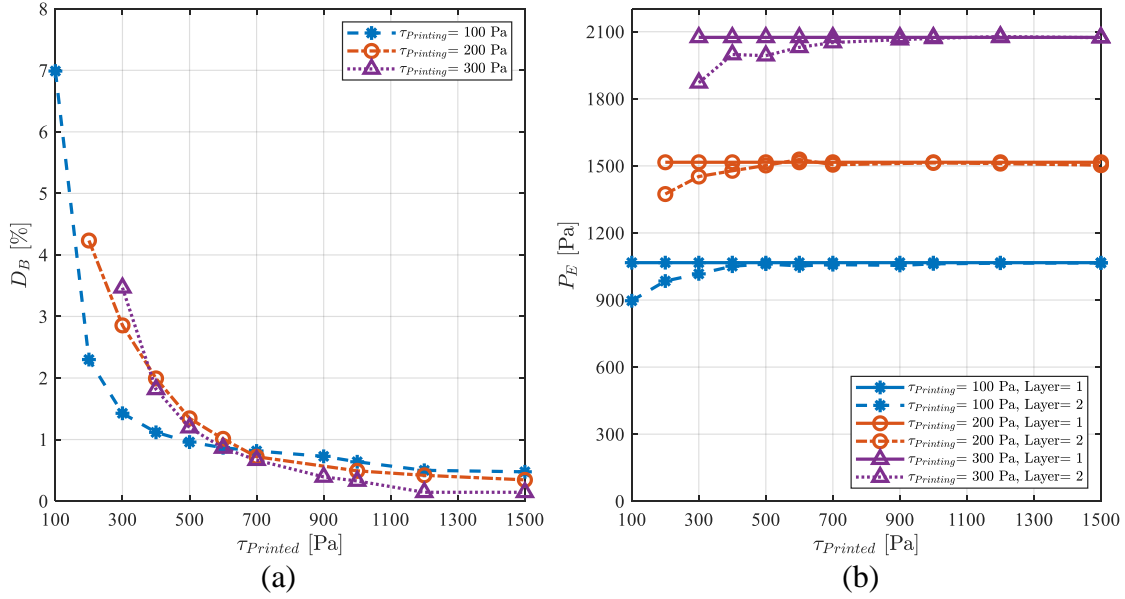


Figure 4: (a) Relative deformation of first layer D_B and (b) extrusion pressure P_E as a function of printed yield stress $\tau_{printed}$, for different printing yield stress $\tau_{printing}$.

3.2 Stability of layers in different processing conditions

This subsection investigates the stability of the first layer when considering variations in both processing conditions and the yield stress buildup of the first layer. Case IDs 1 to 10 (cf. Table 1) are simulated with $\tau_{printing} = 100$ Pa.

Printing speed:

The printing speed's effect on geometrical stability is presented in Figures 5 and 6 for Case ID 1 to 3, where $U = 40$ mm/s and $\eta_p = 33$ Pa.s. Figure 5 illustrates that both less material is deposited per unit length and less deformation is obtained in the first layer when increasing V . The drivers for the latter observation are: 1) less deposited material leads to lower effective layer height, which reduces the hydrostatic pressure and thereby the deformation; 2) higher printing speed leads to lower extrusion pressure (cf. Figure 6-b) and less deformation; 3) higher printing speed means that the extrusion pressure will act for a shorter period of time on the first layer, which will reduce the deformation. These findings are in accordance with the results reported in [29].

Figure 6-a shows a similar non-linear relationship between D_B and $\tau_{printed}$ as is seen in Figure 4-a. For $\tau_{printed} \leq 200$ Pa, printing with a higher speed leads to substantially less deformation, but as the D_B values are relatively high for all printing speeds (and the deformation takes place due to the hydrostatic- and extrusion-pressure), it is unattractive for any application seeking geometrically stable layers. The figure also illustrates that strands printed with lower V converge faster to the smaller values of deformation D_B . This can be attributed to the higher initial deformation in those cases, especially in the range when the hydrostatic pressure is above the yield stress ($\tau_{printed} \leq 200$ Pa). At $\tau_{printed} = 600$ Pa, D_B becomes ~ 1 % for all printing speeds showing that for the investigated time-dependent viscoplastic materials no substantial gain in terms of geometrical stability is obtained by changing V .

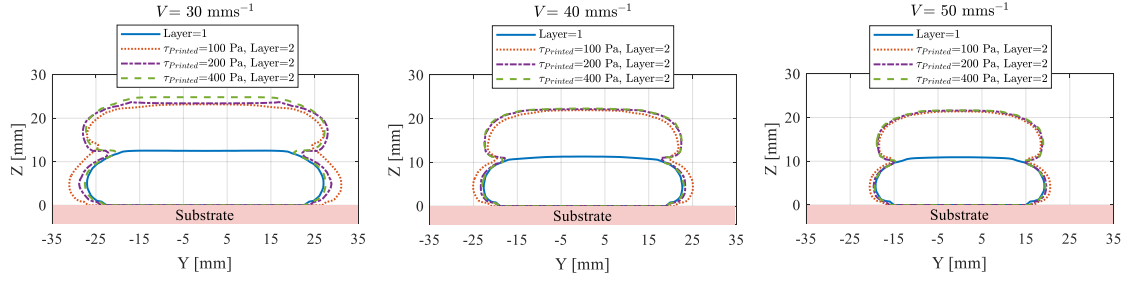


Figure 5: Cross-sections of deposited layers for different printing speed V and printed yield stress $\tau_{printed}$.

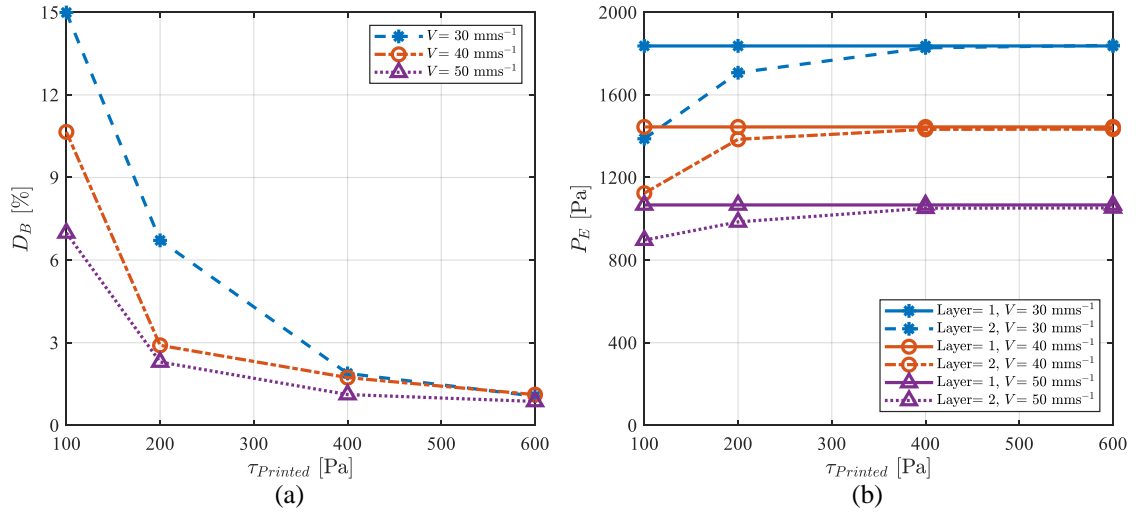


Figure 6: (a) Relative deformation of first layer D_B and (b) extrusion pressure P_E as a function of printed yield stress $\tau_{printed}$, for different printing speed V .

Extrusion speed:

The extrusion speed's effect on geometrical stability is presented in Figures 7 and 8 for Case ID 3 to 5, where $V = 30$ mm/s and $\eta_p = 33$ Pa.s. Figure 7 shows that more material is deposited per unit length when increasing U , which in most cases lead to larger relative deformation in the first layer due to the larger effective layer height and increased extrusion pressure (see Figure 8). The only exemption is for $U = 30$ mm/s at $\tau_{printed} = 200$ Pa, which is attributed to the fact that the results are plotted as a relative deformation and not an absolute deformation. Figure 8-a shows, similarly as for Figures 6-a, that the relative deformation decreases with increasing $\tau_{printed}$. However, the tendency of the combined effect of the extrusion speed and yield stress buildup on the deformation is opposite as compared to the tendency obtained in the relationship between the nozzle speed and yield stress buildup. For higher extrusion speeds, when the nozzle speed remains constant the deformation gets bigger, while for higher nozzle speeds, when the extrusion speed remains the same, the deformation gets smaller. Interestingly, considering that the speed ratio is defined as $S_r = V/U$, the effect of the combined speed ratio and yield stress buildup does not show a monotonic behaviour. This means that in the case, for example, when $S_r = 1.25$ (cf. purple curve in Figure 6-a) and $S_r = 1.5$ (cf. blue curve in Figure 8-a) for $\tau_{printed} = 100$ Pa the deformation is similar (around 7%), while for $\tau_{printed} = 200$ Pa, unexpectedly a smaller deformation is obtained for the lower speed ratio of 1.25. This indicates that both speeds have an independent effect on

the deformation when combined with the yield stress buildup of the already printed strand. The anomalous relative deformation value for $U = 20$ mm/s and $U = 30$ mm/s when $\tau_{printed} = 200$ Pa can be attributed to an unexpectedly high deformation when $U = 20$ mm/s. Such high value can be justified with the rounder shape of the layer, which in depth will be discussed in the next section. Figure 8-a also shows that for the investigated material- and process-parameters stable prints (i.e., $D_B = \sim 1\%$) is first achieved when $\tau_{printed} = 600$ Pa, and at this stage the extrusion pressure has a relatively limited effect on the geometrical stability.

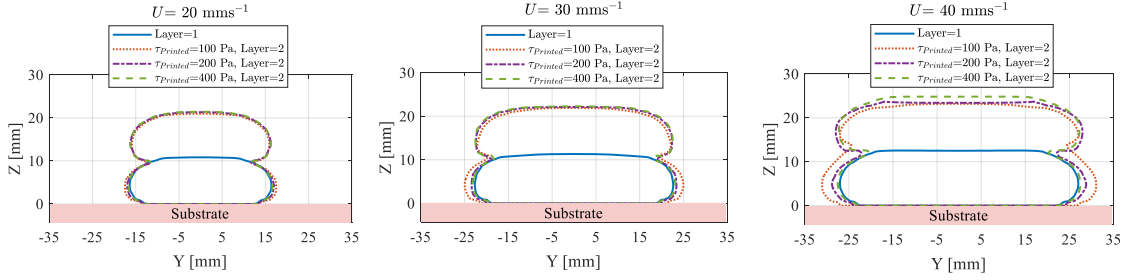


Figure 7: Cross-sections of deposited layers for different extrusion speed U and printed yield stress $\tau_{printed}$.

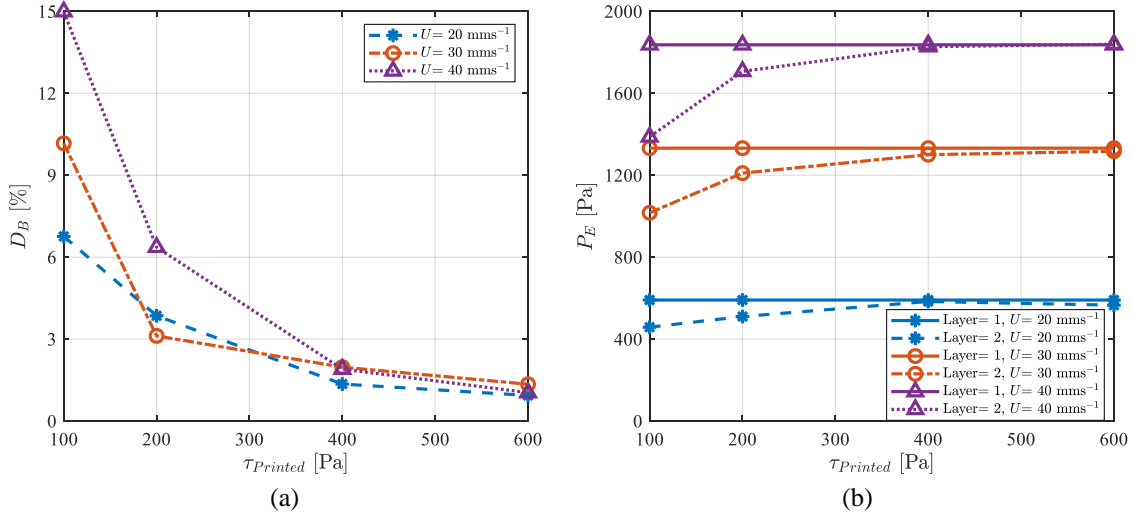


Figure 8: (a) Relative deformation of first layer D_B and (b) extrusion pressure P_E as a function of printed yield stress $\tau_{printed}$, for different extrusion speed U .

Layer height:

The layer height's effect on geometrical stability is presented in Figures 9 and 10. The simulations include $h = 12.5$ mm (Case ID 1), $h = 18.75$ mm (Case ID 6), and $h = 25$ mm (Case ID 7) (cf. Table 1), where $U = 40$ mm/s, $V = 50$ mm/s, and $\eta_p = 33$ Pa.s are constant. Figure 9 shows that by increasing the layer height the cross-section becomes higher and less wide, while the shape of the individual layers get more round. A reduced cross-sectional height leads to a reduced hydrostatic pressure, which results in a smaller relative deformation when $P_H > \tau_{printed}$. At larger $\tau_{printed}$ values, reducing the layer height also leads to lower D_B (cf. Figure 10), which is due to the complex interplay between extrusion pressure, shape of the strands, and the contact area between layers. This complex interplay can be interpreted in the following way: when layers have a

smaller height the extrusion pressure increases (see Fig. 10-b), which promotes larger deformation. However, the applied load of the deposited material is not exerted on the same contact area between layers (see Figure 9) and in the cases with higher h , the contact area is smaller, which as an isolated effect leads to larger deformation. The latter effect is dominating in this case as seen in Figure 10-a.

In Figure 10-a, it is also seen that the relative deformation is less than 1 % for $h = 12.5$ mm and 18.75 mm when $\tau_{printed} = 500$ Pa and 700 Pa, respectively. This illustrates that by decreasing the layer height, the requirements for the yield stress buildup when aiming for geometrically stable layers is not as high, which as previously mentioned can be beneficial for some materials as a slower yield stress buildup can reduce crack formation in concrete as well as reduce the risk of residual stresses and thermal warpage in thermosets. The rounder shape in the case of $h = 25$ mm, creates a situation where the relative deformation is ~ 1.8 % at $\tau_{printed} = 700$ Pa, which can be unsatisfactory for many application that require geometrical precision. As conclusion, rounder shapes with smaller interlayer contact area require a higher yield stress buildup to control the deformation.

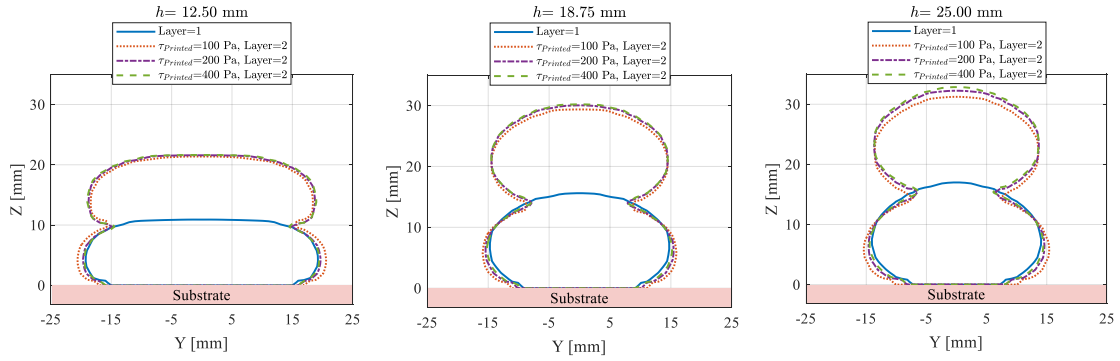


Figure 9: Cross-sections of deposited layers for different layer height h and printed yield stress $\tau_{printed}$.

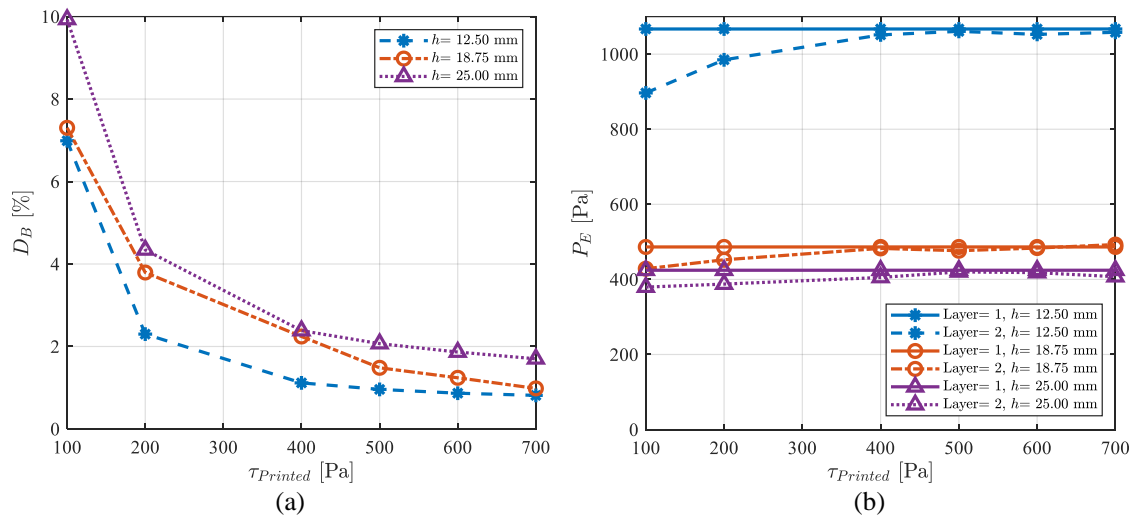


Figure 10: (a) Relative deformation of first layer D_B and (b) extrusion pressure P_E as a function of printed yield stress $\tau_{printed}$, for different layer height h .

Nozzle diameter:

The stability of the first layer is investigated for different nozzle diameters, $D = 0.4$ mm (Case ID 8), $D = 1.5$ mm (Case ID 9), $D = 25$ mm (Case ID 1), and $D = 50$ mm (Case ID 10) (see Table 1), where $U = 40$ mm/s, $V = 50$ mm/s, and $\eta_p = 33$ Pa.s. Figure 11 compares the cross-sections of deposited layers for different printed yield stresses. Note that the axes are non-dimensionalized by the nozzle diameter. The largest relative deformation is seen for the smallest nozzle diameter, while the smallest relative deformation is observed for $D = 25$ mm. This non-monotonic behavior between relative deformation and nozzle diameter was also observed and discussed in [33], although in that study the minimum was found at $D = 1.5$ mm, which is attributed to the difference in printing yield stress applied in the two studies. Later in this section, more information about the effect of materials' rheology on geometrical stability will be addressed for different D . In Figure 12-a, it is seen that for the two smallest nozzle diameters only limited improvement in D_B is obtained by increasing $\tau_{printed}$, which is due to the very high extrusion pressure (Figure 12-b). In fact, it seems that the extrusion pressure increases with a magnitude when the nozzle diameter is reduced with a magnitude for these rheological parameters ($\tau_{printing} = 100$ Pa and $\eta_p = 33$ Pa.s). The high extrusion pressure for $D = 0.4$ mm forces the second layer to penetrate much more into the first layer, as compared to $D = 25$ mm where the second layer flows more horizontal (see Figure 11).

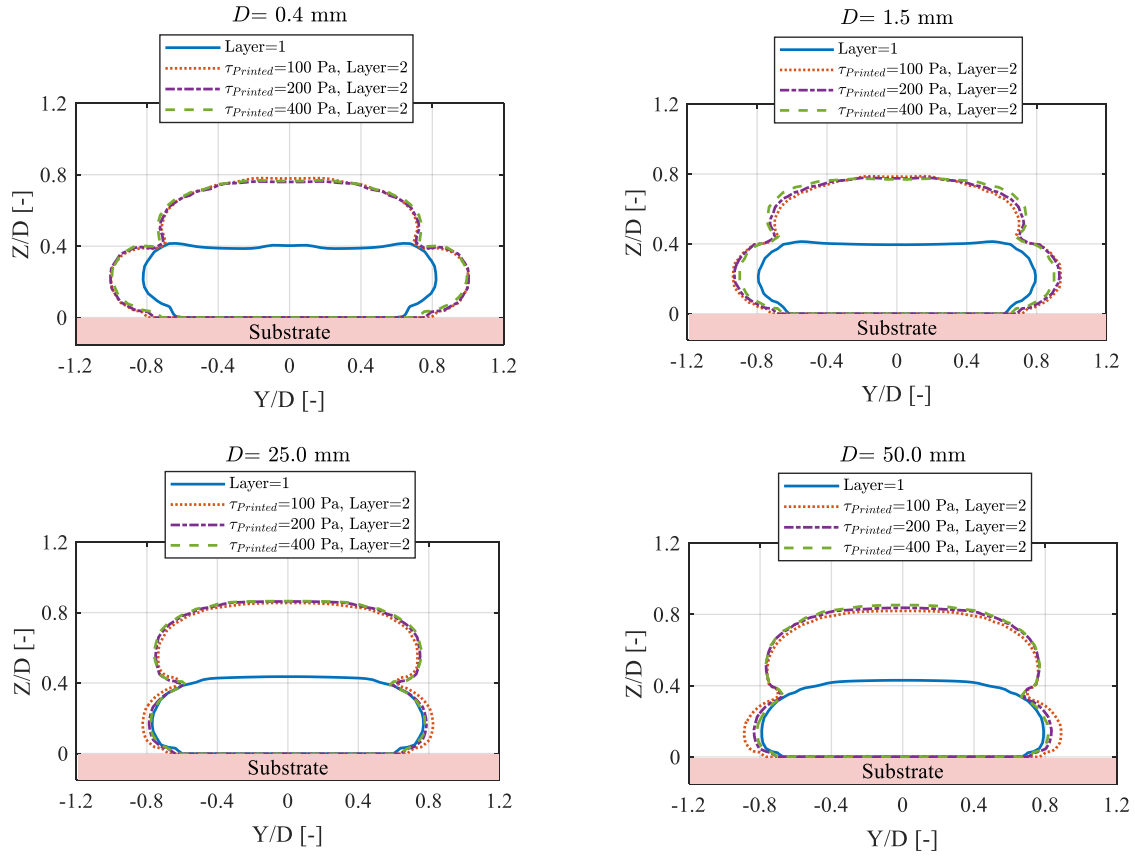


Figure 11: Cross-sections of deposited layers for different nozzle diameter D and printed yield stress $\tau_{printed}$.

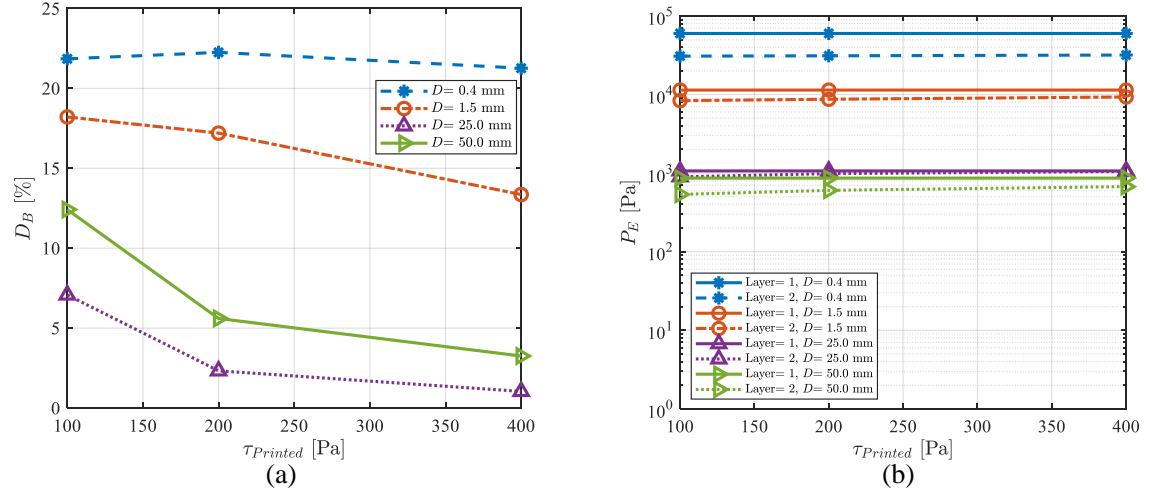


Figure 12: (a) Relative deformation of first layer D_B and (b) extrusion pressure P_E as a function of printed yield stress $\tau_{printed}$, for different nozzle diameter D .

The extrusion pressure is highly dependent on the rheological behavior of the material during printing as seen in Figure 13. For large nozzle diameters, the extrusion pressure can be reduced by decreasing $\tau_{printing}$, but of course it cannot be lower than the hydrostatic pressure, as this would result in unwanted deformations. The plastic viscosity dominates the extrusion pressure for small nozzle diameters. This is due to the fact that most of the material inside the nozzle is yielded when the diameter is so small, and hence the value of the yield stress does not play a significant role. At a plastic viscosity of 0.05 Pa.s, the extrusion pressure is lowest but different in magnitudes for the two smallest nozzle diameters. In addition, the hydrostatic pressure is substantially lower for the small nozzle diameters, which reduces the yield stress buildup requirement. Consequently, geometrically stable prints can be obtained with the two smallest nozzle diameters with a limited yield stress buildup as long as the plastic viscosity is low enough, as seen in Figure 14, which depicts examples of stable printing scenarios (<1% deformation) for all the investigated nozzle diameters.

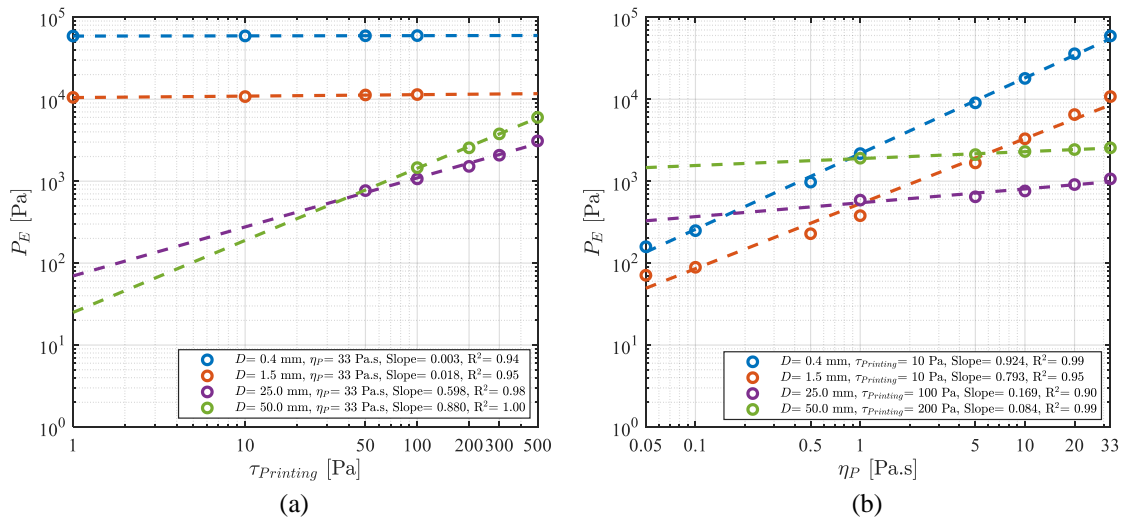


Figure 13: Extrusion pressure P_E for different nozzle diameters D , (a) as a function of the printing yield stress $\tau_{printing}$ and (b) as a function of the plastic viscosity η_P . Note that $U = 40$ mm/s and $V = 50$ mm/s.

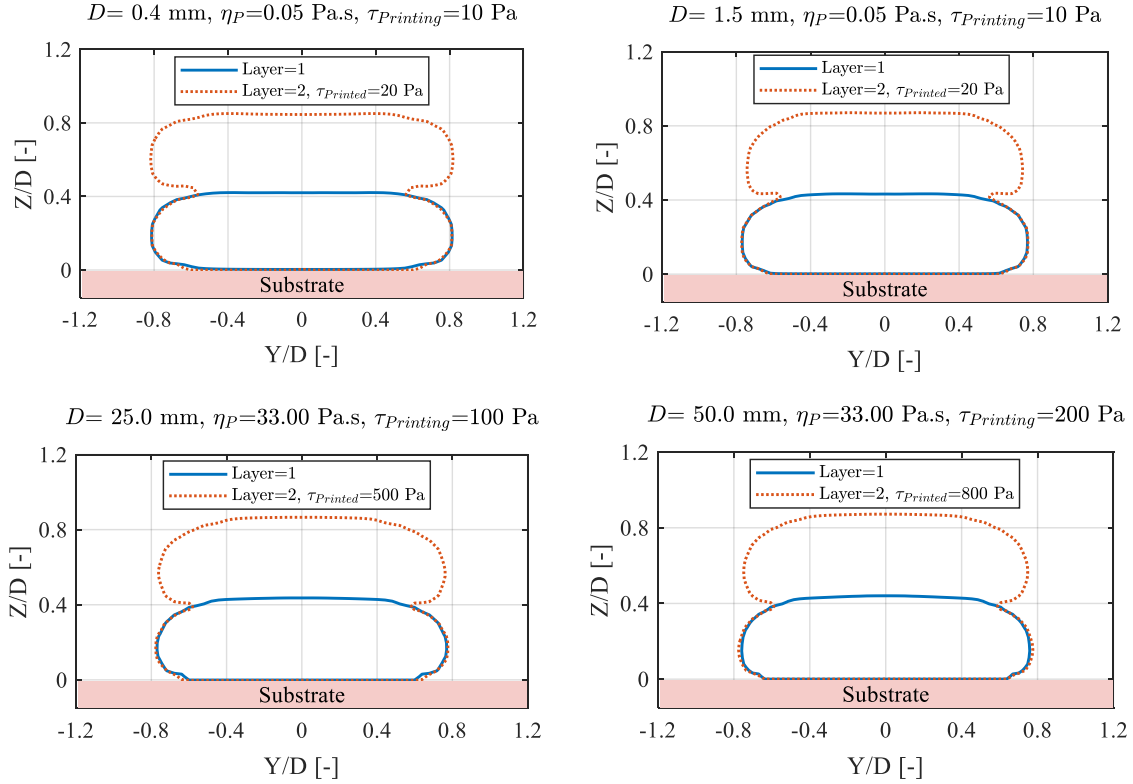


Figure 14: Stable printing scenario for different nozzle diameters D . Note that $U = 40 \text{ mm/s}$, and $V = 50 \text{ mm/s}$.

4. Conclusions

A computational fluid dynamics model was used to predict the stability of deformable layers during MEX-AM of viscoplastic materials. The model applied a scalar approach to alter the viscous behaviour of the fluid within the layers. The fluid was modelled using two Bingham constitutive models with different yield stress to represent the printing of wet material onto a semisolid printed layer. The cross-sections of deposited layers, relative first layer deformation, as well as extrusion pressure were investigated for different yield stress buildup of the already printed material and for different processing conditions. It was found that when the yield stress of the printed layer is higher, the printing of a new layer produces less deformation than what can be seen for no yield stress buildup (i.e., wet-on-wet print). This is of course attributed to the higher effective viscosity of the first layer when printing wet-on-semisolid. It was also found that the increase in yield stress buildup reduced the deformation in a non-linear manner and that the largest improvement was obtained from the initial increase in yield stress.

When increasing the printing speed or reducing the extrusion speed, the study showed that less material is deposited, which leads to less extrusion- and hydrostatic-pressure and thereby less deformation. The combined effect of printing/extrusion speed and yield stress buildup has the largest influence on the speeds that leads to more material deposition, which is ascribed to the larger deformation observed at low yield stresses where the hydrostatic pressure exceeds it. Nevertheless, the yield stress at which geometrically stable prints were observed (i.e., a relative deformation of $\sim 1 \%$) was the same for all investigated printing- and extrusion-speeds indicating the limited gain by varying these two parameters at least when combined with the process parameters applied in this study.

An interesting finding was though that the speed ratio (i.e., the printing speed divided by the extrusion speed) and the yield stress buildup did not show a monotonic behaviour, which indicated that each speed had an independent effect on the deformation. This was attributed to the complex interplay between extrusion pressure, shape of the strands, and the contact area between layers, which especially was pronounced when varying the layer height. By increasing the layer height, a more round-shaped cross-section was formed, which led to a smaller contact area between the layers where the load from the deposited layer was distributed on. Consequently, a larger relative deformation was observed when increasing the layer height even though such increase reduced the extrusion pressure. In regards to time dependent material properties, it meant that stable prints could be obtained at a lower yield stress buildup when printing with a reduced layer height, which can be beneficial for some materials as a too quick material development can result in crack formation and warpage.

For all the investigated nozzle diameters, it was possible to obtain geometrically stable prints when taking into account a time-dependent yield stress. For the small nozzles, the extrusion pressure was substantially reduced by decreasing the plastic viscosity of the material and thus stable prints could be obtained by a limited yield stress buildup. For the larger nozzles, conversely, the extrusion pressure is dominated by the yield stress of the printing material, but this property could not be reduced too much as it needed to be higher than the hydrostatic pressure in order not to result in unwanted deformations. Therefore, larger nozzles required a larger yield stress buildup (both in absolute and relative terms) to produce stable prints.

In future works, the developed CFD model could be extended to include non-isothermal printing as some materials generate heat when solidifying/curing, which can affect the rheological behavior of the material and thereby the stability of the prints.

Acknowledgements

The authors would like to acknowledge the support of the Danish Council for Independent Research (DFF) | Technology and Production Sciences (FTP) (Contract No. 8022-00042B). The author BŠ would like to acknowledge the support of the Innovation Fund Denmark (Grant no. 0223-00084B). Moreover, the authors thank **FLOW-3D®** for their support regarding licenses.

References

- [1] R.A. Buswell, W.R. Leal de Silva, S.Z. Jones, J. Dirrenberger, 3D printing using concrete extrusion: A roadmap for research, *Cem. Concr. Res.* 112 (2018) 37–49. <https://doi.org/10.1016/j.cemconres.2018.05.006>.
- [2] S. Singh, G. Singh, C. Prakash, S. Ramakrishna, Current status and future directions of fused filament fabrication, *J. Manuf. Process.* 55 (2020) 288–306. <https://doi.org/10.1016/j.jmapro.2020.04.049>.
- [3] S.B. Balani, S.H. Ghaffar, M. Chougan, E. Pei, E. Şahin, Processes and materials used for direct writing technologies: A review, *Results Eng.* 11 (2021) 100257. <https://doi.org/10.1016/j.rineng.2021.100257>.
- [4] B. Brenken, E. Barocio, A. Favaloro, V. Kunc, R.B. Pipes, Fused filament fabrication of fiber-reinforced polymers: A review, *Addit. Manuf.* 21 (2018) 1–16. <https://doi.org/10.1016/j.addma.2018.01.002>.

- [5] Z. Chen, Z. Li, J. Li, C. Liu, C. Lao, Y. Fu, C. Liu, Y. Li, P. Wang, Y. He, 3D printing of ceramics: A review, *J. Eur. Ceram. Soc.* 39 (2019) 661–687. <https://doi.org/10.1016/j.jeurceramsoc.2018.11.013>.
- [6] Q. Yuan, D. Zhou, K.H. Khayat, D. Feys, C. Shi, On the measurement of evolution of structural build-up of cement paste with time by static yield stress test vs. small amplitude oscillatory shear test, *Cem. Concr. Res.* 99 (2017) 183–189. <https://doi.org/10.1016/j.cemconres.2017.05.014>.
- [7] A. Bellini, L. Shor, S.I. Guceri, New developments in fused deposition modeling of ceramics, *Rapid Prototyp. J.* 11 (2005) 214–220. <https://doi.org/10.1108/13552540510612901>.
- [8] J. Lindahl, A.A. Hassen, S. Romberg, B. Hedger, P.H. Jr, T. Deluca, W. Morrison, S. Kim, A. Roschli, D. Nuttal, B. Post, L. Love, V. Kunc, Large-scale additive manufacturing with reactive polymers, in: Oak Ridge National Lab. (ORNL), Oak Ridge, TN (United States), 2017: p. 8. <https://www.osti.gov/servlets/purl/1511953>.
- [9] A. du Plessis, A.J. Babafemi, S.C. Paul, B. Panda, J.P. Tran, C. Broeckhoven, Biomimicry for 3D concrete printing: A review and perspective, *Addit. Manuf.* 38 (2021) 101823. <https://doi.org/10.1016/j.addma.2020.101823>.
- [10] J. Jiang, Y. Ma, Path Planning Strategies to Optimize Accuracy, Quality, Build Time and Material Use in Additive Manufacturing: A Review, *Micromachines.* 11 (2020) 633. <https://doi.org/10.3390/mi11070633>.
- [11] T.T. Le, S.A. Austin, S. Lim, R.A. Buswell, R. Law, A.G.F. Gibb, T. Thorpe, Hardened properties of high-performance printing concrete, *Cem. Concr. Res.* 42 (2012) 558–566. <https://doi.org/10.1016/j.cemconres.2011.12.003>.
- [12] R.J.M. Wolfs, T.A.M. Salet, N. Roussel, Filament geometry control in extrusion-based additive manufacturing of concrete: The good, the bad and the ugly, *Cem. Concr. Res.* 150 (2021) 106615. <https://doi.org/10.1016/j.cemconres.2021.106615>.
- [13] N. Ashrafi, S. Nazarian, N.A. Meisel, J.P. Duarte, Experimental calibration and compensation for the continuous effect of time, number of layers and volume of material on shape deformation in small-scale additive manufacturing of concrete, *Addit. Manuf.* 47 (2021) 102228. <https://doi.org/10.1016/j.addma.2021.102228>.
- [14] M.K. Mohan, A.V. Rahul, G. De Schutter, K. Van Tittelboom, Extrusion-based concrete 3D printing from a material perspective: A state-of-the-art review, *Cem. Concr. Compos.* 115 (2021) 103855. <https://doi.org/10.1016/j.cemconcomp.2020.103855>.
- [15] F. Bos, R. Wolfs, Z. Ahmed, T. Salet, Additive manufacturing of concrete in construction: potentials and challenges of 3D concrete printing, *Virtual Phys. Prototyp.* 11 (2016) 209–225. <https://doi.org/10.1080/17452759.2016.1209867>.
- [16] P. Wu, J. Wang, X. Wang, A critical review of the use of 3-D printing in the construction industry, *Autom. Constr.* 68 (2016) 21–31. <https://doi.org/10.1016/j.autcon.2016.04.005>.
- [17] T.D. Ngo, A. Kashani, G. Imbalzano, K.T.Q. Nguyen, D. Hui, Additive manufacturing (3D printing): A review of materials, methods, applications and challenges, *Compos. Part B Eng.* 143 (2018) 172–196. <https://doi.org/10.1016/j.compositesb.2018.02.012>.
- [18] N. Ashrafi, Experimental prediction of material deformation in large-scale additive manufacturing of concrete, *Addit. Manuf.* 37 (2021) 101656. <https://doi.org/10.1016/j.addma.2020.101656>.
- [19] M.P. Serdeczny, R. Comminal, D.B. Pedersen, J. Spangenberg, Experimental validation of a numerical model for the strand shape in material extrusion additive

- manufacturing, *Addit. Manuf.* 24 (2018) 145–153. <https://doi.org/10.1016/j.addma.2018.09.022>.
- [20] R. Comminal, W.R.L. da Silva, T.J. Andersen, H. Stang, J. Spangenberg, Influence of Processing Parameters on the Layer Geometry in 3D Concrete Printing: Experiments and Modelling, in: F.P. Bos, S.S. Lucas, R.J.M. Wolfs, T.A.M. Salet (Eds.), *Second RILEM Int. Conf. Concr. Digit. Fabr.*, Springer International Publishing, Cham, 2020: pp. 852–862. https://doi.org/10.1007/978-3-030-49916-7_83.
- [21] H. Xia, J. Lu, G. Tryggvason, A numerical study of the effect of viscoelastic stresses in fused filament fabrication, *Comput. Methods Appl. Mech. Eng.* 346 (2019) 242–259. <https://doi.org/10.1016/j.cma.2018.11.031>.
- [22] R. Comminal, M.P. Serdeczny, D.B. Pedersen, J. Spangenberg, Motion planning and numerical simulation of material deposition at corners in extrusion additive manufacturing, *Addit. Manuf.* 29 (2019) 100753. <https://doi.org/10.1016/j.addma.2019.06.005>.
- [23] R. Comminal, M.P. Serdeczny, D.B. Pedersen, J. Spangenberg, Numerical Modeling of the Material Deposition and Contouring Precision in Fused Deposition Modeling, in: *Proc. Annu. Int. Solid Free. Fabr. Symp.*, 2018: pp. 1855–1864.
- [24] M.T. Mollah, A. Moetazedian, A. Gleadall, J. Yan, W.E. Alphonso, R. Comminal, B. Šeta, T. Lock, J. Spangenberg, Investigation on corner precision at different corner angles in material extrusion additive manufacturing: An experimental and computational fluid dynamics analysis, in: *Solid Free. Fabr. Symp. 2022 33rd Annu. Meet.*, The University of Texas at Austin, 2022: pp. 872–881.
- [25] M.P. Serdeczny, R. Comminal, D.B. Pedersen, J. Spangenberg, Numerical prediction of the porosity of parts fabricated with fused deposition modeling, in: *Proc. Annu. Int. Solid Free. Fabr. Symp.*, Laboratory for Freeform Fabrication, n.d.: pp. 1849–1854.
- [26] M.P. Serdeczny, R. Comminal, D.B. Pedersen, J. Spangenberg, Numerical simulations of the mesostructure formation in material extrusion additive manufacturing, *Addit. Manuf.* 28 (2019) 419–429. <https://doi.org/10.1016/j.addma.2019.05.024>.
- [27] R. Comminal, M.P. Serdeczny, D.B. Pedersen, J. Spangenberg, Numerical modeling of the strand deposition flow in extrusion-based additive manufacturing, *Addit. Manuf.* 20 (2018) 68–76. <https://doi.org/10.1016/j.addma.2017.12.013>.
- [28] R. Comminal, W.R. Leal da Silva, T.J. Andersen, H. Stang, J. Spangenberg, Modelling of 3D concrete printing based on computational fluid dynamics, *Cem. Concr. Res.* 138 (2020) 106256. <https://doi.org/10.1016/j.cemconres.2020.106256>.
- [29] M.T. Mollah, R. Comminal, M.P. Serdeczny, D.B. Pedersen, J. Spangenberg, Stability and deformations of deposited layers in material extrusion additive manufacturing, *Addit. Manuf.* (2021) 102193. <https://doi.org/10.1016/j.addma.2021.102193>.
- [30] J. Spangenberg, W.R. Leal da Silva, R. Comminal, M.T. Mollah, T.J. Andersen, H. Stang, Numerical simulation of multi-layer 3D concrete printing, *RILEM Tech. Lett.* 6 (2021) 119–123. <https://doi.org/10.21809/rilemtechlett.2021.142>.
- [31] E.C. Bingham, *An investigation of the laws of plastic flow*, US Government Printing Office, 1917.
- [32] E.J. O'Donovan, R.I. Tanner, Numerical study of the Bingham squeeze film problem, *J. Non-Newton. Fluid Mech.* 15 (1984) 75–83. [https://doi.org/10.1016/0377-0257\(84\)80029-4](https://doi.org/10.1016/0377-0257(84)80029-4).

- [33] FLOW-3D® Version 12.0 [Computer software], (2019). <https://www.flow3d.com> (accessed May 10, 2022).
- [34] Modeling Capabilities- Immersed Boundary Method | FLOW-3D | Solving The World's Toughest CFD Problems, FLOW Sci. (n.d.). <https://www.flow3d.com/modeling-capabilities/immersed-boundary-method/> (accessed August 21, 2021).
- [35] C.W. Hirt, B.D. Nichols, Volume of fluid (VOF) method for the dynamics of free boundaries, *J. Comput. Phys.* 39 (1981) 201–225. [https://doi.org/10.1016/0021-9991\(81\)90145-5](https://doi.org/10.1016/0021-9991(81)90145-5).
- [36] R. Comminal, J. Spangenberg, Three-dimensional cellwise conservative unsplit geometric VOF schemes, *J. Comput. Phys.* 442 (2021) 110479. <https://doi.org/10.1016/j.jcp.2021.110479>.
- [37] S. Markin, V. Mechtcherine, Measuring Plastic Shrinkage and Related Cracking of 3D Printed Concretes, in: R. Buswell, A. Blanco, S. Cavalaro, P. Kinnell (Eds.), *Third RILEM Int. Conf. Concr. Digit. Fabr.*, Springer International Publishing, Cham, 2022: pp. 446–452. https://doi.org/10.1007/978-3-031-06116-5_66.
- [38] P. Sreejith, K. Kannan, K. Rajagopal, A thermodynamic framework for additive manufacturing, using amorphous polymers, capable of predicting residual stress, warpage and shrinkage, *Int. J. Eng. Sci.* 159 (2021) 103412. <https://doi.org/10.1016/j.ijengsci.2020.103412>.

**Publication [A.6]: Integrating reinforcement with 3D Concrete Printing:
Experiments and numerical modelling**

Jon Spangenberg*, Wilson Ricardo Leal da Silva§, Md. Tusher Mollah*,
Raphaël Comminal*, Thomas Juul Andersen§, Henrik Stang†

*Department of Mechanical Engineering, Technical University of Denmark, Denmark.

§Danish Technological Institute, Denmark.

†Department of Civil Engineering, Technical University of Denmark, Denmark.

Published in:

Third RILEM International Conference on Concrete and Digital Fabrication, Vol. 37,
pp. 379-384, 2022. https://doi.org/10.1007/978-3-031-06116-5_56.

Reproduced with permission from Springer.

The layout has been revised.

Abstract

3D Concrete Printing (3DCP) is a technology that recently has attracted the attention of both academia and industry. The technology offers an increased design flexibility and has been used at various scales, e.g. from furniture to bridges and houses. One of the current challenges in 3DCP is to produce load bearing structures in a single process, i.e. reinforced elements as part of 3DCP process. This is because the integration of vertical reinforcement during the printing process is not trivial. Although few reinforcement methods have been studied, a robust and efficient 3DCP reinforcement solution is yet to be coined. To support these studies in finding a reinforcement solution fit for 3DCP, while limiting experimental efforts, we offer a computational fluid dynamics (CFD) model that simulate concrete flow around rebars. The numerical model applies 1) an elasto-viscoplastic constitutive law to mimic the flow behavior of the concrete and 2) the volume of fluid method to track the free surface of the concrete. To validate the proposed model, 3DCP experiments are carried out by printing around horizontal and vertical rebars. The rheological behavior of the concrete is characterized on a rheometer using a vane-in-cup measuring system, and such data is included in the CFD model. The experimental and numerical results agree relatively well; providing a new venue for identifying printing strategies that ensures a good bonding between concrete and reinforcement.

Keywords: 3D Concrete Printing, Reinforcement, Computational Fluid Dynamics, Rheology.

1. Introduction

Extrusion-based 3D Concrete Printing (3DCP) is a very promising digital construction technology that offers geometrical one-off structures in a time and cost-efficient manner. The 3DCP process is typically carried out by a gantry system or a robot arm, which guides a print head that deposits material along a toolpath to create a concrete structure in a layer-by-layer manner [1]. At present, one of the greatest challenges for this digital construction technology is to integrate printed layers and reinforcement. Therefore, researchers around the world have intensified their pursuit in finding robust methodologies to produce load-bearing 3DCP structures.

Examples of 3DCP reinforcement strategies that have been proposed include: a) penetrating reinforcing bars through printed layers [2] and b) the use of fiber reinforcement [3], to mention a couple. For a comprehensive review on 3DCP reinforcement strategies and classification thereof, refer to [4].

As in any research endeavor, the concepts described above require an extensive number of tests to be validated, yielding limitations to the number of reinforcement concepts that can be tested in practice. Therefore, numerical models have the potential to be a significant driver for 3DCP development [5] as they can reduce the experimental campaign necessary to explore a phenomenon as well as provide a mechanistic understanding of the process [6]. The latter was exemplified by Wolfs et al. [7], who used finite element method (FEM) simulations to investigate the early-age mechanical behavior of 3DCP. In addition, Computational Fluid Dynamics (CFD) models have been used to study the geometrical conformity of single- and multi-layer 3DCP deposition [8, 9].

These abovementioned models, however, have not been used to simulate the interactions between fresh printed layers and reinforcement rebars. To overcome that, this paper presents the first study where a CFD model is used to simulate 3DCP around horizontal and vertical rebars. The objective of the study is to investigate the CFD model's ability to predict the bonding behavior between concrete and reinforcement. The numerical simulations are compared to 3DCP experiments carried out with mortars.

2. Methodology

2.1. Materials and experiment

The 3DCP around rebars was done with a cement-based mortar made of CEM I 52.5 R-SR 5 (EA), fine sand (< 0.5 mm), limestone filler, admixtures, and water. The water: binder ratio was set at 0.39, and fine aggregates content accounts for 45% of the total dry mass. The admixtures dosage (by weight of cement) was set at 0.1% high-range water-reducing agent, a 0.5% hydration retarder, and 0.1% viscosity-modifying agent. The use of retarders enabled an open time of 2 hours, i.e. the rheology of the mortar can be considered time-independent during the printing process (which took 15 minutes).

The mortar was prepared in an Eirich Intensive Mixer Type R08W. An Anton Paar rheometer MCR 502 was used to characterize the rheology of the mortar, which had a density of $\rho = 2100$ kg/m³. Both the rotational and oscillatory tests were carried out using a vane-in-cup measuring device. The rotational rheometric tests, with a ramp-down controlled shear rate (CSR), determined the plastic viscosity $\eta_p = 7.5$ Pa and yield stress $\tau_y = 630$ Pa.s. In addition, the oscillatory test showed that the unyielded mortar had a $G' = 200$ kPa within the linear viscoelastic (LVE) region. Thus, the mortar's rheology can be modelled with an elasto-visco-plastic (EVP) material behavior.

The 3DCP experimental setup is shown in Figure 1. It included a 6-axis industrial robot with a custom-designed round nozzle and a progressive cavity pump equipped with a hopper and a long steel-wire rubber hose (refer to [8, 9] for details). The built platform included a 25mm thick plywood plate above which a rebar of diameter 8 mm was placed horizontally at the height of 14 mm rebar height from the base plate and held in place by vertical rebars. The setup was used to print a structure of four successive layers around the rebars. Details on the printing toolpath are illustrated in Figure 2.

The extrusion Ø20mm nozzle was placed at a height of 10 mm (nozzle height) above the built plate. For subsequent layers, the nozzle height was automatically increased by the 10 mm (i.e. the nominal height of a layer equals 10 mm). The extrusion speed was set at 0.91 dm³/min and a nozzle travel speed was set at 35 mm/s. After the printed layers hardened, cross-sections were collected to analyze the interface between concrete and rebars. The cross-section for the rebar regions were obtained by slicing the printed element and scanning the cross-sectional area. To avoid damaging the printed samples during cutting, the samples were impregnated with epoxy resin in a vacuum chamber.

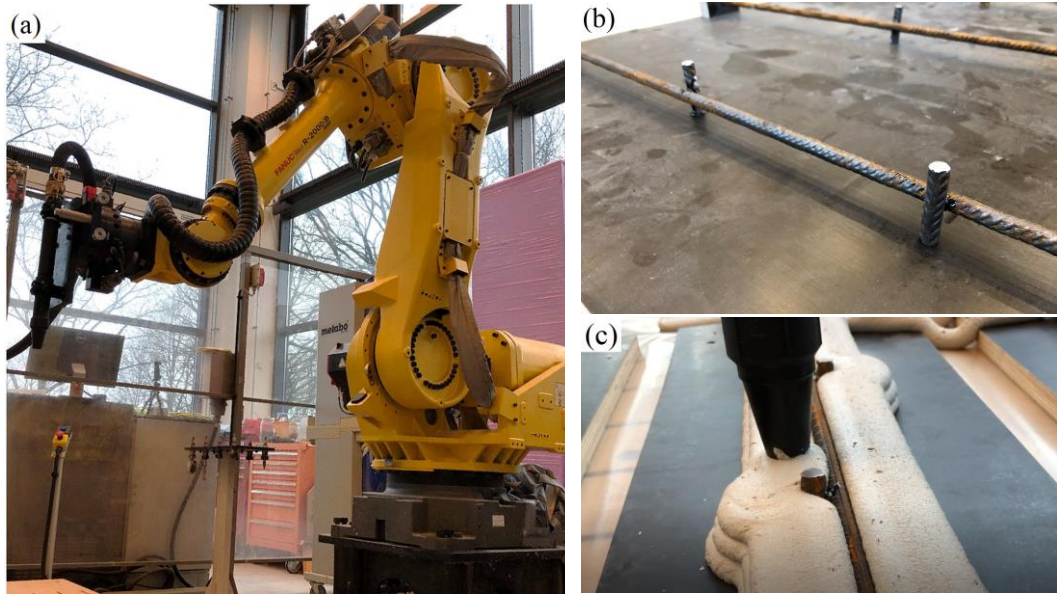


Figure 1. 3DCP Experiment: (a) setup of 6-axis robot [8]; (b) built platform with placed rebars; (c) example of printing at the middle of third layer.

2.2. Computational fluid dynamics model

The flow of the cementitious mortar was assumed incompressible and isothermal, and thus governed by the mass and momentum conservation equations. These were solved numerically using the commercial software FLOW-3D® v. 12.0. The software has previously been used for prediction of cementitious material flow, e.g. [10, 11]. The rheological behavior of the mortar was modelled as an EVP fluid, where the visco-plastic response followed a Bingham model with the plastic viscosity and yield stress that were determined experimentally as discussed in the previous section. The unyielded material was modelled with an elastic response that followed Hooke's law. The elastic shear modulus was set at 100 kPa, which is lower than the 200 kPa determined by rheological measurements. This reduction was applied to ease the numerical convergence, without substantially altering the numerical results. This assumption seemed reasonable since no substantial difference was found in the results when applying an elastic shear modulus of 50 and 100 kPa. The equations that describe the EVP fluid can be found in [8], while the free surface of the mortar was modelled with the volume-of-fluid method.

To simulate the 3DCP experiments, two separate models were developed: deposition around the horizontal rebar (Model 1) and cross-shaped rebars (Model 2), cf. Figure 2. Both models include an extrusion nozzle, build plate, and computational domain (with size of 170 x 112 x 80 mm) in which the mortar was printed. The toolpath of the extrusion nozzle for the two models are also shown in Figure 2. The top plane of the domain was an inlet boundary that holds an artificial solid component to prevent the flow outside the boundaries of the nozzle orifice. A no-slip boundary condition was imposed on the substrate and the domain was meshed with a Cartesian grid. The CFD model simulates four successive layers of length 125 mm around the horizontal rebar of length 50 mm and vertical rebar of height 40 mm (only for Model 2). The computational time of the simulations was around 18 days using 20 cores.

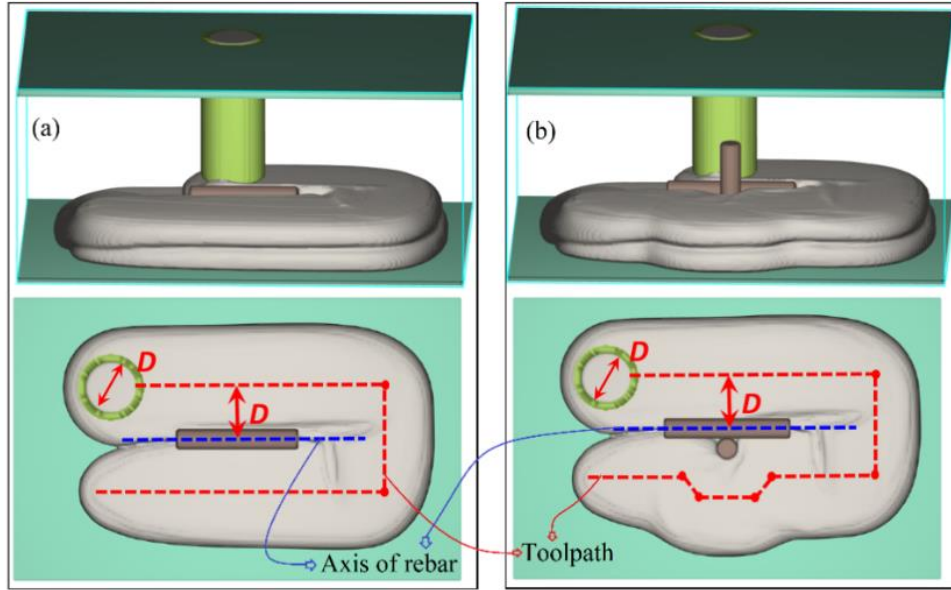


Figure 2. Computational domain and toolpath. (a) Model 1: Deposition around horizontal rebar; (b) Model 2: Deposition around cross-shaped rebars.

3. Results and discussions

The cross-sectional shape of the deposited layers around rebars in experiments and simulations are presented in Figures 3a-d. The experimental results for the horizontal rebar in Figure 3a illustrate that air voids are present both below and above the rebar as well as between layers 3 and 4. The latter is likely formed due to the deformation of previously printed layers, which increased the gap distance between the nozzle and layer 3, reducing the width of each independent strand in layer 4. A similar trend was observed in meso-structures produced with thermoplastic additive manufacturing [12]. The air voids around the horizontal rebar in Figure 3a are smaller than the one between layers 3 and 4. This was attributed to the rebar occupying some of the space in between layer 2 and 3, which forced the mortar to be squeezed around the rebar. Another contributing factor was the subsequent deformation of the layers when printing layer 4. In Figure 3b, the mortar is printed around the cross-shaped rebars, in this scenario a greater number of air voids are observed. This is likely due to the vertical rebar restricting the mortar that was printed on either side of the reinforcement to merge. Especially, this scenario underlines the challenges related to integrating rebars with 3DCP.

Figure 3c,d presents the cross-sectional shapes of the simulations for both Model 1 and 2; showcasing that both models predict with high accuracy the location of air voids found in the printing experiments. The primary discrepancy between simulation and experiments was the width of the strands in the bottom layer (Figure 3e,f). This might be attributed to slight differences in the rheological behavior and processing conditions (i.e. slight deviations between the distance of the nozzle to the rebars and base plate). Despite of that, the numerical results clearly illustrate the potential of the CFD model predictions. As such, the model can be exploited to find printing strategies that minimize or fully remove air voids in reinforced concrete structures produced with 3DCP.

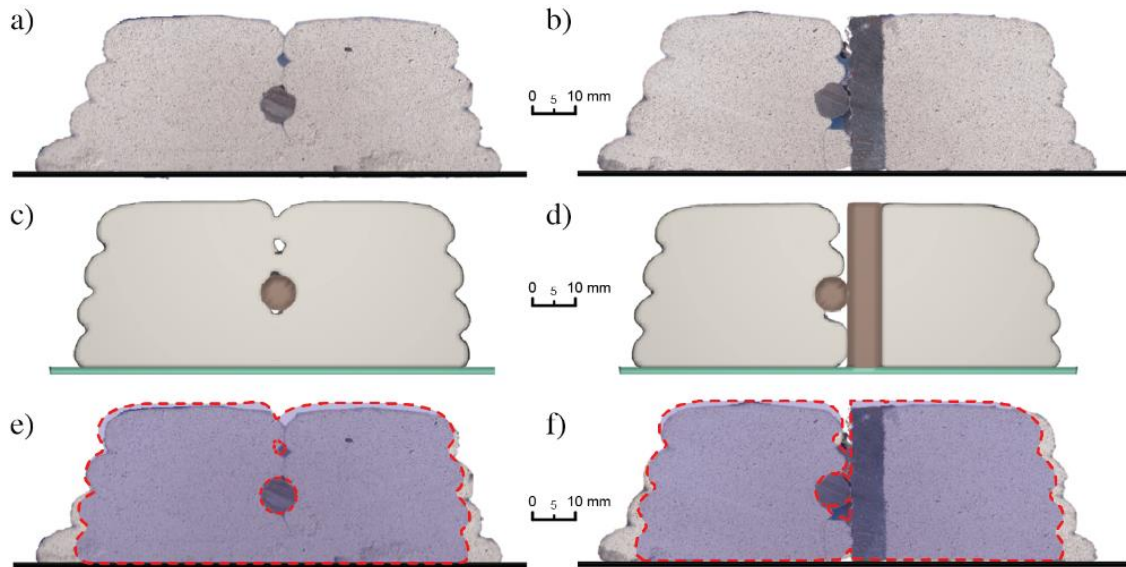


Fig. 3. Cross-sections of printed layers: (a,b) 3DCP experiment; (c,d) horizontal rebar (Model 1) and cross-shape rebars (Model 2); (e,f) overlay of simulation and printing results.

4. Conclusion

This paper presents experimental and numerical work on 3DCP around horizontal and vertical rebars. The printing results show that the printing strategy entrapped air voids both below and above the horizontal rebar as well as on the side of the vertical reinforcement. This highlights the non-trivial task of getting sufficient reinforcement encapsulation when applying 3DCP. A CFD model was developed to simulate the printing process, and a comparison between experimental and numerical results show that the model could predict the formation of voids around the rebars with great accuracy. Altogether, our research underlines the potential of using digital tools such as CFD modelling to digitally test and evaluate the outcome of printing strategies addressing reinforcement solutions for 3DCP applications.

Acknowledgement

The authors would like to acknowledge the support of the Innovation Fund Denmark (Grant no. 8055-00030B: Next Generation of 3D-printed Concrete Structures), the Danish Council for Independent Research (DFF) | Technology and Production Sciences (FTP) (Contract no. 8022-00042B), COWIfonden, and FLOW-3D® license support.

References

- [1] R.A. Buswell, W.R. Leal da Silva, S.Z. Jones, J. Dirrenberger. 3D printing using concrete extrusion: a roadmap for research. *Cem. Concr. Res.* 112: 37–49 (2018).
- [2] T. Marchment, J. Sanjayan, Bond properties of reinforcing bar penetrations in 3D concrete printing, *Autom. in Constr.* 120: 103394 (2020).
- [3] T. Ding, J. Xiao, S. Zou, J. Yu, Flexural properties of 3D printed fibre-reinforced concrete with recycled sand, *Con. Build. Mat.* 288: 123077 (2021).
- [4] V. Mechtcherine, R. Buswell, H. Kloft, F.P. Bos, N. Hack, R. Wolfs, J. Sanjayan, B. Nematollahi, E. Ivaniuk, T. Neef, Integrating reinforcement in digital fabrication with

- concrete: A review and classification framework, *Cem. and Concr. Comp.* 119: 103964 (2021).
- [5] N. Roussel, J. Spangenberg, J. Wallevik, R. Wolfs, Numerical simulations of concrete processing: from standard formative casting to additive manufacturing, *Cem. Concr. Res* 135:106075 (2020).
- [6] V. Mechtcherine, F.P. Bos, A. Perrot, W.R. Leal da Silva, V.N. Nerella, S. Fataei, R.J.M. Wolfs, M. Sonebi, N. Roussel, Extrusion-based additive manufacturing with cement-based materials – production steps, processes, and their underlying physics: a review, *Cem. Concr. Res.* 132 (2020):106037.
- [7] R.J.M. Wolfs, F.P. Bos, T.A.M. Salet, Early age mechanical behaviour of 3D printed concrete: numerical modelling and experimental testing, *Cem. Concr. Res* 106:103–116 (2018).
- [8] R. Comminal, W.R. Leal da Silva, T.J. Andersen, H. Stang, J. Spangenberg, Modelling of 3D concrete printing based on computational fluid dynamics, *Cem. and Concr. Res.* 138 (2020):106256.
- [9] J. Spangenberg, W.R. Leal da Silva, R. Comminal, M.T. Mollah, T.J. Andersen, H. Stang, Numerical simulation of multi-layer 3D concrete printing, *RILEM Lett.* 6:119–123 (2021).
- [10] J. Spangenberg, N. Roussel, J.H. Hattel, J. Thorborg, M.R. Geiker, H. Stang, J. Skocek, Prediction of the Impact of Flow-Induced Inhomogeneities in Self-Compacting Concrete (SCC), in: K.H. Khayat, D. Feys (Eds.), *Design, Production and Placement of Self-Consolidating Concrete*, Springer Netherlands, Dordrecht, pp. 209–215 (2010).
- [11] S. Jacobsen, R. Cepuritis, Y. Peng, M. R. Geiker, J. Spangenberg, Visualizing and simulating flow conditions in concrete form filling using pigments, *Con. Build. Mat* 49: 328-342 (2013).
- [12] M. P. Serdeczny, R. Comminal, D. B. Pedersen, J. Spangenberg, Numerical prediction of the porosity of parts fabricated with fused deposition modeling, In *Proceedings of the 29th Annual Int. Solid Freeform Fabrication Symposium*, Austin, TX, USA pp. 13-15 (2018).

Publication [A.7]: Integration of reinforcement bars in 3D concrete printing

Md. Tusher Mollah*, Raphaël Comminal*§, Wilson Ricardo Leal da Silva†, Berin Šeta*, Jon Spangenberg*

*Department of Civil and Mechanical Engineering, Technical University of Denmark, Denmark.

§ Flow Science, Inc., USA.

†Danish Technological Institute, Denmark.

Submitted to:
Cement and Concrete Research, ELSEVIER.

The layout has been revised.

Abstracts

A challenge for 3D Concrete Printing is to incorporate reinforcement bars without compromising the concrete-rebar bonding. In this paper, a Computational Fluid Dynamics (CFD) model is used to analyze the deposition of concrete around pre-installed rebars. The concrete is modelled with a yield-stress dependent elasto-viscoplastic constitutive model. The simulated cross-sections of the deposited layers are compared with experiments under different configurations and rebar sizes, and found capable of capturing the air void formation with high accuracy. This proves model robustness and provides a tool for running digital experiments prior to full-scale tests. Additionally, the model is employed to conduct a parametric study under three different rebar-configurations: i) no-rebar; ii) horizontal rebar; and iii) cross-shaped (horizontal and vertical) rebars. The results illustrate that air voids can be eliminated in all investigated cases by changing the toolpath, process parameters, and rebar joint geometry, which emphasizes the great potential of the digital model.

Keywords: 3D Concrete Printing (3DCP), Reinforcement bar (rebar), Computational Fluid Dynamics (CFD), Multilayer deposition, Air voids.

1. Introduction

3D Concrete Printing (3DCP) [1] is an extrusion-based automated construction process that belongs to Digital Fabrication with Concrete (DFC) [2]. The 3DCP offers high-quality built-structures with customizable structural design in a cost- and time-efficient manner [3,4]. Structures in 3DCP are fabricated in a layer-by-layer approach, where a concrete extrusion nozzle is controlled by a robotic arm, cylindrical robot, gantry system, or delta system [5–9]. Despite the enormous potential of 3DCP, one of its crucial limitations is the integration of reinforcement for the production of load-bearing structures.

Most structural applications require the use of reinforcement to withstand tensile forces and introduce structural ductility. However, the introduction of reinforcement with 3DCP has never been an easy task, and difficulties were recognized at early stages of the technology [3] and various design solutions have been tested in practice to either circumvent the need for reinforcement or integrate reinforcement after the concrete is printed [9]. As a result, several reinforcement techniques have been proposed, such as bar reinforcement [10], micro-cable reinforcement [11,12], fiber reinforcement into the cementitious material [13,14], steel reinforcement using robotic arc welding [15,16], and in-process mesh reinforcement [17]. For comprehensive details on the reinforcement strategies, refer to [18]. Nevertheless, these reinforcement strategies are still rudimentary in many instances.

This study focuses on bar reinforcement methods, where rebars are integrated with freshly deposited cementitious material. A few approaches can be found in the literature, for example, penetration of vertical bars through multiple printed layers [19], placement of horizontal bars into a printed layer along the printing direction and then covered by the next layer on top [20], and depositing around pre-installed bi-directional rebars [21]. However, in most approaches, the bonding between the rebar and concrete was compromised by the air void around the rebar [10,22]. To overcome this constraint, a large amount of trial and error is required, which is costly and time-consuming.

An approach to mitigate extensive experimental campaigns is to apply numerical models. In the context of 3D printing technologies, like Fused Filament Fabrication (FFF), Robocasting, and 3DCP, CFD modelling has been found to be very beneficial [23–25]. The morphology of the deposited strands in FFF was studied by Comminal et al. [26]. Furthermore, Serdeczny et al. [27,28] addressed how to reduce the porosities and enhance the bonding between subsequent layers. Mollah et al. [29,30] studied ways to minimize the deformation and thereby stabilize layers printed by Robocasting, while for 3DCP, the geometrical shapes of the single- and multiple-deposited layers have been investigated in detail in [31,32].

This paper uses the CFD model and extends the preliminary results recently published in [33]. The model uses elasto-viscoplastic constitutive equations to approximate the rheology of the concrete. The CFD model is validated by comparison with a number of experiments, and the model is subsequently exploited to make an in-depth analysis of air void formation between rebars and concrete using the cross-sections of the deposited part and the calculated volume fraction of air voids. Different material properties, such as yield stress and plastic viscosity, and processing parameters, like the rebar diameter, nozzle-rebar distance, a geometric ratio (i.e., the distance from nozzle to the substrate divided by the nozzle diameter), as well as a speed ratio (i.e., the printing speed divided by the extrusion speed) are varied. Section 2 describes the methodology of the study, along with the experimental and numerical details. Next, section 3 presents and discusses the results. Finally, section 4 summarizes the results with the conclusion.

2. Methodology

2.1. Materials' properties and 3DCP experiments

A fresh cement-based mortar was used to perform the 3DCP experiment around the rebars. The mortar includes a binder system with white cement CEM I 52.5 R-SR 5 (EA), limestone filler with sand of maximum particle size 0.5 mm, admixtures, and water. The binder was prepared with a 75 litres Eirich Intensive Mixer Type Ro8W. The water to cement ratio was 0.39. The admixtures dosage (by weight of cement) was set at 0.1% high-range water-reducing agent, 0.1% viscosity-modifying agent, and 0.5% hydration retarder. The mortar was designed to have an open time of about 2 hours, which led to time-independent rheological characteristics during the real printing process (which took 15 minutes).

The rheological characterization of the mortar was done using an Anton Paar rheometer MCR 502. The rotational and oscillatory tests were performed with a vane-in-cup measuring device. The obtained flow curve of the mortar from the rotational rheometric tests, with a ramp-down controlled shear rate (CSR), was fitted by a linear regression to determine the yield stress $\tau_y = 630$ Pa.s and plastic viscosity $\eta_p = 7.5$ Pa. The oscillatory test showed that the constitutive behavior of the unyielded mortar had a factorized relationship between the storage modulus G' and loss modulus G'' within the linear viscoelastic (LVE) region, where $G' = 200$ kPa was captured. Therefore, the mortar's rheology was modeled as a yield stress limited elasto-viscoplastic material, where the storage modulus is used as the linear elastic shear modulus of the unyielded mortar. The density of the mortar was $\rho = 2100$ kg/m³. Refer to [31,32] for more details on the rheological characterization.

The setup for 3DCP experiments around the rebars is presented in Figure 1. It comprised a 6-axis industrial robot (Fanuc R-2000iC/165F) with a custom-designed nozzle $\varnothing 20$ mm (i.e., nozzle diameter, $Dn = 20$ mm) made by fused filament fabrication of ABS thermoplastic, cf. Figure 1-a. The robot also included a progressive cavity pump (NETZSCH) equipped with a hopper and a long steel-wire rubber hose (cf. Refs. [31,32] for details). A 25 mm thick plywood plate was used as the built substrate as seen in Figure 1-b. The 1000 mm long rebars of diameter $Dr = 8$ and 12 mm were placed horizontally on top of the substrate at a distance $Hr = 14$ mm. The horizontal rebars were held in place by two vertical rebars with a height of 37 mm. The setup was used to print a structure of four successive layers of parallel strands around the rebars. Details on the printing toolpath around the rebars are illustrated in the subsections below.

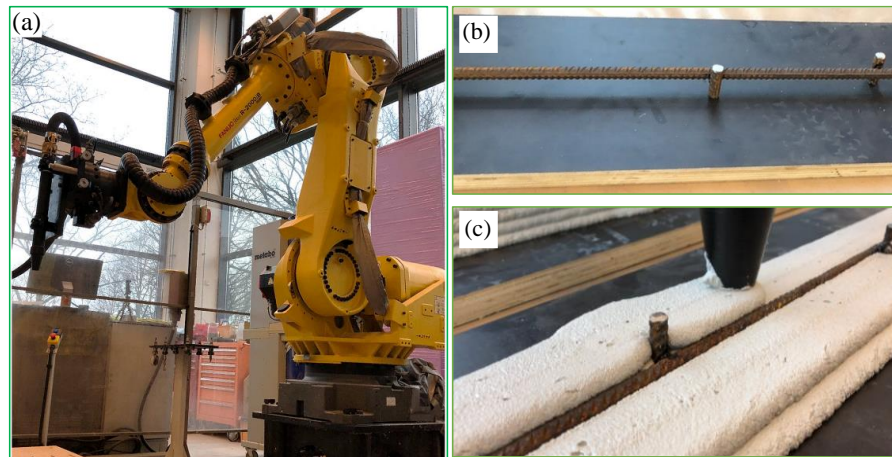


Figure 1: 3DCP experiment around rebars: (a) 6-axis robotic arm [31]; (b) plywood built platform with integrated rebars; (c) example of printing (picture is taken during printing of the third layer).

The extrusion nozzle was placed above the substrate with a nozzle height $Dn/2$ for the first layer, whereas for subsequent number of layers (Nl), the nozzle height was set at $Nl * Dn/2$. Thus, the nominal height of a layer was $h = Dn/2$. The print was done with a material extrusion rate $0.91 \text{ dm}^3/\text{min}$ and nozzle speed 35 mm/s . An example of a physical print is presented in Figure 1-c. After the prints hardened, cross-sections were collected to investigate the rebar-concrete bonding. The cross-section slices were taken at specific positions to analyze the print around the horizontal rebar and cross-shaped rebar (i.e., horizontal and vertical rebars). To avoid destroying the specimens while cutting them, the printed part were impregnated with epoxy resin in a vacuum chamber.

2.2. Computational models and governing equations

Three different CFD models are built. The first model only simulated the mortar flow to understand the void formation pattern without rebars. The last two models simulated the 3DCP experiment around rebars: one model simulated the mortar flow around the horizontal rebar, while the other considered the cross-shaped rebar. This subdivision enabled the CFD models to consider a smaller computational domain than if the two scenarios were combined.

The CFD models comprised a cylindrical nozzle, a solid-substrate, and an artificial solid component (at the top) within the computational domain of size $8.5D \times 6D \times (2D + 4h)$ as shown in Figure 2 (top), where Model 1 excluded rebars (left), Model 2 included the horizontal rebar (middle), and Model 3 considered the cross-shaped rebar (right). The printing toolpath of the models are illustrated in Figure 2. The toolpath for Models 1 and 2 are presented in 3D (left bottom figure), where the only difference was the presence of the horizontal rebar. The toolpath in 2D presented at the bottom right is for Model 3. For all the models, the toolpath of the extrusion nozzle kept a distance of D_{nr} from the axis of the nearest rebar. The lengths of the horizontal and vertical rebars were 50 and 40 mm, respectively. The other printing parameters were similar to the ones used in the experiment, cf. subsection 2.1. Finally, the models were used to simulate four successive layers with a length of 125 mm.

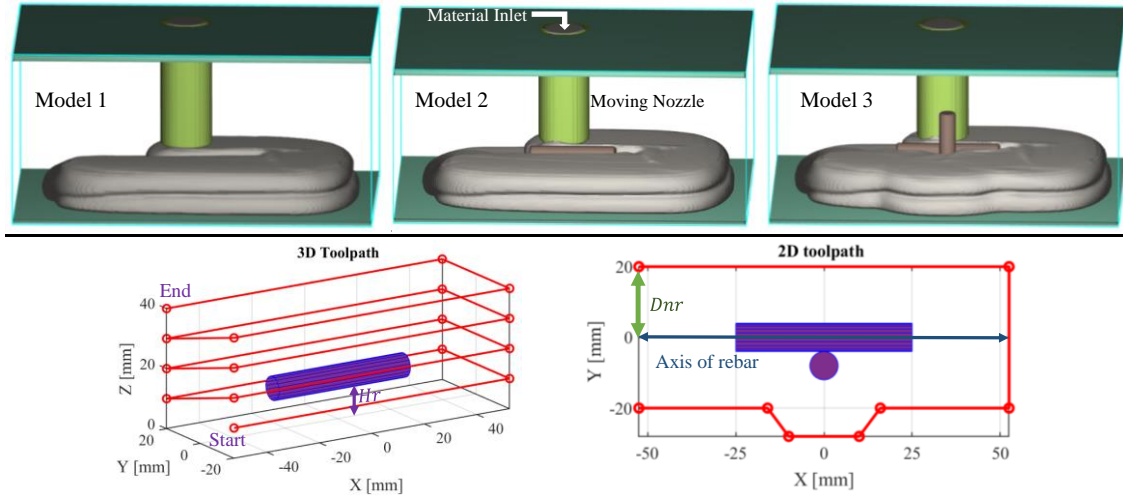


Figure 2: Model geometry with the extrusion nozzle, substrate, integrated rebars, and computational domain (top) and toolpath (bottom).

The computational domain was meshed by a uniform Cartesian grid. A mesh sensitivity test was performed for different meshes with cell sizes 0.9, 1.0, and 1.1 μm . Even if the change in absolute size of the cells were small, the total number of cells within the domain was 1.1, 1.5, and 2.0 million, respectively. A cell size of 1.0 μm was chosen as that was found to be time-efficient and had a negligible effect on the accuracy of the results. The top plane of the domain was an inlet boundary, where the artificial solid component was defined in order to prevent material flow outside the nozzle orifice, cf. Figure 2 (top). On the bottom plane, a wall boundary was applied to represent the solid substrate. The other planes were assigned continuative boundary conditions, but had no influence on the results. Furthermore, no-slip boundary conditions were applied between fluids and solids. Table 1 lists the printing parameters and their values for each of the investigated cases. All the models and cases are simulated for 4 successive layers.

Table 1: Description of case IDs with printing parameters and accompanying values. The reference values (corresponding to the experimental print) are written in bold, while the parameter change for each case is highlighted by underlining the value.

Model/ Case ID Parameters	Model 1 (no rebar), Model 2 (horizontal rebar), and Model 3 (cross-shaped rebar)								
	Case 1 (ref.)	Case 2	Case 3	Case 4	Case 5	Case 6	Case 7	Case 8	Case 9
Nozzle diameter D_n (mm)	20	20	20	20	20	20	20	20	20
Rebar diameter D_r (mm)	8	<u>6</u>	<u>12</u>	8	8	8	8	8	8
Nozzle-rebar distance D_{nr} (mm)	20	20	20	<u>19</u>	<u>18</u>	20	20	20	20
Layer height h (mm)	10	10	10	10	10	<u>9</u>	<u>8</u>	10	10
Geometric ratio $Gr = h/D_n$	0.5	0.5	0.5	0.5	0.5	<u>0.45</u>	<u>0.4</u>	0.5	0.5
Printing speed V (mm/s)	35	35	35	35	35	35	35	35	35
Extrusion speed U (mm/s)	48.42	48.42	48.42	48.42	48.42	48.42	48.42	<u>51.47</u>	<u>53.84</u>
Speed ratio $Sr = V/U$	0.72	0.72	0.72	0.72	0.72	0.72	0.72	<u>0.68</u>	<u>0.65</u>

The cementitious mortar flow was assumed transient and isothermal. Thus, the flow dynamics of the mortar are governed by the mass and momentum conservation equations of incompressible fluid:

$$\nabla \cdot \mathbf{u} = 0 \quad (1)$$

$$\rho \left(\frac{\partial \mathbf{u}}{\partial t} + \mathbf{u} \cdot \nabla \mathbf{u} \right) = -\nabla p + \rho \mathbf{g} + \nabla \cdot \boldsymbol{\sigma} \quad (2)$$

where \mathbf{u} is the velocity vector, ρ is the density, $\mathbf{g} = (0, 0, -g)$ is the gravitational acceleration vector, t is the time, p is the pressure, and $\boldsymbol{\sigma}$ is the deviatoric stress tensor.

The rheological behavior of the mortar was modelled by the following elasto-viscoplastic constitutive equation that represents $\boldsymbol{\sigma}$ as the sum of the deviatoric part of the viscous stress $\boldsymbol{\sigma}_V$ and elastic stress $\boldsymbol{\sigma}_E$ tensors; i.e.:

$$\boldsymbol{\sigma} = \boldsymbol{\sigma}_V + \boldsymbol{\sigma}_E \quad (3)$$

The deviatoric viscous stress tensor was predicted as:

$$\boldsymbol{\sigma}_V = 2\eta_P \mathbf{D}_T \quad (4)$$

where $\mathbf{D}_T = ((\nabla \mathbf{u}) + (\nabla \mathbf{u})^T)/2$ is the deformation rate tensor, and T represents the transpose notation.

The deviatoric elastic stress tensor was modelled by the Hookean assumption of a small strain rate tensor \mathbf{E} between each small time steps $\Delta t = t - t_0$, to represent the elastic response of unyielded materials $\boldsymbol{\sigma}_E^*$:

$$\boldsymbol{\sigma}_E^* = 2G \mathbf{E} \quad (5)$$

where G is the shear modulus and $\mathbf{E}(t) = \mathbf{E}(t_0) + \Delta t \mathbf{D}_T$ is the incremental strain rate tensor approximated by integrating the deformation rate tensor over Δt .

The incremental representation of Equation 5 can be written as:

$$\frac{\partial \boldsymbol{\sigma}_E^*}{\partial t} + \nabla \cdot (\mathbf{u} \boldsymbol{\sigma}_E^*) - (\boldsymbol{\sigma}_E^* \cdot \mathbf{W}_T + \mathbf{W}_T' \cdot \boldsymbol{\sigma}_E^*) = 2G \mathbf{D}_T \quad (6)$$

where $\mathbf{W}_T = ((\nabla \mathbf{u}) - (\nabla \mathbf{u})^T)/2$ is the vorticity tensor. The first term of the left-hand side of Equation 6 represents the change in stress at a fixed location in space. The change in stress due to advection and rotation of material particle is approximated by the second and third terms, respectively. The right-hand side takes into account the change in stress due to shearing.

The elastic stress tensor of the yielded material was approximated by imposing the yield stress τ_0 limit as follows:

$$\boldsymbol{\sigma}_E = \min \left(1, \frac{\tau_0}{\sigma_{vM}} \right) \boldsymbol{\sigma}_E^* \quad (7)$$

where σ_{vM} is the von Mises stress predicted as:

$$\sigma_{vM} = \sqrt{\frac{2}{3} II \boldsymbol{\sigma}_E^*} \quad (8)$$

where $II \boldsymbol{\sigma}_E^* = tr(\boldsymbol{\sigma}_E^{*2})$ is the second invariant of $\boldsymbol{\sigma}_E^*$. The material was yielded when σ_{vM} exceeded the yield stress. The properties of the material used in the different models and cases are presented in Table 2.

Table 2: Material properties.

Parameter with symbol	Unit	Value	Value for reference simulation
Density, ρ	kg. m ⁻³	2112	2112
Shear modulus, G	kPa	20 – 100	20
Dynamic yield stress, τ_0	Pa	400 – 800	630
Plastic viscosity, η_P	Pa.s	3.5 – 10	7.5

2.3. Numerical method

The computational model was developed in the commercial CFD tool **FLOW-3D**[®] (V12.0; Flow Science Inc.) [34]. It uses the FAVOR technique (Fractional Area/Volume Obstacle Representation) to embed solid objects (i.e., the nozzle, rebars, substrate, etc.) in the computational domain. The computational domain was meshed with a Cartesian grid and discretized with the Finite Volume Method.

The governing equations of the mortar flow were solved by the implicit pressure-velocity solver GMRES (Generalized Minimum Residual) [35–37]. The predictions of pressure and forces near solid objects were modelled by the immersed boundary method [38]. The yield stress limited elasto-viscoplastic criterion was built in the software, and the elastic stress was calculated explicitly. An implicit technique, successive under-relaxation, was used to solve the viscous stress of the momentum equation (equation 2). The free surface of the mortar was captured by the Volume-of-Fluid technique, see details in Ref. [39,40]. The momentum advection was calculated explicitly by an upwind-difference technique and ensured first-order accuracy. The time step size was controlled dynamically with a stability limit in order to avoid numerical instabilities [34]. All the simulations were run with 20 cores on a high-performance computing cluster. The study was carried out with a first-order accuracy in both space and time in order to reduce the computational time, which was extensive due to the elasto-viscoplastic material model (e.g., the computational time was six days for model 1 case 1).

2.4. Results post-processing

The simulated results were processed in two steps. The first step was to show the cross-sectional shapes which was done in the post-processing tool **FLOW-3D**[®] **POST**, and the second step was to calculate the volume fraction of air voids inside the printed structure. The cross-sectional shapes were used to investigate the interior of the structure and the rebar-concrete bonding. The cross-sectional shapes were obtained in the plane parallel to the yz- plane at the middle of the layer's length, as shown in Figure 3-d. Figure 3-c sketches the nominal positions of the air void creation in a four-layered structure. The positions of the air voids were defined as outer-bottom, bottom, mid, top, and outer-top in this study. The presence of the air void was quantified by calculating the volume fraction of air voids around the middle of the layer's length. The calculation enabled to capture the presence of air voids for Model 3, i.e., around the vertical rebar, as seen in the dashed-box of Figure 3-b.

In order to calculate the volume fraction of air voids, a cuboid of size $20 \times 25 \times 3h$ mm³ was introduced to the CFD models as a volume sampling object, as seen in Figure 3-a. Note that the size and position of the object were the same for all the models. The volume sampling was a three dimensional data collection tool built in the software that enabled calculating the amount of material as well as air void inside of it. Finally, the volume fraction of air voids V_v was calculated as below:

$$V_v = \frac{\text{Volume of air voids}}{\text{Volume of cuboid}} \times 100 \% \quad (9)$$

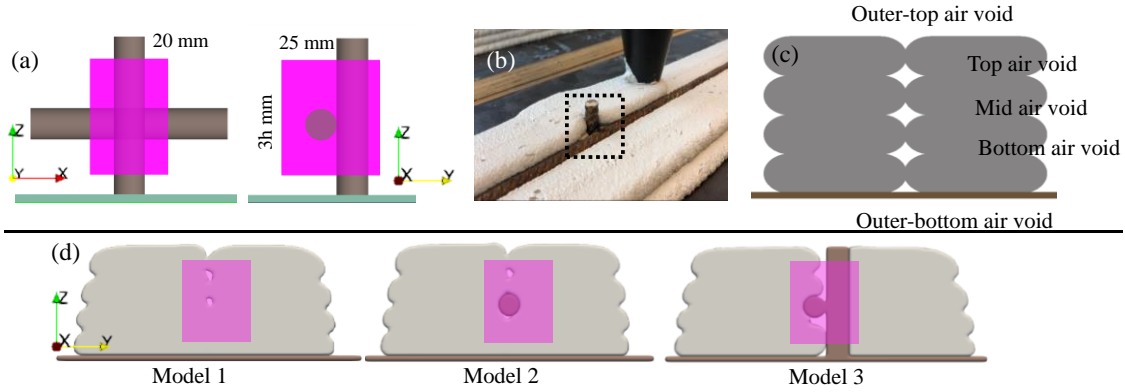


Figure 3: Post-processing of results; (a) Introduction of volume sampling cuboid to calculate the volume fraction of air voids; (b) Presence of air voids around the vertical rebar in the experiment; (c) Schematic of air void creation; (d) Cross-sectional shapes and void sampling area for the different models.

3. Results and discussions

This section compares the simulated and experimental results of 3DCP around the rebars. Furthermore, it discusses the influence of different parameters on the air void formation in the cross-sectional shapes of printed parts and the volume fraction of air voids inside the structure. The parametric study includes the material properties (i.e., yield stress and plastic viscosity) and the printing properties (i.e., rebar diameter, rebar-nozzle distance, geometric ratio, and speed ratio).

3.1. Experiments and validation of the CFD model

The CFD models (Models 2 and 3) are compared and validated with the experiments. The results are presented in Figures 4 and 5. Two rebar diameters, i.e., $Dr = 8$ and 12 mm, are taken into account, where the nozzle-rebar distances are 20 and 24 mm, respectively. The other printing and material parameters are kept constant in the experiments with different rebar diameters, see Table 1 (cases 1 and 3). In the case of the simulations, all parametric details are the same as implemented in the experiments except for the elastic shear modulus. The choice of shear modulus is subject to the following analysis.

The analysis varies the shear modulus (i.e., 20, 50, and 100 kPa) in the case $Dr = 8$ mm, as seen in Figure 4, which presents the cross-sectional shapes (top) and the volume fraction of air voids (bottom). It can be seen that increasing the shear modulus slightly reduces the air void formation. This is because the larger shear modulus enhances the ability of the material to act against the shear deformation. However, an increase in shear modulus also extensively increases the computational time of solving the non-linear elastic response of the elasto-viscoplastic material. For example, the computational time of Model 3 is about 6, 12, and 18 days for a shear modulus of 20, 50, and 100 kPa, respectively. Therefore, the shear modulus is reduced to 100 kPa from the measured value (i.e., 200 kPa) to compare the simulated results with experiments. Furthermore, the shear modulus 20 kPa is chosen for the parametric study in the later sections. These assumptions seem reasonable to avoid extensive computational time consumption since the differences found in Figure 4 are not substantial.

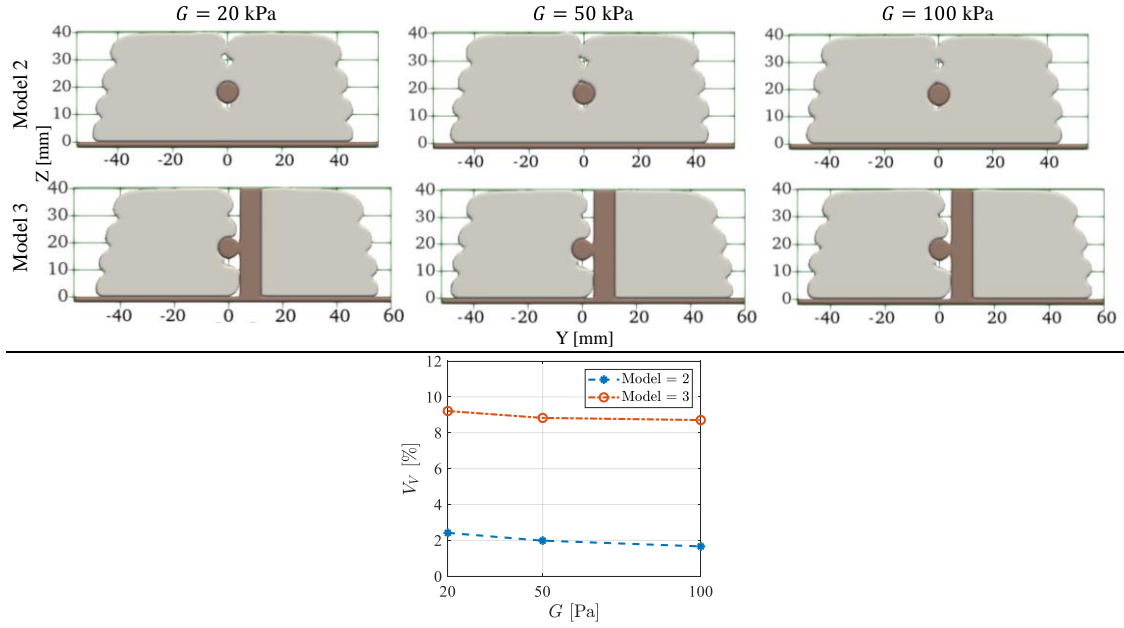


Figure 4: Air void formation in the cross-sections of the printed parts (top) and the volume fraction of air voids (bottom) for different shear modulus.

The cross-sectional shapes of the 3DCP experiments around the horizontal rebar of $Dr = 8$ mm in Figure 5-a illustrate the presence of a top air void as well as mid and bottom air voids positioned respectively above and below the horizontal rebar. The mid and bottom air voids are found to be smaller than the top one. This is due to the presence of the rebar that occupies the mortar's flowable space as well as the deformation of the previously printed layers. For a detailed analysis of the deformation pattern, refer to [33]. The air voids at the top and bottom are significant when the rebar diameter is increased to 12 mm (Figure 5-b). This is due to the fact that the nozzle-rebar distance was increased, which enhances the flowable space between the strands. In addition, the larger size of the rebar creates larger channels below and above itself, where the mortar of the second and third layers is forced to be squeezed into. The mid air void is found to be absent as its area is fully occupied by the larger rebar. In the case of the cross-shaped rebars, the existence of the vertical rebar seems to restrict the merging of parallel strands, and therefore, the presence of air void content increases, cf. Figure 5-c, d. This limitation is found to be pronounced for the larger rebar diameter with the larger nozzle-rebar distance.

The cross-sectional shapes of the simulations (middle column in Figure 5) illustrate high accuracy predictions of the position and size of the air voids when compared with the experiments. Particularly, the models capture small details around the vertical rebar for both diameters. This can clearly be seen in the comparison of experiments and simulation, cf. right column in Figure 5. However, a little discrepancy is found in the strand's width of the bottom layer as well as the shape of the printed part, specifically in the shape of strands of all the layers next to the vertical rebar and the height of the part for the smaller rebar diameter. These could be due to a combined effect of the idealized rheological model, as well as slight differences in the processing parameters, e.g. nozzle height above the printing surface, nozzle-rebar distance, as well as printing- and extrusion-speed. Note that the height of the vertical rebar in the experiments is a bit shorter than the one in the simulations (40 mm), although it does not influence the results.

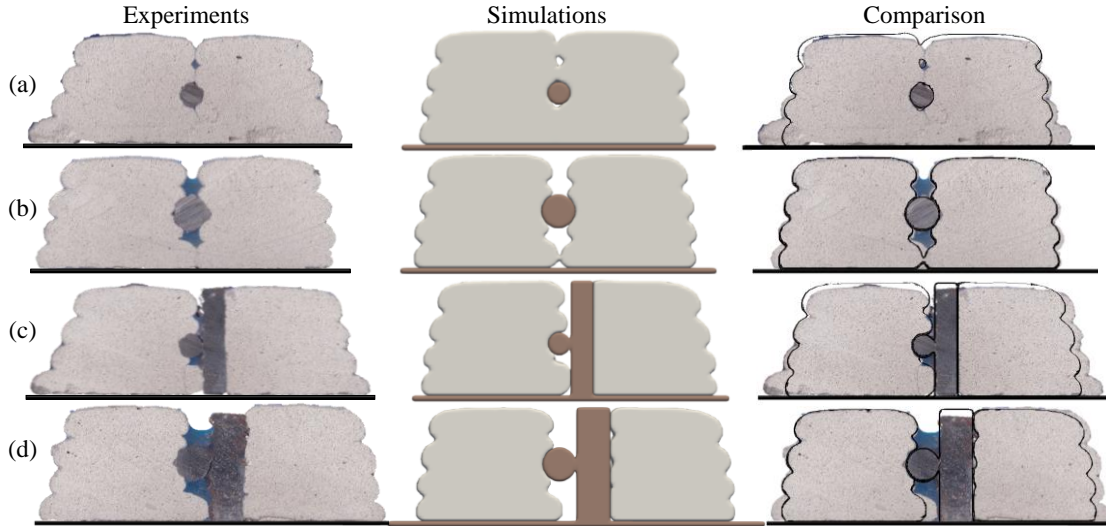


Figure 5: 3DCP experiments (left column), simulations (middle column), and comparison (right column). (a) Horizontal rebar with $Dr = 8$ mm and $Dnr = 20$ mm; (b) horizontal rebar with $Dr = 12$ mm and $Dnr = 24$ mm; (c) cross-shaped rebar with $Dr = 8$ mm and $Dnr = 20$ mm; and (d) cross-shaped rebar with $Dr = 12$ mm and $Dnr = 24$ mm. The blue part in the experiments is epoxy resin.

3.2. Influence of materials properties

Yield stress:

The process parameters of Case 1 (cf. Table 1) are utilized to investigate the influence of the yield stress on the air void formation. Models 1 and 2 predict a top air void, while for Model 3 the two topmost strands to the left are not in contact with the vertical rebar, see Figure 8. The cross-sections illustrate that an increased yield stress causes less deformation of the printed layers and creates strands with less round shape. This is due to the reduced effective gap (i.e., the distance between the nozzle and previous printed layer), which results in a reduced air void content for most models as seen quantitatively in Figure 9. An exception is seen in case of Model 2 with $\tau_0 = 800$ Pa, where the top air void is slightly larger as compared to the one for $\tau_0 = 630$ Pa. Another exception is that an outer bottom air void appears for Models 1 and 2 when increasing the yield stress to 800 Pa. Both exceptions are a consequence of the yield stress now restricting the flow in confined spaces, which illustrates that it is a non-trivial task to fully eradicate air voids only by increasing the yield stress.

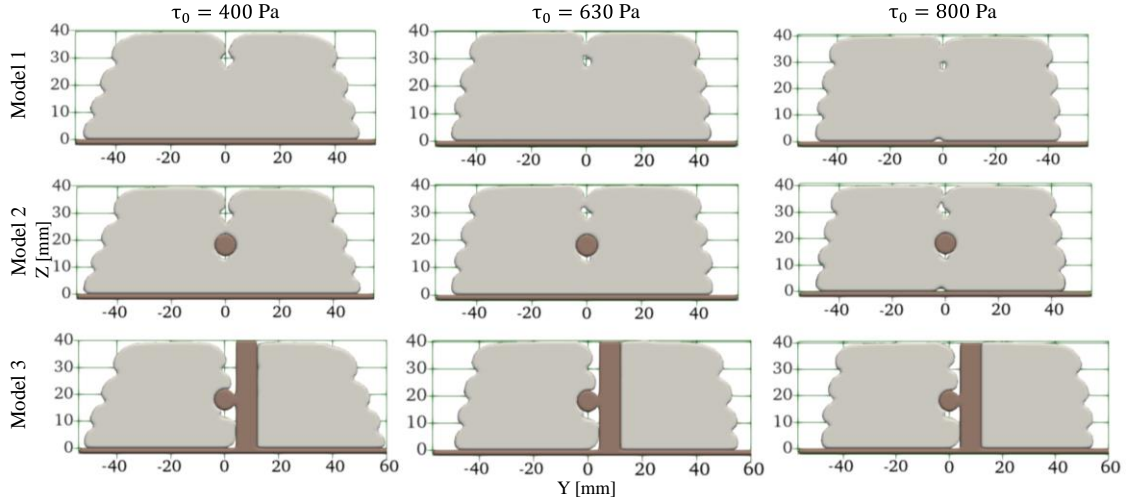


Figure 6: Air void formation in the cross-sections of the printed parts for different yield stress.

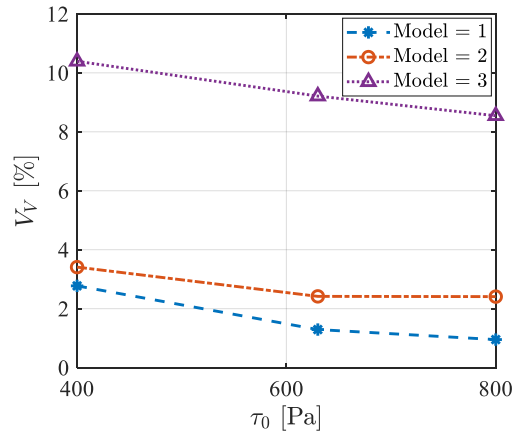


Figure 7: Volume fraction of air voids as a function of yield stress for different models.

Plastic viscosity:

The influence of the plastic viscosity on the air void formation is presented in Figures 10 and 11. All the models are simulated with Case 1, cf. Table 1. Figure 8 shows a slight change in air voids of Model 1. A mid air void is produced when the plastic viscosity is small, while the two largest plastic viscosities only produce the top air void. This is due to the increase in extrusion pressure that leads to larger deformation of the printed layers when the plastic viscosity is increased, cf. details in ref. [29]. When integrating a horizontal rebar (see Model 2), the air void formation increases at higher plastic viscosities. This could be due to the fact that the sideways flow of the depositing material (i.e., y-velocity) is limited by the flow resistance that comes from both the larger plastic viscosity and the presence of the solid rebar. No noticeable change can be seen in the cross-sections of Model 3 for different plastic viscosities. The same findings are quantitatively highlighted in Figure 11, which illustrates that the volume fraction of air voids is not influenced much by the plastic viscosity except for Model 2.

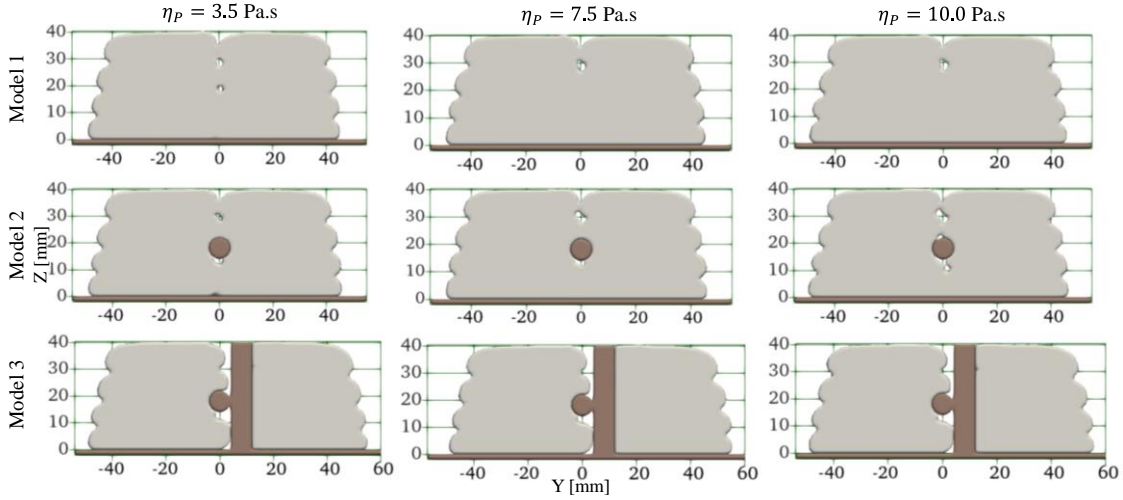


Figure 8: Air void formation in the cross-sections of the printed parts for different plastic viscosity.

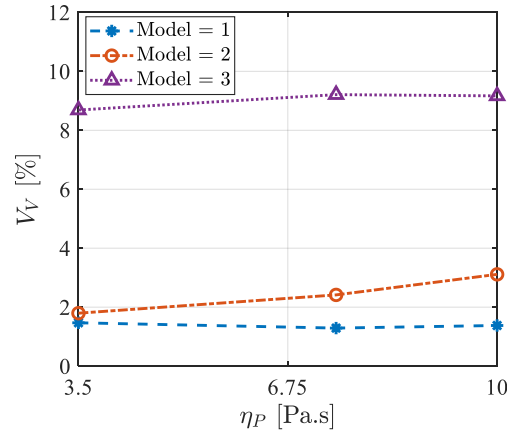


Figure 9: Volume fraction of air voids as a function of plastic viscosity for different models.

3.3. Influence of processing conditions

Rebar diameter:

The influence of the rebar diameter on the air void formation is presented in Figures 12 and 13. Models 2 and 3 are simulated (Model 1 does not contain a rebar) for Cases 1, 2, and 3 with the reference material properties, cf. Table 1 and Table 2. Figure 10 illustrates that the top air void appears almost constant for Model 2, whereas the air void below the rebar increases with an enlarged rebar diameter. Two phenomena with opposite effects on the void formation play a role in this regard. On the one hand, increasing the rebar size reduces the space that the strands need to occupy to fully merge and thereby eliminate voids. On the other hand, the resistance towards flow and merging of the parallel strands next to the rebar increases proportionally with the size of the reinforcement. The latter effect is dominating in this case. For Model 3, the air void formation also increases when increasing the reinforcement. In addition to the previously mentioned argument, this is due to the left strands having to flow longer to reach the vertical rebar (i.e., $D_{nr} + D_r/2$). Conversely, additional air voids take place on the right-hand side of the vertical rebar for the smallest rebar diameter, because the nozzle-rebar distance $D_{nr} = 20$ mm is kept

constant. Figure 13 underlines quantitatively that the volume fraction of air voids reduces when the rebar diameter is small. The trend is more pronounced for the cross-shaped rebar (Model 3), but in absolute values the air voids are substantially less for Model 2.

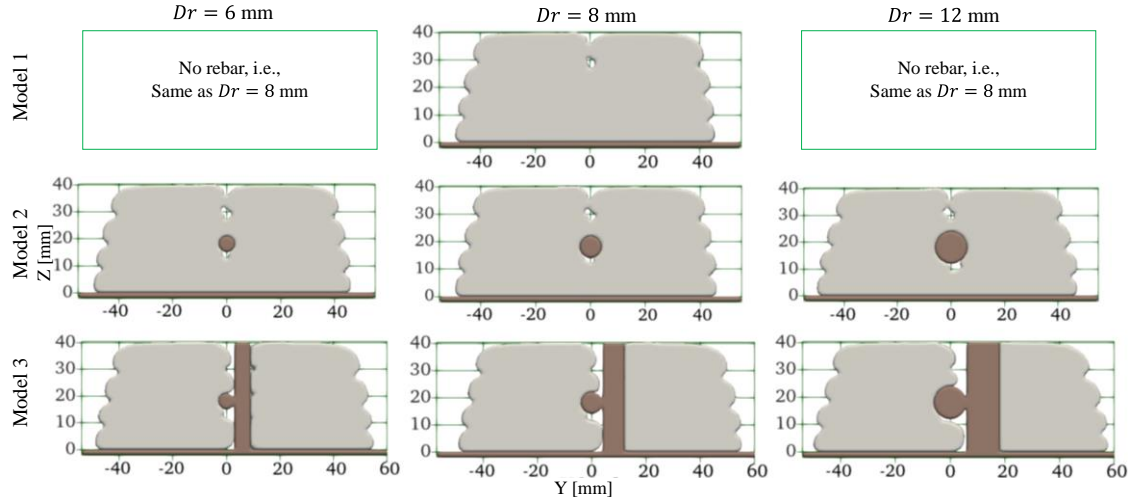


Figure 10: Air void formation in the cross-sections of the printed parts for different rebar diameters.

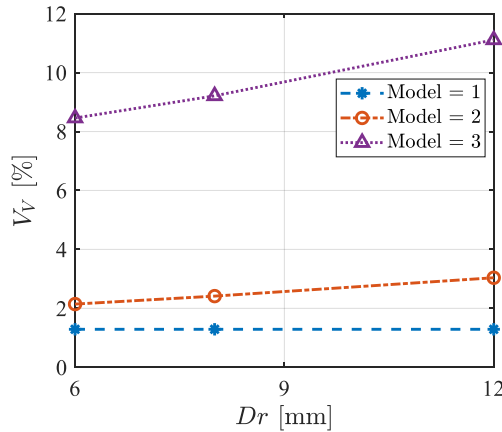


Figure 11: Volume fraction of air voids as a function of rebar diameter for different models.

Nozzle-rebar distance:

Figures 14 and 15 show the effect of different nozzle-rebar distances on the formation of air voids. All the models are simulated for Cases 1, 4, and 5, cf. Table 1. Figure 12 shows that the presence of air voids is reduced when the nozzle-rebar distance reduces. This is because the flowable space around the rebars shrink. Interestingly, no significant air voids are present in Model 1 and 2 when $Dnr = 18$ mm, see Figure 15. One should be careful though about decreasing the nozzle-rebar distance too much, as a ridge is forming on the top layer since material from the left strand starts to flow on top of the right strand (Figure 14), which potentially could affect the final shape of the structure. In case of the cross-shaped rebar model, air voids are formed for all investigated Dnr . One could potentially with benefit reduce the Dnr further, but not more than the sum of half of the nozzle

diameter (10 mm), the nozzle wall thickness (2.5 mm), and half of the rebar diameter (4 mm), i.e., 16.5 mm, otherwise the nozzle will collide with the rebar.

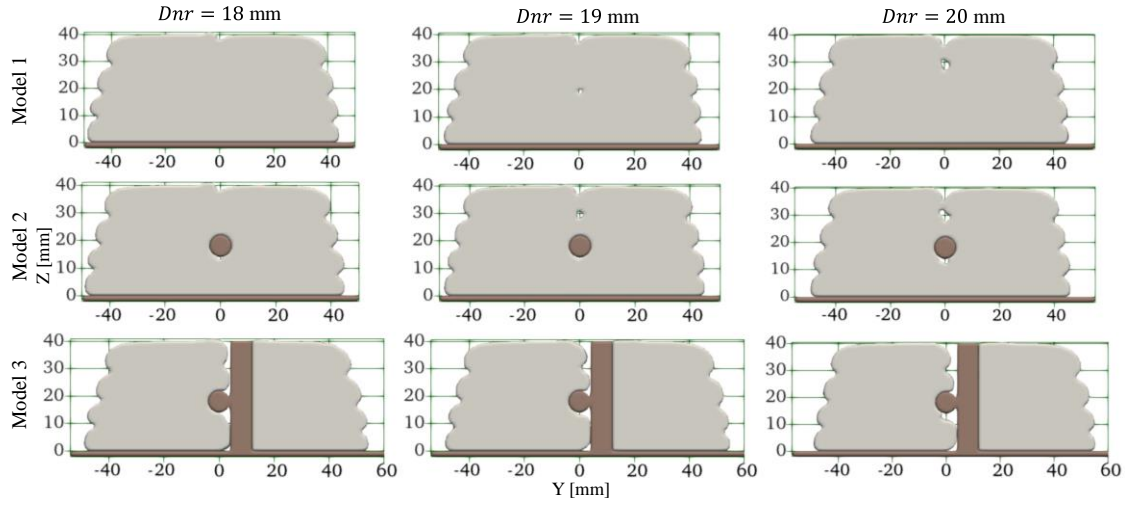


Figure 12: Air void formation in the cross-sections of the printed parts for different nozzle-rebar distances.

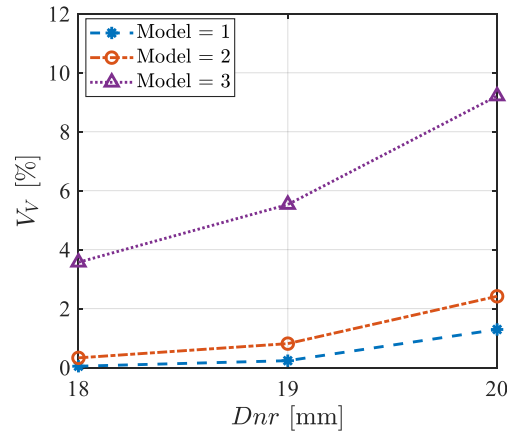


Figure 13: Volume fraction of air voids as a function of nozzle-rebar distance for different models.

Geometric ratio:

The effect of the geometric ratio on the formation of air voids is presented in Figures 16 and 17. The considered simulations are Cases 1, 6, and 7 cf. Table 1. Figure 14 illustrates that decreasing the geometric ratio can reduce the presence of air voids in the cross-sections. This is because a smaller geometric ratio results in wider strands, which then occupy more of the flowable space around the rebars. Note that when $Gr = 0.50$, 0.45 , and 0.40 the layer height is 10, 9, and 8 mm, respectively. No air voids are formed for Model 1 and 2 when $Gr = 0.45$, and 0.40 . However, for the smallest ratio ridges are obtained on either side of the strands as clearly seen for the top layer. These ridges can as previously mentioned have a negative effect on the final shape of the structure. Consequently, $Gr = 0.45$ is preferable for these two models. In the case of Model 3, air voids are still present next to the vertical rebar, even for the smallest investigated geometric ratio. The volume fraction of air voids is approximately 1.5 %, see Figure 17. The geometric ratio could be reduced further in order to decrease the air voids even more,

but the ridges already form at $Gr = 0.40$. Consequently, it is not possible to fully eliminate air voids while at the same time avoiding ridges when only varying the geometric ratio for Model 3.

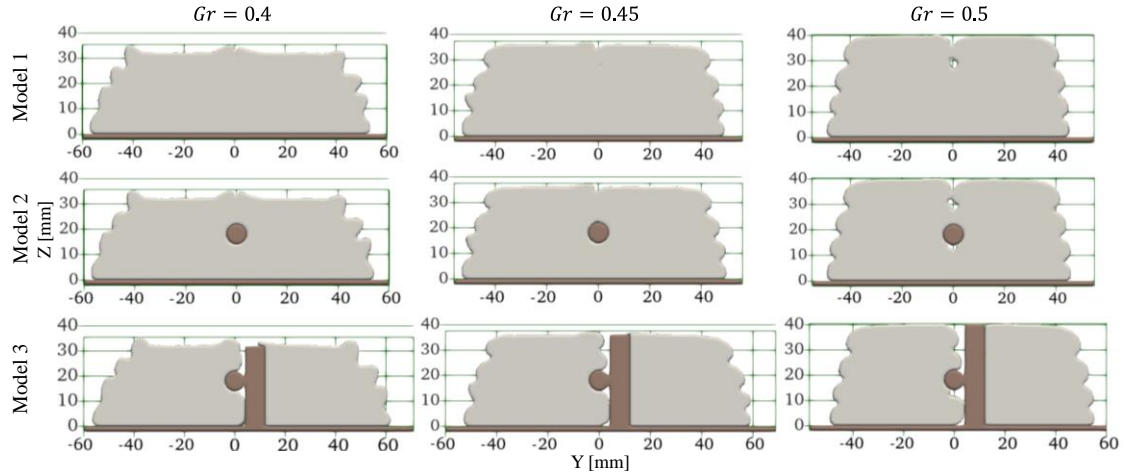


Figure 14: Air void formation in the cross-sections of the printed parts for different geometric ratios.

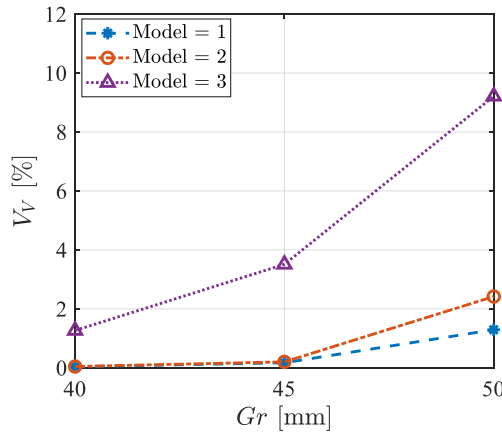


Figure 15: Volume fraction of air voids as a function of geometric ratio for different models.

Speed ratio:

Figures 18 and 19 illustrate the formation of air voids for different speed ratios. The considered simulations are Case 1, Case 8, and Case 9, cf. Table 1. The three speed ratios are obtained by applying an extrusion speed of 48.4 mm/s, 51.5 mm/s, and 53.8 mm/s. Figures 18 and 19 show that less air voids are formed when decreasing the speed ratio (i.e., higher extrusion speed). Reducing the speed ratio increases the cross-sectional area of the strands proportionally, thereby decreasing the air voids. Model 1 obtains no air voids for the two smallest ratios, and the same is almost the case for Model 2; only a very small air void is formed when $Sr = 0.68$. Model 3 forms air voids for all speed ratios. For the lowest speed ratio, the third strand to the left is in contact with the vertical rebar, but air voids are still formed around the horizontal reinforcement, which underlines the fact that it is difficult to fully eliminate air voids for the cross-shaped rebars.

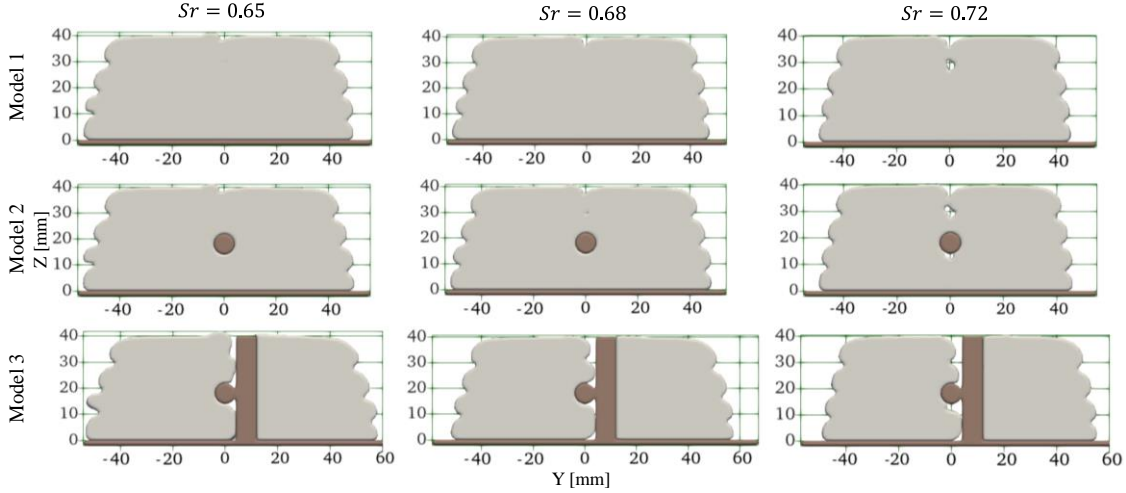


Figure 16: Air void formation in the cross-sections of the printed parts for different speed ratios.

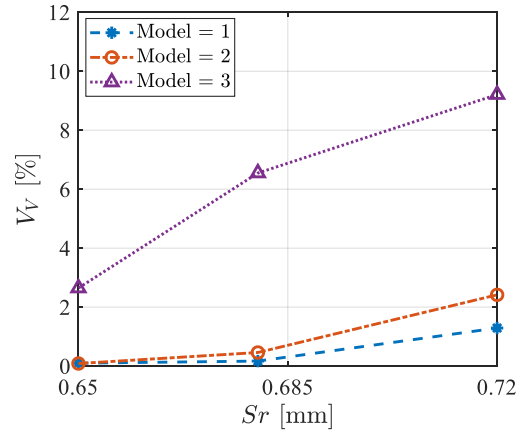


Figure 17: Volume fraction of air voids as a function of speed ratio for different models.

3.4. Cross-shaped reinforcement

Based on the above analysis, it is clear that the air voids around the horizontal rebar can be eliminated by changing some of the processing conditions, such as the nozzle-rebar distance, geometric ratio, and speed ratio. However, it remains unsolved to fully omit the presence of air voids around the cross-shaped rebar, although the processing conditions can reduce the volume fraction of air voids. In order to solve this predicament, a new stepped toolpath is investigated (see Figure 20) along with three different rebar geometries: 1) cylindrical rebars as in the previous analysis; 2) a squared horizontal rebar, cf. Figure 21-b; and 3) cylindrical rebars with a smooth transition between them, see Figure 21-c. In all scenarios, the speed ratio is 0.665, the size (i.e., diameter or side of square) of the rebars are 6 mm, and the horizontal rebar is placed at a height of 8 mm from the substrate. The other processing parameters are the same as for Case 2 and reference material properties are applied. For scenarios one and two small air voids are formed, but for scenario three air voids are eliminated, see Figure 21. This illustrates that although it is difficult to get rid of air voids for the cross-shaped rebars, one can do it when carefully selecting the material- and processing-parameters and remembering to have a smooth transition between the rebars.

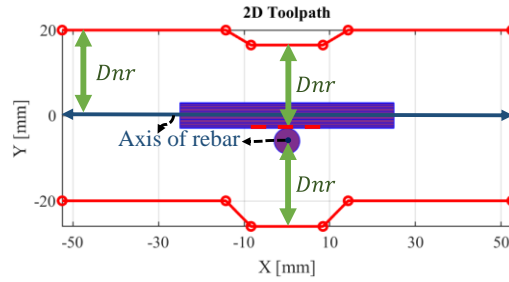


Figure 18: New toolpath planning around the cross-shaped rebar.

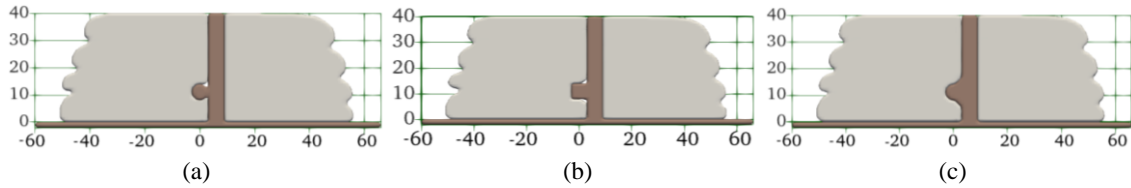


Figure 19: Simulated structure with new toolpath and different rebar geometries. (a) Cylindrical horizontal- and vertical-rebar, (b) square horizontal rebar and cylindrical vertical rebar, (c) cylindrical horizontal- and vertical-rebar with smooth transition. Note that $Dr = 6$ mm, $Sr = 0.665$, and $Hr = 8$ mm.

4. Conclusions

A CFD model was used to predict the morphology of strands and the formation of air voids around reinforcement bars when integrated with 3DCP. The model used an elasto-viscoplastic constitutive model to mimic the cementitious mortar flow. The CFD model was compared with experiments that constituted a horizontal and a cross-shaped rebar configuration. The results illustrated that the model with high-accuracy could predict the air void formation in the structures. The simulations had though slightly less wide bottom strands as compared to the experimental counterpart, which was attributed to small differences in material behavior and processing parameters.

The CFD model was exploited to investigate the effect of material properties on the air void formation. The results illustrated that by increasing the yield stress less air voids were formed due to the reduced effective gap. However, the air voids could not be eliminated as the increased yield stress also restricted the flow in confined spaces. In contrast to the effect of the yield stress, the void formation decreased somewhat when decreasing the plastic viscosity (although not enough to omit air voids fully).

The process parameters were found to have a substantial effect on the air void formation. The air void formation increased when increasing the rebar diameter, because the resistance towards flow around the reinforcement and thereby merging of the strands increased proportional with the size of the rebars. The air voids could be reduced and in some of the horizontal cases fully avoided by reducing the nozzle-rebar distance, but it could come with the expense of ridges (which could affect the final geometry of the structure), since material from one strand would flow on top of a previously deposited strand. Similarly, decreasing the geometric ratio was found to reduce the presence of air voids, because a smaller geometric ratio resulted in wider strands that occupied more of the space around the rebars. However, the smallest ratios also resulted in ridges. It was also found that less air voids were formed when decreasing the speed ratio, since the

cross-sectional area of the strands increased proportionally, thereby occupying more space around the rebars.

By decreasing the nozzle-rebar distance, geometric ratio, and speed ratio, voids were omitted around the horizontal rebar, but air voids would still be introduced for the cross-shaped rebar. Those air voids could be eliminated by changing the toolpath and some processing parameters, as well as altering the geometry of the reinforcement joint to a smooth transition between the horizontal and vertical rebar. The results highlight that it is non-trivial to avoid air voids when integrating rebars in 3DCP, but that the CFD model is a very strong digital tool when it comes to securing a good bonding between the reinforcement and concrete.

Acknowledgements

The authors would like to acknowledge the support of the Danish Council for Independent Research (DFF) | Technology and Production Sciences (FTP) (Contract No. 8022-00042B). Also, the authors would like to acknowledge the support of the Innovation Fund Denmark (Grant No. 8055-00030B: Next Generation of 3D-printed Concrete Structures and Grant no. 0223-00084B: ThermoForm - Robotic ThermoSetting Printing of Large-Scale Construction Formwork), Moreover, the support of FLOW-3D regarding licenses is acknowledged.

References

- [1] B. Khoshnevis, R. Russel, H. Kwon, S. Bukkapatnam, Contour crafting—a layered fabrication technique, *Spec. Issue IEEE Robot. Autom. Mag.* 8 (2001) 33–42.
- [2] R.A. Buswell, W.R.L. da Silva, F.P. Bos, H.R. Schipper, D. Lowke, N. Hack, H. Kloft, V. Mechtcherine, T. Wangler, N. Roussel, A process classification framework for defining and describing Digital Fabrication with Concrete, *Cem. Concr. Res.* 134 (2020) 106068. <https://doi.org/10.1016/j.cemconres.2020.106068>.
- [3] B. Khoshnevis, Automated construction by contour crafting—related robotics and information technologies, *Autom. Constr.* 13 (2004) 5–19. <https://doi.org/10.1016/j.autcon.2003.08.012>.
- [4] R. Hague, I. Campbell, P. Dickens, Implications on design of rapid manufacturing, *Proc. Inst. Mech. Eng. Part C J. Mech. Eng. Sci.* 217 (2003) 25–30. <https://doi.org/10.1243/095440603762554587>.
- [5] Meet ICON's next generation Vulcan construction system., ICON. (n.d.). <https://www.iconbuild.com/vulcan> (accessed July 10, 2022).
- [6] FABRICANT D'IMPRIMANTES 3D POUR LA CONSTRUCTION AUTOMATISÉE DE BÂTIMENTS, *Constr.-3D*. (n.d.). <https://www.constructions-3d.com/> (accessed July 9, 2022).
- [7] 3dWasp, 3dWasp. (n.d.). <https://www.3dwasp.com/> (accessed August 12, 2022).
- [8] G. Ma, R. Buswell, W.R. Leal da Silva, L. Wang, J. Xu, S.Z. Jones, Technology readiness: A global snapshot of 3D concrete printing and the frontiers for development, *Cem. Concr. Res.* 156 (2022) 106774. <https://doi.org/10.1016/j.cemconres.2022.106774>.
- [9] F.P. Bos, C. Menna, M. Pradena, E. Kreiger, W.R.L. da Silva, A.U. Rehman, D. Weger, R.J.M. Wolfs, Y. Zhang, L. Ferrara, V. Mechtcherine, The realities of additively manufactured concrete structures in practice, *Cem. Concr. Res.* 156 (2022) 106746. <https://doi.org/10.1016/j.cemconres.2022.106746>.

- [10] B. Baz, G. Aouad, P. Leblond, O. Al-Mansouri, M. D'hondt, S. Remond, Mechanical assessment of concrete – Steel bonding in 3D printed elements, *Constr. Build. Mater.* 256 (2020) 119457. <https://doi.org/10.1016/j.conbuildmat.2020.119457>.
- [11] G. Ma, Z. Li, L. Wang, G. Bai, Micro-cable reinforced geopolymer composite for extrusion-based 3D printing, *Mater. Lett.* 235 (2019) 144–147. <https://doi.org/10.1016/j.matlet.2018.09.159>.
- [12] Z. Li, L. Wang, G. Ma, Mechanical improvement of continuous steel microcable reinforced geopolymer composites for 3D printing subjected to different loading conditions, *Compos. Part B Eng.* 187 (2020) 107796. <https://doi.org/10.1016/j.compositesb.2020.107796>.
- [13] A.R. Arunothayan, B. Nematollahi, R. Ranade, S.H. Bong, J. Sanjayan, Development of 3D-printable ultra-high performance fiber-reinforced concrete for digital construction, *Constr. Build. Mater.* 257 (2020) 119546. <https://doi.org/10.1016/j.conbuildmat.2020.119546>.
- [14] B. Nematollahi, P. Vijay, J. Sanjayan, A. Nazari, M. Xia, V. Naidu Nerella, V. Mechtcherine, Effect of Polypropylene Fibre Addition on Properties of Geopolymers Made by 3D Printing for Digital Construction, *Materials*. 11 (2018) 2352. <https://doi.org/10.3390/ma11122352>.
- [15] V. Mechtcherine, J. Grafe, V.N. Nerella, E. Spaniol, M. Hertel, U. Füssel, 3D-printed steel reinforcement for digital concrete construction – Manufacture, mechanical properties and bond behaviour, *Constr. Build. Mater.* 179 (2018) 125–137. <https://doi.org/10.1016/j.conbuildmat.2018.05.202>.
- [16] J. Müller, M. Grabowski, C. Müller, J. Hensel, J. Unglaub, K. Thiele, H. Kloft, K. Dilger, Design and Parameter Identification of Wire and Arc Additively Manufactured (WAAM) Steel Bars for Use in Construction, *Metals*. 9 (2019) 725. <https://doi.org/10.3390/met9070725>.
- [17] T. Marchment, J. Sanjayan, Mesh reinforcing method for 3D Concrete Printing, *Autom. Constr.* 109 (2020) 102992. <https://doi.org/10.1016/j.autcon.2019.102992>.
- [18] V. Mechtcherine, R. Buswell, H. Kloft, F.P. Bos, N. Hack, R. Wolfs, J. Sanjayan, B. Nematollahi, E. Ivaniuk, T. Neef, Integrating reinforcement in digital fabrication with concrete: A review and classification framework, *Cem. Concr. Compos.* 119 (2021) 103964. <https://doi.org/10.1016/j.cemconcomp.2021.103964>.
- [19] T. Marchment, J. Sanjayan, Bond properties of reinforcing bar penetrations in 3D concrete printing, *Autom. Constr.* 120 (2020) 103394. <https://doi.org/10.1016/j.autcon.2020.103394>.
- [20] V2 Vesta Beton-3D-Drucker baut kleines Haus, (n.d.). <https://3druck.com/drucker-und-produkte/v2-vesta-beton-3d-drucker-baut-kleines-haus-2846225/> (accessed October 27, 2022).
- [21] M. Classen, J. Ungermann, R. Sharma, Additive Manufacturing of Reinforced Concrete—Development of a 3D Printing Technology for Cementitious Composites with Metallic Reinforcement, *Appl. Sci.* 10 (2020) 3791. <https://doi.org/10.3390/app10113791>.
- [22] L. Gebhard, L. Esposito, C. Menna, J. Mata-Falcón, Inter-laboratory study on the influence of 3D concrete printing set-ups on the bond behaviour of various reinforcements, *Cem. Concr. Compos.* 133 (2022) 104660. <https://doi.org/10.1016/j.cemconcomp.2022.104660>.
- [23] M.P. Serdeczny, R. Comminal, D.B. Pedersen, J. Spangenberg, Experimental validation of a numerical model for the strand shape in material extrusion additive

- manufacturing, Addit. Manuf. 24 (2018) 145–153. <https://doi.org/10.1016/j.addma.2018.09.022>.
- [24] H. Xia, J. Lu, G. Tryggvason, A numerical study of the effect of viscoelastic stresses in fused filament fabrication, *Comput. Methods Appl. Mech. Eng.* 346 (2019) 242–259. <https://doi.org/10.1016/j.cma.2018.11.031>.
- [25] M.T. Mollah, M.P. Serdeczny, R. Comminal, B. Šeta, M. Brander, J. Spangenberg, A Numerical Investigation of the Inter-Layer Bond and Surface Roughness during the Yield Stress Buildup in Wet-On-Wet Material Extrusion Additive Manufacturing, in: 2022 Summer Top. Meet. Adv. Precis. Addit. Manuf., American Society for Precision Engineering, 2022: pp. 131–134.
- [26] R. Comminal, M.P. Serdeczny, D.B. Pedersen, J. Spangenberg, Numerical modeling of the strand deposition flow in extrusion-based additive manufacturing, *Addit. Manuf.* 20 (2018) 68–76. <https://doi.org/10.1016/j.addma.2017.12.013>.
- [27] M.P. Serdeczny, R. Comminal, D.B. Pedersen, J. Spangenberg, Numerical prediction of the porosity of parts fabricated with fused deposition modeling, in: *Proc. Annu. Int. Solid Free. Fabr. Symp., Laboratory for Freeform Fabrication*, n.d.: pp. 1849–1854.
- [28] M.P. Serdeczny, R. Comminal, D.B. Pedersen, J. Spangenberg, Numerical simulations of the mesostructure formation in material extrusion additive manufacturing, Addit. Manuf. 28 (2019) 419–429. <https://doi.org/10.1016/j.addma.2019.05.024>.
- [29] M.T. Mollah, R. Comminal, M.P. Serdeczny, D.B. Pedersen, J. Spangenberg, Stability and deformations of deposited layers in material extrusion additive manufacturing, Addit. Manuf. (2021) 102193. <https://doi.org/10.1016/j.addma.2021.102193>.
- [30] M.T. Mollah, R. Comminal, M.P. Serdeczny, D.B. Pedersen, J. Spangenberg, Numerical Predictions of Bottom Layer Stability in Material Extrusion Additive Manufacturing, *JOM*. (2022). <https://doi.org/10.1007/s11837-021-05035-9>.
- [31] R. Comminal, W.R. Leal da Silva, T.J. Andersen, H. Stang, J. Spangenberg, Modelling of 3D concrete printing based on computational fluid dynamics, *Cem. Concr. Res.* 138 (2020) 106256. <https://doi.org/10.1016/j.cemconres.2020.106256>.
- [32] J. Spangenberg, W.R. Leal da Silva, R. Comminal, M.T. Mollah, T.J. Andersen, H. Stang, Numerical simulation of multi-layer 3D concrete printing, *RILEM Tech. Lett.* 6 (2021) 119–123. <https://doi.org/10.21809/rilemtechlett.2021.142>.
- [33] J. Spangenberg, W.R. Leal da Silva, M.T. Mollah, R. Comminal, T. Juul Andersen, H. Stang, Integrating Reinforcement with 3D Concrete Printing: Experiments and Numerical Modelling, in: R. Buswell, A. Blanco, S. Cavalaro, P. Kinnell (Eds.), *Third RILEM Int. Conf. Concr. Digit. Fabr.*, Springer International Publishing, Cham, 2022: pp. 379–384. https://doi.org/10.1007/978-3-031-06116-5_56.
- [34] FLOW-3D® Version 12.0 [Computer software], (2019). <https://www.flow3d.com> (accessed May 10, 2022).
- [35] S.F. Ashby, T.A. Manteuffel, P.E. Saylor, A Taxonomy for Conjugate Gradient Methods, *SIAM J. Numer. Anal.* 27 (1990) 1542–1568. <https://doi.org/10.1137/0727091>.
- [36] R. Barrett, M. Berry, T.F. Chan, J. Demmel, J.M. Donato, J. Dongarra, V. Eijkhout, R. Pozo, C. Romine, H.V.D. Vorst, *Templates for the Solution of Linear Systems: Building Blocks for Iterative Methods*, 1994.

- [37] Y. Saad, Iterative Methods for Sparse Linear Systems, The PWS Series in Computer Science, 1996. <http://books.google.com/books?id=jLtiQgAACAAJ>.
- [38] Modeling Capabilities- Immersed Boundary Method | FLOW-3D | Solving The World's Toughest CFD Problems, FLOW Sci. (n.d.). <https://www.flow3d.com/modeling-capabilities/immersed-boundary-method/> (accessed August 21, 2021).
- [39] C.W. Hirt, B.D. Nichols, Volume of fluid (VOF) method for the dynamics of free boundaries, J. Comput. Phys. 39 (1981) 201–225. [https://doi.org/10.1016/0021-9991\(81\)90145-5](https://doi.org/10.1016/0021-9991(81)90145-5).
- [40] R. Comminal, J. Spangenberg, J.H. Hattel, Cellwise conservative unsplit advection for the volume of fluid method, J. Comput. Phys. 283 (2015) 582–608. <https://doi.org/10.1016/j.jcp.2014.12.003>.

DTU Construct
Section of Manufacturing Engineering
Technical University of Denmark

Produktionstorvet, Bld. 425
DK-2800 Kgs. Lyngby
Denmark
Tlf.: +45 4525 4763
Fax: +45 4525 1961

www.construct.dtu.dk

February 2023

ISBN: 978-87-7475-718-4